Techniques and Applications for Satellite SAR Altimetry over water, land and ice

Heft 56 Darmstadt, Januar 2020
Schriftenreihe der Fachrichtung Geodäsie
Fachbereich Bau- und Umweltingenieurwissenschaften
Technische Universität Darmstadt
ISBN 978-3-935631-45-7

TECHNISCHE
UNIVERSITÄT
DARMSTADT

Heft 56

Darmstadt, Januar 2020

Salvatore Dinardo

Techniques and Applications for Satellite SAR Altimetry over water, land and ice

Schriftenreihe

Fachrichtung Geodäsie

Fachbereich Bau- und Umweltingenieurwissenschaften

Technische Universität Darmstadt

ISBN 978-3-935631-45-7

Techniques and Applications for Satellite SAR Altimetry over water, land and ice

Vom Fachbereich Bau- und Umweltingenieurwissenshaften

der Technischen Universität Darmstadt

zur Erlangung des akademischen Grades eines

Doktor-Ingenieurs (Dr-Ing.) genehmigte Dissertation

vorgelegt von:

Salvatore Dinardo, M.Sc.

aus Neapel

Referent: Prof. Dr-Ing. Matthias Becker

1. Korreferent: Dr. Jérôme Benveniste

2. Korreferent: Dr. Luciana Fenoglio-Marc

Tag der Einreichung: 22 Januar 2019

Tag der mündlichen Prüfung: 15 März 2019

Darmstadt, Januar 2020
D17

Schriftenreihe Fachrichtung Geodäsie der Technischen Universität Darmstadt

Online unter: http://tuprints.ulb.tu-darmstadt.de/id/eprint/11343

Verantwortlich für die Herausgabe der Schriftenreihe:

Der Sprecher der Fachrichtung Geodäsie
im Fachbereich Bau- und Umweltingenieurwissenschaften
der Technischen Universität Darmstadt

Bezugsnachweis:

Technische Universität Darmstadt
Institut für Geodäsie
Franziska-Braun-Str. 7
64287 Darmstadt

ISBN 978-3-935631-45-7

Zusammenfassung

Diese Arbeit hat die Entwicklung von neuen Prozessierungstechniken für die Synthetic Aperture Radar (SAR) Satellitenaltimetrie zum Ziel. Satellitenaltimetrie misst die Höhe eines flächen- oder punkthaften Zieles auf der Erde unter Ausnutzung des Doppler-Effektes zwischen Satellit und Ziel. SAR hat die beleuchtete Fläche (Footprint) in Flugrichtung um eine Größenordnung gegenüber dem klassischen Radar verringert und dadurch eine wesentlich bessere Auflösung und Genauigkeit erhalten. Diese Technik ist für Anwendungen auf dem offenen Ozean etabliert und validiert. Hier werden nun neue Algorithmen entwickelt, die es erlauben, die Vorteile von SAR universell für die Anwendung über Ozean, Küstenzone, Inland-Wasserflächen und See-Eis zu nutzen. Neben der Bestimmung des globalen Meeresspiegelanstiegs und der regionalen Variabilität kann so vor allem der Beitrag bisher kaum berücksichtigter kurzskaliger und hochfrequenter Änderungen in der Küstenzone zur Gesamtbilanz in der Untersuchung von Klimawandel und Bedrohung durch Fluten.

Dazu wird die Standard SAR-Altimetrie Prozessierungskette mit speziellen Ansätzen und Erweiterungen des Delay-Doppler-Algorithmus in der Prozessierung der L1b-Daten ergänzt. Damit wurden die Algorithmen für das Re-Tracking der Wellenformen nach dem standardisierten physikalisch basierten SAR-Wellenformmodell SAMOSA von Ray et al., (2015) verbessert. Durch Einführung einer Look-Up Tabelle und damit einer standardisierten Analyse wird eine genauere Ableitung der geophysikalischen Größen (Meereshöhe, Wind, Wellenhöhe) für den offenen Ozean möglich. Darauf aufbauend wurde ein speziell für die Küstenzone zugeschnittener Algorithmus mit dem Namen SAMOSA+ entwickelt. Umfangreichen Validierungen bestätigen eine signifikante Verbesserung in der Küstenzone durch dieses spezielle SAR-Retracking. Dieser Retracker ist auch in die Prozessierung der nominellen ESA-Produkte des Bodensegmentes einbezogen worden. Darüber hinaus derselbe Algorithmus ebenso erstmals mit einem physisch basierten Retracker sehr genaue Messungen des Meereis-Freibords.

Um auch eine von SAMOSA+ nicht gewährleistete optimale Erfassung von Inland-Gewässern, Flüssen und Seen zu erreichen, wurden der Algorithmus erneut verbessert. Die Weiterentwicklung, als SAMOSA++ bezeichnet, berücksichtigt diemit SAR verfügbare und bisher kaum genutzte Range Integrated Power (RIP), die als zusätzliche Wellenform betrachtet werden kann. Dadurch konnte eine universelle Anwendbarkeit des Re-Trackers erreicht werden. Dies wird an verschiedenen thematischen Anwendungen wie Meeresoberflächen sowohl im offenen Ozean als auch in Küstengebieten und an zwei ausgewählten Testfällen von Binnengewässern präsentiert. Ein Vergleich mit den bisherigen Re-Trackern zeigt deutlich eine signifikante Verbesserung in allen Anwendungsbereichen gegenüber den bisherigen Verfahren. Als Vergleich dienten In Situ Daten, numerische Ozeanmodelle und Datensätze aus der herkömmlichen prä-SAR Methode zur Verarbeitung von Altimeterdaten, allgemein als PLRM bezeichnet.

Die neuen Algorithmen wurden erfolgreich im ESA-GPOD Bodensegment implementiert und werden heute weltweit von der Altimetrie-Benutzergemeinschaft verwendet.

SUMMARY

This thesis deals with proposing novel processing techniques with applications in the field of Satellite Synthetic Aperture Radar (SAR) Altimetry. Satellite SAR Altimetry is the technique capable of measuring the altitude of a target (as ocean, coastal waters, sea ice, inland waters, etc.) on Earth from space exploiting the Doppler effect between the satellite and the target. The thesis is based essentially on the exploitation and processing of SAR data from the ESA Earth Explorer CryoSat-2 and the Copernicus mission Sentinel-3, which are the only two missions having on board a SAR altimeter.

First, a short summary of the concept of SAR altimetry is given, by reviewing as well the state of the art of the discipline and the latest novelties in the field.

Then, the methods used here to enhance the standard SAR Altimetry processing chain (Delay-Doppler Algorithm, K.R. Raney 1998) are presented. The enhancement consists in dedicated processing options at L1b level which may be regarded as complements or additions to the Delay-Doppler algorithm.

Furthermore, a new approach in SAR waveform retracking has been proposed in order to retrieve accurate altitude measurements over open ocean, the coastal zone, inland water and sea ice. This consists in a new algorithm to extract the geophysical information from the radar waveforms, which is a modification of the SAMOSA SAR physically-based SAR return waveform model introduced by Ray et al., (2015). Once the evidence was gathered that this SAMOSA-based open ocean retracker was performing properly (see Fenoglio-Marc et al., 2015), an upgrade of the algorithm specifically tailored to the coastal zone and referred to as SAMOSA+ has been developed.

This algorithm has been described and validated in Dinardo et al., (2018) with success in the coastal zone. Especially in coastal zone this dedicated coastal SAR retracking has brought a significant improvement with respect to the nominal SAR products from the mission ground segments. Moreover, the algorithm produces very accurate measurements of the sea-ice freeboard as well. This is a significant finding, because obtained by a physically-based retracker originally designed for the coastal zone data exploitation.

However, SAMOSA+ has some limitations described in the thesis and does not perform as expected over inland water. For this reason, a further evolution of the SAMOSA+ algorithm, coined SAMOSA++, has been developed. The main novelty consists in accounting for the RIP (Range Integrated Power), which can be regarded as an extra waveform provided by SAR altimetry and has not been exploited by the altimetry community so far. The objective of this last retracker is to be “pan-thematic”, in other words suitable to any possible altimetry application.

The results obtained from this novel technique have been extensively presented on different thematic applications such as marine surfaces (both open ocean and the coastal zone) and inland water (over two selected test cases), and are always outperforming the other retrackers.

Based on the toolkits developed during this thesis, a SAR altimetry service has been developed and is now operational on the ESA G-POD grid platform. The service has been used to process online and on-demand all the data used in the thesis work and is daily used by experts in the field of altimetry. The validation has been done against in situ data, ocean numerical models and against standard altimetry products processed in SAR mode from the missions’ ground segment altimeter datasets against products processed in Pseudo Low Resolution Mode (PLRM). This last product type corresponds to the conventional processing methodology used before SAR era (referred to commonly as PLRM). These results give strong evidence that the improvement brought by the novel technique is significant over all three thematic applications when compared with the state of the art. All these innovations will help scientists to monitor the sea level in the coastal zone, the inland water management and to improve the computation of the sea ice freeboard.

CHAPTER 1: INTRODUCTION

CHAPTER 2: BASICS AND GENERALITIES

CHAPTER 3: METHODOLOGIES

CHAPTER 4: EXPERIMENTS AND RESULTS

CHAPTER 5: CONCLUSIONS AND OUTLOOK

LIST OF FIGURES

Chapter 2

Chapter 3

Chapter 4

LIST OF TABLES

Chapter 2

Chapter 3

Chapter 4

1 Introduction

1.1 Problem Statement

In this section, I place the problem that I want to address in this dissertation work. The problem can be synthesized in one sentence: better altimetry over water, land and ice. Indeed, altimetry can be regarded as the process to measure the absolute height of a target which can be an extended target as ocean or can be a point target as a small lake or river, a coastal lagoon, a water lead in a crack between two ice floes, etc. While in the past years, there has been a clear progress in improving the accuracy of the altimetry over extended targets to reach a level down to few cm, over point targets the accuracy of the altimetric measurements was still not satisfying, and essentially because of the large footprint of the pulse-limited radar altimeters.
A step forward occurred when the Altimetry entered in the SAR (Synthetic Aperture Radar) era. This has entitled to shrink the footprint of the sensor by an order of magnitude in along track but it has also brought the need to design and develop algorithms able to fully exploit the potentialities brought by SAR altimetry in making the final measurements. The first years in the SAR altimetry era have given a certain confidence that the new technology has improved the way to measure and sample the open ocean surface but it is now time to improve the SAR Altimetry measurements on the rest of the thematic applications: coastal zone, sea-ice and inland water bodies, exploiting a suite of physical retrackers and dedicated L1b processing.

In the first place, the importance of having an accurate global altimetric dataset in the coastal zone is emphasized: this is a highly dynamic and lively part of the marine environment, where processes and interactions between sea and land occur very quickly and at very short scales. The coastal zone plays a key role in the life of millions of people, being that more than 10% of the Earth population lives in the low-elevation coastal zone area (Neumann et al., 2015) and hence potentially exposed to the effects of storm surges, sea level rise, global warming and climate change. It is therefore mandatory to develop tools and techniques to monitor the sea level rise in the coastal zone, to include in the near future the coastal data in the global sea level budget and to demonstrate that coastal altimetry data can contribute effectively to the monitoring of regional sea level trends. In spite of its importance for climate change monitoring, dedicated coastal algorithms as coastal retracking (i.e. the process of extracting the geophysical altimetric measurements from the received waveform) are not yet integrated in the operational altimetry Payload Data Ground Segment (PDGS), coastal datasets are being produced only on a prototypal basis and there is still no general consensus on the optimal approach to process altimetric measurements in coastal zone (Vignudelli et al., 2011). Consequently, most of altimetry data collected in the coastal zone over the last 25 years are still largely unexploited or flagged as invalid in the ground segment altimetric products.
The existence of this coastal data exploitation problem and the importance of coastal altimetry in general have been indeed recognized by the major space agencies, which have been supporting research and development (R&D) in this field. Thanks to this effort, progress has been achieved in the last years in the frame of projects such as ALTICORE (Lebedev et al., 2008), COASTALT (Cipollini et al., 2009), X-TRACK (Roblou et al., 2007), PISTACH (CLS Report, 2015), eSurge (Cipollini et al., 2012), CP4O (Cotton, 2015) and Sea Level CCI (Climate Change Initiative) (Ablain et al., 2015). These projects have aimed at improving conventional and SAR altimetry and at improving the range and geophysical corrections (in particular the wet tropospheric path delay and ocean tide) in the coastal zone.
Furthermore, in the last years, relevant advancement has been achieved in the specific field of conventional pulse-limited waveform retracking in the coastal zone by adopting a sub-waveform retracking approach (as Guo et al., 2010, RED3 in CLS Report, 2015, Idris and Deng, 2012) and an adaptive sub-waveform

retracking (as ALES in Passaro et al., 2014). The latter authors succeeded in mitigating the impact of land contamination (off-nadir returns from the land synchronous with nadir return from the ocean) and bright targets (as wetlands, mud flats, reefs, etc.) on the retrieved coastal measurements by retracking only a subset of the waveform. However, due to the novelty of the SAR altimetry mode, not much progress has yet been made in the field of SAR coastal retracking. Recently, (Dinardo et al., 2018) has proposed a first dedicated coastal SAR retracking showing an undisputable improvement achieved with respect the conventional altimetry and a clear capacity by SAR altimetry to measure sea level monthly mean which are closer to the ones predicted by the ocean circulation models. But this analysis was only regional and limited to German Bight and West Baltic Sea and is needed to be repeated on the global scale and confirmed by independent verification of experts in the subject.

In second place, the importance of having accurate altimetric measurement of the sea ice freeboard over the Arctic is emphasized. Arctic sea is a very delicate and sensitive environment which plays a major role on the global climate budget and which can be severely affected by climate change, in particular by global warming. The global warming leads the sea ice to reduce its extension and to shrink with time. And indeed observations report that, along with the sea ice extension reduction (Rothrock and Maykut, 1999), the Arctic sea-ice is thinning (IPCC, 2013) (Kwok and Rothrock, 2009) and several models and projections predict an ice-free summer in the Arctic before the end of the 21st century (Collins et al., 2013), (Stroeve et al., 2012). These long-term changes in the Arctic impact then also the weather in lower latitudes due to the modifications of atmospheric circulation (Rinke et al., 2006) and there is a concern that the melting of ice sheets and glaciers in Greenland could contribute to a substantial rise in sea levels worldwide.
The European Space Agency has recognized the importance and the need to provide reliable, consistent and homogenous sea ice thickness dataset over the Arctic initiating the Climate Change Initiative (CCI) Sea Ice Project (http://esa-cci.nersc.no/). Indeed, Radar Altimetry is a space technique which can measure the sea-ice thickness in a continuous and global way and in particular the CryoSat-2 mission was the first altimeter to provide data products and maps of sea-ice thickness in an operational way and presently also in near real time (Tilling et al., 2016). But, prior to measure sea-ice thickness, it is needed to measure the sea-ice freeboard which can be regarded as the elevation of the ice floes over the free water surface. Only when the freeboard is derived, knowing the weight of the show layer on top of the sea-ice and assuming hydrostatic balance, the sea ice thickness can be finally estimated. Hence, in order to improve the final accuracy of the sea ice thickness, it is first necessary to improve the way the freeboard is measured by the altimeter. So far, the estimation of the sea-ice freeboard is based on empirical methods and algorithms as TFMRA (Threshold First Maximum Retracker Algorithm) (Helm et al., 2014) but a validated method to retrieve sea-ice freeboard based on a physical treatment of the problem is not available. A sea ice freeboard solution based on physical retracking can ensure a seamless transition from open ocean to ice-covered ocean and will not rely on arbitrary and heuristic parametrization of the algorithms. Hence, potentially, it might return a more accurate estimation of the sea-ice freeboard.

In third place, the importance of having accurate altimetric measurement over inland water bodies as rivers and lakes is pointed out. Indeed, rivers and lakes are important and strategic storage and source of fresh water, supplying drinkable water to many people worldwide, especially to people in poverty. Furthermore, they are essential for agriculture, irrigation, navigation, industrial activities, fishery etc. However, these water resources can be very vulnerable to climate change and can be subject to periods of intense flooding as consequence of the urbanization of the surrounding area or can be subject to long periods of drought as consequence of desertification processes or groundwater pumping human activities.
Radar Altimetry is the only technique capable to gauge the level of the water bodies from the space and it has a long history of multi-decadal river and lake monitoring (Berry et al., 2012) (Crétaux et al., 2011) (Birkett, et al., 2010). It guaranties a uniform spatio-temporal coverage of the water bodies worldwide and gives the possibility to track the level of water bodies which are in inaccessible or remote areas or in poorly

instrumented countries. Furthermore, Radar Altimetry allows to infer the river's discharge when the cross-sectional geometry and roughness of the river is known, exploiting the Manning's equation (Manning R., 1889) or by empirical rating curves.
Nevertheless, again limitations in the retracking process still prevent from a global operational monitoring of all the water resources and Radar Altimetry has difficulties in providing accurate time series of water level variation in case of small river or lakes. SAR altimetry has already demonstrated with CryoSat-2 that it has the full potential to give a burst in improving the measurement accuracy (Schneider et al., 2018) (Bercher et al., 2013), (Moore at al., 2018) thanks to the finer ground resolution but however most of the available methods used to retrieve water level are again based on empirical or heuristic approaches as threshold retrackers. And then, even if the altimeter footprint is reduced in SAR mode, the sensor can still miss the acquisition of the water body because of failure of the on board tracking to lock it properly in the receiving window.
Finally, I wish to raise an alert on the growth in size of the altimetry products in the last years: with the advent of SAR altimetry era, the altimetry raw data products have become exponentially more bulky than in the past: a pole-to-pole satellite pass of SAR raw data can reach easily 2.5 GigaByte (once compressed) which means that, in case of Sentinel-3 mission which has 770 passes in a repeat cycle (27 days), the total amount of SAR raw data in a cycle reaches the number of around 2 TB. Hence, in order to store a full mission of SAR raw data (around 10 year), it will occur an archive of 250 TB. Furthermore, the processing of these SAR raw data is much more computationally expensive than before at L1b and L2 and also the ancillary data, such as mean sea surface models, are getting more and more high resolution and hence also high-size.
This means that in the era of SAR altimetry, we have reached a level in which a simple expert with his own personal computer cannot handle anymore this huge flow of data and cannot think to process them in a reasonable time.
The only solution to address this problem is to exploit the technologies offered by the modern human progress such as grid computing and cloud storage: one unique repository of raw data which are interfaced by multiple users at request and which are processed by a grid of computing nodes in parallel in a scalable environment. In this paradigma, the expert is called only to deploy on this environment his/her application, to set up a task and to collect the output of submitted task, relieving him/her from the tedious and time-consuming burden to collect all the input data and to process the data on his/her machines or limited means.
Even more, these deployed applications can be imagined to be shared between different experts via simple graphic interface, customizable and the data generated by them cross-compared to each other or used by a plethora of independent users. With this inter-comparison and data analysis process, the applications can grow up, become validated and, once mature, turns into operational services providing prototype data on demand and online to all user community.
This was the vision I had in mind when firstly I have attempted to initiate SAR altimetry services on the ESA G-POD system (https://gpod.eo.esa.int/) in the frame of this PhD.

Therefore, having placed these problems and considerations, the dissertation aims to address the following fundamental questions:

- Can we say that SAR Altimetry over open ocean is a consolidated and well-established technology which has now reached a state of full maturity?
- Has SAR Altimetry delivered on the promise to allow a more accurate retrieval of the sea level in the coastal zone?
- Has SAR Altimetry delivered on the promise to allowing the monitoring of small rivers and lakes which were not possible to monitor with pulse limited altimetry?
- Beyond pursuing it with the conventional empirical methods, will it be possible now with SAR Altimetry to have a physically-based solution to the sea ice freeboard retrieval problem?

— Is possible to design and build a retracker capable to work efficiently and reliably over any kind of surface and topography granting seamless transition from one surface to the other one?
— Can we measure with SAR Altimetry new marine geophysical quantities?
— With the modern progress in media and computer science technologies such as grid computing and cloud storage, can be given to the scientists finally the possibility to focus essentially on the scientific aspects of the data exploitation delegating all the cumbersome processes of data processing, data storage and data interface to external and "ad hoc" pools or platforms?
— Can we create on line and on demand altimetry services where users can easily process and personalize own processing and share all the results within the whole altimetry community?
— Can we push the limits of SAR Altimetry even further?

1.2 Thesis Outline

The thesis is structured in 5 chapters. In the first chapter, I place the problem which I intend to solve and underline the importance and the need to find a solution to this problem.
In the second chapter, I introduce the concept and generalities of SAR Altimetry, I go through a review of the present state of the art and then I outline the existing satellite SAR Altimetry missions and the basics of the SAR processing from L1b and L2. The usual reference techniques for SAR Altimetry data validation are briefly listed towards the end.
In the third chapter, all the methodologies which have been followed and conceived to pursue the objectives of the thesis are exposed: I present my novel approaches based on the heritage and on state of art and I propose solutions to the current problems encountered at L1b and L2 processing.
In the fourth chapter, the results and the outcome of the data processing are presented, analyzed and discussed. Finally, in the fifth chapter, I reach the conclusions and I come back to the questions which have been raised in the thesis introduction in order to verify whether they have been fulfilled. An outlook towards the future with the remaining work to accomplish and the next steps to undertake is the conclusion of the thesis. In the Appendix A, I introduce the ESA G-POD SAR altimetry services which have been conceived and developed in the frame of this thesis work and that have been used to process and extract all the prototype data products presented in this thesis work.

1.3 Acknowledgments

I wish to thank the whole ESRIN G-POD team for tireless and invaluable support that have spent in making the SAR altimetry services reality and in particular a special thanks to Giovanni Sabatino. Then I wish to thank Prof. Matthias Becker for his patience and guidance through the obstacles of the PhD path and the PhD jury's members Prof. Dr.-Ing. Michael Vormwald and Prof. Dr. Britta Schmalz for their work review. Heartfelt thanks are dedicated also to Dr. Luciana Fenoglio for her rigour and her constructive criticisms which helped me in shaping my research and also to unveil very subtle errors. Then I wish to thank Dr. Joana Fernandez for her wise words and Dr. Remko Scharroo for his expert view over all the altimetry problems. I wish to thank my family who suffered me being far away from them and my friends who have supported me in these years and in particular my partner Francesca Haack.
Finally, I wish to dedicate special thanks to Dr. Jérôme Benveniste who long time ago called me to work with Altimetry with him and who made this thesis possible, as well as for co-supervising it. Also I thank him warmly for launching and supporting the ESA GPOD SARvatore Service mentioned above, which hosts, for the benefit of all, the software I have developed, and which boosted the computations done for this thesis.

2 Basics and Generalities

Introduction

The advent of SAR Altimetry era has brought the necessity to define the new processing algorithms necessary to build the SAR waveform in the L1b processing chain.
In the conventional pulse-limited altimetry missions (as Topex/Poseidon, ERS ½, Envisat, Jason 1/2/3), the waveform was or is always built on board whereas only Envisat Radar Altimeter had the possibility to downlink on ground a 1-second long set of individual I/Q echoes every 1 minute (Berry et al., 2007) (Abileah, 2017).
Hence the, L1b processing was essentially consisting in calibrating the waveforms, applying the gain control correction, computing the tracker range, and deriving the geo-location and the time stamp but the waveforms could not be processed or built in another way.
This "paradigma" has changed completely with SAR Altimetry: the SAR altimeters downlink the raw digitized I/Q echoes after the classical deramping operation (Fu and Cazenave, 2001). The rationale behind this choice is that the L1b SAR processing is too complex and it needs necessarily some external information (as precise orbit) in order to be carried out on board with success.
This has brought the necessity to build on ground more complex L1b processing chains in the operational mission ground segments but it has also the distinctive advantage that expert users can process the waveforms "as they like" or that they can experiment new processing ways for some specific thematic applications.
Very likely, it will be difficult to identify one single way to process waveforms that is the ideal one for all the possible altimetric science applications, fulfilling as well the stringent timeliness requirements of altimetry missions but, at this stage of evolution, some processes in the SAR L1b processing block-scheme can be regarded as "standard" or as ones that necessarily need to be applied in order to synthesize in a ground point a SAR waveform with a dictated resolution along track.

As second point, being the SAR footprint radically different at the bouncing time and at times following the bouncing time, SAR waveform has a shape which strongly diverges from the classical pulse-limited "Brown" Echo (Brown, 1977).
Hence, if some L2 conventional processes keep to apply in L2 SAR processing (as the concept of retracking and the concept of waveform physical model), the mathematical formulation at the base of this physical model assumes a completely new flavour, with also new variables to be provided in input.

In this chapter, I go through and examine in a broad-view sense all the most common processes executed in the L1b and L2 SAR processing chain while the final formulation of the specific SAR waveform mathematical model used in this thesis work and all the technical aspects inherent to the SAR waveform retracking will be given in chapter 2.
I also give some basics about the ocean numerical modelling and tide gauges, because they have a long historical record as cross-comparison reference in validating altimetry data and they have been used in thesis's chapter 4.

2.1 Introduction to SAR Altimetry and State of the Art

In this section, I briefly introduce the concept of SAR altimetry and highlight its differences with respect to conventional pulse-limited altimetry. The main difference between these two measurement modes is related to the frequency used to transmit the pulses, which is called the Pulse Repetition Frequency (PRF). In pulse-limited mode, transmitted and received pulses are interleaved, i.e. pulses are received and transmitted continuously and reflections from the transmitted pulses are processed incoherently on a pulse-by-pulse basis (for more details see Fu and Cazenave, 2001).

In SAR closed-burst mode, the pulses are transmitted and received in bursts with much higher PRF, so that successive received pulses in a burst are correlated (Raney, 1998). After the transmission of the burst, the altimeter exploits the empty inter-bust interval to receive the pulses reflected back from the surface. The pulse-to-pulse coherence due to this high PRF allows the application of the Delay-Doppler concept (Raney, 1998), which exploits the additional information coming from the relative Doppler phase between subsequent burst pulses to synthesize a synthetic antenna aperture much larger that the real one. As result, a SAR altimeter will have a finer along track resolution than a pulse-limited altimeter but, since the sharpening is just in the along-track direction, the SAR altimeter and the pulse-limited altimeter share the same across-track resolution. Hence, after the acquisition of the high-rate digitized burst pulses, the data get coherently processed using the Delay-Doppler algorithm, producing the multi-looked SAR waveform (L1B).

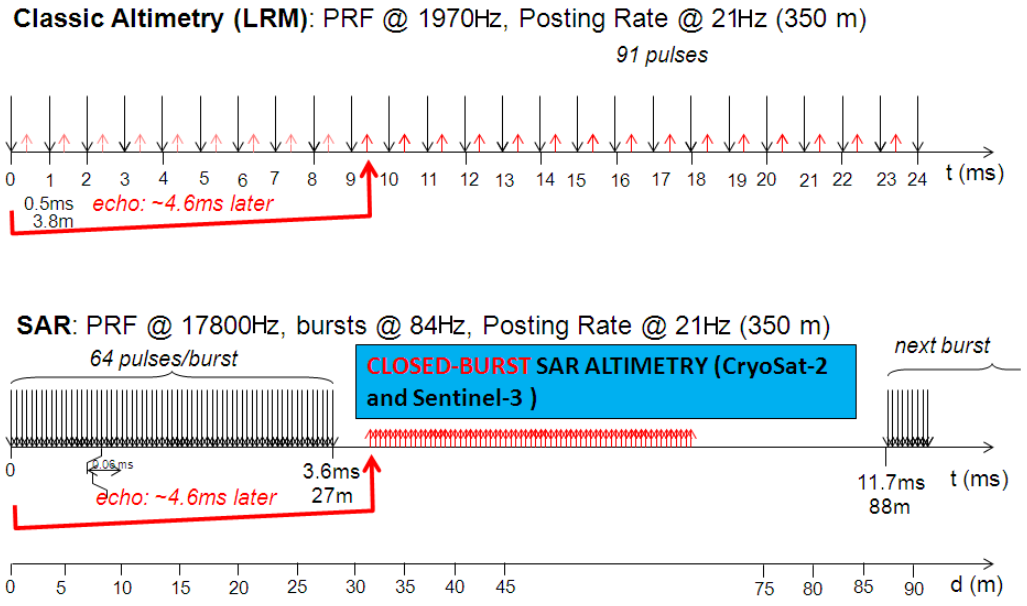

Figure 2.1: Pulse Transmission Scheme in case of Pulse-Limited Altimetry (LRM) and closed-burst SAR Altimetry

The first expected advantage of SAR altimetry over the ocean is a higher precision, due to the noise reduction made possible by the larger number of averaged echoes reflected from the same surface location (looks) and higher SNR (signal to noise ratio) of the received signal. This benefit was demonstrated and reported by several authors e.g. Fenoglio-Marc et al., (2015), Gommenginger et al., (2014). The second prominent advantage is a finer along track spatial resolution, thanks to the smaller footprint in the along-track direction which does not increase with the Significant Wave Height (SWH) as in conventional altimetry. Such a reduction of the altimeter footprint gives to SAR mode the potentiality to resolve shorter scale ocean features and the capacity to provide more robust and accurate sea state measurements in the coastal zone, being less sensitive to the land contamination.

Anyhow, because the footprint reduction occurs only in along track direction while the across track resolution remains basically unaltered with respect to the conventional altimetry case, it is expected that SAR

altimetry brings altimetric measurements closer to coast especially when approaching the coast in orthogonal direction (Dinardo et al., 2011).

In Figure 2.2, a representation of the evolution with time of the pulse-limited and SAR altimetry footprint is sketched. At t=0 (bouncing time), the SAR footprint is no longer circular as in pulse-limited Altimetry but rectangular. At t=0 the SAR across-track resolution is the same as Pulse-Limited Altimetry (determined by the Pulse-Limited diameter) but at t>0 the SAR footprint size decreases with the time delay while the pulse-limited footprint maintains a constant area (rings). In a certain sense, a SAR altimeter footprint can be said to be beam-limited in along-track direction (and here the beam is the synthetic Doppler beam) and is pulse-limited in across-track direction. Because the SAR footprint is no longer constant with time delay, this drives to the decaying behaviour of the SAR return waveform's tail.

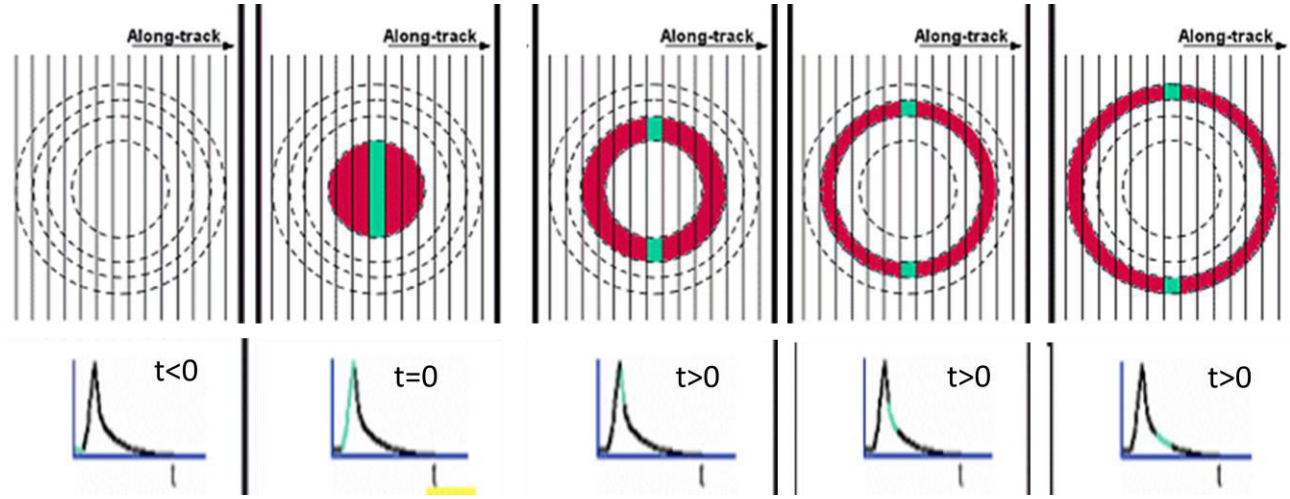

Figure 2.2: Evolution of the footprint's geometry with the time in case of pulse-limited altimetry (red) and in case of SAR Altimetry (green). From radar altimetry tutorial (Rosmorduc et al., 2011)

Hence, as a step forward from conventional altimetry, SAR altimetry is expected to provide the three geophysical marine parameters, sea surface height (SSH), significant wave height (SWH) and wind speed at 10 meter height (U10) with enhanced precision, accuracy and resolution over open ocean and coastal zone but, because of the smaller footprint of a SAR altimeter, the ocean return waveform in SAR mode will have a different shape than the pulse-limited ocean return waveform. This brings to the need to develop a novel return waveform model for SAR altimetry to accurately extract the three marine geophysical parameters.

Clearly, all the improvements brought in the coastal waters by SAR altimetry continue to be applicable also over inland water bodies. The full exploitation of the potentialities of SAR altimetry over inland water bodies has been partially hindered with CryoSat-2 mission because of its long period repeat cycle (369 days), which does not permit to build a time series on a specific river crossing with a time step useful for hydrologists (say less than 35 days, optimally less than one day). Therefore, to better exploit CryoSat-2 data over the inland water, the objective is to build monthly time series on a river crossing and this requires to develop a water level slope correction in order to migrate the CryoSat-2 measurements upstream and downstream onto a selected position (called a virtual station) and hence to build the time series (Villadsen et al., 2015) (Nielsen et al., 2017). With Sentinel-3 mission, which has a shorter repeat cycle of 27 days, the need to develop a slope correction does not stand anymore and time-series with a temporal sampling of 27 days can be easily built worldwide. Furthermore, the Sentinel-3 mission brings the novel capacity to command the tracking range of the radar receiving window by a priori DEM (Digital Elevation Model) uploaded on board (OLTC, Open-Loop Tracking Command). This DEM has been upgraded with more than 32'500 virtual stations defining lakes, reservoirs, rivers, and glaciers worldwide. This will ensure that Sentinel-3 will be able to maintain a reliable and stable tracking over those inland water targets. It is hence expected that per effect of the joint combination of SAR altimetry and OLTC commanding, Sentinel-3 mission will represent a significant milestone towards the establishment of an operational monitoring of the inland water bodies worldwide.

As to the results in open ocean from SAR altimetry, experts have already demonstrated that the sea level wave number spectra from SAR altimetry don not show the typical "hump" of spectral energy characteristic of the pulse-limited altimetry at meso-scale lengths and the level of "white noise" plateau is much lower than the one achieved in pulse-limited Altimetry (Boy et al., 2017a). For long and very long scale, the pulse-limited and SAR altimetry share the same spectral behaviour. Hence, there is a clear evidence that SAR Altimetry sample better (and finer) the sea surface. Concern has been raised on the effect of directional train of waves, as swell, entering in the SAR Altimetry footprint as the SAR footprint loses the typical isotropy of the pulse-limited altimetry footprint (Moreau et al., 2016) (Abdalla et al., 2018). This effect has been indeed detected in the Sentinel-3 SAR data (as range noise increase and biases in SWH) and a novel technique entailing processing SAR data without the Doppler beam steering and stacking, as usually done in the Delay-Doppler algorithm, has been proposed to mitigate the impact of this effect (Boy et al., 2017b). Besides the closed-burst SAR altimetry, recently it has been proposed an open-burst SAR altimetry concept (Raney, 2012). In the open burst SAR altimetry concept, the interleaved transmission and reception of the radar pulses will be maintained (as in conventional pulse-limited altimetry) but the PRF will be much higher (around 9 KHz) than the one generally used in pulse-limited altimetry (2 KHz). The high PRF will allow the successive pulses to be still correlated and with high pulse-to-pulse coherence and hence processable "a la Delay-Doppler". However, the PRF will not be sufficiently high to sample the Doppler spectrum satisfying the Nyquist's criteria and hence azimuth ambiguities from the aliasing effect will arise in the Doppler spectrum data, folding with the signal received within the 3dB along-track antenna beamwidth. Hence, dedicated techniques need to be put in place during the processing chain in order to mitigate any detrimental impact from these azimuth ambiguities.

The prominent advantage of the open burst technique is that it allows for simultaneous and continuous operations in LRM (pulse-limited) mode (with the same number of looks as in conventional altimetric mission) and in SAR mode (hence responding to the stringent need of continuity with the past missions from altimetry user community). Furthermore, in SAR mode, it allows for the accumulation of a much higher number of looks, which will result in measurements of the marine quantities with higher precision (it is expected a range noise of 0.5 cm at 1 Hz). Finally, it is the ideal transmission mode in order to implement a fully-focused SAR processing (Curlander and McDonough, 1991). In the fully-focused SAR (FFSAR) concept, all the beams within the antenna aperture are coherently summed after a phase compensation in order to increase the along-track resolution up to its theoretical limit of around 0.5 meter (i.e. half the along-track antenna length) (Guccione et al., 2018) whereas in Delay-Doppler concept only the beams in one burst length are coherently summed to form the Doppler Beam Fan (see section 2.1.2.4) and reach an along-track resolution of around 300 meter (unfocused SAR, UFSAR in short). Fully focused SAR processing has been already attempted with the CryoSat-2 data by several experts and results are promising (Egido and Smith, 2017) but still the data exploitation of this data flavour is hampered by azimuth ambiguities (grating lobes) arising because of the existing gaps between bursts in the CryoSat-2 (and Sentinel-3) transmission mode (Guccione et al., 2018).

2.1.1 Satellite SAR Altimetry Missions

2.1.1.1 CryoSat-2 Mission

CryoSat-2 is an ESA (European Space Agency) Earth explorer mission, launched on 8 April 2010, devoted to the measurement of the sea ice thickness, land ice sheets and mountain glaciers elevations (ESA report, 2007). CryoSat-2 flies on a Low Earth polar orbit with a long repeat cycle of 369 days and a sub-cycle of 30 days. In order to fulfil the tight cryospheric mission requirements, CryoSat-2 was equipped with a SAR interferometric radar altimeter named SIRAL (Wingham et al., 2004) operating at a single frequency in Ku Band (13.575 GHz). SIRAL is able to work in three measurement modes: SAR, SARin (SAR interferometry), and LRM (Low Rate Mode, i.e. the CryoSat-2 terminology for conventional pulse-limited mode) according to a predefined geographical mask. Because it is a single-frequency altimeter, it cannot

estimate autonomously the ionosphere propagation delay. It has a high orbital inclination around 92° in order to cover as much as possible the polar caps with a perigee altitude of 720 km and apogee altitude of 732 km. The CryoSat-2 orbit is not sun-synchronous and hence it will experiment very different illumination and thermal conditions during its repeat cycle.
Furthermore, CryoSat-2 embarks a DORIS (Doppler Orbit and Radio Positioning Integration by Satellite) system and laser retro-reflectoarray (LRR) to calculate precisely the spacecraft's orbit but it does not embark any microwave radiometer to measure the atmosphere's wet tropospheric propagation delay. In order to control and guide its attitude, it is three-axes stabilized and has been equipped with a set of three star tracker mounted directly on the antenna optical bench.
A distinctive feature of CryoSat-2 SIRAL, different to all the former radar altimeters, is that it does not carry out any processing on board to build the multilooked waveforms when operating in SAR and SARin mode, but it downlinks to ground all the received pulses, after digitizing them. On ground, the unprocessed pulses are geo-located, time-referenced and combined with calibration quantities to form a L1A product named FBR (Full Bit Rate, the CryoSat-2 specific terminology for Level 1A). Given the technical design of CryoSat-2 altimeter, simultaneous operations in SAR mode and LRM are not possible.

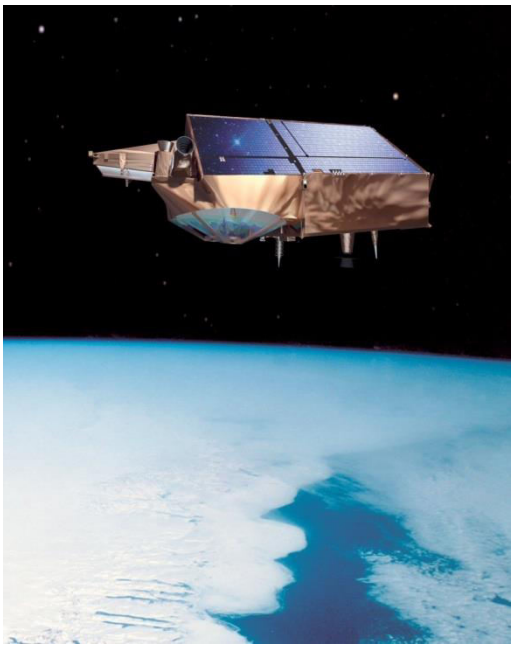

Figure 2.3: Artistic Impression of CryoSat-2 (Image: ESA)

2.1.1.2 Sentinel-3 Mission

Sentinel-3 is an Earth Observation satellite constellation developed by ESA and operated by EUMETSAT as part of the European Commission's Copernicus Programme. The first satellite of the Sentinel-3 constellation (Sentinel-3A) has been launched on 16 February 2016 and nominated operational on July 2016.
Sentinel-3A embarks a suite of sensors devoted to optical imagery acquisition (as OLCI and SLSTR) and surface topography measurement (as SRAL). SRAL (Synthetic Radar ALtimeter) is a dual-frequency radar altimeter operating in Ku Band (15.575 GHz) and C Band (5.41 GHz). SRAL can operate in SAR processing mode or in LRM processing mode. By design, it is operated in SAR mode globally.
SRAL has a strong heritage from CryoSat-2's SIRAL and the two sensors SIRAL and SRAL share a very similar design. The mission objective of SRAL is to provide accurate, continuous and timely topography

measurements over ocean, sea ice, ice sheets, glaciers and rivers & lakes during its nominal life duration of seven years. It will also provide wind&wave measurement over marine surfaces.
In order to fulfil to this scope, it is supported by a microwave radiometer providing the wet tropospheric propagation delay and by the OLTC (Open Loop Tracking Command) Tracking Mode which allows the sensor to maintain a stable tracking control over complex topographic surfaces as coastal and inland waters thanks to a DEM uploaded a priori on board storing a coarse height of the overflown surface.
Furthermore, Sentinel-3 embarks a DORIS (Doppler Orbit and Radio Positioning Integration by Satellite) system, a redundant GNSS receiver and a laser retro-reflectoarray (LRR) to calculate precisely the spacecraft's orbit.
In order to control and guide the platform attitude, the spacecraft is three-axes stabilized and equipped with a set of three star tracker placed in tetrahedral configuration.
The Sentinel-3 orbit is near-polar sun-synchronous (Ascending Node LST at 10 am) with a reference altitude of 814 km, an orbital inclination of 98.6° and repeat cycle of 27 days. The Sentinel-3 orbit is a new orbit for Radar Altimetry that means it has been never charted by any altimeter before. This will entail a certain amount of error in the derivation of the sea level anomalies at early mission stage.
Since the orbital inclination is not as high as the CryoSat-2's one, the Sentinel-3 sea ice coverage will be less extended than CryoSat-2.

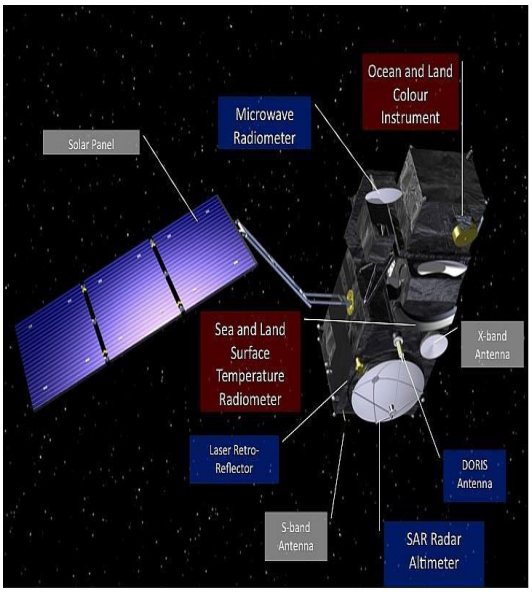

Figure 2.4: Sentinel-3 with the different sub-systems (Image: ESA)

Finally, on 25 April 2018, Sentinel-3A has been complemented by its second member of the constellation (Sentinel-3B) which has doubled the coverage offered by Sentinel-3 mission flying in an orbit phased 140 degree a part from Sentinel-3A.

2.1.2 L1B Processing in SAR Mode

Generally, it can be said that the Radar Altimetry L1B processing consists mainly in all the processes apt to build a radar waveform backscattered from a certain surface location, starting from the received and digitized raw data. These processes are different according to the processing mode (pulse-limited, SAR, etc,) under analysis. In this section, I will refer to the SAR L1B processing mode and I will summarize the major processes that the L1A data undergo in a standard SAR L1B (Delay-Doppler) Processing Scheme (Raney, 1998)

2.1.2.1 Calibration

After being extracted from L1A data products, the received burst pulses need to be calibrated and corrected by all the sensor's instrumental artefacts. Indeed internal calibrations are regularly performed on-board of radar altimeters and afterwards calibration data are processed on-ground in order to extract the calibration corrections.
The following internal calibration corrections are generally applied to SAR data:

1) Internal Path Delay Calibration: to calibrate the internal path delay of the Range Impulse Response (or range Point Target Response) and correct for any range drift due to instrument aging.
2) Internal Power Drift Calibration: to calibrate the power level drift of the Range Impulse Response due to instrument aging.
3) SAR Intra-Burst Phase and Amplitude Differences Calibration: to calibrate variation in phase and amplitude between the pulses within each burst.
4) Receiver Transfer Function Mask Calibration: to calibrate the received waveform's shape for the Receiver LPF (Low Pass Filter) Mask.

The first 3 calibrations (relatively to the Range and Azimuth Impulse Response) are generally referred as CAL1 whereas the fourth one is usually referred as CAL2.

In addition to internal calibration, the echoes power level is compensated for:

1) AGC (Automatic Gain Correction) values (dynamic power correction, updated every radar cycle).
2) Fixed Receiver Chain Gains and Harness Losses (static power correction), as characterized prior to launch.

Furthermore, the AGC values are calibrated in a specific internal calibration mode referred as AutoCAL.

2.1.2.2 Ground Cell Gridding

The purpose of this stage is to identify along the over-flown surface elevation profile a set of surface locations (or surface samples or ground cells or reference points) wherein the synthesized Doppler Beams will be afterwards formed, steered and multi-looked, as described in the next sections.
In a SAR (Delay-Doppler) processing scheme, a Doppler Beam is each of the the 64 synthetic beams in which the antenna 3dB along-track beamwidth can be split by exploiting the Doppler effect due to the satellite motion with respect the ground (see also section 2.1.2.4).
The position of the surface locations is determined using an iterative method consisting in enforcing between the surface samples the same along-track angular separation, (in order to obtain a regular angular grid) and placing the surface samples on the sub-satellite elevation profile. The along-track angular separation between surface samples is fixed equal to the one by which the Doppler beams are in average separated.
The used approximated over-flown elevation profile is derived from the on-board calculated tracker range converted to a surface elevation.
Each surface sample is assigned a time-tag equal to the time at which the satellite passes ellipsoidally normal to the sample.
The level 1B multi-looked waveforms will be afterwards time-referenced to these surface sample time-tags (posted with a rate of around 20 Hz) and no longer dependent on the burst structure of the input L1A data (i.e. around 80 Hz).
This means that the posting rates of the L1A and Level 1B data are independent of each other.

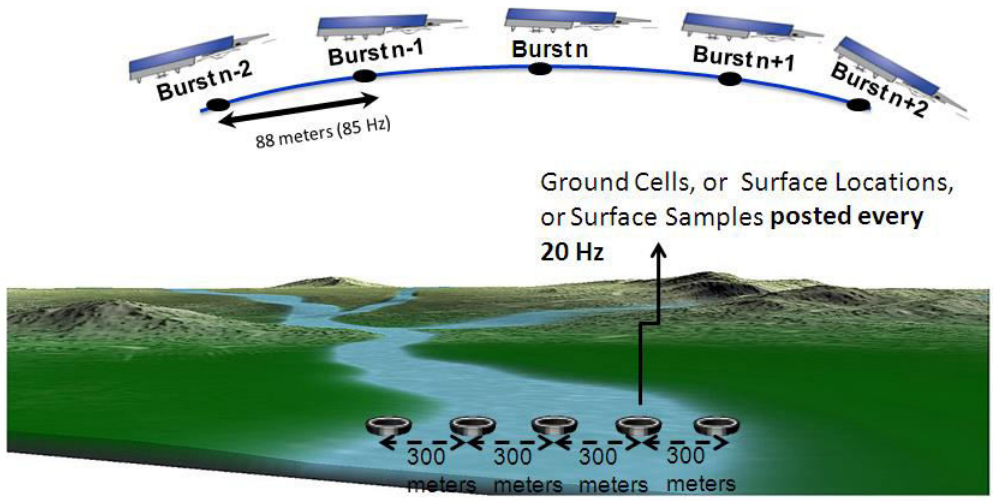

Figure 2.5: Ground Cell Gridding: the Ground Cell are placed along the over-flown surface at a distance of around 300 meter (around 20 Hz). The burst center has a repetition frequency of around 80 Hz

2.1.2.3 Beam Pointing

Given the set of surface sample locations, the purpose of this stage is to determine for each burst center:

1) vectors joining the position of the current burst center to the positions of the all surface samples (surface sample direction vectors).
2) the angles between surface sample direction vectors and satellite velocity vector evaluated in the burst center (Doppler beam direction angles or Doppler angles).
3) the angles between surface sample direction vectors and satellite nadir vector evaluated in the burst center (look direction angles or look angles).
4) the ranges between the position of satellite CoM (Center of Mass) at burst center and the positions of all the surface samples (surface samples direction ranges).

Hence, at the end of this stage, all the geometry of the scene is known.
Based on all the calculated direction angles, only the burst data[1], whose directions angles are included in the antenna 3dB along-track beamwidth are selected and retained in memory for processing. In the case of Sentinel-3 altimeter, the antenna 3dB along-track beamwidth amounts to around 1.28 deg, which translates to an antenna footprint of around 20 km from an orbit altitude of 850 km. Since each burst covers 88 meters, as shown in Fig. 2.1, this means that for each surface location around 220 burst data are selected and retained in memory for the subsequent processing. For more information about the definition of antenna 3dB beamwidth, please refer to Balanis (2016).

[1]For geometrical reasons, the number of burst data in the antenna 3dB along-track beamwidth is variable along the orbit

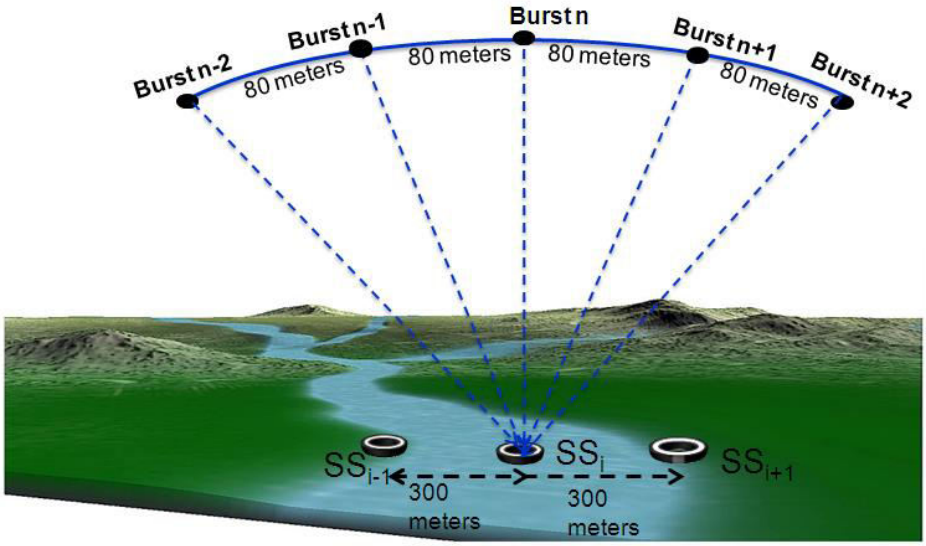

Figure 2.6: Beam Pointing: all the geometry between the ith surface location and the burst centres is computed

2.1.2.4 Beam Steering & Beam Forming

The purpose of this stage is to synthesize a set of 64 Doppler Beams per burst, exploiting the Doppler effect due to the satellite motion with respect the ground.
For each burst (64 time-domain deramped pulses), a Fast Fourier Transform is performed on the burst data in the along-track direction (Beam Formation).
This operation produces a set of 64 contiguous Doppler Beams (Doppler Beam Fan) equally[2] spaced in angle over the antenna 3dB along-track beamwidth and located in a plane defined by the satellite velocity and Doppler Axis. The angle of separation between the Doppler Beams is a function of platform speed, instrument PRF and carrier wavenumber.
The Doppler Beams have a beam-limited illumination pattern in along-track direction, while maintaining the pulse-limited form in across-track direction: this means that the instrument spatial along-track resolution is now sharpened (now it will be around 300 meter for CryoSat-2 and Sentinel-3 case) whereas in the across-track direction it will be still constrained to the diameter of the pulse-limited circle.
The footprint of each Doppler Beam on ground is referred to as Doppler Cell.

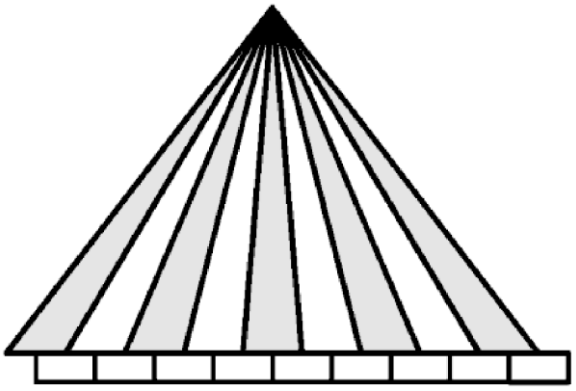

Figure 2.7: Formed Doppler Beam Fan - For sake of simplicity, only 9 beams are shown in the figure. The Doppler Beams are not "exactly" co-located with surface locations. Image courtesy of Keith Russel Raney

[2]In reality, given Earth curvature, they are **nearly** equally spaced in angle over the antenna 3dB along-track beamwidth

The Doppler Beams in the Fan will be symmetrically distributed around the Doppler Axis, and hence in general the Doppler Beam Fan will have a non-null central Doppler frequency (Doppler Centroid frequency) and it will not be pointed to nadir.

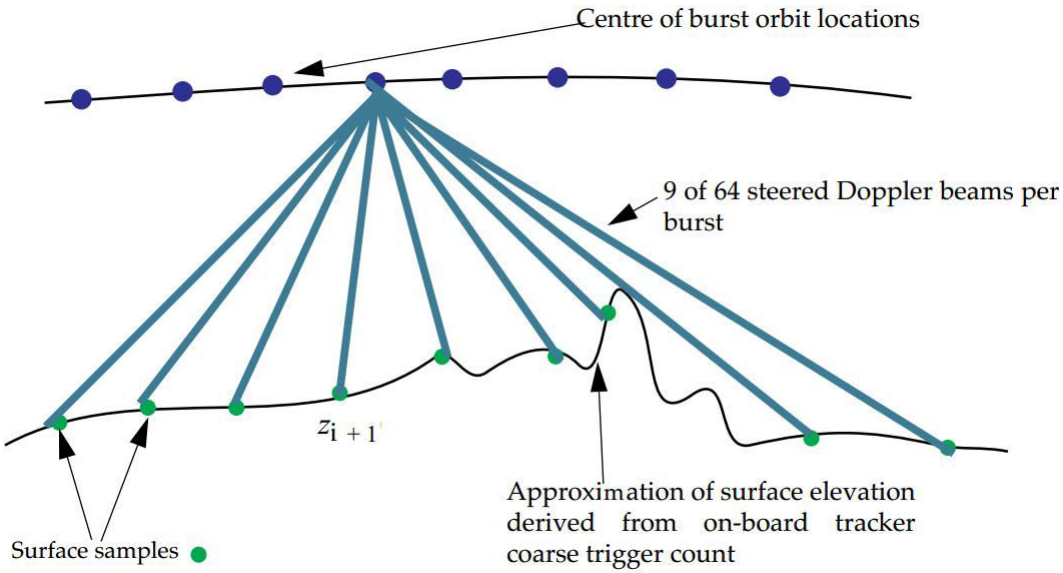

Figure 2.8: Formed Doppler Beam Fan - in the image the beams are already steered on surface samples. For sake of simplicity, only 9 beams are shown in the figure. Image courtesy of Robert Cullen

Hence, in order to steer the Doppler Beam Fan to the nadir direction, it is necessary to implement a Doppler Centroid Compensation or Doppler Centroid Shift.

For each burst, the angle between the nadir direction and the Doppler axis direction needs to be calculated (Doppler Centroid Angle). This angle is converted in Doppler frequency Δf_c and a pre-FFT phase rotation of Δf_c is applied to each along-track cut of the burst by means of the shift theorem of Fourier Transform.

After the Doppler Centroid compensation, the Doppler Beam with Doppler Beam angle closest to 90 degrees is assumed to be the central beam for the current burst.

Nevertheless, even after the Doppler Centroid compensation, due to the irregular topography of the overflown elevation profile, none of the synthesized Doppler beam footprints will be perfectly co-located with any of the 64 surface sample locations actually in view by sensor.

If this effect is not corrected, it will translates in an unwanted smearing of the SAR waveform after the multi-looking (i.e. not efficient application of multi-looking).

Hence, a steering of the Doppler beams in order to make the 64 Doppler footprints perfectly co-located with the 64 surface sample locations actually in view by the current burst is necessary (Beam Steering).

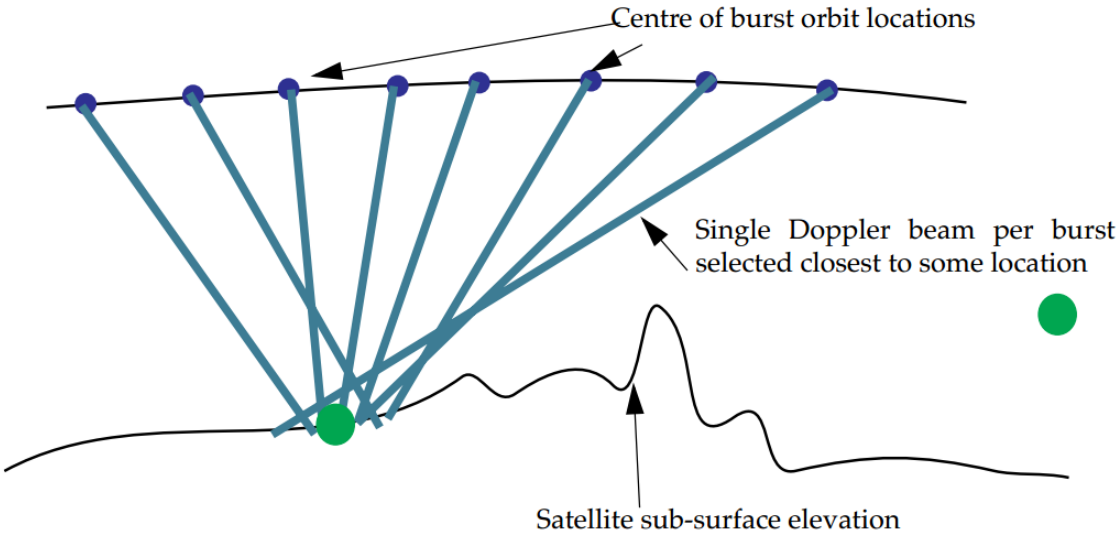

Figure 2.9: Doppler Beams synthesized at centre of bursts after stacking are not directed "exactly" towards the position of the surface sample and hence in this case the multilooking will not be efficient. Image courtesy of Robert Cullen

According to the degree of precision requested, this beam steering can be approximate or exact.

a) Approximated Beam Steering

In the approximate beam steering, all the Doppler Beams will be steered by the same angle (here referred as Rock Angle). In order to apply the aforesaid steering, for each burst, the angle between the central beam direction and the Doppler Axis needs to be calculated (Rock Angle). This angle is converted in a Doppler frequency Δf_r and a pre-FFT phase rotation of Δf_r is applied to each along-track cut of the burst by the shift theorem.

By the effect of this rock steering, only the Doppler central beam footprint will be co-located" exactly"[3] with own closest surface sample location whereas the other beams are steered by the same rock angle but each of them will be only approximately co-located with the own closest surface samples location.

This approximation can be considered acceptable on gentle undulating surfaces.

b) Exact Beam Steering

For effect of the application of the Beam Formation, the Doppler Beams are angularly equispaced[4] but it can happen that angularly equispaced Doppler beams produce strongly unevenly spaced projections on the ground, in event of highly variable Earth topography.

In this case, the approximate steering solution does not hold anymore and it needs now to apply an "exact" beam steering.

In the "exact" beam steering, each of the Doppler Beams will be steered by a different angle (Rock Angles); by effect of these phase rotations, **each** Doppler beam footprint (i.e. not only the central Doppler Beam) will be now co-located" exactly"[5] with the own closest surface sample location.

The exact beam forming needs to be applied in case of highly variable topographic surfaces.

[3]Clearly, in the practical implementations, perfect exactness of the co-location can't be achieved due to uncertainties in the knowledge of satellite's elliptical orbit, Earth ellipsoid as well as topographic relief.

[4]in reality, given Earth curvature, they are only nearly equally spaced in angle over the antenna 3dB along-track beamwidth

[5]Clearly, in the practical implementations, perfect exactness of the co-location can't be achieved due to uncertainties in the knowledge of satellite's elliptical orbit and of the overflown topographic relief.

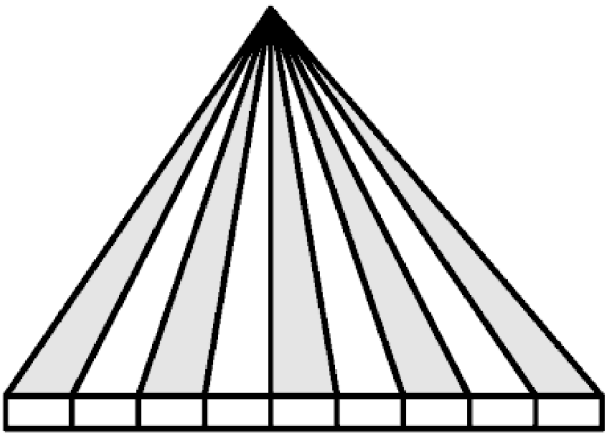

Figure 2.10: Formed and Steered Doppler Beam Fan - For sake of simplicity, only 9 beams are shown in the figure. The Doppler Beams are now "exactly" co-located with the pre-fixed surface locations. Image courtesy of Keith Russel Raney

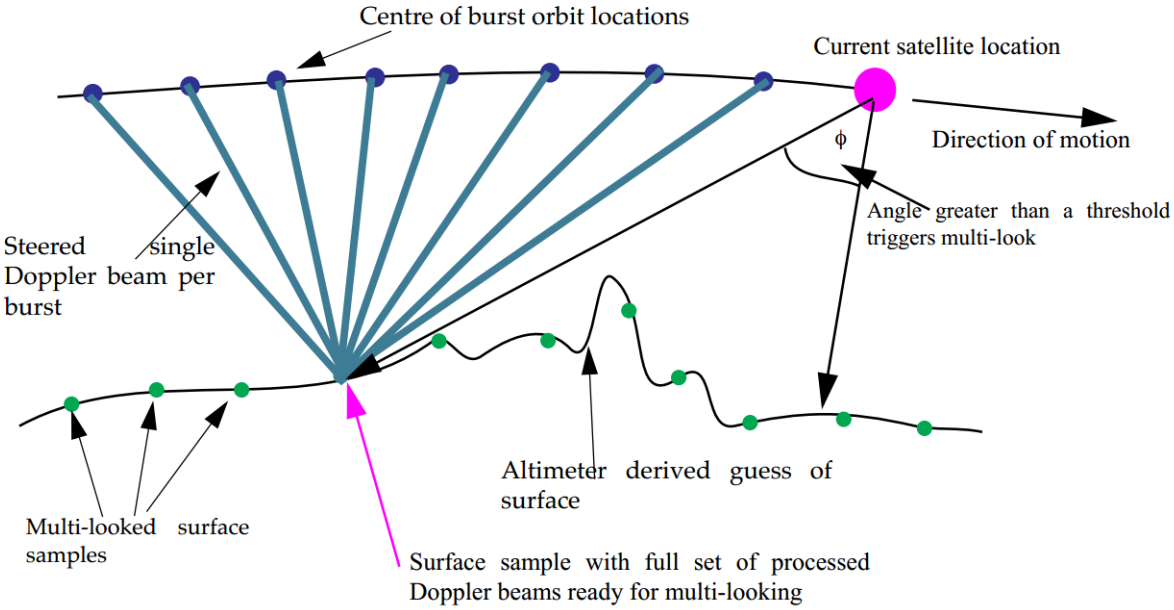

Figure 2.11: As consequence of the "exact" Doppler Steering, Doppler Beams after stacking are now directed "exactly" on the position of the surface sample. Image courtesy of Robert Cullen

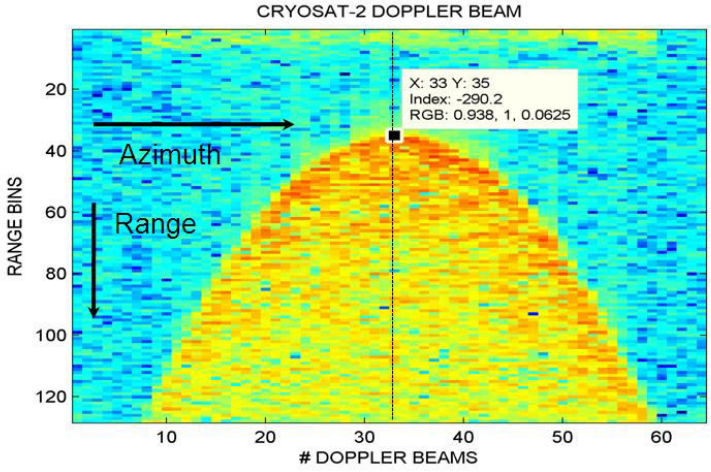

Figure 2.12: Burst Data in Power after Beam formation and beam steering (Range compression is also applied for visualization reasons). The burst beams are placed around a parabola per effect of scene geometry.

During the beam formation, the intra-burst range alignment can be as well carried out. In the L1A products the orbit altitude is given only at burst center (i.e. at 80 Hz) but clearly the orbit altitude will be slightly different for the several beams inside a burst. Knowing the orbital height rate, the orbital height shift for the different beams inside the burst can be computed and applied as phasor shift in range. This way all the beams will be referenced to the same orbital height at burst center.
It is expected that the effect of this correction to be non-negligible in regions where the satellite height rate is high (more than 20 meter/sec) or in general in case the orbit is slightly elliptical.

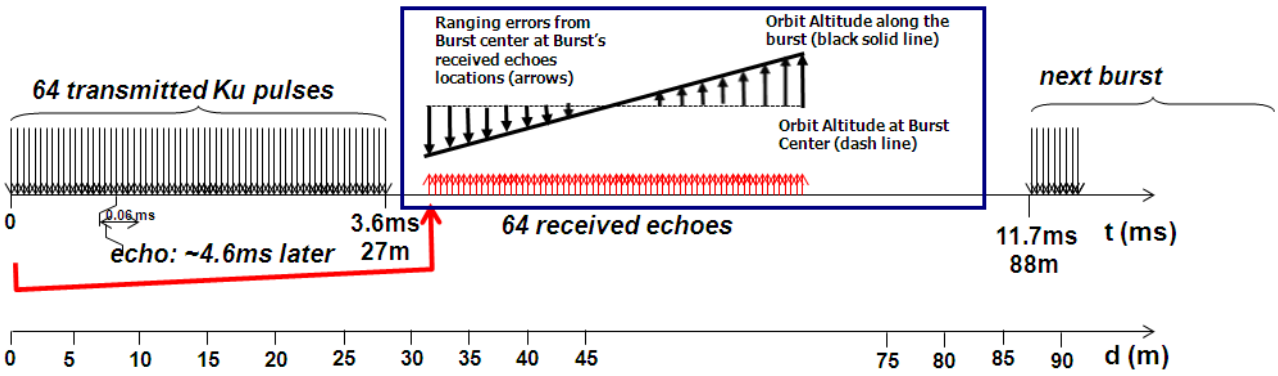

Figure 2.13: Intra-burst range correction: each beam inside the burst has a different orbit altitude (see the frame in blue): considering one orbit altitude for the whole burst entails non-negligible errors in regions with high height rate

SAR altimetry data can be plagued by an effect known as sidelobes ambiguity or "ghosting". This effect may occur when bright backscattering patches are placed on the surface in the along track antenna footprint.
In this eventuality, the signal backscattered from the nadir cell may be so strong (around 60 dB) to end up to leak in the off-nadir Synthetic Doppler Beams through its sidelobes (see Figure 2.14). The final effect on the data is to have a stripe of spurious received power at nadir position all along the burst data (see Figure 2.14).

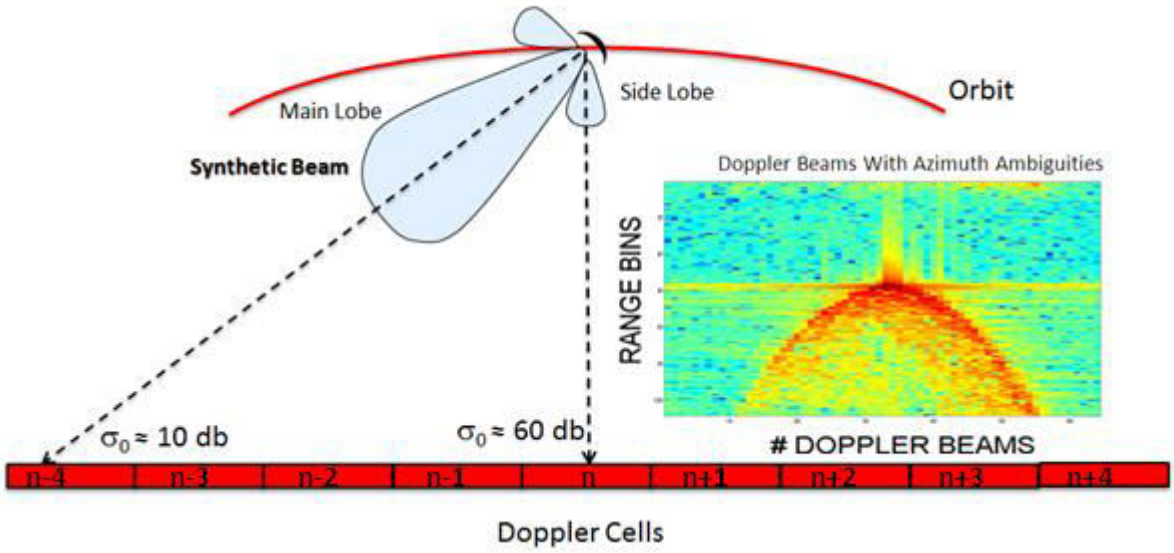

Figure 2.14: Side-Lobe Ambiguity Effect: the signal originating from the Doppler Cell n at nadir (bright scattering patch) sneaks into the synthetic beam through its side lobe, and overlaps and aliases the signal originating from Doppler Cell n-4 (Doppler Cell which the synthetic beam main lobe in figure is oriented to). In the Figure's frame, the effect of the leakage on the burst data is shown with the spurious stripe of energy at nadir.

The phenomenon is frequent over sea ice (where bright targets are represented by the water's leads between ice floes), and in coastal zone or inland water (where bright targets can be ponds with still water, wetlands, sand banks, cliffs, etc.).
In order to mitigate this effect of side-lobes ambiguity, during the beam formation process, a weighting window (e.g. a Hamming Function) may be applied in the along-track direction on burst data prior the along-track FFT operation. The effect of the weighting window is to depress the level of the side lobes of synthetic beam and hence it will cancel the spurious signal out (see Figure 2.15) but this comes at expense of a degradation of the along-track resolution.

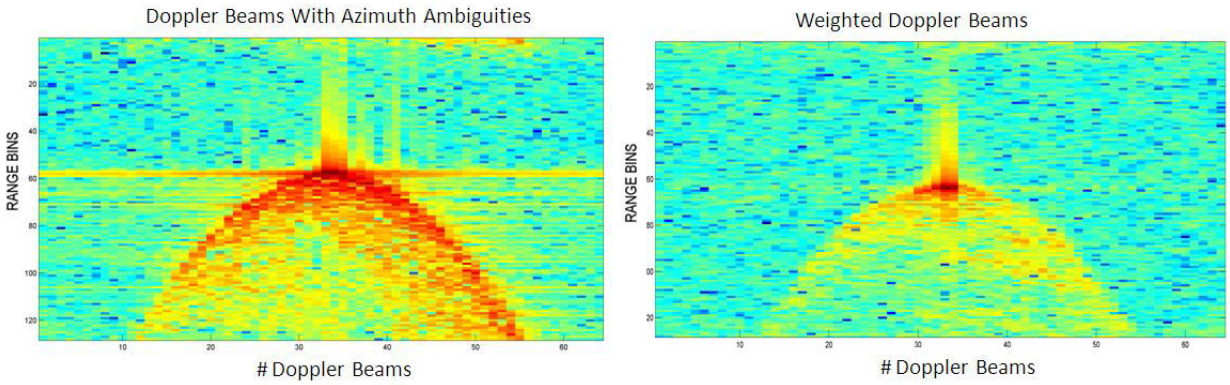

Figure 2.15: Burst Data with azimuth ambiguity (on the left) and after Hamming weighting application (on the right)

2.1.2.5 Beam Stacking

The purpose of this stage is to re-sort all the synthesized Doppler Beams in order to gather in one stack of data all the Doppler Beams that are pointing "exactly"[6] to the same surface sample location (Doppler Space/ Ground-Position Mapping).
Hence, from all the synthesized burst beams, all the Doppler Beams staring at the same surface location are selected and stacked in sequence in a data matrix. This data matrix is referred generally as Stack or Doppler Beam Stack.
Only one beam per burst is selected: the beam in the burst having the Doppler footprint co-located with other Doppler Beam footprints from other bursts.
Hence, these Doppler Beams illuminate the same surface location at different look angles from different burst center positions (and hence they represent independent looks).
The number N_L of Doppler Beams staring the same surface location (i.e. the looks) is variable depending on the orbital geometry (in case of Closed-Burst Transmission Mode). This number is around 220 for CryoSat-2 and Sentinel-3 altimeters.

[6]Clearly, in the practical implementations, perfect exactness of the co-location can't be achieved due to uncertainties in the knowledge of satellite's elliptical orbit and of the over-flown topographic relief.

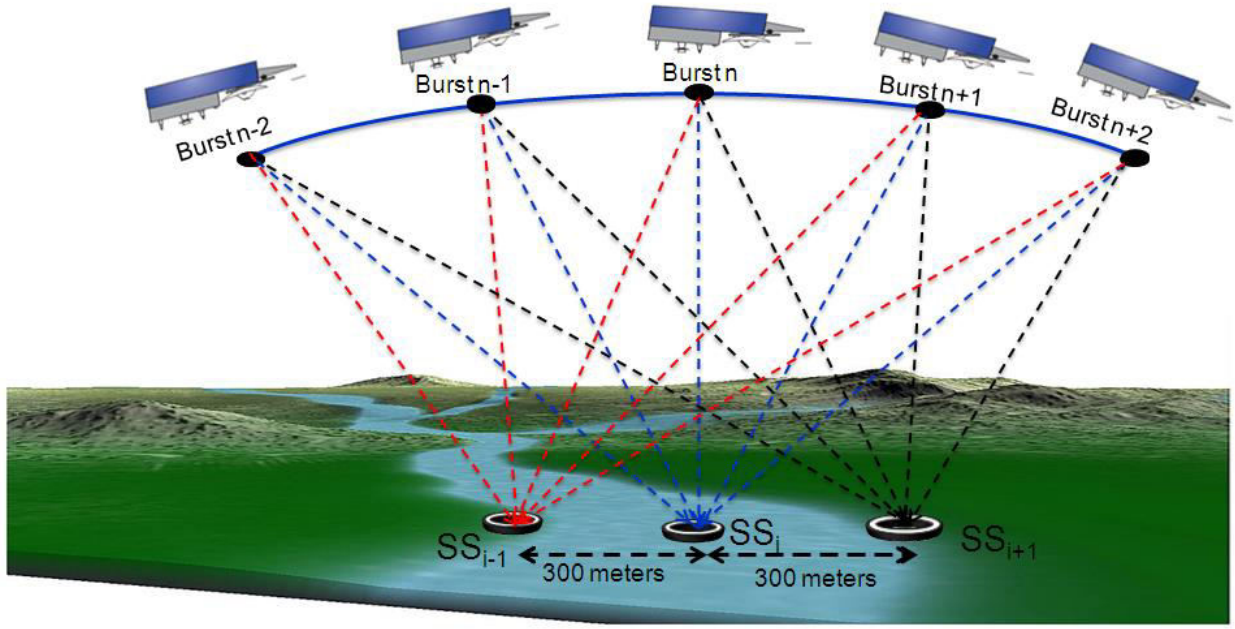

Figure 2.16: Doppler Space/Ground Position Mapping: all the Doppler Beams, synthetized at burst centres n, (for sake of simplicity here only three beams are shown per burst) staring at the same Surface Sample SS_i position are selected and are contributing to the generation of the SAR Echo at position SS_i (by multi-looking).Therefore, the SAR Processor posts SAR Echoes at the posting rate of SSi. The numbering of n (burst centre) and SS_i (Surface Sample)are totally independent of each other: for CryoSat-2, the inter-distance between surface sample locations is around 300 meter (~20 Hz) whereas for bursts is 80 meters (~85 Hz). In the picture, the black and white circles represent the centres of the surface locations.

2.1.2.6 Range Alignment

The purpose of this stage is to correct all the misalignment in range between the beams of the same stack. Indeed, if it is wished to operate an efficient multi-looking, all the misalignment in range between the stack beams needs to be corrected.

Three range corrections need to be operated and they are described in the following sub-sections:

a) Slant Range Correction

The purpose of this correction is to compensate the slant range migration, i.e. the different radial distance at which the surface sample is seen when the satellite moves along its orbit over the surface location. Multi-looking requires averaging the returns from the same surface location seen from different look angles: in order this average to be effective, it is necessary to compensate such range migration effect. For each stack beam, this stage computes the slant range shift in meters, necessary to compensate the range migration effect and converts it in phase shift. The slant range shift is referred to a reference range.

The reference range can be the distance between the surface sample of the current stack and satellite CoM position on the vertical to the surface sample.

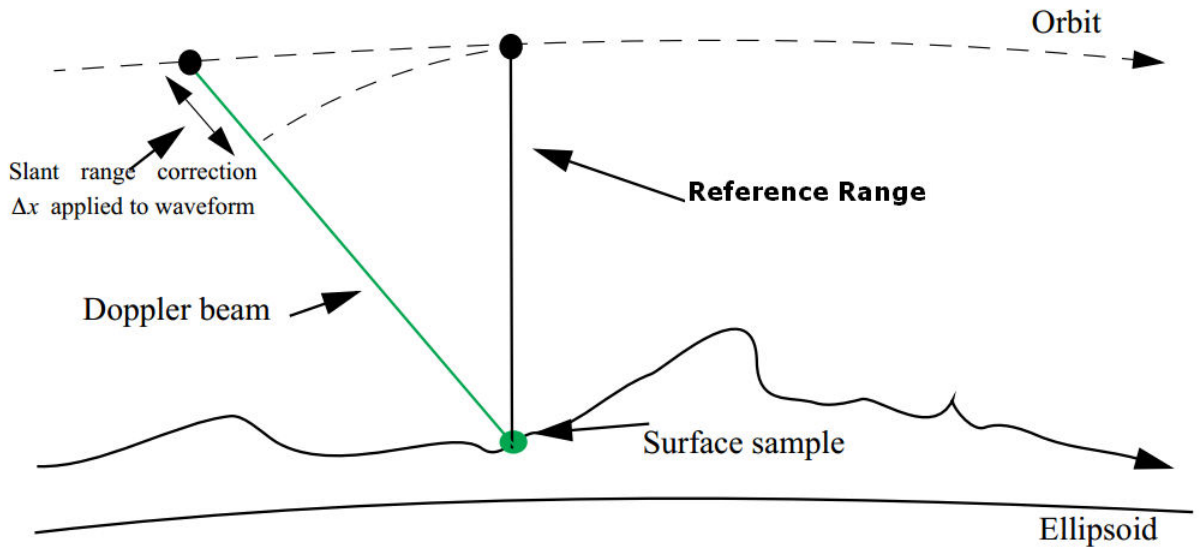

Figure 2.17: Slant Range Shift to be compensated between the Doppler Beams in a stack. Image Courtesy of Robert Cullen

b) Tracker Range Correction

The purpose of this correction is to compensate the shift in range of the on board tracker across all the beams in the current stack.

For each stack beams, this stage computes the range shift in meters, necessary to compensate the tracker movement, and converts it in phase shift. Also the tracker range shift needs to be referred to a reference range. The tracker reference range can be the maximum of the tracker range.

c) Doppler Range Correction

The purpose of this correction is to compensate the Doppler shift in range for all the Doppler beams in the current stack.

For each beam of the stack, knowing the angle that Doppler beam makes with the velocity vector, this stage computes the Doppler frequency shift, necessary to compensate the Doppler effect induced by sensor motion during the pulse transmission and echo reception, and converts it in phase shift.

Once these three range shifts have been computed, their sum is applied to shift in range the stack beams exploiting the shift theorem of the Fourier Transform.

Hence, after compensation, the range delay at which the return from a given surface location is placed is that corresponding to its minimum distance from the satellite.

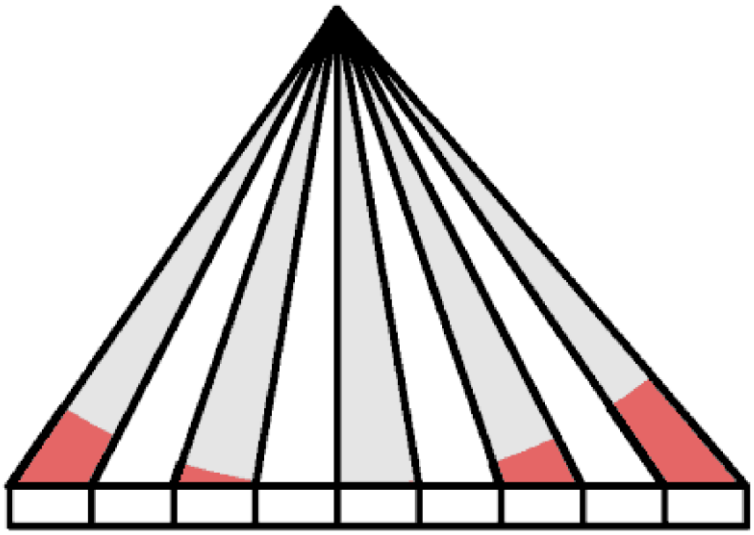

Figure 2.18: Formed, Steered and Range-Aligned Doppler Beam Fan - For sake of simplicity, only 9 beams are shown in the figure. The range mis-alignment between Doppler Beams is now compensated. Image courtesy of Keith Russel Raney.

2.1.2.7 Range Compression

The purpose of this stage is to perform, for each range cut of the stack, the range compression of the Doppler Beams in the stack.

The range compression is implemented as simple Fast Fourier Transform (FFT) in range (or delay) direction of the stack. After the range FFT, the signal is square-law detected (i.e. the power is extracted).

In order to avoid aliasing of the signal that would normally occur due to the doubling of the signal bandwidth when square-law detecting the signal itself (Smith and Scharroo 2014), prior of the range compression the Doppler Beams waveforms can be zero-padded, doubling this way their extension. The net effect is to over-sample the range compressed signal by a factor of 2. This technique proves to be very beneficial in case of peaky waveforms from bright targets since it allows having more range samples in the narrow waveform's peak (see Figure 2.22) and is the same technique applied during CAL1 calibration mode to better measure the internal path delay of the Range Impulse Response.

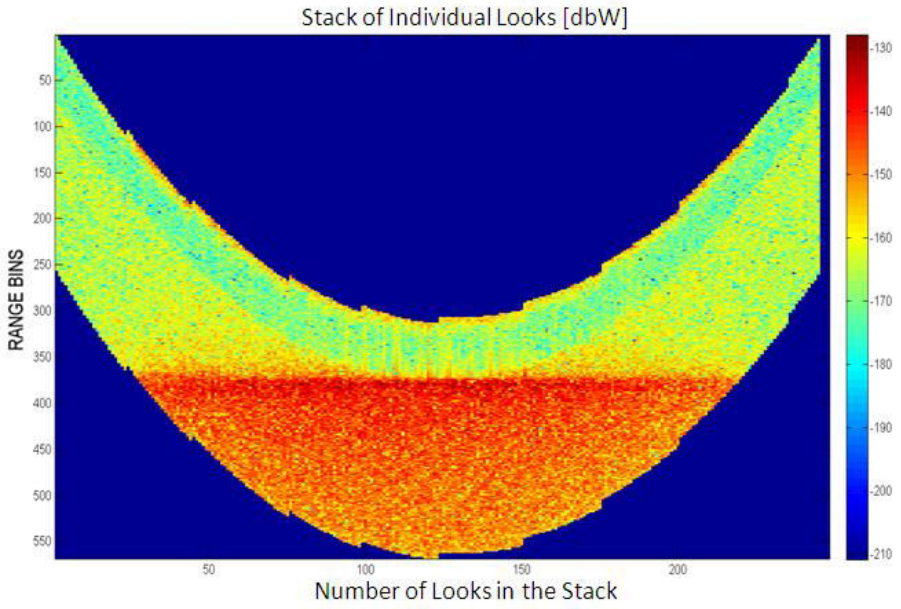

Figure 2.19: Stack of co-located and range-compressed Doppler Beams (Looks) over ocean surface. The Doppler Beams have been aligned in range, range compressed and square-detected.

2.1.2.8 Multi-Looking

The purpose of this stage is to carry out the multi-looking of the individual echoes in the stack.
This multi-look procedure is simply the incoherent summation in along-track direction of the square-law detected range-compressed Doppler Beams in the stack. Indeed, these Doppler Beams are now echoes which represent “looks” of the same surface location. The scope of the multi-looking is to knock down the speckle noise, accumulating statistically independents looks of the same measurement as shown in Figure 2.20.
The speckle noise is a multiplicative noise created by the randomness of the relative phases of the ensemble of scatterers which reflect the coherent (in phase) transmitted radar pulse. Because of this randomness, the relative phases of the reflected signals from the scatterers can be now out of phase and hence interfere between each other in constructive or destructive way. This constructive and destructive interference between scatterers phases will appear as granular black and white noise on top of a radar image or as random noise on top of the radar waveforn.
The final result of the multi-looking is the generation of a single SAR Return Power Waveform.
Some Doppler Beam (Looks) can be discarded out of the summation by mean of a noise thresholding or of Doppler angle thresholding. Anyhow, the outer looks in the stack data are less efficient than the looks closer to the zero-Doppler (Gommenginger et al., 2014).
The need to apply a thresholding and discard looks comes because not all looks come useful in same way (useful in term of noise reduction), but the most outer (i.e. with larger Doppler angles) looks may degrade the SAR Echo.

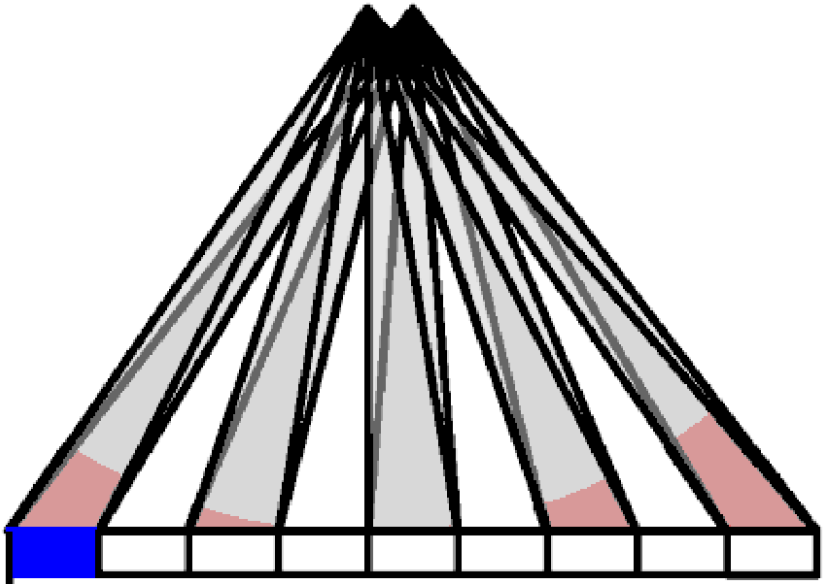

Figure 2.20: Multi-Looking Concept: in the Figure, Doppler Beams synthesized from two adjacent bursts are staring at the same surface locations; in the multi-looking operation, all these Doppler Beams, staring at the same surface location from the all useful bursts, are incoherently summed in power. For sake of simplicity, only 9 beams are shown in above figure. Image courtesy of Keith Russel Raney.

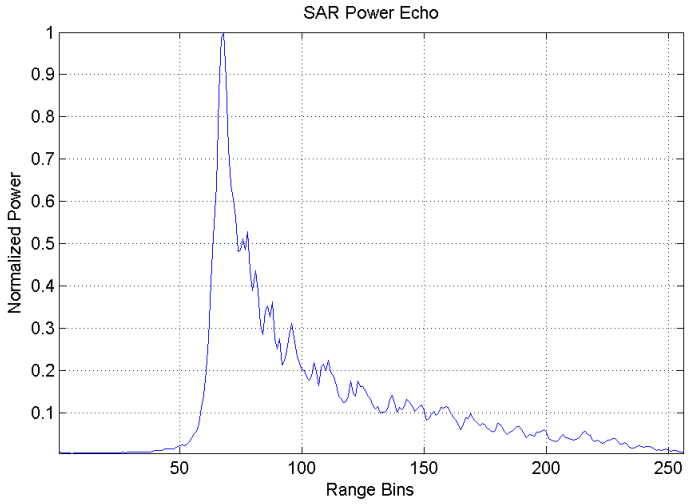

Figure 2.21: Cryosat-2 Multi-looked SAR Return Power Waveform over open ocean

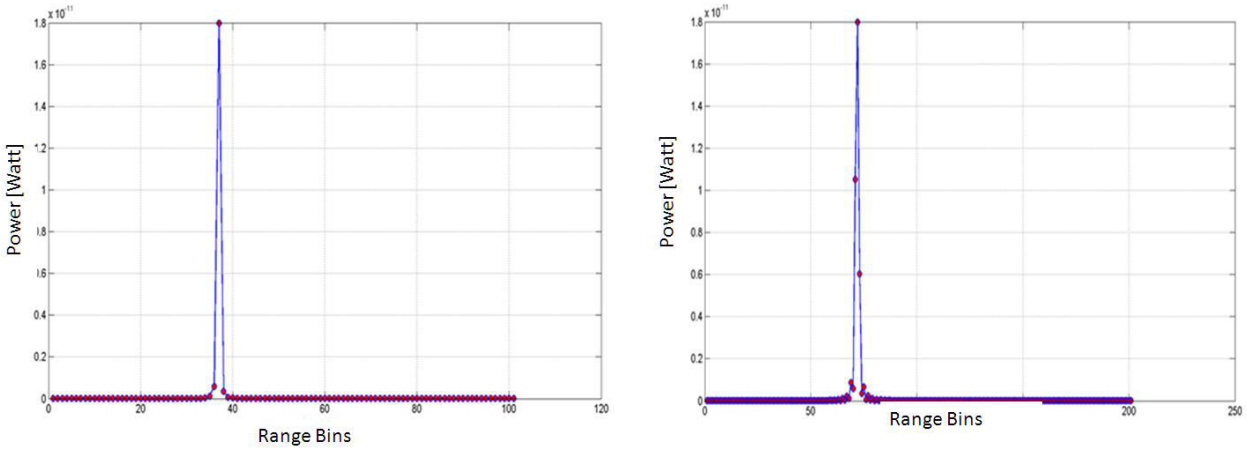

Figure 2.22: Zero-padding Concept: on the left a waveform with standard gridding (128 range bins) from a bright target is shown; on the right the same waveform with zero padding (256 range bins) is shown and features more range samples in correspondence of the peak

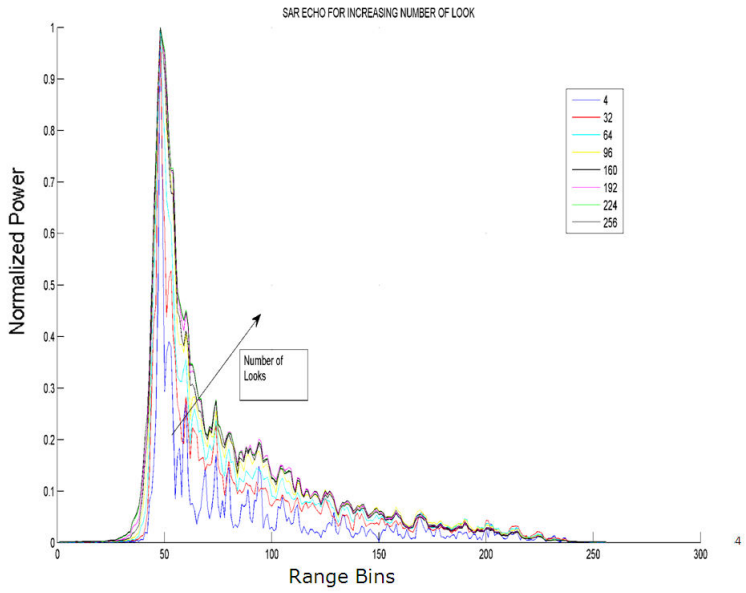

Figure 2.23: Increasing the number of accumulated looks the waveform will make it less and less noisy

When, on the other side, the incoherent summation is carried out in range direction (range multilooking), a different waveform is achieved which is referred as stack RIP (Range Integrated Power).

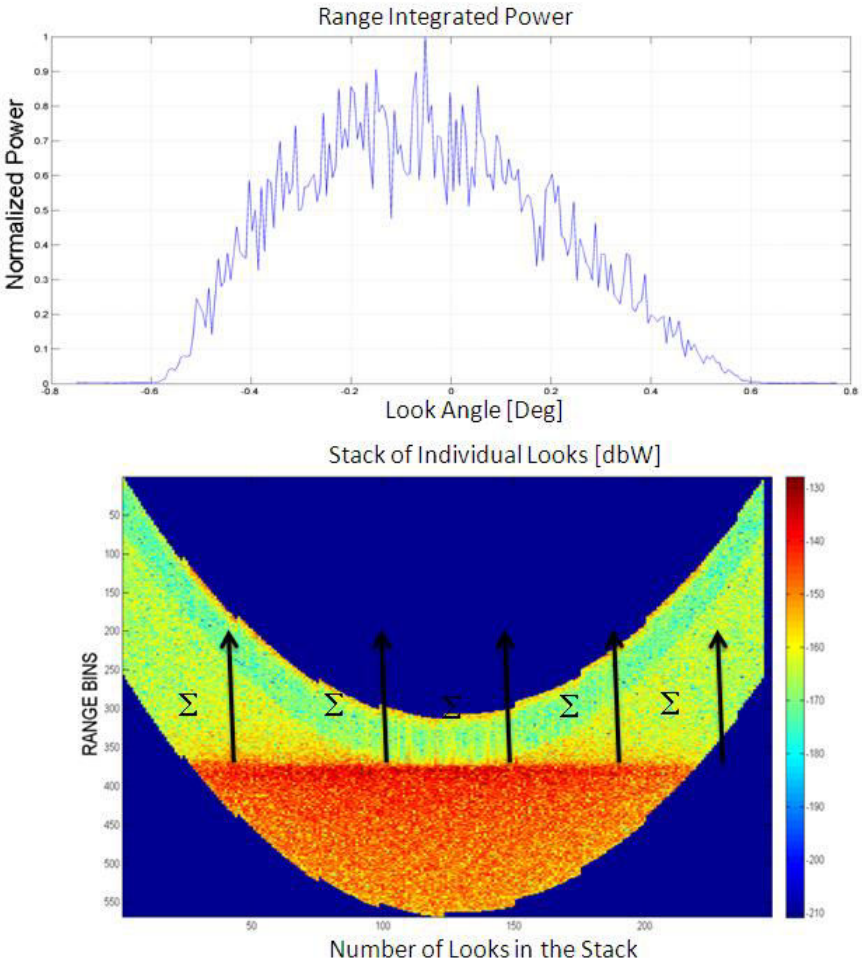

Figure 2.24: Summation (bottom picture) of the stack power in range direction builds the RIP (top picture). The symbol Σ stands for the summation.

A typical RIP over open ocean is shown in Figure 2.24 versus the look angle.

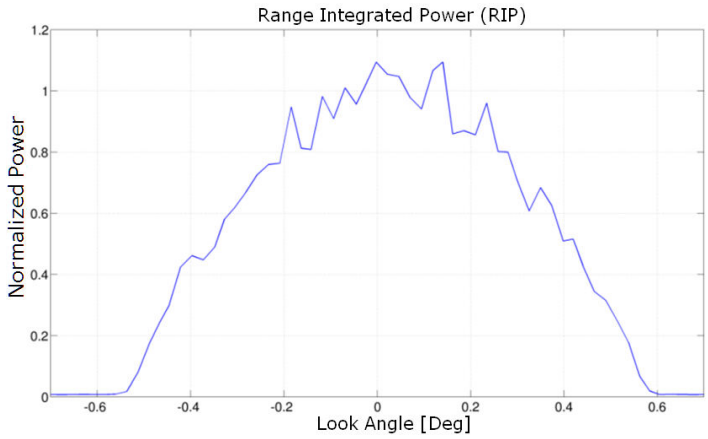

Figure 2.25: Sub-RIP versus look angle

While, in Figure 2.25, what I am showing is the "Sub-RIP" which is constructed, from the RIP, averaging 4 adjacent RIP samples (reducing hence the number of samples from the original 210 to around 50). The

reason for this is that the RIP is quite a noisy signal (as can be seen in Figure 2.24-top) and hence it is necessary to make a sort of internal averaging to knock down the level of its noise.
Then, all the RIP of the pass can be stacked in sequence and build what can be called "ripgram" as in Figure 2.26. In this Figure 2.26, the Cryosat-2 altimeter is passing over the sea ice and the red points are bright reflections from the surface as water leads between ice floes.

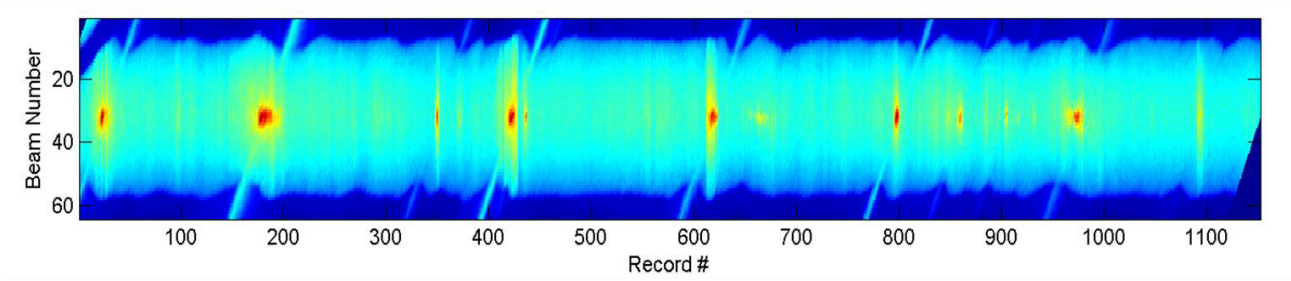

Figure 2.26: Stack in sequence of the RIP in the pass, or ripgram

In summary, the block-scheme of the SAR L1B Processing is represented in Figure 2.27.

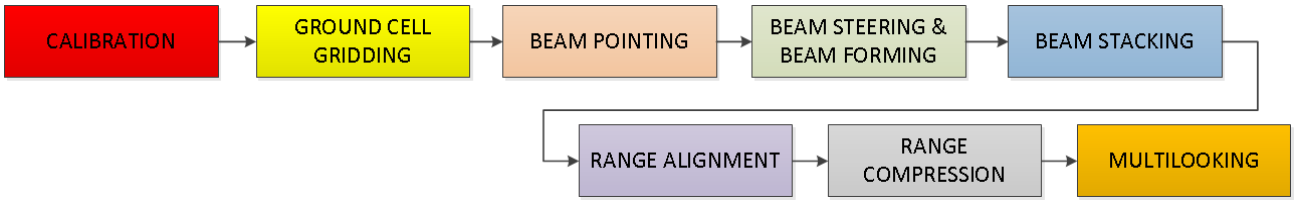

Figure 2.27: Block-Scheme for the Delay-Doppler Processing

The Table 2.1 lists the customization of the L1b SAR Processing configuration for CryoSat-2 and Sentinel-3 SAR Altimeter Ground Segment. Indeed, even if the two sensors are very similar, the processing presently carried out in the payload ground segment (PDGS) of the two missions at L1b is different, reflecting the different mission's primary objective: Ice for CryoSat-2 Processor and Ocean for Sentinel-3.

PROCESS	CRYOSAT-2	SENTINEL-3
Burst Data Weighting	YES, Hamming Window	NO
Approximated/Exact Beam Forming	Both available, approximated method is used	Both available, approximated method is used
Zero-Padding (ZP)	YES (ZP=2)	NO
Number of Range Window Samples	256 (2-ZP)Samples	128 (1-ZP) Samples
Range Bin Width	0.2342 m	0.4684 m
Stack Beam Weighting	NO	NO
Stack Thresholding	Applied	Applied

Table 2.1: CryoSat-2 and Sentinel-3 L1b SAR Processing Configuration

2.2.1 L2 Processing in SAR Mode

Generally, it can be said that the Radar Altimetry L2 processing consists mainly in all the processes apt to extract from a radar waveform, returned from a certain surface location, the geophysical quantities of interest relative to that surface location. Hence, essentially, at L2 a measurement of these geophysical quantities is carried out. These processes are different according to the processing mode (pulse-limited, SAR, etc) under analysis. In this section, I will refer to the SAR L2 processing mode.

2.2.1.1 Waveform Retracking

The algorithm deputed to measure from the radar return waveform the geophysical quantities of interest is referred as waveform retracking or simply retracking.
The retracking family can be categorized in three big branches:

- Empirical Retracking
- Physically-Based Retracking
- Statistical Retracking

In the empirical retracking, the measurement of the geophysical quantities is based on heuristic methodologies which have been defined based on the regress experience or on a "guess & try" approach.
The empirical retrackers are appealing for their easiness of implementation and fastness of computational execution but they require a long and non-easy exercise of fine-tuning for all the parameters and thresholds which are part of the retracker.
Empirical retrackers are used typically in case of thematic applications wherein the physics of the problem is too complex to be theoretically addressed and solved (as inland waters and sea ice).
Examples of empirical retrackers are OCOG (Offset Center Of Gravity) (Wingham et al., 1986) or Threshold Retracker (Bamber, 1994).

In the physically-based retracking, the geophysical quantities are retrieved basically by cross-comparing the received return waveform with a waveform's model which best-approximates the received waveform shape and which is based on the physics of the electromagnetic interaction between the transmitted pulse and the scattering surface. Also this waveform model is modelling as much as possible all the sensor characteristics and the signal processing which the waveform has undergone on board and on ground.
Hence, one of most distinguished element of any physically-based retracker is the waveform's model which represents the expected waveform backscattered from the surface.
Thanks to the physically-based retracking process and to this "expectation" of the power return from the surface, the final vertical resolution of the altimetry range over ocean can be improved more than an order of magnitude with respect to original vertical resolution (which is around 45 cm).

The return waveform's physical model can be classified in two types as well:

- Numerical
- Analytical (or semi-analytical)

In case of physically-based numerical retracker, the waveform's model is computed solving numerically all the integrals and equations governing the shape of the received waveform.
In case of physically-based analytical retracker, these integrals and equations have been solved analytically and hence the waveform's model can be expressed by a closed-form equation. In case of semi-analytical model, part of the final model formulation is still expressed in term of integral functions.

While the numerical models are known to be the most accurate in representing the expected return waveform as they may include all the instrumental and physical effects, the analytical model necessarily have to make assumptions and approximations in order to derive a closed form solution of the model.
On the other side, being the model expressed by a simple equation, retrackers based on analytical model are more numerically robust, versatile, computationally fast and easy to be reproduced and used by third part experts. Having an analytical formulation of a waveform model brings along also the benefit to be able to understand and predict the behaviour of the model when changing the input variables.
Furthermore, the approximations made in deriving the analytical model can be a posteriori corrected by application of a Look-up Table (LUT).
Anyhow, whether the model is analytical or is numerical, and whether is derived in pulse-limited case or in Delay-Doppler case, the starting point for the derivation of a physical model is always the triplefold convolution between the Flat Surface Impulse Response P_{FS}, system point target response P_{PTR} and the sea surface elevation probability density function PDF_{σ_z} (Brown, 1977)**:**

$$\mathrm{Pr} = \mathrm{P_{FS}} * \mathrm{P_{PTR}} * \mathrm{PDF}_{\sigma_z} \tag{2.1}$$

The system point target response encompasses all the peculiar characteristics of the radar sensor (it can be considered the transfer function of the sensor), the Flat Surface Impulse Response is the response from a flat surface to the ideal impulse function while the statistical distribution of the ocean surface elevations is included in the surface elevation PDF (Probability Density Function).
The SAMOSA SAR return waveform model (which will be used in this thesis work) belongs to this latter category. The SAMOSA model has been derived originally for open ocean thematic applications by (Ray et al., 2015) in the frame of the ESA-funded project SAMOSA (SAR Altimetry MOde Studies and Applications), it is widely used over this type of surface and is setting up as a standard waveform's model for SAR ocean retracking, having being adopted as well in the Sentinel-3 STM mission ground segment. Furthermore, being an analytical model, it has the versatility to be very easily adaptable to any scattering surface once that a proper scattering model of the surface is considered in its formulation.

In case of physically-based retracker, the extraction of the geophysical quantities from the waveform data is accomplished maximizing a certain objective function or, on the other way around, minimizing a certain function cost, given the waveform data and a certain functional model of the waveform.
Hence, one can consider the waveform retracking as a kind of optimization technique, the retracking problem as an optimization problem and all the unknown geophysical measurements as state variables.
The available physically-based retrackers differ on the adopted approach in the minimization of the cost function (or maximization of the objective function). For sake of its simplicity, the most used minimization algorithms is the Least Square Estimator (LSE) (Björck, 1996) which minimizes a cost function represented by the sum of the square residuals between waveform model and waveform data. Hence, in this case the solution to the retracking problem will be the one providing, in least square sense, the best fitting between the waveform data and waveform model. In any case, it is always necessary to provide an initial state to the state variables, when starting the minimization process, which should be the closest possible to the searched solution.
Also common is the Maximum Likelihood Estimator (MLE) which is an unbiased estimator which maximizes the likelihood function of the model waveform given the waveform data and which guarantees asymptotically the smallest variance in the estimate error (Kay, 1993). In this case, the solution to the retracking problem will be the one providing a model waveform which better resembles (or looks like) the waveform data.

Finally, the statistical retrackers search the solution to the retracking problem trying to minimize (or maximize) the statistical properties of a set of consecutive waveforms (like to find the shortest paths between

neighbouring sub-waveforms from a large set of multiple likely heights) as in (Roscher et al., 2017). They are hence also physical-model free.

Once one has settled down the type of retracking to use (between empirical, physical and statistical), the next step is decide how many "unknowns" or geophysical measurements you want to retrieve from the waveform. Over the open ocean and coastal zone thematic applications, the geophysical quantities of interest which are aimed to be measured after a physical-based retracking are:

- Sea Surface Height (SSH)
- Significant Wave Height (SWH)
- Marine Wind Speed at 10 meter (U10)

The sea surface height is the height of the sea surface as measured by the altimeter with respect a reference ellipsoid.
The significant wave height is the average height (trough to crest) of the highest one-third waves in a wave spectrum and is usually taken as 4 times the standard deviation of the sea surface elevation.
The wind speed is the speed of wind at a height of 10 meter from the sea surface.
Because a physically-based SAR ocean retracking usually gives in output (as it will be shown in chapter 3):

- Two way epoch t_0, defined as time delay between the retracking point and a reference tracking point
- SWH (in case of SAR Altimetry)
- Amplitude Pu, defined as retracked waveform power

the sea surface height over a reference ellipsoid is derived after the retracking by:

$$\begin{cases} \mathrm{SSH} = \mathrm{h} - (\mathrm{R} + \mathrm{R\_cor\_sea}) \\ \mathrm{R} = \mathrm{Tracker\_Delay} \cdot \mathrm{c}/2 + \mathrm{t_0} \cdot \mathrm{c}/2 \end{cases} \tag{2.2}$$

where:

- R is Radar Altimeter Retracked Range
- h is the altitude of the satellite center of mass above the reference ellipsoid
- c is the speed of light in the vacuum
- Tracker_Delay is the on board tracker's time delay (two way) between the pulse transmission and reference tracking point, corrected by all the instrumental effects
- R_cor_sea is the range and geophysical correction over the sea, defined in section 2.2.1.3

The wind speed is derived converting the amplitude Pu to backscattering coefficient (sigma nought) and subsequently the sigma nought in wind speed.
The formula to convert the amplitude Pu to sigma nought is based on the radar-link budget equation in SAR mode (ESA Report 2016):

$$\sigma_0 = 10 \cdot \log10\left(\frac{\mathrm{P_u}}{\mathrm{Tx\_Pwr}}\right) + 10 \cdot \log10(\mathrm{K}) \tag{2.3}$$

where:

$$K = \frac{(4\pi)^3 \cdot R^4 \cdot L_{atm}}{\lambda_0^2 \cdot G_0^2 \cdot A_{SAR}} \quad (2.4)$$

where A_{SAR} is the resolution ground-cell area in SAR-mode:

$$A_{SAR} = (2 \cdot L_y) \cdot (L_x) \quad (2.5)$$

with:

$$\begin{cases} L_y = \sqrt{\frac{c \cdot R \cdot \sigma_p}{\alpha}} \\ L_{x=} \frac{\lambda_0 \cdot R}{2 \cdot V_s \cdot \tau_B} \end{cases} \quad (2.6)$$

and:

$$\alpha = 1 + \frac{R}{R_{Earth}} \quad (2.7)$$

- L_{atm} are the two ways atmosphere losses
- λ_0 is the RF carrier wavelength
- c is the speed of light in the vacuum
- R_{Earth} is the mean Earth radius
- G_0 is the antenna gain at boresight
- σ_p is 3dB range Point Target Response time width
- Vs is the satellite velocity
- τ_B is the burst time duration
- Tx_Pwr is the transmitted peak power

L_y is usually referred as pulse-limited radius.
Regarding the wind speed model to be used to convert the sigma nought in wind speed, the same model can be used both in pulse-limited Altimetry and in SAR altimetry. One of the most used wind speed model is the ECMWF's one (Abdalla, 2012) which is a heuristic model computed making a statistical regression between collocated Envisat Ku sigma nought, ECMWF wind speed model and buoys wind speeds.

Over inland water bodies, the geophysical information extracted from the waveform is essentially the inland water height:

$$IWH = h - (Tracker\_Delay \cdot c/2 + t_0 \cdot c/2 + R\_cor\_land) \quad (2.8)$$

Where R_cor_land is the range and geophysical correction over land, defined in section 2.2.1.3

2.2.1.2 Pseudo-LRM Processing

Given the technical design of CryoSat-2 and Sentinel-3 altimeter, simultaneous operations in SAR mode and LRM (Low Resolution Mode, the CryoSat-2 and Sentinel-3 name for the pulse-limited mode) are not possible. However, when the CryoSat-2 or Sentinel-3 radar altimeter is in SAR mode, it is possible to process the SAR burst data in the pulse-limited sense, to obtain a proxy of LRM, called Pseudo-LRM (PLRM) or also Reduced-SAR (RDSAR) (Scharroo et al., 2016; Martin-Puig et al., 2008). I point out that PLRM data are expected to feature lower performance (in terms of precision) than standard LRM mode data (Fenoglio-Marc et al., 2015). This occurs because the number of independent looks accumulated to build a PLRM waveform is in PLRM less than in LRM mode as consequence of the empty interval between two transmitted bursts. When in this thesis I assess the benefit of SAR altimetry against the pulse-limited altimetry, I use as reference a PLRM mode dataset and, hence, I am strictly assessing the performance of the SAR mode in comparison to the PLRM mode.
To build the PLRM waveforms from the L1A data, the standard pulse-limited processing for open-ocean was followed, as described in Fenoglio-Marc et al., (2015) and by Fenoglio-Marc and Buchhaupt (2017a). The processing is based on Scharroo (2016) with a different ordering of some processing steps and with updated input data for calibration. The procedure consists in an incoherent averaging of the individual echoes from four bursts of 64 pulses each. First, each echo within a burst is calibrated in amplitude and phase and compensated for the receiver low pass filter mask. The echoes are then aligned horizontally in range time, by applying two phase shifts to account for change in range between the echoes in the same burst and between the four consecutive bursts. A zero-padding is performed for each echo by adding 64 complex zeros on each side of the 128 bins. A 1-dimensional Fast Fourier Transform (FFT) is then applied horizontally to each of the echoes. In the last step the 20 Hz waveform W is calculated by summing the power of each pulse:

$$W_k = \sum_{p=0}^{255} I_p(k)^2 + Q_p(k)^2 \quad (2.9)$$

Where $I_p(k)$ is the in-phase component of pulse p at bin k and $Q_p(k)$ the quadrature component. The mean value of the datation of burst two and three is used as time stamp for the computed 20 Hz waveform.
Once that the PLRM waveform is built, the L2 processing operated on the waveform (retracking) is not dissimilar to what has been done and is done in conventional pulse-limited altimetry missions as ERS 1/2, Envisat and Jason 1/2/3. For further details, the reader can refer to (Scharroo, 2016).

2.2.1.3 Geophysical and Range Corrections

The measurement of the sea surface height from the radar altimeter range measurements involves the application of number of range and geophysical corrections: the first ones deal with the slow-down of radar pulse speed through a refractive medium (as wet, dry tropospheric and ionospheric correction) and with the actual scattering surface of the radar pulse (as sea state bias correction) whereas the second ones remove from the measured sea surface height the variation of the largest time-variable external contributors as ocean tide and atmospheric pressure (Vignudelli, 2011) in order to observe only purely ocean topographic dynamics.
Over sea surfaces (open sea and coastal zone), the geophysical and range correction to apply in the derivation of the sea surface height are:

$$R\_cor\_sea = dry\_tropo + wet\_tropo + equi\_tide + load\_tide + longperiod\_tide + iono\_delay + dac + solidearth\_tide + pole\_tide + ssb \quad (2.10)$$

with:

- dry_tropo is the dry tropospheric path correction
- wet_tropo is the wet tropospheric path correction
- iono_delay is the ionospheric path delay
- equi_tide is the ocean equilibrium tide
- load_tide is the ocean loading tide
- longperiod_tide is the ocean long period equilibrium tide
- dac is the dynamic atmospheric correction
- solidearth_tide is the solid earth tide
- pole_tide is the geocentric polar tide
- ssb is the sea state bias

Over inland water, the geophysical and range correction to apply in the derivation of the surface elevation are:

$$R\_cor\_land = dry\_tropo + wet\_tropo + iono\_delay + solidearth\_tide + pole\_tide \quad (2.11)$$

Since the inland water bodies are closed systems, the dynamic atmospheric correction is not applied (Fernandes and Lázaro, 2018). Furthermore, also sea state bias is not applied since the inland water bodies have usually a very low sea state driven by winds and waves (Fernandes and Lázaro, 2018).

2.2 Numerical Ocean Circulation and Wave Modeling

The numerical ocean circulation models are mathematical models able to represent and reproduce real-world physical ocean processes.

In practice, ocean models provides a numerical solution to a set of primitive partial differential equations (PDE) governing the ocean dynamics and circulation in 4D domain (3D space and time) or 3D domain (2D space and time). These PDEs are based on an approximated version of Navier-Stokes equations adapted to different regimes of interest and assume water as incompressible fluid (Boussinesq approximation) and hydrostatic balance. They can also simplified making further assumption of baroclinic or barotropic fluid conditions, geostrophy balance, free surface or rigid lid conditions and usually the modellers resort to sub-gridscale parameterizations to modelize the sub-grid interactions between the several grid nodes.

These equations get discretized in time and space and solved in each grid point of the time-space domain (Finite Difference Grid). This domain grid can be nested with another high resolution grid in some localized areas where is expected more short scale variation and hence high resolution capacity by the model is necessary. The equations can be solved also in a spatial grid of finite elements (in general triangular shaped volume) in place of points and in this case the numerical models are known as Finite Elements Models (FEM). An advantage of finite element grids is that the size of the triangles can be varied continuously throughout the domain which more easily allows variable resolution, and which is especially good at following complex coastlines, as in an estuary.

The space domain can be a very localized region of the ocean where the equations are solved in an high resolution grid (and in this case we speak about regional ocean model), can be have basin-scale size or can encompass all the globe at low resolution (and in this case we speak about global ocean model).

Then, in order to solve a system of equations mathematically, boundary conditions and initial conditions need to be necessarily set up.
There are two basic types of boundaries:

- close-boundary (no water flows across the boundary), used usually in global models
- open boundary (allowing waves and disturbances originating within the model domain to leave the domain), used in regional models

while the initialization can be based on the climatology or on previous runs. Usually the open boundary condition is implemented nesting the regional model grid with a global ocean model.
One of the necessary input to a numerical ocean model is an accurate sea floor bathymetry which needs to constrain the model at the interface (as instance bottom stress by friction).
Finally, in order to drive the model, it is necessary to set all the external forcing acting on model's domain.
Generally, the forcing can be of several types:

- wind forcing (wind stress)
- buoyancy forcing (as heat fluxes and salinity fluxes)
- tidal forcing
- fresh water forcing (run-off)
- sea ice forcing

Through the forcing at interface between ocean and atmosphere, modellers can set up the coupling between an ocean numerical model and an atmospheric numerical model. Hence atmosphere and ocean can interact with each other and evolve together.
In order to determine the forcing acting in model's domain or to determine the initial state of the ocean, modellers resort to data assimilation from in situ or space satellites.
The final objectives of a numerical ocean model are:

- predict accurately the state of the ocean in a very near or more far-away future (nowcast and forecast)
- reproduce accurately the state of the ocean for a certain period of time in the past (hindcast)

Usually, the physical variables of interest which are predicted by ocean circulation models are temperature, salinity, sea level, velocities, currents, waves, tides, pressure, etc.

2.3 Tide Gauges and Buoys

Tide gauges are devices which measure the in situ sea level elevation with respect to vertical datum.
There are three main types of tide gauges:

- Acoustic tide gauges – These stations make use of transit time of an acoustic pulse to measure sea surface distance.
- Pressure tide gauges – They monitor sub-surface pressure and convert it into height with reference to water density and gravity of acceleration.
- Radar tide gauges – These stations employ radio frequencies to measure sea surface distance.

The tide gauges may provide accurate sea level elevation data but can be greatly influenced by errors caused by vertical land motion (as a result of post-glacial rebound, tectonic uplift or crustal subsidence) or in general by the stability of the surface they are built upon.

Modern tide gauges are equipped with a GNSS station to provide an absolute height reference and to monitor the vertical land motion.

The wave buoys are in situ stations with the goal to measure ocean wave height. They can be floating or moored to the seafloor. Basically, they measure the movement of the water surface as a wave train. The wave train is analyzed to determine statistics like the significant wave height and period, and wave direction. Eventually, they can also measure wind speed.
The modern buoys exploit acoustic waves to measure the ocean wave height (intensity and direction) and the currents as AWAC (Acoustic Wave and Current Profiler) or ADCP (Acoustic Doppler Current Profiler).

2.4 Discussion

In this section, I discuss and summarize briefly the content of this chapter.
I have presented the concept of SAR altimetry, I have passed in review the main contributions and last recent novelties in this area of research, I have outlined the processes by which the SAR waveforms are built at L1b and processed at L2 to extract out of them the geophysical information of interest and I have described the two Satellite SAR Altimetry missions which are the source of the all L1A SAR Altimetry data I have used in the thesis.
I have introduced then the source of the dataset which are used as reference to validate SAR Altimetry data in this thesis work:

- Pseudo-LRM
- Ocean Numerical Circulation and Wave Model
- Tide Gauges

Therefore, this chapter is intended to be a kind of broad-view introduction for the next chapter where I will enter more in details about how practically the processes have been implemented in the specific cases treated here to pursue my thesis objectives.

3 Methodologies

Introduction

As said in chapter 1, the SAR Altimetry gives to an expert the possibility to process the altimetry raw data as "he/she likes". Therefore, in this chapter, I am going to describe how in practice I have chosen to implement my dedicated SAR processing chain from L1A to L2 and the innovations and methodologies I have brought at L1b and L2 in order pursue my objective to have the most accurate altimetric measurements over water, land and ice. Since the SAR processing can be divided in two main categories: L1b and L2, I have divided as well this methodology chapter in two main sections: L1b and L2.

As far it concerns the L1b, all the options can be regarded as additions or complements to a standard way to process SAR altimetry data at L1b, which can be applied or not during the processing chain, while, as far it concerns L2, the described processing options can be regarded as fully alternative because they concern the retracking itself, which is the core of the L2 processing. In this L2 regard, I have proposed firstly my design and development of a SAR open ocean retracker (SAMOSA-based), then I have proposed a "generalization" of the open ocean SAR retracker to all the marine surfaces (open ocean, coastal zone and sea ice), named SAMOSA+ and finally I have proposed a more elegant alternative to the SAMOSA+ retracker referred as SAMOSA++ which overcomes some limitations in the SAMOSA+ retracking and that would like to be a real "pan-thematic" SAR retracking, which means capable to work properly and accurately for all the altimetry thematic applications (open ocean, coastal zone, sea ice and inland water) and which is supposed to over-perform the SAMOSA+ in the marine applications as well.
But, prior to describe the retrackers in the specific, I have provided a clear formulation of the SAMOSA SAR return waveform as function of beam angle and time delay, based on Ray et al., (2015).
Furthermore, I have described how the Pseudo-LRM dataset has been procured for CryoSat-2 and Sentinel-3 and finally, because the data screening for outliers is an important (and critical) part of the data analysis, the final section outlines the methods which have been followed in order to screen the alleged outliers out from the dataset. The guideline followed was to try to screen the data out as little as possible in order to preserve the completeness of the dataset and avoid to remove data which are considered outliers when in reality they are perfectly valid measurements.
These described processing options at L1b and L2 are embedded as Graphic User Interface options in the G-POD SAR altimetry services portal which users can pick up on line in order to customize with few mouse clicks the processing as he/she likes.

3.1 Methodologies in L1B SAR Processing

In order to produce altimetric measurements as accurate as possible also over non-open ocean surfaces, I have decided to process the SAR L1A data up to L1b using the standard SAR processing stages: ground cell gridding at 20 Hz, Doppler Beam Forming (approximated), Doppler Beam Stacking, Slant Range Compensation, Range Compression and Multilooking (Raney, 1998), (Cullen and Wingham, 2002), (ESA Report, 2013). Furthermore, they have been complemented with some specific enhancements specifically tailored for the non-open ocean domain, which are:

- Application of a Hamming weighting window on the burst data prior to the azimuth Fast Fourier Transform (FFT) just over coastal and inland waters
- Application of the zero-padding technique (radar waveform oversampling of a factor 2) prior to the range FFT

- Doubling of the extension of the radar range swath (radar receiving window)
- Noise Floor estimated from Doppler beams in Stack data which are out of the expected receiving radar window.
- Ground Cell Gridding at 20 Hz or 80 Hz

The steps of the Delay-Doppler processing are represented in Figure 3.1:

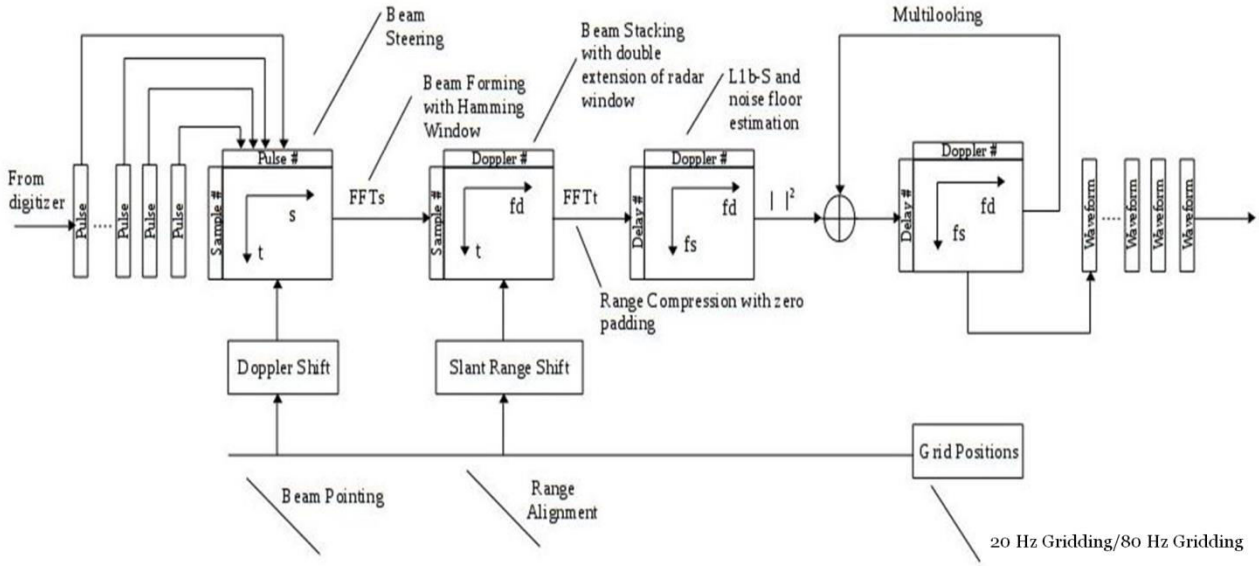

Figure 3.1: Delay-Doppler Altimetry block diagram adapted from R. K. Raney (pers. comm.) with the descriptions relative to the new options used in the L1A to L1B processing. The time in range direction is denoted as t whereas the time in azimuth direction is denoted as s. The Doppler frequency and range sampling frequency are denoted as fd and fs

a) Hamming Window Weighting

The first option, Hamming window, allows to mitigate the impact of "ghost" signals coming from bright targets (such as ponds, wet lands or coastal mudflats) in the antenna footprint and has the purpose of reducing the side-lobes of a Delay-Doppler beam, but at expense of enlarging the Delay-Doppler beam main lobe. This option is applied only in the coastal and inland waters whereas it is not considered necessary in the open ocean where the backscattering scenario is more homogenous and hence is not applied over open ocean.

A bitwise flag 1/0 is stored in the L1b products denoting whether the ℓ^{th} Doppler Beam has been weighted by the Hamming Window or not.

When the radar waveform is weighted by the Hamming window, the following effects occur:

- Along track resolution gets worst (from 300 meters to around 400 meters)
- the Delay-Doppler Beam side-lobes get depressed (the peak side-lobe ratio will pass from -13 dB to around -42 dB)
- Peak Power gets lower

Furthermore, experts are presently raising a question about whether the Hamming window is the best weighting windows for altimetry data exploitation or whether it would suffice to use "ad hoc" weighting windows with less side-lobe ratio improvement but with less loss in resolution (Smith et al., 2018).

In this thesis work, the Hamming window was used as default weighting window because is the one applied in the PDGS (Payload Ground Segment) baseline-C products from the CryoSat-2 mission (ESA Report, 2012). Other authors as (Smith et al., 2018) propose weighting windows more tailored for applications over sea ice. Anyhow, in case of usage of a physical retracker, mandatorily it is needed to proper model the

application of the weighting function in the retracker's functional model to avoid data quality degradation. First results using G-POD L2 data processed with Hamming window in the coastal zone have been shown in Passaro et al., (2016).

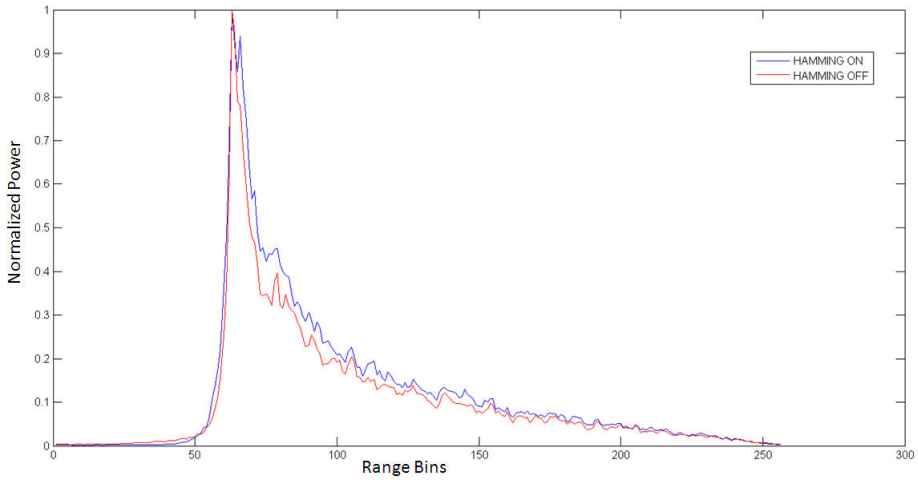

Figure 3.2: Same SAR waveform once weighted by Hamming window (blue curve) and once non-weighted by Hamming window (red curve). Both waveforms are normalized

b) Waveform Zero-Padding in range direction

The second option, zero-padding in the range direction, consists in over-sampling the return radar waveform adding 64 zeroes before and after the waveform data prior the FFT in range.
It has the convenience to sample more efficiently very peaky echoes from bright targets, in accordance to the Nyquist's theorem, as in (Smith and Scharroo, 2014).
Indeed, when the surface is specular or with a degree of surface roughness below a certain threshold, the return waveform will be very peaky and essentially concentrated around the reflection direction. This reflection direction shall be the nadir direction in case of surface with no significant topographic slope and in case of nadir-pointed altimeter. Being the waveform so peaky, the zero-padding will mitigate the aliasing effect and the under-sampling of the peaky waveform. This is fully in analogy with the actual process to estimate the range path delay of the instrument PTR (Point Target Response) during the Close-Loop internal Calibration (CAL1) mode or during a transponder calibration: in this case the PTR is always largely oversampled in order to estimate the correct range path delay with an error of few mm.
In this thesis work, the zero-padding is always applied over any surfaces (open ocean, coastal, inland water, etc).

c) Double Extension of the receiving Window

The third option, the double extension of the receiving window, allows to mitigate on board tracker errors on rough topography (Dinardo et al., 2018). The on board radar tracker predicts the likely position of the following echo, based on the information derived from the previously received echoes, and commands the opening time of the radar receiving window. It is well known that over very rough topography, as in the transition between land and the coastal ocean, errors in positioning in time the radar receiving window can occur. In this situation the double extension of the receiving window consists in using a larger receiving window of 512 samples (with zero-padding) to store the stack data in range dimension after the slant range compensation.
In the CryoSat-2 baseline-C PDGS a simple max-power detector is implemented at L1b stage to position the stack data in the receiving window with a fixed-size of 256 samples (with zero-padding). Hence, it may

happen that the choice in positioning the receiving window of 256 samples can be erroneous, being the stronger return not always coincident with the nadir return. To overcome this problem, indeed the receiving window was expanded from 256 to a fixed-size of 512 samples in order to always be sure to well-accommodate the L1b echo in the receiving window.

Figure 3.3 illustrates a case in the German Bight where the waveform leading edge is occasionally truncated because of abrupt changes of the topography between land and sea in two occurrences. Figure 3.4 shows the stack data for the second occurrence of the leading edge truncation in Figure 3.3-top (case 2).

As expected, in the stack there is the return power from the sea surface at leading edge and a strong off-nadir reflection due to land contamination in the trailing edge.

The central Doppler beams, which correspond to near-nadir looking direction, miss the leading edge due to the tracker error; however the leading edge is correctly preserved in the outer side-looking Doppler beams. Using a window of 256 samples (with zero-padding) and storing in the L1b product the return power starting from the stack's bottom (sample 512), the leading edge cannot be preserved and a full waveform complete from leading edge till trailing edge cannot be built. Instead, when a window of 512 range samples (with zero-padding) is used to store the waveform in the L1b product, the leading edge (along with the off-nadir reflection) can be preserved. Using the double extension of the radar window, one can see from Figure 3.3-bottom how the leading edge is always properly preserved.

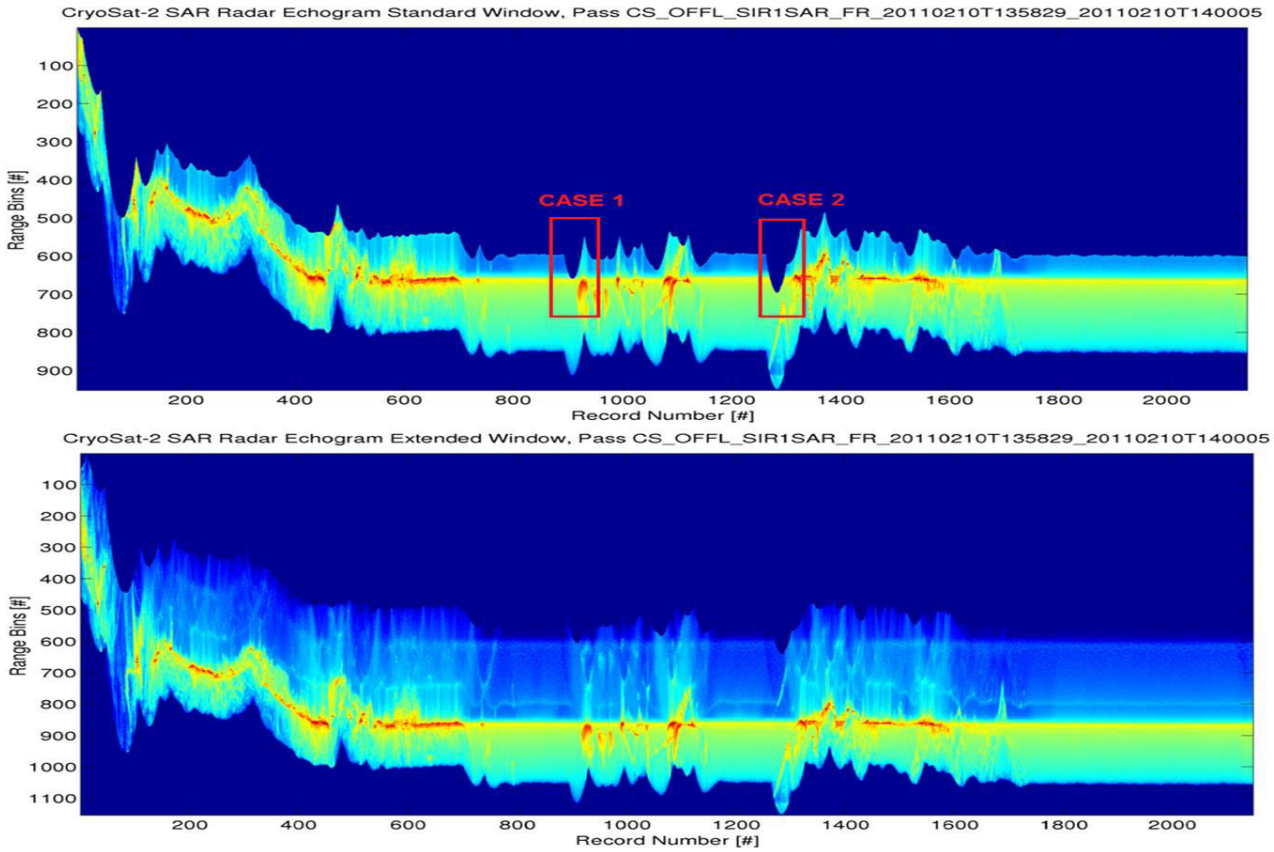

Figure 3.3: Radar Echogram of L1b SAR echoes after tracker shift compensation: (Top) Case of bad positioning of the L1b echo in the radar window (128 samples), i.e. echoes in the red rectangles suffer for truncation of the leading edge; (Bottom) Case of double extension in the radar window (256 samples); the L1b echoes leading edge is now always preserved.

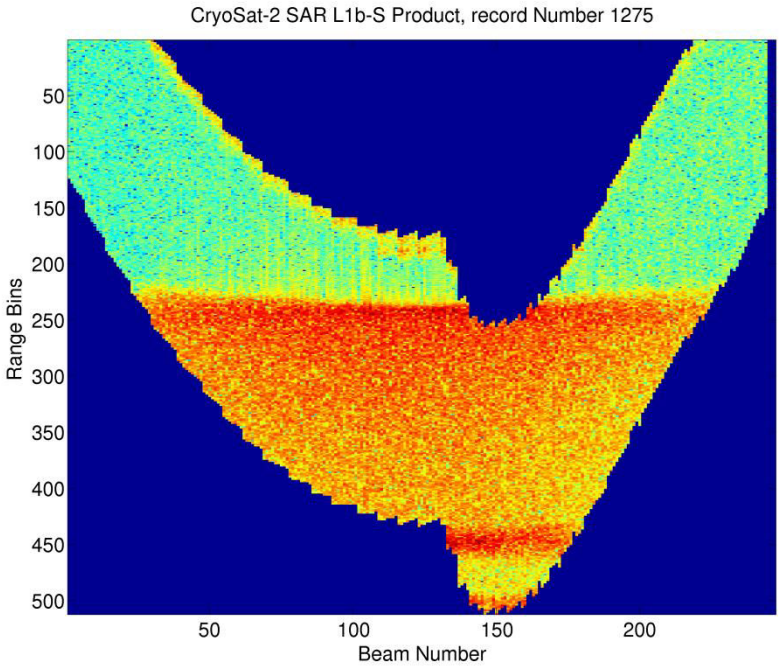

Figure 3.4: stack data for the record number 1275 (case 2 in Figure 3.3-top). In the picture, dark blue is the zero value

This option has proven to be very useful for CryoSat-2 mission while it holds a minor importance for Sentinel-3 mission as the Sentinel-3 altimeter is supported by the OLTC tracking technique which enables the altimeter to maintain a reliable tracking over most of coastal zone and inland water targets exploiting a DEM uploaded on board.

d) Thermal Noise Floor from the stack data

The fourth option, Noise Floor from Stack data, enables to estimate the waveform thermal noise floor using the portions of the stack data that are not affected by land reflections (Dinardo et al., 2018). Indeed, since the early waveform samples are potentially affected by land contamination in the coastal zone, in order to achieve a more accurate and robust estimation of the thermal noise level (and independent from land contamination), this noise is estimated as the median value of the power of the non-null stack beams satisfying the conditions:

$$\Delta R_\ell > RW \tag{3.1}$$

where ΔR_ℓ is the ℓ-th stack beam slant range shift and RW is the size of the radar receiving window (around 60 m for CryoSat-2 and Sentinel-3).

e) 20 Hz/80 Hz Ground Cell Gridding

The fifth option, Ground Cell Gridding at 20 Hz or 80 Hz, consists in placing the ground cells over the ground with a rate of 20 Hz or 80 Hz (Dinardo et al., 2013).
Indeed, SAR Altimetry makes possible to steer the Doppler Beams to any point along-track of the over-flown surface. This means that with SAR Altimetry, it is possible to post an altimetric measurement at any desired point along the satellite track.
This is a quite intriguing novelty for inland water or coastal domains wherein scientists would like to achieve an altimetric measurement exactly over quite sensible locations as river/coast banks or river-cross

centers (spotlight observation), or , looking beyond, the application of this concept shall make feasible the usage of customized grids where users "a priori" request altimetric measurements exactly over the provided grid points (as done over a transponder). SAR Altimetry gives the possibility for the first time to realize this principle. Hence one can decide to process a series of SAR data at usual 20 Hz space grid or a finer space grid step. For convention, in Delay-Doppler Altimetry, the grid step has been fixed at 300 meters (to be coincident with the instrument along-track resolution). Now, instead of the conventional 300 meter grid step (i.e. at posting rate of 20 Hz), I process the SAR data at a grid step of about 80 meters (or at a posting rate of 80 Hz). This number, 80 meter, is a convenient one: it has been chosen since it corresponds to the CryoSat-2 and Sentinel-3 burst repetition interval (BRI) and the datation time and geo-location information are provided at each burst center in the L1A products. Hence, fixing the grid center locations exactly at burst centers (as is done herein) allows as well to avoid the cumbersome operation to interpolate the satellite orbit at the grid locations which are 300 meter distant. I remark that in this process, the SAR altimeter space resolution is not altered: the theoretical resolution keeps to be set at a value around 300 meters.

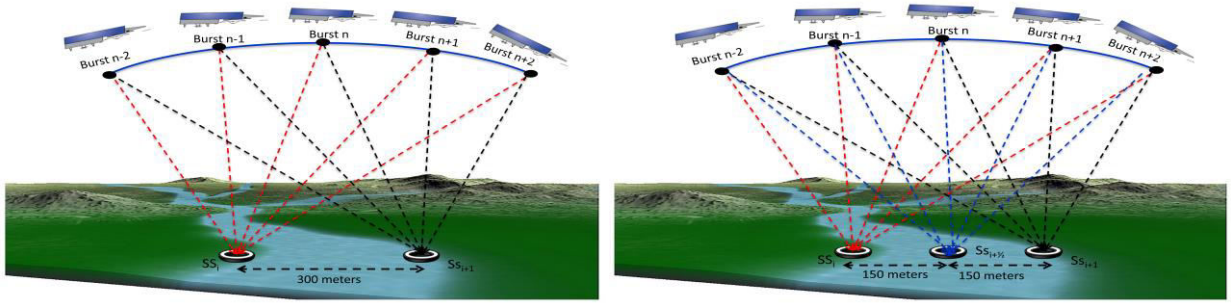

Figure 3.5: At 20 Hz the ground cells may be localized on river banks: potentially one may miss to observe the river cross center (left). At 80 Hz one can steer the Doppler beams at the river cross center: a new measurement exactly at river cross center is now achieved (right)

Furthermore, it has to be considered that because the along track resolution of the SAR altimeter is 300 meter, for the Nyquist's Theorem the sampling frequency to be used in order to resolve an altimetric signal at that scale is at least 150 meter (40 Hz). Hence, with the current posting rate at 20 Hz, one may risk to sub-sample the radar image of the surface (radar echogram) and hence to miss the very short scale part of the topographic signal. This technique has been applied on the Amazon river Rio Tapajos (see Figure 3.6 and Figure 3.7) and has proven to add independent information in the radar echogram with respect the standard 20 Hz case, being the radar echogram sharper at 80 Hz.

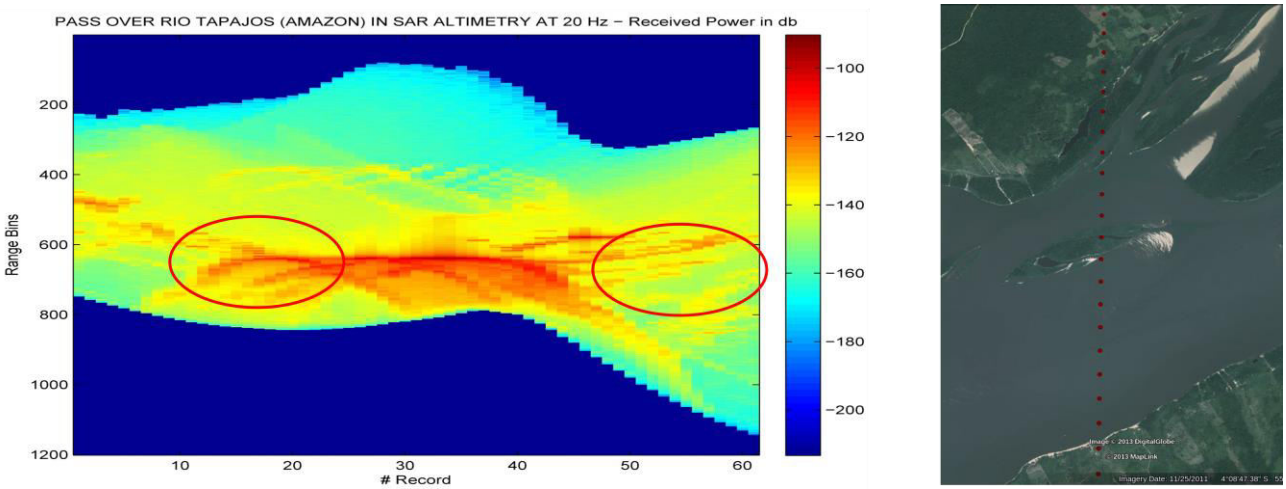

Figure 3.6: On left, the radar image (radar rchogram) for the Rio Tapajos River Transect at standard 300 m grid step. On right, the gridding over the river cross (red points). Some short scale structures in the radar image are circled in red and they look blurred.

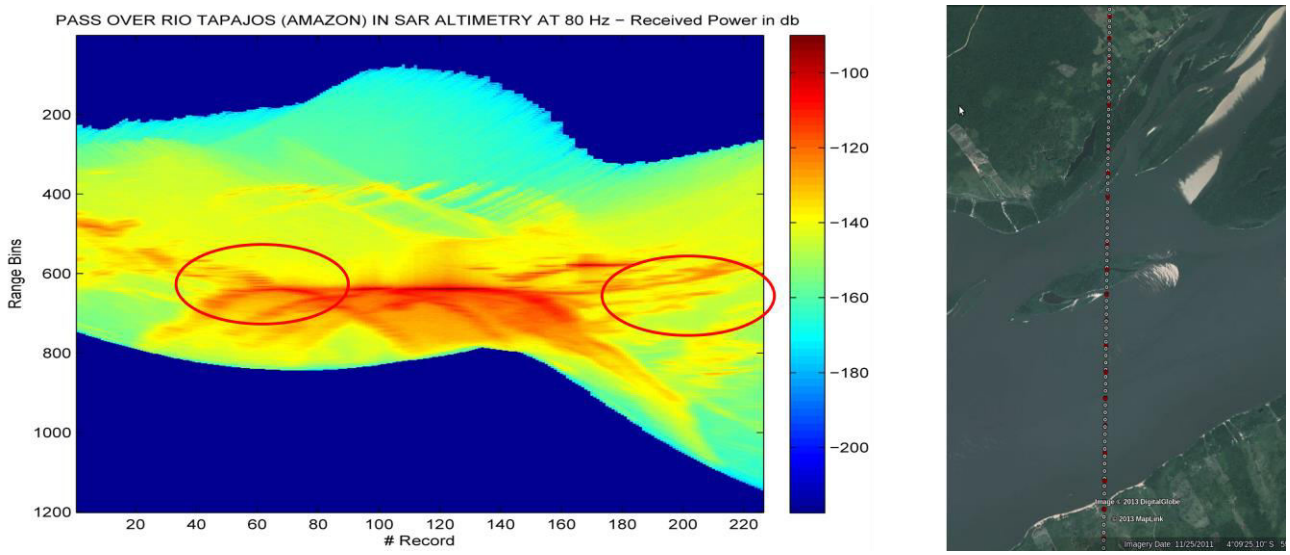

Figure 3.7: On left, the radar image (radar echogram) for the Rio Tapajos River Cross at finer 80 m grid step. On right, the finer gridding over the river cross (white points). The echogram gets much sharper with a 80 m grid step, see for instance the short scale structures inside the red circles.

This technique will be applied over the River Po in order to derive the time series at the Po's Sentinel-3 virtual stations. Indeed, being the River Po a quite narrow river (sometime around 200-300 meter), in order to ensure a sufficient number of radar reflections from the watercourse of the river, it makes sense to post the SAR waveforms every 80 meters.

3.2 METHODOLOGIES IN L2 SAR PROCESSING

3.2.1 THE SAMOSA SAR RETURN WAVEFORM MODEL

Regarding the SAR Return Waveform Model which has been used in the retracking, I start from the SAMOSA SAR waveform model described in Ray et al., (2015). The SAMOSA model has already been implemented in two formulations: the first one is SAMOSA3 which uses only the zero-order term of the model and the second one is SAMOSA2 which uses both the zero and the first-order terms. Sometimes a SAMOSA2-based retracker is referred as SAMOSA-2 retracker. The SAR data from SAMOSA2 retracker have been used in open-ocean by Fenoglio-Marc et al., (2015).

In this sub-section, I present the analytical expression of the SAMOSA2 model used in the dissertation, as function of the Beam Look Angle and of the waveform time delay. The model formulation is fully analytical, expressed in terms of the Scaled Bessel Functions and depending on the three altimetric unknowns: epoch t_0, SWH and amplitude P_u. It follows here the derivation of the analytical expression of this model.

The analytical solution for the f_0 term and f_1 term in Eq. 36 in Ray et al., (2015) have been worked out and expressed for any variable ξ different from zero in Eq. (3.2) and in Eq. (3.3):

$$f_0(\xi) = \int_0^{+\infty} e^{-\frac{1}{2}\left(\xi-u^2\right)^2} du = \frac{\pi}{4}(|\xi|)^{1/2}\left[I^{sc}_{-\frac{1}{4}}\left(\frac{1}{4}\xi^2\right) + sign(\xi)\cdot I^{sc}_{\frac{1}{4}}\left(\frac{1}{4}\xi^2\right)\right] \quad (3.2)$$

$$f_1(\xi) = \int_0^{+\infty} e^{-\frac{1}{2}\left(\xi-u^2\right)^2}(\xi-u^2)du = \frac{\pi}{8}|\xi|^{\frac{3}{2}}\left[\left(I^{sc}_{\frac{1}{4}}\left(\frac{1}{4}\xi^2\right) - I^{sc}_{-\frac{3}{4}}\left(\frac{1}{4}\xi^2\right)\right) + sign(\xi)\cdot\left(I^{sc}_{-\frac{1}{4}}\left(\frac{1}{4}\xi^2\right) - I^{sc}_{\frac{3}{4}}\left(\frac{1}{4}\xi^2\right)\right)\right] \quad (3.3)$$

And for ξ equal to zero in Eq. 3.4 and Eq. 3.5:

$$f_0(0) = \frac{\pi\cdot 2^{\frac{3}{4}}}{4\cdot\Gamma\left(\frac{3}{4}\right)} \quad (3.4)$$

$$f_1(0) = -\frac{2^{\frac{3}{4}}\cdot\Gamma\left(\frac{3}{4}\right)}{4} \quad (3.5)$$

Where:

- I^{sc}_{nu} is the Scaled Modified Bessel function of first kind and order nu, defined as :

$$I^{sc}_{nu}\left(\frac{1}{4}\xi^2\right) = e^{-\frac{1}{4}\xi^2}\cdot I_{nu}\left(\frac{1}{4}\xi^2\right) \quad (3.6)$$

- I_{nu} is the Modified Bessel function of first kind and order nu (Abramowitz and Stegun, 1964)

- sign(ξ) is the sign function defined as:

$$sign(\xi) = \frac{\xi}{|\xi|} \quad (3.7)$$

|| is the absolute value function and Γ is the Gamma function.

The Figure 3.8 shows how the differences between the numerical and analytical solution for f_0 and f_1 are less than 10^{-13}.

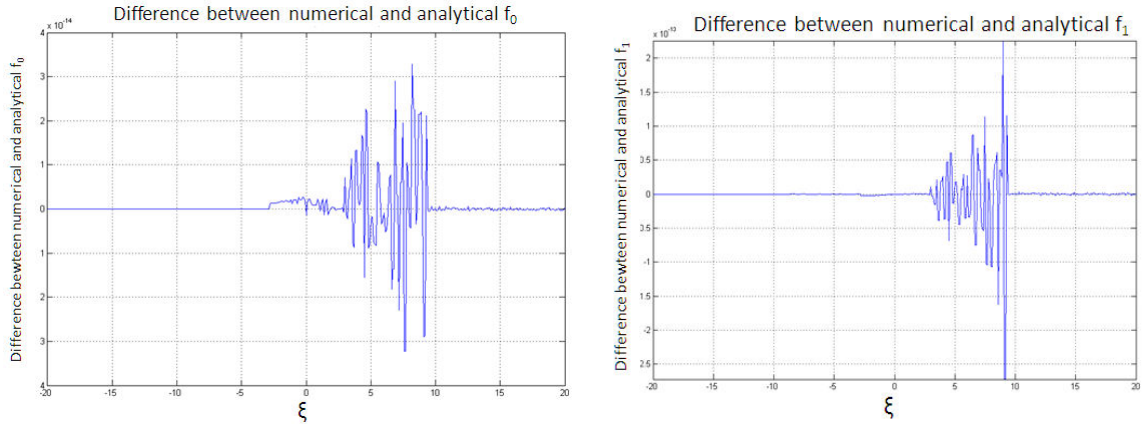

Figure 3.8: Difference between numerical and analytical solution for f_0 and f_1 are lesser than 10^{-13}

In order to derive the analytical expression of the model, Ray et al., (2015) approximated the squared Radar System Range Point Target Response (PTR), also called Range Impulse Response (RIR), with a Gaussian, introducing a Gaussian approximation parameter σ_g (see Eq. 35 in Ray et al., (2015)). This last parameter σ_g can be considered equivalent to the dimensionless width α_p of PTR. Exploiting this equivalence, the term $g_l \cdot k$ can be re-written from g_l from Eq. 39 in Ray et al., (2015) as:

$$g_\ell \cdot k = \frac{k}{\sqrt{\alpha_p^2 + 4\alpha_p^2 \left(\frac{L_x}{L_y}\right)^4 (\ell)^2 + \left(\frac{\sigma_z}{L_z}\right)^2}} = \frac{\frac{k}{B_r}}{\sqrt{\left(\frac{\alpha_p}{B_r}\right)^2 + 4\left(\frac{\alpha_p}{B_r}\right)^2 \left(\frac{L_x}{L_y}\right)^4 (\ell)^2 + \left(\frac{2\sigma_z}{c}\right)^2}}$$
$$= \frac{\tau}{\sqrt{\sigma_p^2 + 4\sigma_p^2 \left(\frac{L_x}{L_y}\right)^4 (\ell)^2 + \left(\frac{2\sigma_z}{c}\right)^2}} = \frac{\tau}{\sqrt{\sigma_p^2 \left[1 + \left(\frac{L_x}{L_z}\right)^2 (\alpha \cdot \theta_{Look})^2\right] + \left(\frac{2\sigma_z}{c}\right)^2}}$$

(3.8)

with L_x along track resolution, L_y pulse-limited radius and L_z vertical resolution (see Eqs. 14 and 21 in Ray et al., (2015)), ℓ Doppler beam index, k range bin index, σ_p PTR time width, B_r received radar bandwidth, c speed of light, σ_z=SWH/4 and α=1+(h/R_{EARTH}), with R_{EARTH} the mean Earth radius (α is referred as Earth roundness coefficient).
The beam look angle and waveform time-delay τ are defined in Eq. (3.9) and Eq. (3.10):

$$\theta_{Look} = \left(\frac{L_x}{h}\right)\ell$$

(3.9)

$$\tau = \frac{k}{B_r} = t - t_0$$

(3.10)

The angle θ_{Lim} is defined as in Eq. 3.11. See Figure 3.9 for its geometrical representation in case of Earth with roundness coefficient α:

$$\theta_{Lim} = \frac{L_z}{\alpha L_x}$$

(3.11)

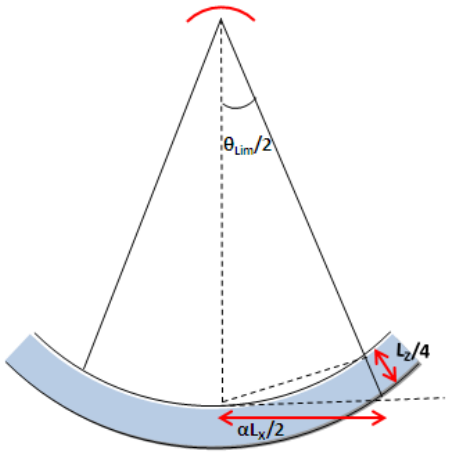

Figure 3.9: Geometrical relationship between Lz, αLx and θ_{Lim}

Hence, finally Eq. 3.12 shows that, in analogy with conventional pulse-limited altimetry, σ_c can be interpreted as the sigma composite for SAR altimetry.

$$g_\ell \cdot k = \frac{\tau}{\sqrt{\sigma_p^2 \left[1 + \left(\frac{\theta_{Look}}{\theta_{Lim}}\right)^2\right] + \left(\frac{2\sigma_z}{c}\right)^2}} = \frac{\tau}{\sigma_c}$$

(3.12)

Hence, at difference of pulse-limited Altimetry wherein sigma composite is a number, the sigma composite in SAR Altimetry is a function of the model's independent variable look angle.

One can express the Eq. (3.12) in terms of SWH (Significant Wave Height) and introduce the term sign(SWH) to allow negative SWH as output of the retracking scheme:

$$g_\ell \cdot k = \frac{\tau}{\sqrt{\sigma_p^2 \left[1 + \left(\frac{\theta_{Look}}{\theta_{Lim}}\right)^2\right] + sign(SWH) \cdot \left(\frac{|SWH|}{2c}\right)^2}} = \frac{\tau}{\sigma_c}$$

(3.13)

The scattering amplitude decay is expressed in terms of the parameter ν, defined as the inverse of the mean square slope of the sea surface (s^2), by Eq. 3.14:

$$\nu = \frac{1}{s^2}$$

(3.14)

Finally, in Eq. 36 and 38 in Ray et al., (2015), I set the sea surface skewness λ_s, the Electro-Magnetic bias z_{EM} and the sea height mean $\langle z \rangle$ to zero and all the constant terms are regrouped in a term referred to as P_u (amplitude). The Electro-Magnetic bias will be taken into account in a specific correction applied after retracking (sea state bias correction) whereas, as sea height mean, a mean sea surface provided by external

entities and computed from all the already available altimetry data will be used after the retracking. The skewness effect will be neglected.

Collecting all these contributions, I achieve the final expression of the SAMOSA analytical model as function of the beam look angle and waveform time-delay:

$$P_{SL}(\theta_{Look}, t-t_0) = P_u \cdot \frac{\sqrt{2\pi}\cdot\alpha_p^2}{\sqrt{\mathrm{B_r}}} \cdot \frac{\Gamma_{k\ell}(0)}{\sqrt{\sigma_c}} \cdot \left[f_0\left(\frac{t-t_0}{2\sigma_c}\right) + \frac{\sigma_z}{L_\Gamma}\cdot T_k \cdot g_\ell \cdot \frac{\sigma_z}{\mathrm{L_z}} \cdot f_1\left(\frac{t-t_0}{2\sigma_c}\right)\right] \tag{3.15}$$

where:

$$f_0\left(\tfrac{t-t_0}{2\sigma_c}\right) = \frac{\pi}{2\sqrt{2}}\left|\tfrac{t-t_0}{2\sigma_c}\right|^{\frac{1}{2}}\left[I^{sc}_{-\frac{1}{4}}\left(\left(\tfrac{t-t_0}{2\sigma_c}\right)^2\right) + sign(t-t_0)\cdot I^{sc}_{\frac{1}{4}}\left(\left(\tfrac{t-t_0}{2\sigma_c}\right)^2\right)\right] \tag{3.16}$$

$$f_1\left(\frac{t-t_0}{2\sigma_c}\right) = \frac{\pi}{2\sqrt{2}}\left|\frac{t-t_0}{2\sigma_c}\right|^{3/2}\left[\left(I^{sc}_{\frac{1}{4}}\left(\left(\frac{t-t_0}{2\sigma_c}\right)^2\right) - I^{sc}_{-\frac{3}{4}}\left(\left(\frac{t-t_0}{2\sigma_c}\right)^2\right)\right) + sign(t-t_0)\cdot \cdot \left(I^{sc}_{-\frac{1}{4}}\left(\left(\frac{t-t_0}{2\sigma_c}\right)^2\right) - I^{sc}_{\frac{3}{4}}\left(\left(\frac{t-t_0}{2\sigma_c}\right)^2\right)\right)\right] \tag{3.17}$$

$$\Gamma_{k,\ell}(0) = exp\left[-\gamma_y(\theta^2_{Roll}) - \nu\cdot(\theta_{Look}-\theta_{Pitch})^2 - \gamma_x(\theta_{Look}-\theta_{Pitch})^2\right] \cdot \begin{cases} exp\left[-(\gamma_y+\nu)\left(\frac{c\cdot(t-t_0)}{\alpha h}\right)\right] cosh\left(2\gamma_y\theta_{Roll}\sqrt{\left(\frac{c\cdot(t-t_0)}{\alpha h}\right)}\right) & t > t_0 \\ 1 & t \le t_0 \end{cases} \tag{3.18}$$

$$T_k = \begin{cases} \left(1+\frac{\nu}{\gamma_y}\right) - \frac{\theta_{Roll}}{\sqrt{\left(\frac{c\cdot(t-t_0)}{\alpha h}\right)}} tanh\left(2\gamma_y\theta_{Roll}\sqrt{\left(\frac{c\cdot(t-t_0)}{\alpha h}\right)}\right) & t > t_0 \\ \left(1+\frac{\nu}{\gamma_y}\right) - 2\gamma_y\theta^2_{Roll} & t \le t_0 \end{cases} \tag{3.19}$$

$$\gamma_x = \frac{8\cdot ln(2)}{\theta_x^2} \quad ; \quad \gamma_y = \frac{8\cdot ln(2)}{\theta_y^2} \quad ; \quad L_\Gamma = \frac{\alpha\cdot h}{2\gamma_y} \tag{3.20}$$

The parameters θ_x, θ_y are defined in Table I in Ray et al., (2015).
The equations above show the explicit dependence of the model on the three altimetric unknowns (epoch t_0, SWH and P_u), on roll and yaw platform angles and on the sea surface mean square slope.
The model formulation is hence fully analytical and expressed only in terms of the Scaled Bessel Functions of fractional order and positive argument. The use of Scaled Bessel Functions guarantees numerical stability and absence of singularities in the model for the full span of the argument range.

The representation of Eq. (3.15) in the time-delay/beam Doppler angle plane is referred to as Delay-Doppler Map (DDM).
Finally, the multi-looked SAR (Delay-Doppler) waveform model is provided by:

$$P_{ML}(t-t_0) = \frac{1}{L} \cdot \sum_{\ell=-\frac{L}{2}}^{\frac{L}{2}-1} P_{SL}(\theta_{Look}, t-t_0) \tag{3.21}$$

where L is the total number of Doppler beams to be accumulated.
In Figure 3.10, a realization of the SAMOSA multi-looked waveform for SWH=2 meter is displayed: a very distinctive feature of the model is the asymptotic trailing edge.

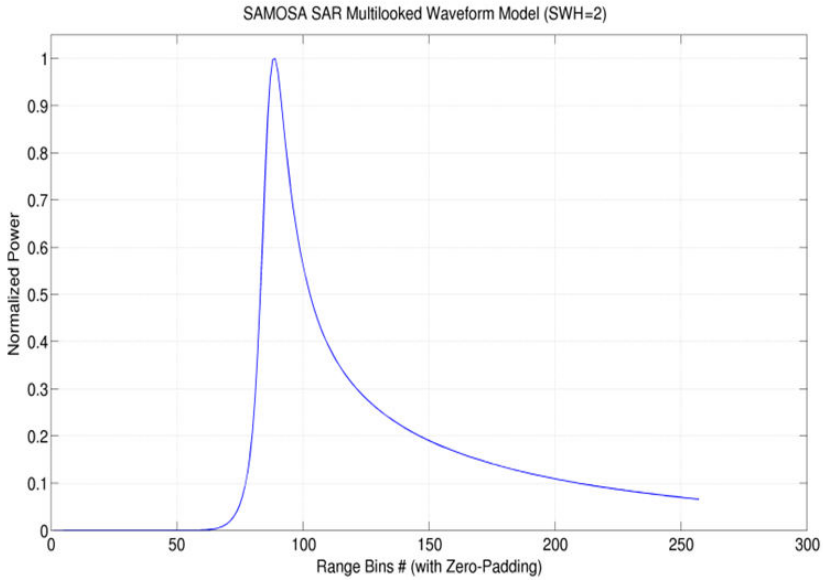

Figure 3.10: SAMOSA SAR Multi-looked Return Waveform Model for SWH=2 meter

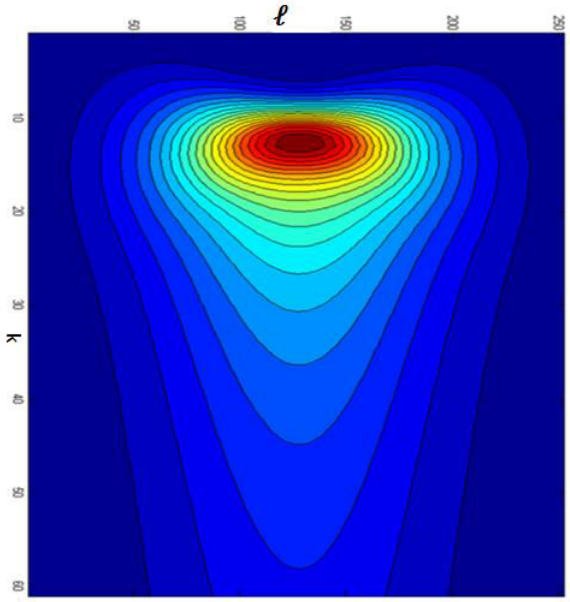

Figure 3.11: The SAMOSA SAR Return Waveform Model as function of looks ☐ (columns) and range bins k (rows), i.e. Delay-Doppler Map

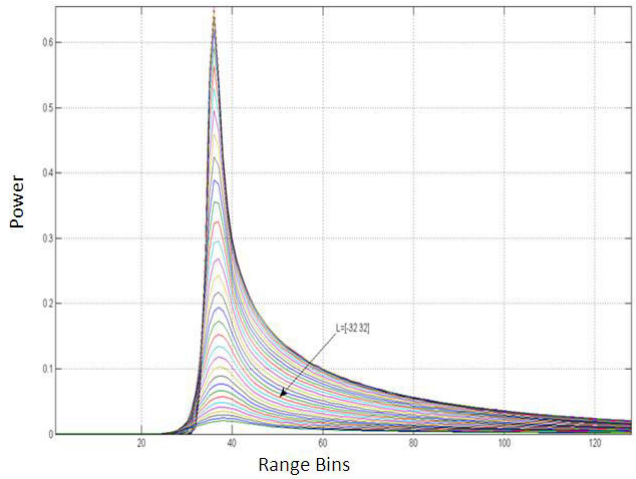

Figure 3.12: The ℓ Doppler Beams reproduced by the SAMOSA Model

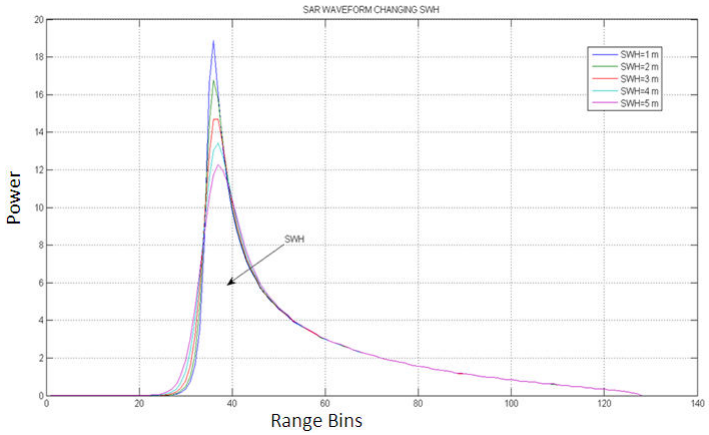

Figure 3.13: The effect of the SWH variation on the SAMOSA Model

The maximum of the function f_0 is reached at the abscissa:

$$\xi_{max} = 0.7650 \tag{3.22}$$

Hence, the retracking point in SAR Altimetry for a generic Doppler beam is positioned around:

$$\frac{f_0(0)}{f_0(\xi_{max})} = 0.8422 \tag{3.23}$$

that is 84.22 % from the maximum. This is also a difference with respect pulse-limited altimetry where the retracking point was halfway of the leading edge.

Given the analytical expression of the SAR Waveform Model and being the model equation an even function with respect to the roll, one can conclude that both the single-look and the multi-looked SAR waveform model are not sensitive to the sign of the roll mispointing.

Regarding the behaviour with respect the pitch, the pitch mispointing is only present in the $\Gamma_{k,\ell}(0)$ and hence the effect of the pitch is only to modulate the amplitude of the ℓ^{th} single-look beam. The single-look Power Return is hence depending on the sign of the pitch's mispointing but, being the $\Gamma_{k,\ell}(0)$ a function symmetrical with respect the look angle and the terms f_0, f_1, T_k independent on the pitch, the multi-looked SAR waveform model is not sensitive on the sign of the pitch mispointing.

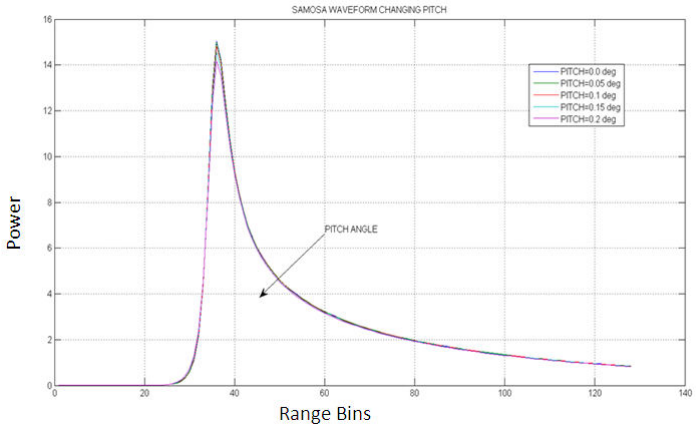

Figure 3.14: The effect of the pitch mispointing on the SAMOSA Model: the model waveform's amplitude gets down-scaled but the model does not change the shape

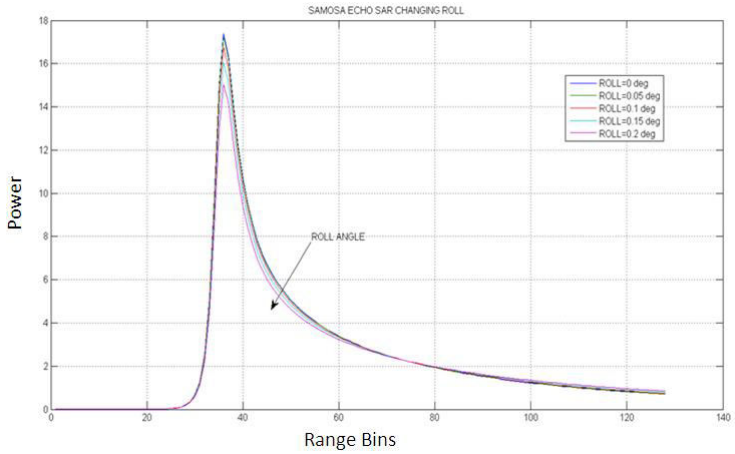

Figure 3.15: The effect of the roll mispointing on the SAMOSA Model: the model waveform's amplitude gets down-scaled and also the model waveform's shape and trailing edge level changes

3.2.2 SAMOSA-BASED OPEN OCEAN SAR RETRACKER

The SAR waveform model expressed in section 2.2.1 (i.e. involving both the zero and first order term) represents the key element for the open ocean SAR retracker used in (Fenoglio-Marc et al., 2015).
In this section I proceed to describe this open ocean SAR retracker.
However, as premise, it is not recommended to use over sea ice or over coastal or inland waters a pure open ocean physical retracker as described in this section: the fitting between the peaky echo and the diffusive waveform model is expected to be necessarily poor, driving to large errors.

The SAMOSA-based open ocean SAR retracker has the following characteristics:

- introduction of an α_p LUT
- mean square slope set to infinite
- tabulation of f_0 and f_1 functions
- Constrained Least-Square Estimator (LSE) using Levenberg-Marquard approach (LSE-LM)
- Model Zero-Masking by exact range shifts
- Model evaluated at the exact look angles
- Thermal Noise from the waveform's early samples
- Mispointing Angles as input from the star trackers

a) α_p LUT

The SAR multi-looked return waveform model in its final formulation (Eq. 3.21) approximates the instrument point target response (PTR) with a Gaussian curve having a shape-factor coefficient α_p:

$$\mathrm{sinc}^2(x) \approx e^{-\left(\frac{x}{\sqrt{2}\alpha_p}\right)^2} \quad (3.24)$$

This approximation is expected to lead to sea-state related errors in range and significant wave height which are not negligible (Fenoglio-Marc et al., 2015).
In order to mitigate those errors, it has been conceived to use for this α_p parameter a different value for a different condition of sea state regime.
The objective is to create a Look Up Table (LUT) of α_p values versus SWH. This LUT will then used at run time during the L2 retracking.
The α_p LUT has been built following the herein listed steps:

- for each SWH value in input (SWH ranging between 0.1 meter and 10 meter with step of 0.1 m) and for a fixed epoch value (zero), the numerical SAMOSA model (eq. 23 in Ray et al., (2015)) and the analytical SAMOSA (eq. 36 in Ray et al., (2015)) model have been generated using exactly the same radar sensor parameters and geometrical configuration.
- The α_p table is built finding, for each SWH in input, the α_p value providing the best fit, in rms error term, between the SAMOSA numerical model and the SAMOSA analytical model. Before the fit, these models have been normalized by the respective model's maximum.
- after this computation of the LUT with a SWH step of 0.1 m, the α_p LUT has been interpolated by spline at a SWH step of 0.01 m between 0 and 10 m whereas has been extrapolated linearly between 10 m and 20 m.

The α_p LUT is meant to be applied at run time, (i.e. during the re-tracking algorithm execution), extracting, from the table, the α_p value corresponding to the SWH value under iteration. The numerical SAMOSA model (eq. 23 in Ray et al., (2015)) uses the non-approximated representation for the PTR (i.e. squared sinc). Hence, this approach will give me the confidence that the α_p LUT is exclusively compensating for the approximation of the PTR with a gaussian function.
Because it has been computed after normalizing the analytical and numerical SAMOSA model, it is supposed to not have any effect on the retracker power. Hence it is used only inside the sigma composite term whereas for the α_p term next to Pu in Eq. 3.15 a constant value is used. This value has been computed as to be about 0.5, making a cross-comparison between the analytical and numerical SAMOSA model power for the same epoch and SWH equal to 2 meter.
This LUT has been recomputed also for Sentinel-3 using the Sentinel-3 sensor parameters.

The biggest advantage of this method is that does not use any altimetry data to build the LUT and hence a LUT can be computed way in advance prior the mission launch. Furthermore, it makes the LUT completely independent of the sea surface skewness, sea state bias, speckle noise and other non-linear processes.

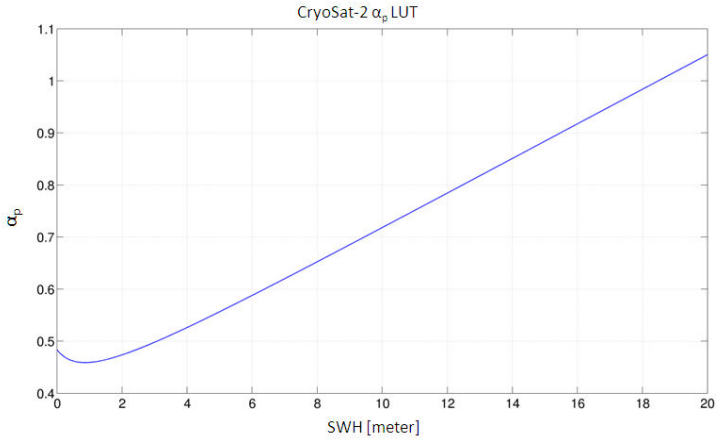

Figure 3.16: CryoSat-2 α_p LUT: α_p versus SWH

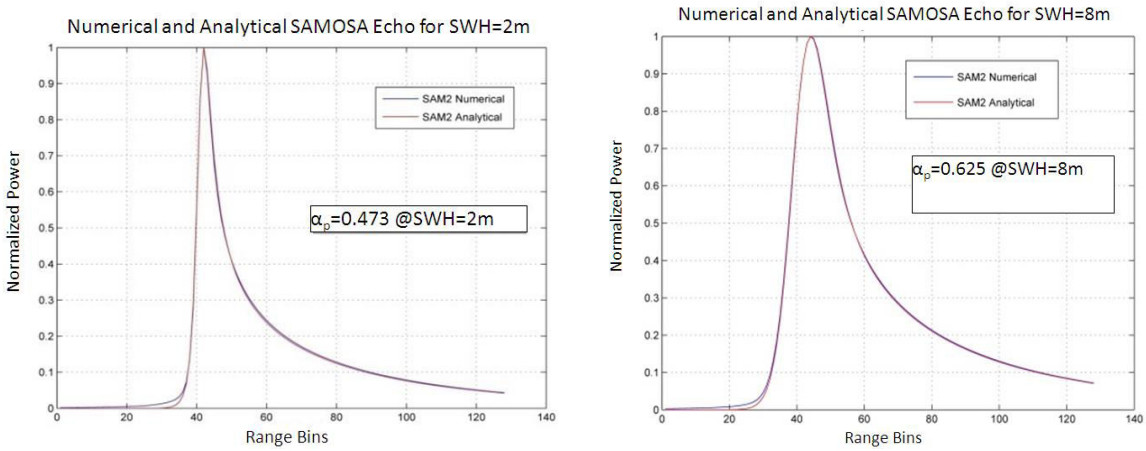

Figure 3.17: CryoSat-2 α_p LUT: varying the SWH, the value of α_p, returning the best fit (in least square sense) between the SAMOSA numerical and analytical model, changes

From Figure 3.17, one can observe how the analytical SAMOSA model does not fit the numerical model at leading edge's toe; this toe in the leading edge is indeed considered to be a result of the side lobes of the PTR.

b) Mean Square Slope set to infinite

In the SAR open ocean retracker as used in Fenoglio-Marc et al., (2015), the mean square slope has been set to infinite, i.e. the parameter ν gets set to zero. This position of the mean square slope set to infinite means that the ocean surface is considered an infinitely diffusive surface over the antenna footprint. Hence the backscattering profile of the ocean surface at near-nadir incidence of the altimeter is assumed to be uniform and not depending on the look angle. This assumption is in analogy with pulse-limited altimetry.
This assumption can be considered valid for an incoherently diffusive reflective surface as open ocean but does not hold over inland waters, coastal waters and sea ice where bright targets (as ponds, sand banks, wetlands, water's leads between ice floes) may be encountered within the antenna footprint. Anyhow, even over open ocean, the hypothesis sporadically can break for the presence of oil slicks, algae blooms, ships, etc.

c) Tabulation of f_0 and f_1 functions

Even if the f_0 and f_1 functions in Eq. 3.15 are expressed in closed form and there are open source implementations of Scaled Bessel Function (see GNU Scientific Library (GSL) freely distributed under GNU

GPL license), it has been decided to make a tabulation of the f_0 and f_1 functions versus the argument ξ and read this tabulation at run time in order to evaluate the model's equation. The reason for this was to make the retracking computationally as fast as possible. Furthermore, these tabulations are not depending on any sensor parameters (the sensor parameter enter solely in the argument ξ) and hence they do not need to be recomputed for new or others missions.
Finally, for high values of the argument ξ (more than 9), the following asymptotic approximation for f_0 has been used:

$$f_0(\xi) = \sqrt{\frac{\pi}{2}} \cdot \frac{1}{\sqrt{\xi}} \left[1 + \frac{3}{8} \cdot \frac{1}{\xi^2} + \frac{105}{128} \cdot \frac{1}{\xi^4}\right] \quad (3.25)$$

For ξ >6, the difference between the exact solution and the approximated one is lesser than 1e-4.
Similarly, for high values of the argument ξ, the f_1 function has been approximated by its asymptotic formulation:

$$f_1(\xi) = \sqrt{\frac{\pi}{8}} \cdot \frac{1}{\sqrt{\xi^3}} \quad (3.26)$$

d) Least Squares Estimator with Levenberg-Marquardt approach (LSE-LM)

The LSE-LM algorithm (Least Squares Estimator with Levenberg-Marquardt approach) (Gill and Murray, 1978) is a minimization technique of a function F(x) which is sum of squares of non linear functions f_i:

$$F(x) = \frac{1}{2} \sum_{i=1}^{M} [(f_i(x))]^2 \quad (3.27)$$

Denoted as $J_i(x)$ the Jacobian of $f_i(x)$, then the LSE-LM searches the solution δ_k of the equation :

$$(\boldsymbol{J}_k^T \boldsymbol{J} + \lambda_k \boldsymbol{I}) \delta_k = -\boldsymbol{J}_k^T \boldsymbol{f}_k \quad (3.28)$$

where λ_k are non-negative scalar and I is the identity matrix. The factors λ_k are known as damping factors and usually are taken identical for all the k unknowns of the problem.

The LSE-LM can be imagined as a generalization of the classic LSE-GN (Least Squares Estimator with Gauss-Newton approach) which searches the solution δ_k of the equation:

$$(\boldsymbol{J}_k^T \boldsymbol{J}) \delta_k = -\boldsymbol{J}_k^T \boldsymbol{f}_k \quad (3.29)$$

and therefore LSE-LM is usually referred also as damped Least-Squares Estimator.

It can be demonstrated (Madsen et al., 2004) that the LSE-LM:

- does not have a specific direction search
- for very low value of the damping factors, it reduces to Gauss-Newton approach while for high values of the damping factor it tends to behave as Descent Gradient Method

An initial value λ of the damping factor is needed to be passed in input to the algorithm. This value is then internally updated by the algorithm at each iteration using the gain ratio formula (Madsen et al., 2004). If the reduction of the sum of the squared residuals is fast and the algorithm gets close to the solution, the damping factor undergoes only small changes or it gets reduced whereas, if the reduction is not achieved and algorithm is far from the solution, the algorithm automatically increases the value of the damping factor to accelerate the convergence and the direction search will be nearly the gradient direction (which is good if the

current iteration is far from the solution). Hence LSE-LM is an adaptive algorithm because it controls its own damping.
In the altimetry case, the function f_i in Eq. (3.27) are the residuals between waveform data and waveform model while δ_k are the deviations from the truth for the retracked variables.
The retracked (unknown) variables are three: epoch, SWH and Pu.
As far it concerns the customization of the algorithm for the waveform's fitting, in order to avoid rounding problems inside the minimization process, the epoch has been expressed in nanoseconds while both the waveform data and the waveform model are normalized in order to make the waveform data and waveform model close to each other in amplitude.
Anyhow, it is important to bear in mind that LSE will find only a local minimum which will not be necessarily a global minimum. As consequence, it is fundamental to initialize proper the estimator to ensure a fast convergence. For the open ocean retracker, it has been set as first guess value:

- the maximum point of the waveform data for the epoch, knowing that the true epoch is very close to maximum point of the waveform
- 2 meter for SWH , being most typical value of SWH
- 1 for Pu, being the true Pu very close to the waveform's maximum

Furthermore, for each of the retracked variables some constrains have been placed in order to avoid not physical solutions.
These upper and lower values of the used constrains are:

	Epoch	SWH	Pu
lower bound	first sample of the epoch array	-0.5 meter	0.2
upper bound	last sample of the epoch array	20 meter	1.5

Table 3.1: Constrains (lower and upper bound for epoch, SWH and Pu)

e) Model Zero-Masking by exact range shifts

Due to the limited size of the radar receiving window (around 60 meters), after the range alignment process, the Doppler beams in the stack get padded with zeroes or with place-holder as NaN (Not a Number).

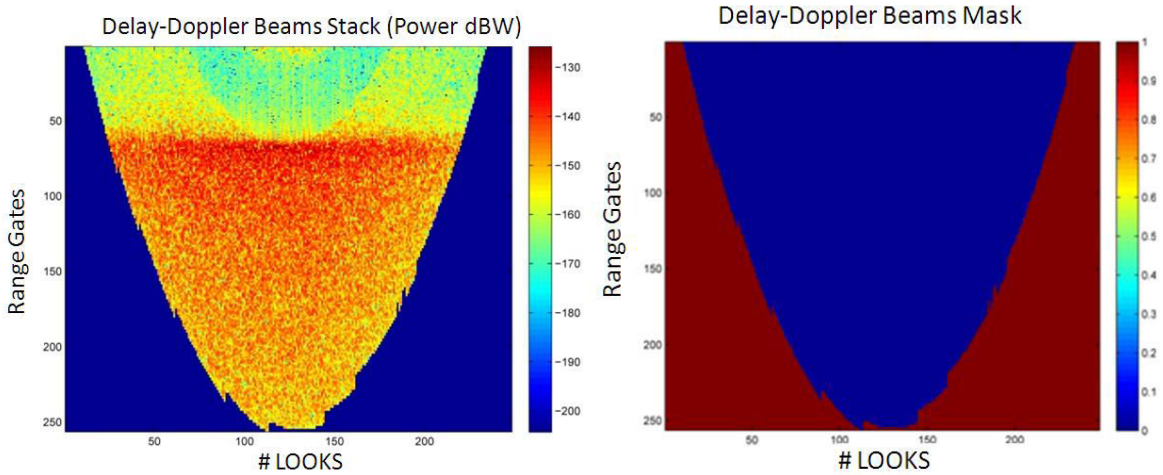

Figure 3.18: CryoSat-2 Stack Data (left) and bitwise mask (1/0) of the stack zeroes (right)

Hence in order to maintain the consistency between model's Delay-Doppler Map (DDM) and stack data, it is necessary to compute from the stack a bitwise mask (1/0) giving the position of the pixels in stack data matrix wherein the zeroes are located and then apply this mask during the retracking to place the zeroes in the model's DDM (CP40 Project Report (2014a) and CP40 Project Report (2014b)).
In the retracker, this zero-mask has been constructed using the total range shift (sum of slant range shift, tracker range shift and Doppler range shift) as computed and applied at L1b to align in range the Doppler beams (i.e. exact range shifts). Specifically, the model's DDM values are replaced by zeros in the pixels (ℓ, k) where:

$$\Delta R_{\ell} \geq R_k \tag{3.30}$$

with ΔR_{ℓ} is the total range shift (with minimum removed) and R_k is given by:

$$R_k = \Delta R \cdot [N - 1 : -1 : 0] \tag{3.31}$$

where ΔR is the range bin width, N is the number of range bins, and [a:s:b] denotes an array starting from a until b with step s.

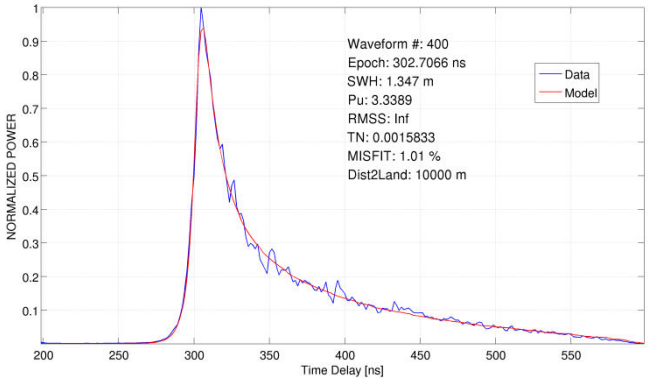

Figure 3.19: Model Zero-Masking: thanks to the model's zero-Masking process, the waveform model trailing edge (in red) is not anymore asymptotic but decays to zero as the waveform data (in blue).

f) Model Evaluated at exact look angles

One of the inputs necessary to the SAMOSA model evaluation are the look angles.
In order to be fully consistent with the L1b stack data, the look angles used in input to the SAMOSA model are the ones computed at L1b stage from the burst center and range locations positions (i.e. exact look angles).
These look angles theoretically have an angular separation of:

$$\Delta\theta_{Look} = \frac{V_s \cdot BRI}{h \cdot \alpha} \tag{3.32}$$

with:

$$\alpha = 1 + \frac{h}{R_{Earth}} \tag{3.33}$$

where V_s is the satellite velocity, BRI is the Burst Repetition Interval (around 11.79 ms for CryoSat-2), h is the satellite altitude and R_{Earth} is the mean Earth radius.

Converting this angular separation in Doppler frequency separation by:

$$\Delta f_{dop} = \frac{2 \cdot V_s \cdot BRI}{\lambda_0} \sin(\Delta\theta_{Look}) \tag{3.34}$$

one can see how the Doppler frequency step size given by Eq. 3.34 is lower than the sampling Doppler frequency given by:

$$\Delta f_{Samp} = \frac{PRF}{N_{pulses}} \tag{3.35}$$

where N_{pulses} is the number of pulses in a burst (64). Hence, if one evaluates the DDM for all the look angles, it means that one is oversampling the DDM, i.e. evaluating it with a Doppler frequency resolution lower than it was physically sampled by PRF. In order to reduce the computational time, the look angles are rounded so as they have a frequency step given by Eq. 3.35. This way, the beam index ℓ in equation (3.21) will only take integer values.

g) Thermal Noise from early samples

On top of the signal received from the surface, the waveform exhibits an additive random noise known as thermal noise (or better equivalent thermal noise) (Vignudelli et al., 2011) which can be considered as the sum of the radar receiver's electronic noise, atmospheric noise, the galactic noise and else.
In case of open ocean waveforms, because the on board tracker will place the waveform around the range gate 44, the waveform's early samples are just a measurement of this thermal noise level and generally are not influenced by signal reflected from the surface.
Hence, a very reliable and common technique to estimate the thermal noise floor from the waveform in pulse-limited altimetry is to compute the average of the waveform's early samples. This method was followed also in the SAR open ocean retracker in which the "noise range bins" used are [5,10] .

h) Mispointing Angles as input from Star Tracker

Though the satellite attitude control subsystem has the task to ensure a platform attitude pointed to geodetic nadir, a perfect nadir-pointing can never be reached. Hence, each radar altimeter on board of a satellite will be slightly mispointed.
In case of the SAR retracking, the mispointing angles (roll and pitch) have been always derived from the satellite platform files (or L1A products) and injected in the retracker as input to the SAMOSA model. Hence, the mispointing angles are not estimated from the waveform in my approach and in general in SAR Altimetry. The rationale behind this is that there is a clear coupling (or cross-talk) between roll mispointing and SWH variables (as shown in Figure 3.13 and in Figure 3.15), resulting both of them to have a very similar effect on the SAR waveform shape, making impossible for a SAR retracker to discriminate whether this effect has been triggered from a variation of SWH or a variation of the roll mispointing.

3.2.3 SAMOSA-BASED MARINE SAR RETRACKER (SAMOSA+)

As stated in the previous section, the SAMOSA-based open ocean retracker is expected to underperform over the coastal zone, inland water and sea ice wherein bright targets as sandbanks, off-nadir cliffs, ponds of still water, wetlands, water lead between ice floes, etc. etc. will break the assumption of incoherent backscattering surface on which the physical model bases. Even over open ocean, this retracker may sporadically fail to have a good fit to the waveform data because of oil slicks, ships and algae blooming events. In this section, I propose a way to generalize the SAMOSA-based open ocean retracker to any marine surface (at least) making usage of the mean square slope parameter and a better initialization of the retracker itself. This retracker is referred as SAMOSA+ and has been introduced in (Dinardo et al., 2018).
In case of SAMOSA+ retracker, the model in Eq. 3.15 has been implemented in the retracking scheme with two significant additions. The first one concerns the selection of the first-guess epoch. This is not selected

anymore simply as the position of the waveform peak as in open ocean case but as the peak position of a moving point-wise product in a subset of 20 consecutive waveforms, after aligning them for tracker shift. Hence, the waveforms are first range-aligned for tracker shift using the quantity orbit altitude minus tracker range (these parameters are extracted from the L1b products). Let W_n be the n-th range-aligned waveform: I consider a subset of 20 range-aligned waveforms formed by [W_{n-10}, ..., W_n, ..., W_{n+9}] and I compute the point-wise product between the waveforms in the subset. The peak position of this point-wise product (Horn and Johnson, 2012) will be taken as first-guess epoch for W_n. This procedure is then repeated for all the waveforms in the pass. The rationale behind this choice is to attempt to mitigate the typical off-ranging effect in coastal data (see Figure 3.20).

Indeed, in the SAR open ocean retracking, the first-guess epoch is selected to be the epoch of waveform peak. This assumption that final retracked epoch is sufficiently close to the SAR waveform peak is a valid one for open ocean conditions. In presence of off-nadir land contamination or off-nadir lead contamination, the afore-said assumption loses its validity because the maximum power can source as well from the off-nadir target. In this case, if the retracking is initiated with erroneous input information, the fitting very likely will converge to a fitting's relative minimum returning an incorrect value of the radar range. On the other side, the peak position of a moving point-wise product between range-aligned consecutive waveforms will represent a more robust and stable reference from which to start the fitting iterations and by which mitigate the off-nadir ranging effect impact.

Figure 3.20 illustrates an example of the benefit in using the new approach in selecting the first guess-epoch in place of peak position. One can see that in the land-sea transition the first-guess epoch is not driven out by the off-nadir stronger returns (due to land contamination) but follows better the sea surface at nadir. This enables hence a more reliable initialization of the retracking scheme in the coastal zone.

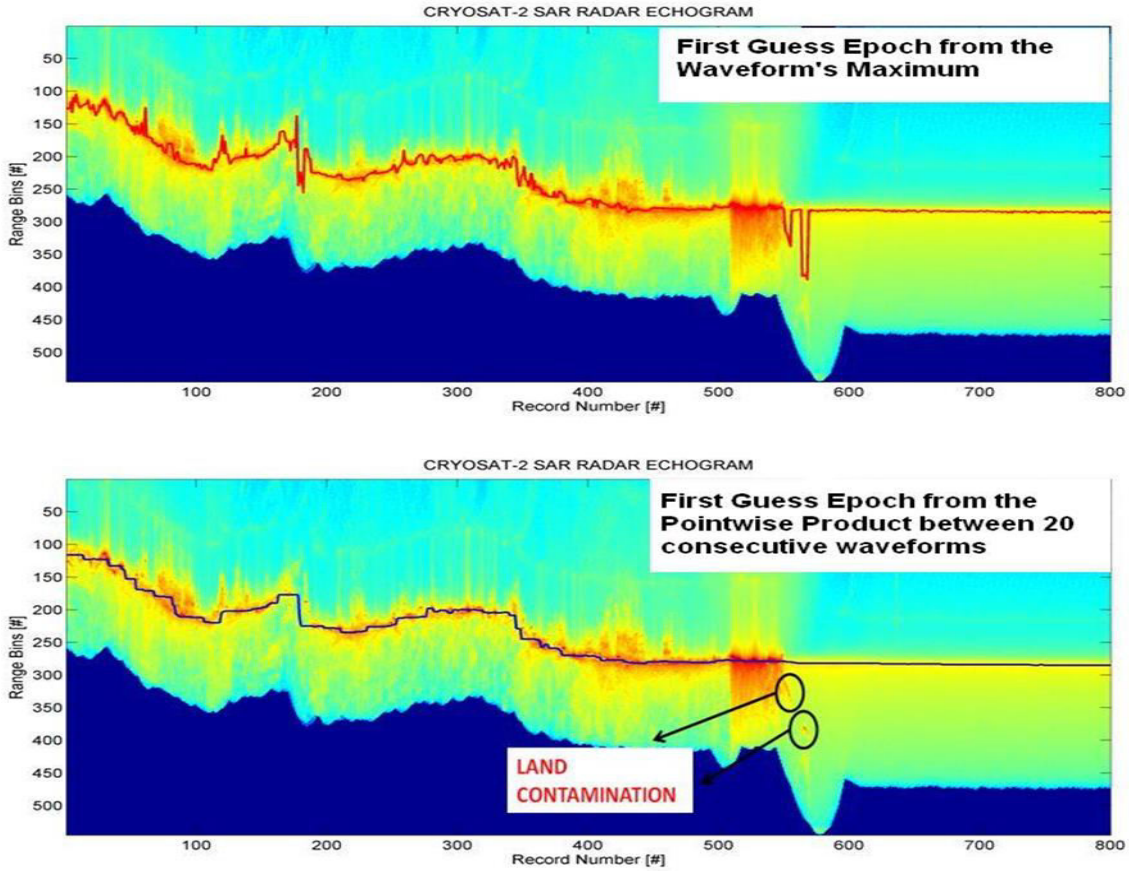

Figure 3.20: CryoSat-2 SAR echogram in the German Bight with a land-sea transition: (Top) first-guess epochs using the peak power position (red line); (Bottom) first-guess epochs using the peak position correlation power (blue line); in the picture, dark blue is the zero value

The second innovation concerns the treatment of land contaminated (or specular) waveforms. In case of waveforms deemed as not contaminated by land and diffusive, the SAMOSA model has been used with the inverse of the mean square slope set to zero, i.e. as described in section 2.2.2 and in Fenoglio-Marc et al., (2015). For waveforms deemed as land contaminated (or specular), a two-step retracking approach is used: in the first step, the SWH is still estimated as in section 2.2.2 while in the second step, the SWH is set to zero and the third free parameter in the retracking becomes the mean square slope (as in Tseng et al., (2013) for pulse-limited altimetry and Kurtz et al., (2014) for SAR altimetry). The output of this second step is the range and the amplitude Pu.
This approach gives the capacity to the model to fit a very peaky waveform which arises from a bright target and to continue to fit the broad diffusive ocean waveforms as good as before. I underline that the continuity between the two steps is ensured by the fact that the same physical waveform model (SAMOSA) is used in both steps.

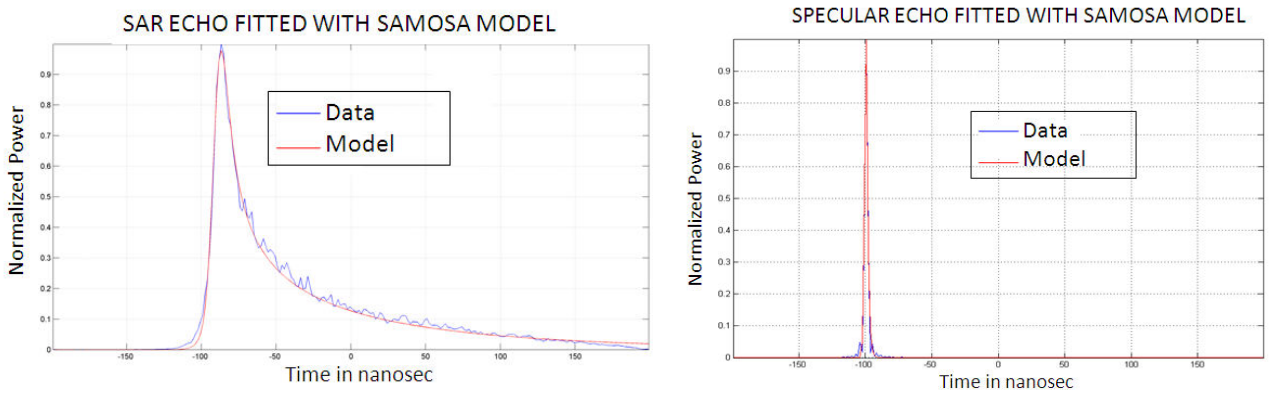

Figure 3.21: Mean Square Slope as third fitting parameter when the wavefom data is contaminated: the usage of the mean square slope as third fitting parameter for a contaminated waveform allows the model to fit open ocean diffusive waveform (left) and peaky waveform from bright target (right)

The quality parameter used to deem whether a waveform is contaminated by land or else is that just one of these conditions occurs:

$$\begin{cases} E \cdot PP < 0.68 \\ E \cdot PP > 0.78 \\ 100 \cdot PP > 4 \\ \frac{E}{misfit} < 8 \end{cases} \tag{3.36}$$

where E is the entropy of the waveform, defined as:

$$E = -\sum_i (|W_i|^2 \cdot \log2(|W_i|^2)) \tag{3.37}$$

PP is the Pulse Peakiness, defined as:

$$PP = \frac{\max(W_i)}{\sum_i (W_i)} \tag{3.38}$$

and W_i are the waveform samples whereas the misfit definition is reported in the equation (3.52). The values of the thresholds in equation (3.36) have been found in a heuristic manner.

Furthermore, it was stated that in the SAR open ocean retracker the SAMOSA SAR return waveform model is complemented by a Look-Up Table (LUT) of the α_p parameter to mitigate the effect of the model's approximation of the squared PTR with a Gaussian curve.

The same LUT keeps on being applicable also in coastal zone but a difference arises whether the Hamming window is applied at L1b. In this specific case, the squared PTR gets approximated quite well by a Gaussian curve (Ray et al., 2015, sect. D) and hence a constant value for α_p (0.55) can be used in place of the LUT.
In conclusion, in the coastal zone, being the Hamming window always applied as stated in section 2.1, a constant value of α_p is used (0.55). A bitwise flag (1/0) stored in the L1b product is used to know whether the Doppler beam has been Hamming-weighted or not.
Since the Hamming window also tapers the waveform power as said in section 2.1, I have compensated this Hamming tapering power as described in section 3.1.1 from (ESA Report, 2016).
The stack masking for the beams padded to zero in the stack data after slant range shift is carried out in the SAMOSA DDM using the exact range shift computed at the L1b stage and stored in the L1b products, as in open ocean case.
The SAMOSA model DDM is evaluated using the exact look angles computed at L1b stage and stored in the L1b products (Dinardo et al., 2015), as in open ocean case.
Regarding the thermal noise floor, since the waveform's early samples can get contaminated by off-nadir returns in the coastal zone, the usual technique to estimate from the waveform early samples does not hold anymore. For this reason, in the SAMOSA+ retracker, the thermal noise is always the one estimated from the stack data as described in section 2.1.
This Thermal Noise Floor as estimated from the stack data is increased by a static amount of 4.84 dB. This amount is deemed attributable to the power from the side lobes of the antenna pattern and the instrument PTR that are not integrated in the SAMOSA model.
The dedicated processing in coastal zone as described in this paper is superior to the open ocean processing used in Fenoglio-Marc et al., (2015), see also Fenoglio-Marc et al., (2017b) and (Dinardo et al., 2018).
About the performance of the SAMOSA+ over sea ice, they have been validated by (Laforge et al., 2019) against NASA Operational IceBridge data.
About retracking over sea ice leads, I have proposed that SAMOSA model may be computed also in "single-look" fashion since this will be sufficient to fit the peaky specular echo, being the power in the stack data concentrated essentially in the nadir Doppler beams. The "single look" approach will bring as benefit a faster computational speed. Anyhow, it has been not tested in this thesis work.

3.2.4 SAMOSA-BASED PAN-THEMATIC SAR RETRACKER (SAMOSA++)

As it will be shown in section 4.1 and in (Dinardo et al., 2018), the SAMOSA+ retracker has proved to provide a significant improvement in coastal zone with respect the open ocean solution. And it has the appealing feature to not degrade the results in open ocean since in open ocean generally it fallbacks to the SAMOSA2 retracker
Furthermore, it has also provided accurate measurement of the sea ice freeboard in case of CryoSat-2 mission and Sentinel-3 (Laforge et al., 2019). Hence, it may be considered already a very efficient "marine retracker" guarantying seamless continuity between coastal zone, open sea and sea-ice.
Anyhow, it was shown to under-perform over inland waters (see CRUCIAL, 2016 and Moore et al., 2018) and it brings along some limitations which here I list:

- It is Two-Step Retracker based on heuristic threshold values to judge whether waveform is land contaminated/specular or not.
- SWH estimation is always coming from the open ocean SAMOSA-based retracker. Hence it does not provide strictly a coastal SWH solution.
- Results show that it can be still improved in the critical strip between 0 and 3 km from the coast.

Furthermore, SAMOSA+ does not make profit of the extra-waveform now available out of the L1b SAR processing, that is the RIP as described in section 2.1.2.

The RIP can be considered as a novel waveform to exploit and to fit in order to extract geophysical information from the surface. It has a very predictable shape over open ocean (Gaussian function) while over bright targets turns into a spike, very similar to the azimuth instrument Impulse Response. Usually, it has been exploited to discriminate between water lead and ice floes over sea ice (Müller et al., 2017), (Passaro et al., 2017) but it has found so far little application in the coastal or inland water domains (Boergens et al., 2017).

The concept at the base of the SAMOSA++ retracker is to involve the RIP in the waveform retracking: the new "plus" in the SAMOSA++ retracker, with respect the SAMOSA+, is hence the RIP.
Indeed, the RIP can be imagined as the backscattering profile of the surface in the along-track direction weighted by the antenna pattern azimuth cut. When represented versus the look angle, the center of the RIP is the result of the sum of the pitch mispointing and slope surface. Hence, over open ocean, where the ocean slope surface are of the order of millideg, the offset of the RIP from zero gives a reliable estimation of the platform pitch mispointing (Scagliola et al., 2015b). Hence, assuming an isotropic Optical-Geometrics surface backscattering (same assumption as made in the SAMOSA model's derivation) and a negligible sea surface slope, the mathematical model of the RIP over open ocean is derived by Eq. 25 in (Dinardo et al., 2018):

$$RIP_{az}(\theta_{Look}) = A_{RIP} \cdot exp\left[-\nu \cdot (\theta_{Look} - \theta_{Pitch})^2 - \gamma_x(\theta_{Look} - \theta_{Pitch})^2\right] \quad (3.39)$$

with:

$$\gamma_x = \frac{8 \cdot ln(2)}{\theta_x^2} \quad (3.40)$$

and where ν is the inverse of the mean square slope (s^2), θ_x is the antenna pattern in azimuth direction, θ_{Look} is the look angle, θ_{Pitch} is the pitch mispointing and $\theta_{Look} = \left(\frac{L_x}{h}\right) \cdot \ell$ is the look angle (Eq. 16 in Dinardo et al., 2018) with L_x along track resolution, ℓ Doppler beam index and h orbit altitude. Eq. 3.39 represents simply the product of two Gaussian functions centered around θ_{Pitch}. It can be demonstrated that the products of two Gaussian functions is again a Gaussian with mean μ and standard deviation σgiven as:

$$\mu = \frac{\mu_1\sigma_2^2 + \mu_2\sigma_1^2}{\sigma_2^2 + \sigma_1^2} \quad (3.41)$$

$$\sigma^2 = \frac{\sigma_2^2\sigma_1^2}{\sigma_2^2 + \sigma_1^2} \quad (3.42)$$

Being $\mu_1 = \mu_2 = \theta_{Pitch}$, the RIP will be indeed centered at pitch's mispointing while the following relationship holds for its standard deviation σ_{RIP}:

$$\sigma_{RIP} = \frac{1}{\sqrt{2 \cdot (\nu + \gamma_x)}} \quad (3.43)$$

and hence:

$$\nu = \left(\frac{1}{2\sigma_{RIP}^2} - \gamma_x\right)$$

(3.44)

In conclusion, fitting the RIP with a Gaussian and hence estimating the standard deviation σ_{RIP} of the RIP, a direct measurement of the ocean mean square slope s^2 can be done from Eq. 3.44 , given the ν definition as $\nu=1/s^2$. Once the mean square slope is estimated, being the amplitude of the RIP A_{RIP} given by Eq. 3.45 (Walsh et al., 1998):

$$A_{RIP} = \frac{|R_f(0)|^2}{2s^2}$$

(3.45)

the surface Fresnel Coefficient $R_f(0)$ for normal incidence can be derived as well. Nevertheless, the RIP data may not be a perfect Gaussian function but it may be characterized by skewness (a measurement of the symmetry degree of the RIP) and kurtosis (a measurement of the flatness of the RIP). The relationship of these statistical moments to sea state parameters will not be investigated in this research activity.
However, the RIP has been computed integrating in range direction a stack of data which get padded with zeroes as consequence of the range alignment shifting (see section 2.1.2). After the summation in range direction, the zeroes will give a spurious weighting to the outer samples of the RIP. This artifact has been compensated by up-scaling the RIP for the number of non-zeros of the stack data in each stack's row.

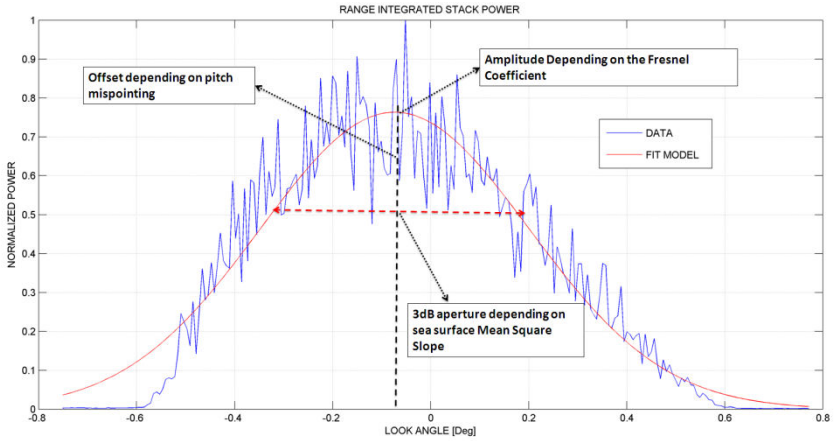

Figure 3.22: RIP fitted with a Gaussian model

Now, recalling the expression of the term $\Gamma_{k,\ell}(0)$ in the SAMOSA SAR waveform model (Ray et al., 2015, Eq. 25), this term $\Gamma_{k,\ell}(0)$ can be rewritten now as:

$$\Gamma_{k,\ell}(0) = RIP_{az}(\theta_{Look}) \cdot exp\left[-\gamma_y(\theta_{Roll}^2)\right] \cdot \begin{cases} exp\left[-(\gamma_y+\nu)\left(\frac{c\cdot(t-t_0)}{\alpha h}\right)\right] cosh\left(2\gamma_y\theta_{Roll}\sqrt{\left(\frac{c\cdot(t-t_0)}{\alpha h}\right)}\right) & t > t_0 \\ 1 & t \le t_0 \end{cases}$$

(3.46)

where γ_y is given in Eq. 27 in Dinardo et al., (2018), θ_{Roll} is the roll mispointing, $\alpha=1+(h/R)$, with R the mean Earth radius, c is the speed of light and $(t-t_0)=\frac{k}{B_r}$ is defined in Eq. 17 in Dinardo et al., (2018) with B_r received radar bandwidth and k range bin index.
Let it be:

$$\phi_k^2 = \left(\frac{c\cdot(t-t_0)}{\alpha h}\right)$$

(3.47)

and, assuming null the roll mispointing (assumption valid in case of Sentinel-3 which has a very stable nadir-pointed platform), one can see how the remaining secondary term in $\Gamma_{k,\ell}(0)$ is again a products of two Gaussians, function of the across track coordinate ϕ_k:

$$\Gamma_{k,\ell}(0) = RIP_{az}(\theta_{Look}) \cdot \begin{cases} exp\left[-(\gamma_y + \nu)\cdot \phi_k^2\right] & t > t_0 \\ 1 & t \le t_0 \end{cases} \quad (3.48)$$

Hence, in definitive, the term $\Gamma_{k,\ell}(0)$ can be rewritten as product of the RIP in along track RIP_{az} and a RIP in across track RIP_{act} directions:

$$\Gamma_{k,\ell}(0) = RIP_{az}(x_l) \cdot RIP_{act}(y_k) \quad (3.49)$$

where $x_l = \mathrm{h}\cdot\theta_{Look}$ is the along track coordinate and $y_k = \mathrm{h}\cdot\phi_k$ is the across track coordinate.
The SAR altimeter is not capable to measure the RIP in across track but, in case of circular antenna pattern ($\gamma_y = \gamma_x$) as for Sentinel-3 and in the hypothesis of isotropy of the surface backscattering, the term $RIP_{act}(y_k)$ can be reconstructed simply by interpolation from $RIP_{az}(x_l)$.
Therefore, in the SAMOSA++ retracker the RIP (as measured by the altimeter and fitted by a mathematical model) will be now used to reconstruct the $\Gamma_{k,\ell}(0)$ term and this reconstructed $\Gamma_{k,\ell}(0)$ will be hence plugged into the waveform model as part of the model.
This approach will give to the waveform model the capacity to automatically adapt to any kind of surface (diffusive, specular or in between) because the RIP will always drive the shape of the term $\Gamma_{k,\ell}(0)$.

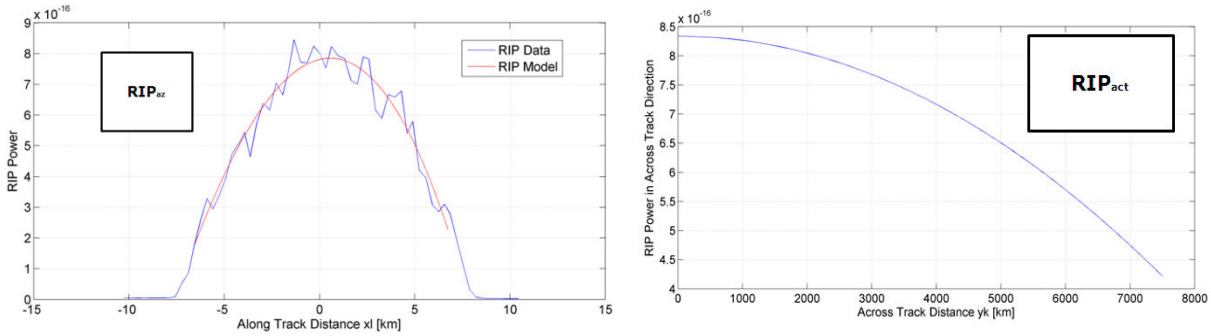

Figure 3.23: RIP_{az} fitted with a model (left) and RIP_{act} reconstructed by interpolation (right)

In Figure 3.24, I have produced the picture of the $\Gamma_{k,\ell}(0)$ term for a case in open ocean (diffusive scattering). In this case, $\Gamma_{k,\ell}(0)$ predicted by SAMOSA model and the $\Gamma_{k,\ell}(0)$ reconstructed in the SAMOSA++ way share a very similar bi-dimensional pattern (circular Gaussian) in the space (x_l, y_k).

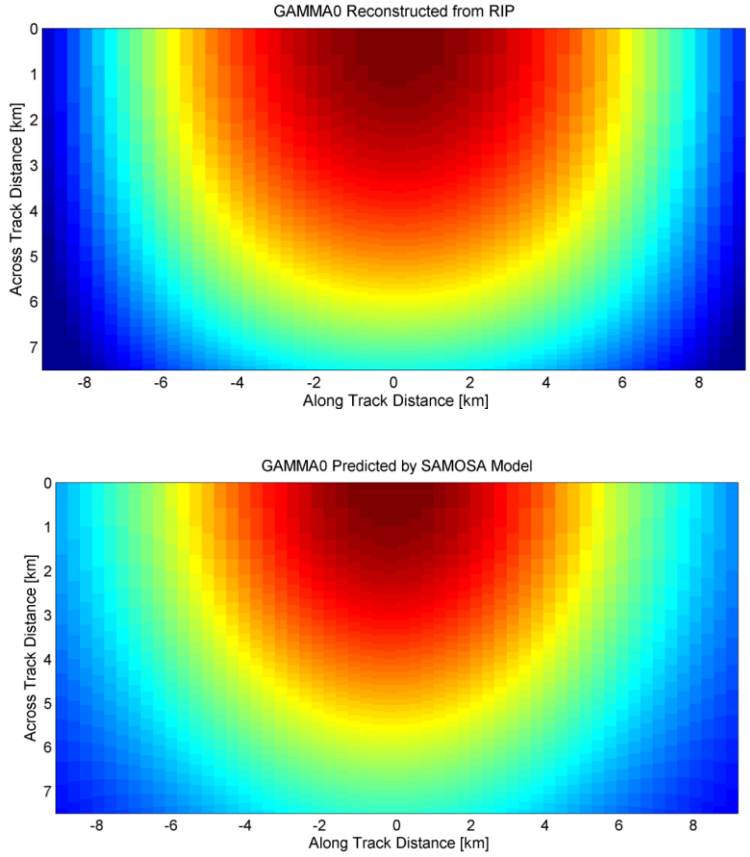

Figure 3.24: Case Diffusive Scattering (Open Ocean): Gamma0 reconstructed from the RIP (top) and Gamma0 predicted by the SAMOSA model (bottom)

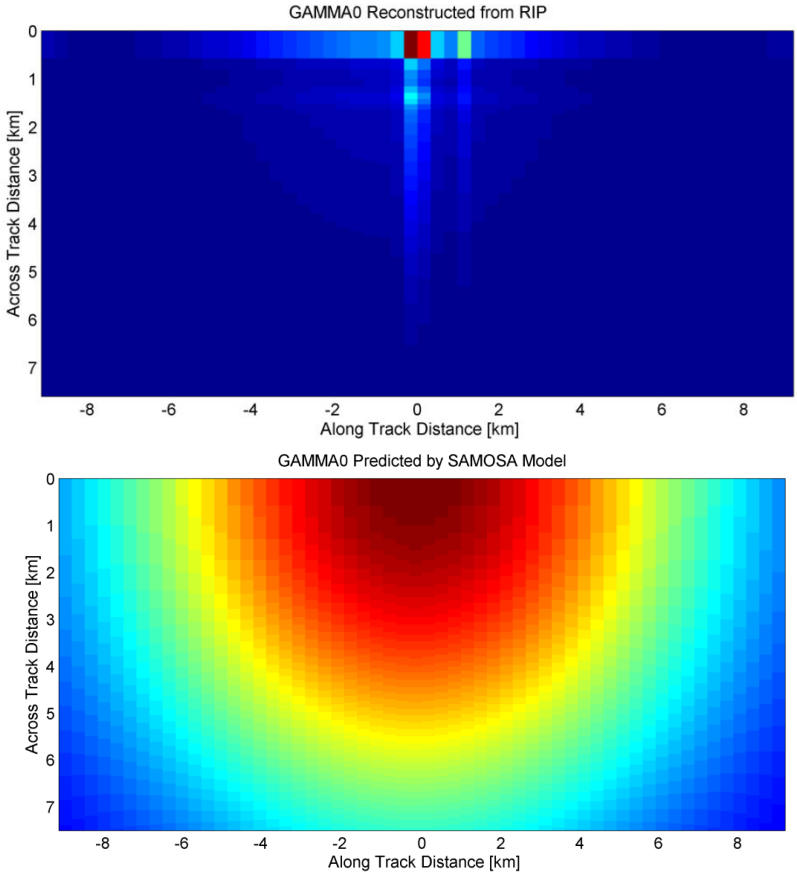

Figure 3.25: Case Specular Scattering (Bright Target): Gamma0 reconstructed from the RIP (top) and Gamma0 predicted by the SAMOSA model (bottom)

On the other side, in Figure 3.25 I have reproduced a case from a bright target (specular backscattering). In this specific case the $\Gamma_{k,\ell}(0)$ predicted by the SAMOSA model keeps to be always the same (indeed the SAMOSA model cannot know a priori whether the surface is diffusive or specular) while the $\Gamma_{k,\ell}(0)$ reconstructed inside the SAMOSA++, exploiting the information coming from the RIP, will change completely shape and it will turn into a very peaky function around zero. Because now the $\Gamma_{k,\ell}(0)$ is a very peaked function, all the waveform's model will change shape and it will succeed to fit the return from the bright target (see Figure 3.26).
Naturally, the waveform model in the SAMOSA++ retracker can fit very well the power return when the surface gets diffusive as in open ocean (see Figure 3.27).

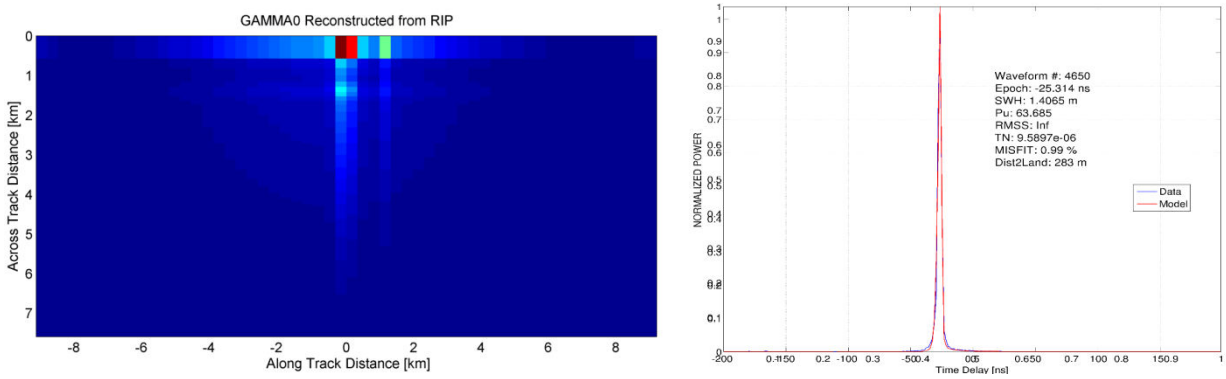

Figure 3.26: When $\boldsymbol{\Gamma_{k,\ell}(0)}$ is a very peaked function, SAMOSA++ can fit very well the return from the bright target

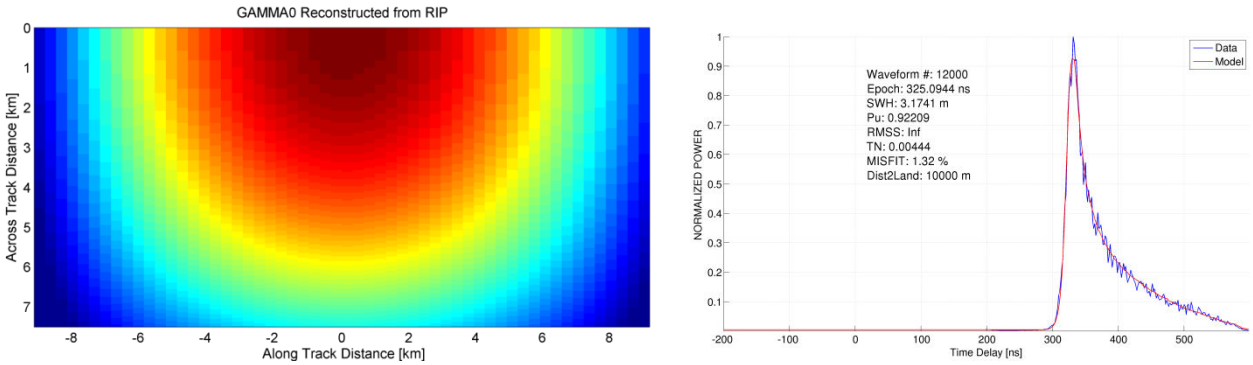

Figure 3.27: when $\boldsymbol{\Gamma_{k,\ell}(0)}$ gets very broad (as circular Gaussian), SAMOSA++ still fits very well the return from the dull target (as open ocean)

In conclusion, the SAMOSA++ is a single-step pan-thematic retracker apt to any surface: introducing inside the SAMOSA model waveform the RIP to reconstruct the $\Gamma_{k,\ell}(0)$ term gives to the model an autonomous capacity to adapt itself to the backscattering state of the surface and to produce hence a physical solution to the retracking problem however the scattering surface is rugged.
Furthermore, being the RIP fitted by a mathematical model as in Eq. 3.39, the SAMOSA++ will return in output the new geophysical quantities:

- RIP mean square slope
- RIP offset (sum of surface slope and pitch-mispointing)
- RIP Fresnel Coefficient

In this regard, because the shape of the RIP can get very peaky in coastal zone, a simple Gaussian model (as given in Eq. 3.39) will fail to fit the RIP properly. Hence, when the RIP Peakiness defined as:

$$PP_{RIP} = \frac{\max(RIP_i)}{\sum_i RIP_i} \tag{3.50}$$

is higher than 6, a functional model made of a sum of 4 Gaussians is used instead to fit the RIP. However, the mean square slope is always derived from the Gaussian model expressed in Eq. 3.39.

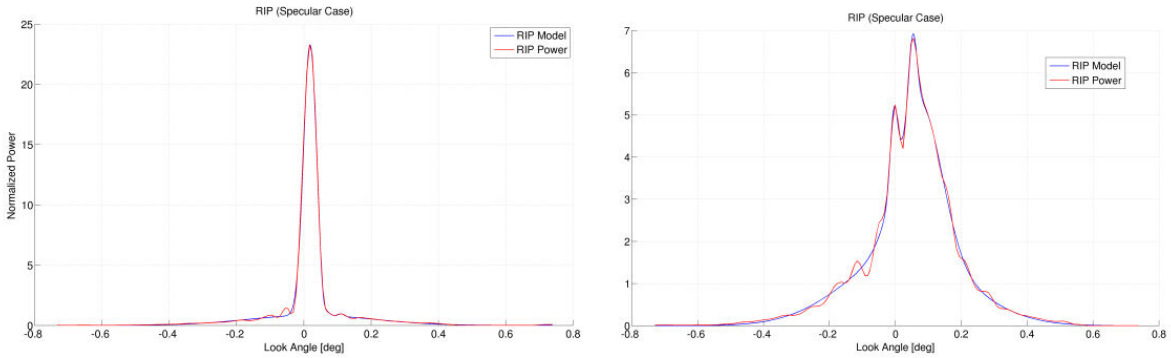

Figure 3.28: When the RIP gets peaky, a sum of 4 Gaussians is used as functional model in the fit

3.3 METHODOLOGIES IN PLRM L2 PROCESSING

For this thesis work, the PLRM waveforms have been retracked by TU-Darmstadt/University of Bonn with a retracker adopting a Signal Model Involving Numerical Convolution (SINC) approach, tailored for PLRM and called SINC2 (Buchhaupt et al., 2018). The SINC2 retracker is based on the Brown model (Brown, 1977) and uses a fast circular convolution algorithm. Main advantage of SINC2 compared to Brown and other standard analytical retrackers, as used for instance in Fenoglio-Marc et al., (2015), is that SINC2 does not approximate the Point Target Response (PTR) as a Gaussian function and therefore a Look-Up Table (LUT) is not needed. The three parameters amplitude Pu, epoch and SWH, given by the relationship $\sigma_s^2 = \left(\frac{SWH}{2c}\right)^2$, are estimated by fitting the model to the waveforms with a Least Squares Estimator (LSE).

The SINC2 retracker is not tailored to the coastal zone. Therefore, a PLRM L2 dataset tailored to coastal zone has been produced for CryoSat-2 mission using the TU-Darmstadt Adaptive Leading Edge Sub-waveform retracker (TALES). This retracker uses the fast circular convolutional Brown model SINC as waveform model and it adopts the approach by Passaro et al., (2014) to select the sub-waveform to be retracked. The end gate number of the estimation window used for the Cryosat-2 PLRM waveforms is the smallest integer which is greater than or equal to k_{stop}:

$$k_{stop} = LP + 8.1212 + 9.2519 \cdot SWH \tag{3.51}$$

where LP and SWH are respectively the leading edge position and the significant wave height estimated in the first step of the TALES retracking. The two coefficients in Eq. 3.51 have been estimated for CryoSat-2 in the second step of the TALES retracking from Monte Carlo simulations.

Regarding the Sentinel-3 mission, the reference dataset used for validation are the Sentinel-3 PDGS (Payload Ground Segment) SAR/PLRM marine data.

3.4 METHODOLOGIES IN DATA SCREENING

When working in challenging areas such as the coastal zone, an ad hoc outlier detection strategy is needed to reject off-range values. The outlier detection criteria adopted here depend on the geophysical parameter to be scrutinized.

- For SLA, the 3-sigma rule (Pukelsheim, 1994) is used. The SLA measurements have a data distribution that can be considered nearly normal (Hayne, 1980); hence the application of the 3 sigma rule in this case can be deemed legitimate. Therefore, firstly the standard deviation of the SLA data in my area of interest is computed. Then all the SLA data not satisfying the 3-sigma rule are screened out.

- SWH measurements do not follow a normal distribution but a Rayleigh distribution (Tayfun, 1980); hence the 3-sigma rule cannot be applied as for SLA. Instead, the measurements are filtered out using a quality parameter, which is the misfit between model and data waveform. The filter rejects SWH measurements when the SAR waveform features a misfit higher than 4 in SAR (see Cipollini and Calafat, 2016) and higher than 10 in PLRM mode. Furthermore, a threshold criterion is enforced wherein SWH must be in the range of [-1.5, 15] meters which allows also for negative SWH following Scharroo (2002), who suggested to shape the retracker in order to retain negative SWH. A high value of misfit is a strong indication for land contamination in the waveform or that the waveform originates from a specular surface. In this case, being the waveform contaminated or specular, the SWH measurement is assumed as erroneous and to be discarded. The formula used for the misfit is:

$$\text{misfit} = 100 \cdot \sqrt{\frac{1}{N}\sum_i (\text{residuals}_i)^2} \tag{3.52}$$

  where residuals are the differences between the modelled waveform and the received echo for each waveform range bin, and N is the number of range bin. For CryoSat-2, N is 128 if zero-padding is not applied or 256 if zero-padding is applied. Figure 3.29 shows an example of SAR return waveform (left) and PLRM return waveform (right) with a misfit value of respectively 4 and 10 to give an idea of the level of waveform's distortion for the misfit threshold values. Figure 3.30 illustrates the cloud of 20 Hz misfit values versus SWH in open-ocean to prove that in the absence of land contamination (open ocean case) the cloud of the points are well within the threshold values: indeed in both cases 99.99% of the values are lower than the respective threshold values.

- For sigma nought, the 3-sigma rule was used as well, being sigma nought also approximately normally distributed.

To ensure a fair cross-comparison between PLRM and SAR, the same outlier detection strategy was used for both SAR and PLRM data.

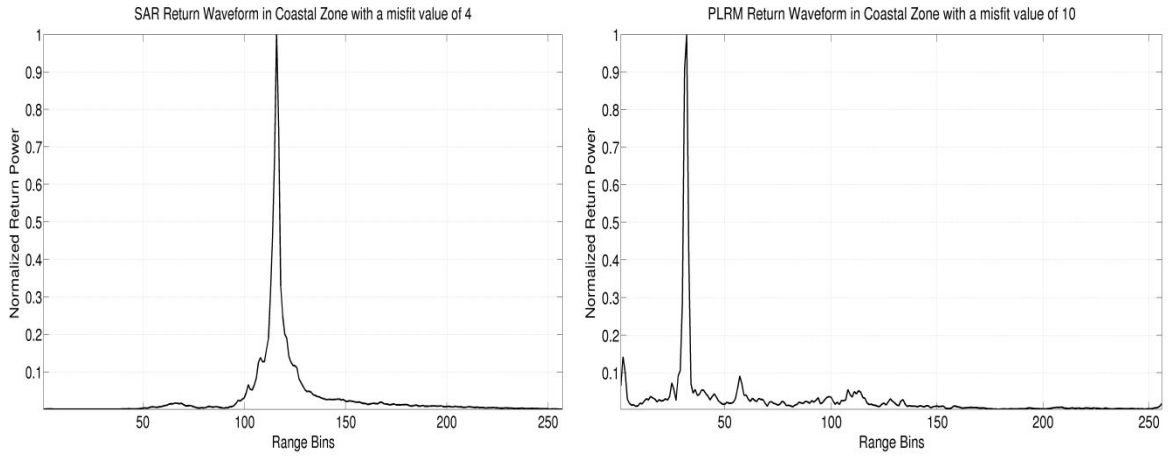

Figure 3.29: Example of a SAR Return Waveform with misfit of 4 (left) and an example of a PLRM return waveform with a misfit of 10 (right)

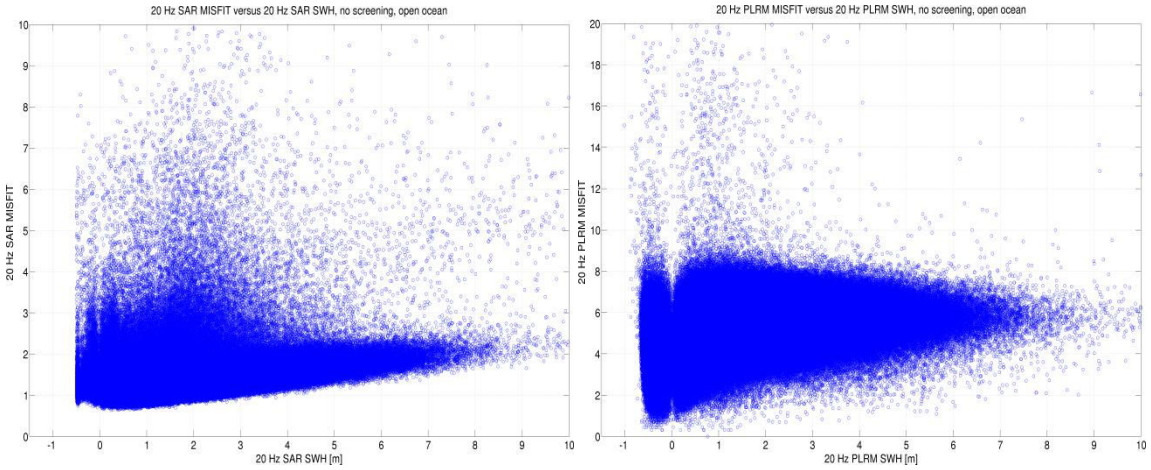

Figure 3.30: Cloud of 20 Hz misfit values for SAR (left) and PLRM (right). Case open-ocean

3.5 DISCUSSION

In this section, I discuss and summarize briefly the content of this chapter.

I have described in detail how the SAR processing has been done in order to infer from the raw satellite data the geophysical quantities of interest.

At L1b, I have designed and developed my own methods (as extended receiving window, 80 Hz gridding, thermal noise from stack) or re-used some methods already known in the community (as Hamming window and zero-padding) and all of them have been treated as complements to the standard SAR L1b processing.

At L2, I have designed and developed my own SAR open ocean retracker based on the formulation of the SAMOSA model which I have reformulated at my convenience. I have introduced key elements in this retracker design as α_p LUT and I have proposed to carry out the residuals minimization by Least-Squares Estimator with Levenberg-Marquardt approach. Also the zero-masking has been implemented in a novel manner using the exact range shifts from the L1b range alignment process.

Furthermore, I have generalized the concept of the SAMOSA-based open ocean retracker proposing and developing the SAMOSA+ retracker which will be validated over the marine surfaces (open ocean, coastal zone and sea ice) in chapter 4. This retracker has a better epoch initialization to mitigate the off-ranging effect (typical in a coastal zone and sea ice scenario) and involves the usage of the mean square slope to better fit the peaky waveform from bright targets. It guarantees a perfect continuity with the open ocean solution because it fallbacks to this open ocean retracker in case the waveform is deemed non-land contaminated and non-specular.

Finally, I moved forward and, building on the current existing limitations and draw-backs of the SAMOSA+ retracker, I have proposed and developed a new "pan-thematic" SAR retracker which, in one single-step approach, provides three geophysical measurements and which can automatically adapt to any surface conditions thanks to the involvement of the RIP in the physical model formulation. Furthermore, it provides in output also the mean square slope, adding a new geophysical measurement in the estimation.

Then, it has been described how the PLRM dataset used in chapter 4 has been retracked and procured. The PLRM mode processed the SAR data at the conventional pulse-limited way and hence it represents a very reliable dataset to be used to validate any SAR data and to identify any improvement brought by SAR altimetry or any drawbacks/glitches in the SAR dataset.

Finally, I have presented my own way to screen the outliers out based on the 3-sigma rule and waveform misfit: the objective was to attempt to preserve the completeness of the dataset as much as possible, avoiding rejecting valid data.

4 Experiments and Results

Introduction

The objective of this chapter is to quantify the capacity of the newly designed retrackers (SAMOSA+ and SAMOSA++), complemented with the new L1b options, in measuring the marine (open ocean and coastal zone) dynamic topography processes, the sea ice freeboard and the inland water bodies elevations when also the state of the art of auxiliary data and range and geophysical corrections are used.

Hence, the chapter is divided in three main parts: presentation of the marine (open ocean and coastal zone) results obtained with CryoSat-2 and Sentinel-3 missions, presentation of the inland water results obtained with Sentinel-3 mission and presentation of the sea ice freeboard results obtained with Cryosat-2 and Sentinel-3 missions.

The results from the SAMOSA-based open ocean retracker have been already presented and reported in the publication (Fenoglio-Marc et al., 2015) and will not be repeated here. This study has shown that over open sea the SAR and PLRM (pseudo-LRM) altimetric measurements feature a good level of consistency between each other and against in situ data, SAR mode data having, anyhow, a higher level of precision.

About the CryoSat-2 marine results with SAMOSA+, relative to the coastal zone part, they are reported in this thesis work and they are based essentially on (Dinardo et al., 2018). This study has reported how SAMOSA+ over-performs PLRM TALES in coastal zone, having the best consistency with respect to tide gauges and ocean circulation/wave models. Distance to coast plots show that land contamination begins to affect sea level and wave measurements at 2 km from the coast in SAR and at 3.5 km in PLRM TALES. The analysis of the monthly mean time-series shows that SAR Altimetry is able to measure the sea level monthly mean in the coastal zone of the region of interest, during the entire mission, more precisely than PLRM.

Instead, relative to the open ocean part, I have used now in this thesis work the same dataset as in (Dinardo et al., 2018) to demonstrate how the SAMOSA+ is consistent over open ocean as well with PLRM, ocean circulation/wave models and in situ data.

About the Sentinel-3 marine results, my goal is to assess the capacity of the SAMOSA++ retracker to bring the altimetric measurements even closer to the coast, in comparison to SAMOSA+ retracker without degrading the results in the open ocean.

The results from SAMOSA+ retracker over sea ice for CryoSat-2 and Sentinel-3 missions are going to be reported in a publication in preparation (Laforge et al., 2019) which I refer to and they are briefly anticipated in this thesis work and validated against NASA operational IceBridge data.

The results over inland water for Sentinel-3 have been obtained over two challenging targets: Bracciano Lake and River Po. Bracciano is a very difficult target to track because of the strong off-nadir reflections from its banks: I will show how Sentinel-3 SAR altimeter, supported by OLTC (open loop) mode, can track and measure the variation of level of this lake with a standard deviation of 6 cm. When Sentinel-3B was in closed loop (autonomous tracking) during the tandem phase, the altimeter was not capable at all to track the lake missing completely the acquisition of the signal from the lake. The Po river has been selected for its limited width (few hundred meters) which gave me the possibility to apply the 80 Hz gridding concept in order to pinpoint the ground cells exactly (and always) on the river water course. For both cases (Bracciano Lake and Po River), SAMOSA++ retracker provides more accurate results than SAMOSA+ retracker compared to in situ data.

Results over inland water from CryoSat-2 are not shown in this thesis work but anyhow results obtained with SAMOSA retracker extracted from G-POD portal for CryoSat-2 are presented in (Moore et al., 2018).

4.1 CRYOSAT-2 MARINE RESULTS

4.1.1 REGION OF INTEREST AND DATA

Prior to presenting the marine results achieved with CryoSat-2 mission, I describe the region of interest, the geophysical and range corrections and the third party data which I have been using to derive my results. Then, the formulation used to apply the range corrections and the terminology for the several geophysical topographic quantities (sea surface height, sea level anomaly, dynamic ocean topography, etc.) is recalled.

4.1.1.1 REGION OF INTEREST

The region of interest, selected for this thesis work in validating the CryoSat-2 results in open ocean and coastal zone, is bound by the geographic coordinates (52° N to 60° N; 4° E to 16° E) and consists of the Eastern North Sea and the West Baltic Sea. CryoSat-2 operates in SAR mode over this region. The study area is depicted in Figure 4.1:

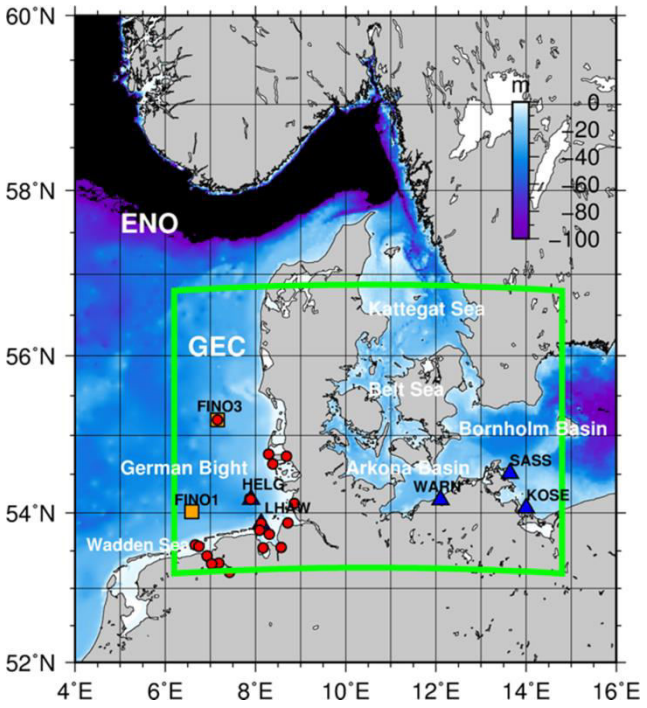

Figure 4.1: Region of analysis showing the location of the five tide gauge stations (triangle), nineteen GNSS stations (circle) and two AWAC stations (square) used in this study. The high-resolution sea level circulation model is available in the region corresponding to the German coasts (GEC) delimited by the green box. Image courtesy of Luciana Fenoglio-Marc.

The bathymetry is deep in the northern part, along the Norwegian coasts, and shallow in the rest of the region. The German Bight is the south-eastern bight of the North Sea bound by The Netherlands and Germany in the south and by Denmark and Germany to the east. Part of the German Bight is the Wadden Sea, an intertidal zone between the Frisian and Western Danish Islands and the north-western European coast. The Wadden Sea is an area of shallow waters, rich of wetlands, mudflats and rocky cliffs, declared a UNESCO World Heritage site owing to its biological diversity.

Along with the German Bight, my area of analysis includes the West Baltic Sea with its sub-basins: the Kattegat Sea, the Belt Sea, the Arkona Basin and the Bornholm Basin. The rationale to extend the study area to West Baltic Sea was to include in my study both a region with high tidal dynamics, high significant wave height regimes and strong winds (the German Bight) as well as an enclosed-sea region with moderate tidal amplitudes and milder sea state (the West Baltic Sea).

It is worth to recall that violent and sudden storm surges (up to 2-3 meter in extreme cases) often sweep the German Bight due to its characteristic L-shape, where long fetch of winds can form and blow toward inland from the North Atlantic (Fenoglio-Marc et al., 2015).
Both SAR and PLRM data are processed from CryoSat-2 FBR up to geophysical level (L2) to provide Sea Surface Height, Significant Wave Height and Wind Speed at 10 meter over the sea surface, posted at a rate of 20 Hz.
The selected time of interest is as long as possible and includes almost 6 years of data going from July 2010 till March 2016. In this time frame, there is a data gap in February 2012 due to an outage time of the CryoSat-2 satellite
In the aforesaid temporal frame, the FBR dataset has been collected from CryoSat-2 PDGS in two diverse processing baselines, which are Baseline B & C. In case of duplicated products (i.e. products available in both baseline B & C), the one with the most recent baseline is used. The baseline C FBR products have been harmonized with baseline B FBR products using the technical note by Scagliola et al., (2015a).
A very first dataset screening is applied rejecting data over land, over inland water (where ocean tide is equal to zero), over very shallow water (depth less than 2 m) and data with departure from the mean sea surface (MSS) larger than 15 meters.

4.1.1.2 AUXILIARY AND THIRD PARTY DATA

This section provides details on the auxiliary and third-party data that were specifically collected for this coastal study.

a) MEAN SEA SURFACE AND GEOID

The mean sea surface (MSS) and geoid models used are respectively the DTU15 MSS model at 1 arcminute resolution (Andersen et al., 2016) and the EIGEN-6C4 Geoid model at 1 arcminute resolution (Förste et al., 2014).

b) WATER/LAND MASK

The water/land mask is the University of Maryland MODIS water/land mask (Carroll et al., 2009), which is called MOD44W. This mask uses SWBD dataset (SRTM Water Body Data, SRTM stands for Shuttle Radar Topography Mission) in combination with MODIS 250 m data to create a complete global map of surface water at 250 m spatial resolution. The water/land mask has been used to compute the distance to coast parameter.

c) NUMERICAL OCEAN MODELS AND IN SITU DATA

The numerical ocean models used for validation purposes are:

- Numerical Sea Level Circulation Model from BSH (German Federal Maritime and Hydrographic Agency) with the fine resolution grid (0.9 x 0.9 km) (Dick et al., 2001)
- Numerical Wave Model (LSM & EWAM) from DWD (German Weather Service) with the grids of 11 x 11 km for LSM and 6x6 km for EWAM (Dick et al., 2001)
- Operational Analysis Wind Speed Model from the European Centre for Medium-Range Weather Forecasts (ECMWF) with the grid of 0.1° x 0.1°

The high-resolution sea level circulation model is available from January 2010 till December 2016 along the German coasts (green box in Figure 4.1: 53° N to 56° N; 6° E to 15° E). It is a prognostic baroclinic hydrodynamic model for the North and Baltic Sea region in three dimensions, driven by the meteorological models GME (Global-Model and Europe) and LM (Local-Model) and by the operational wave model of the

DWD. The former provides wind, air pressure, air temperature, cloud coverage and specific humidity and the latter wave height, direction, frequency of waves and swell.

The DWD numerical wave model is part of the numerical weather prediction system of DWD for the North Sea and Baltic Sea and is operationally run at BSH. It consists of the Local Sea State Model (LSM) until 2012 and of the European Wave model (EWAM) afterwards. It predicts wave height, direction of sea wind, frequency of waves and swells.
LSM is driven by the COSMO-EU winds and uses the Global Sea state Model (GSM) at the open boundaries of the LSM model, which are the English Channel and the Northern and Western boundaries of the North Sea. Since 2008, near-real time SWH altimetry data from ERS-2, Jason-1, and Jason-2 are assimilated in the GSM model.
EWAM is a regional model for Europe, which uses the Global WAM (GWAM) for the open boundary conditions. EWAM is driven by COSMO-EU winds. SWH altimetry data from Jason-2 are assimilated in GWAM.
ECMWF provides a global analysis 10 meter wind speed model. The output of this model was extracted with a grid step of 0.1° in the area and period of interest via ECMWF Mars Service. It assimilates wind vectors from ASCAT, on board the METOP satellite.
In situ sea level and wave measurements from tide gauge stations, from buoys and Acoustic Wave Current (AWAC) profilers are used to validate the corresponding altimetric-derived data. These in situ data are from a network of stations in the German Bight and Baltic Sea belonging to the German Federal Institute of Hydrology (BfG) and to the German Waterway and Shipping Administration (WSV) (Barjenbruch et al., 2002).

4.1.1.3 GEOPHYSICAL AND RANGE CORRECTIONS

This section provides details on the range and geophysical corrections that were specifically selected for this coastal study. While in open ocean the range and geophysical corrections have reached a state of maturity, in the coastal zone the development of accurate range and geophysical corrections is still matter of ongoing research and it is acknowledged as one of the key factors for the unexploitation of the coastal altimetry data (Cipollini et al., 2010). Hence, it is really prominent to proceed to an attentive selection of updated range and geophysical correction in the coastal zone.

a) WET TROPOSPHERIC CORRECTION

For the wet tropospheric correction (WTC), the enhanced solution provided by the University of Porto (Fernandes et al., 2015) and (Fernandes and Lázaro, 2016), which is called GNSS-derived Path Delay Plus (GPD+), was used. This solution computes wet path delays based on: 1) WTC from on-board microwave radiometer (MWR) measurements, whenever they exist and are valid; 2) new WTC values estimated through space-time objective analysis of all available data sources, such as the on-board MWR, water vapour products derived from a set of 17 scanning imaging radiometers (SI-MWR) and tropospheric delays derived from GNSS coastal and island stations. Tropospheric delays derived from 19 GNSS coastal stations in the German Bight have been included in the GPD+ processing (see red dots in Figure 4.1). Due to the fact that the region of interest has relatively low WTC variability, the GPD+ solution and the default CryoSat-2 wet tropospheric correction (ECMWF Model) are very close to each other (stdd, standard deviation of difference, is around 7 mm in the coastal zone) and hence GPD+ brings a very limited added-value for this specific test region (see Figure 4.2 a color-coded density plot of the difference between GPD+ solution and ECMWF solution in the coastal zone). This is also an indicator that, in this region, the WTC errors may be considered negligible when compared to other error sources analysed in this paper.

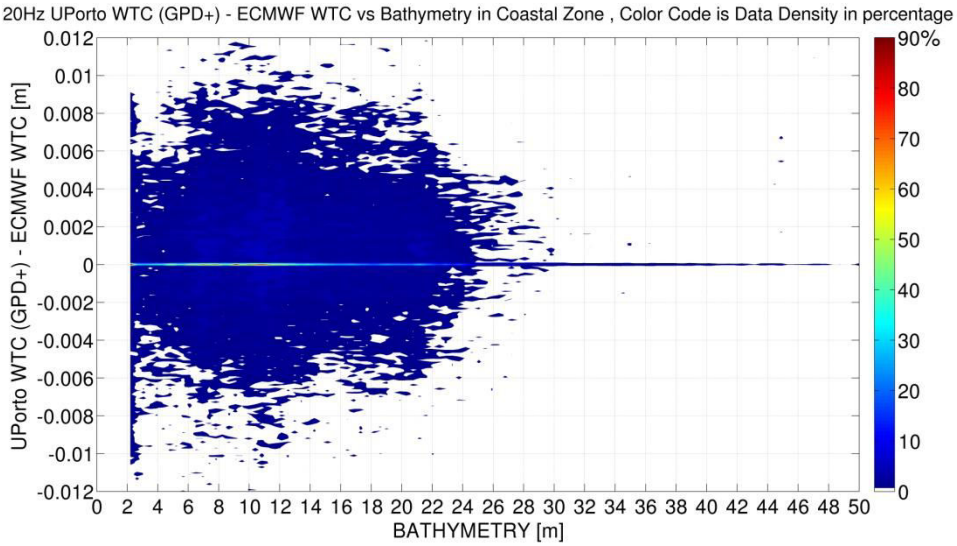

Figure 4.2: Difference between GPD+ and ECMWF wet tropospheric correction (meters) versus bathymetry in the coastal zone; color code is data density in percentage

b) OCEAN EQUILIBRIUM TIDE MODEL

Since the default CryoSat-2 ocean tide correction, i.e. FES 2004 (Lyard et al., 2006), is relatively outdated and hence is expected to perform poorly in the coastal zone (especially in a challenging and dynamic area such as the Wadden Sea), the ocean equilibrium tide correction solution developed in 2014 by OSU TPXO8-ATLAS model (Egbert and Erofeeva, 2002) was selected instead. This solution, available at http:volkov.oce.orst.edu/tides/tpxo8_atlas.html, is a model that combines, in a data fusion approach, a global solution (TPXO8) and local regional high resolution solutions (Egbert et al., 2010). A high-resolution bathymetry model at 2 arcminutes (approx. 3 km) resolution was retrieved from the same source.

Figure 4.3 illustrates the difference (in a colour-coded data density plot) between the TPXO8-ATLAS solution and the default CryoSat-2 equilibrium ocean tide versus the bathymetry in the coastal region. One can observe that the differences between the two tide models are quite significant in a shallow bathymetry scenario (differences can be up to 1 meter), while in deeper bathymetry scenario (bathymetry > 50 m) the differences are relatively minor (stdd is around 2.5 cm). The global stdd between the two tide solutions in the coastal zone is around 15 cm.

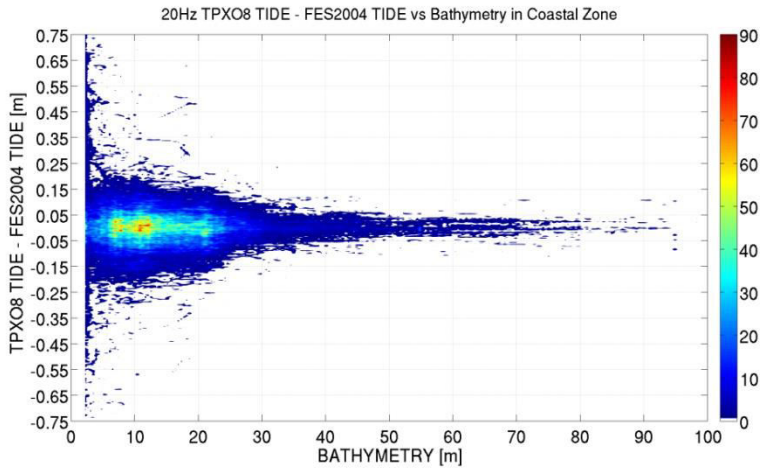

Figure 4.3: Difference between the TPXO8-ATLAS and the FES04 tidal models (meters) versus bathymetry in the coastal zone; color code is data density in percentage

c) SEA STATE BIAS

The sea state bias (SSB) solution used is, in first approximation, a correction equal to -4.7 % of 1 Hz SWH both for the SAR and PLRM datasets. When the SWH is not available (i.e. screened out by the outlier detection criteria), the SSB was set to zero.
The number -4.7 % was found computing the linear slope of the difference between SAR dynamic ocean topography and BSH model ocean dynamic topography plotted versus DWD model SWH. The assumption is that the BSH dynamic ocean topography is not affected by sea state bias errors but the sea state bias is intrinsic to radar altimetry.
I empathize that the solution -4.7% of SWH is a local solution which may not be valid on a global scale.

d) APPLICATION OF THE GEOPHYSICAL AND RANGE CORRECTIONS

As a preamble, the terminology used for deriving sea level data from altimetry is recalled, see also Fenoglio-Marc et al., (2015).
The Sea Surface Height (SSH) is the altimetric height above the adopted reference ellipsoid corrected for all instrumental, range and geophysical corrections, before removing the mean sea surface (Eq. 4.1). The Sea Level Anomaly (SLA) above the mean sea level is computed from SSH by subtracting the reference mean sea surface (MSS) (Eq. 4.2). When the geoid is used instead of the mean sea surface, the resulting quantity is referred to as the dynamic ocean topography (DOT, Eq. 4.3).
The instantaneous SSH (SSHi) is the altimetric SSH corrected for all corrections except for the dynamic atmospheric correction and the ocean tide. Furthermore, SSHi is corrected only for the 46.8% of the pole tide as the remaining part (53.2%) corresponds to the ocean part of the pole tide (Eq. 4.4). SSHi corresponds to the sea level measured by the tide gauge stations. The instantaneous Sea Level Anomaly (SLAi) is computed from SSHi by subtracting the MSS. When the geoid is used instead of the MSS, the resulting quantity is the instantaneous dynamic ocean topography (DOTi). This occurs for example in section 4.1.3.1 when the geoid EIGEN-6C4 is used instead of the MSS. When the SLAi is corrected for the ocean tide, it is indicated as SLAio.
The above defined quantities are given by the following equations:

$$SSH = h - R - dry\_tropo - wet\_tropo - equi\_tide - load\_tide - longperiod\_tide - iono\_delay - dac - solidearth\_tide - pole\_tide - ssb \quad (4.1)$$

$$SLA = SSH - MSS \quad (4.2)$$

$$DOT = SSH - geoid \quad (4.3)$$

$$SSHi = h - R - dry\_tropo - wet\_trop - load\_tide - iono\_delay - solidearth\_tide - 0.468 \cdot pole\_tide - ssb \quad (4.4)$$

$$DOTi = SSHi - geoid \quad (4.5)$$

$$SLAi = SSHi - MSS \quad (4.6)$$

$$SLAio = SSHi - MSS - equi\_tide \quad (4.7)$$

where h is the satellite altitude retrieved from the orbit ephemeris, R is the radar range after the waveform retracking (corrected only for the instrument internal path delay and Doppler range shift), dry_tropo is the dry tropospheric correction, wet_tropo is the wet tropospheric correction, equi_tide is the ocean equilibrium tide, load_tide is the ocean loading tide, longperiod_tide is the ocean long period equilibrium tide,

iono_delay is the ionospheric path delay (JPL GIM model here, Iijima et al., 1999), solidearth_tide is the solid earth tide, pole_tide is the geocentric polar tide, ssb is the sea state bias, dac is the dynamic atmospheric correction (MOG2D here, Carrère and Lyard, 2003), MSS is the DTU15 mean sea surface and geoid is the EIGEN-6C4 geoid.

4.1.2 OPEN OCEAN RESULTS

In this section, I present the results that have been obtained by the SAMOSA+ retracker in open ocean versus the results produced by the TALES PLRM retracker (Buchhaupt et al., 2018) and the numerical ocean circulation/wave models. The validation against the tide gauges and buoys in the open ocean will be treated in section 4.1.3.1 along with the one in coastal zone since it has been used in section 4.1.3.1 and in (Dinardo et al., 2018) to prove the seamless continuity between the open ocean and the coastal zone results. Anyhow, I present in this regard an independent result from (Bonnefond et al., 2018) which has used SAMOSA+ data over the Ajaccio and Senetosa in situ stations.

4.1.2.1 CROSS-VALIDATION BETWEEN SAR, TALES PLRM AND MODEL DATA

a) SLA , SWH AND U10 PRECISION CURVE

I refer to a precision plot (or noise plot) as the plot of the 1 Hz random noise of a geophysical measurement versus the SWH. In order to measure the 1 Hz random noise of a geophysical measurement, the standard deviation of the 20 geophysical measurements at 20 Hz was computed after having detrended them. This amount is then scaled by $\sqrt{20}$ in order to report the noise to a temporal scale of 1 Hz.
The precision plots for the quantities SSH (uncorrected), SWH, U10 and Sigma0 are reported in Figure 4.4:

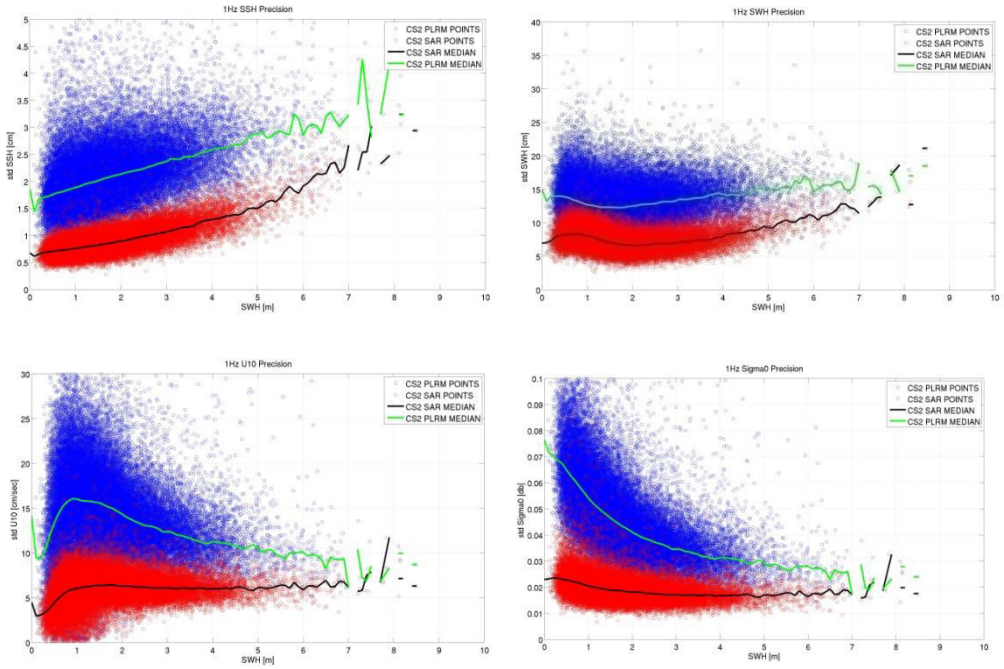

Figure 4.4: Precision plot for SSH (uncorrected), SWH, U10 and Sigma0

From all the above plots, one can conclude that SAR SSH, SWH, U10 and Sigma0 measurements are more precise than the corresponding measurement in PLRM mode. Usually, it is observed an improvement factor of two, as also reported by (Fenoglio-Marc et al., 2015).

b) SLA , SWH AND U10 SCATTER AND DISTRIBUTION

In this section, the consistency between SAR, PLRM (TALES) and ocean model data in the open ocean is analysed via scatter plots and histograms. The quantities considered are SLA, SWH and U10.
The scatter plot between PLRM and SAR SLA data in Figure 4.5 shows the consistency between SAR and PLRM measurements. Median, standard deviation of the differences (stdd) and regression slope are 1.11 cm, 2.6 cm and 0.980 respectively. Only 1.4% of the points of the whole dataset have been discarded after the data screening phase. Hence, the consistency between SAR SLA and PLRM SLA is excellent with a STDD which is much better than the one found in (Fenoglio et al., 2015) (5.8 cm). Still SAR SLA and SAR PLRM exhibit a bias of +1 cm whose origin is presently unknown but that surely does not arise from the range or geo-corrections or mean sea surface, being them identical on both sides.

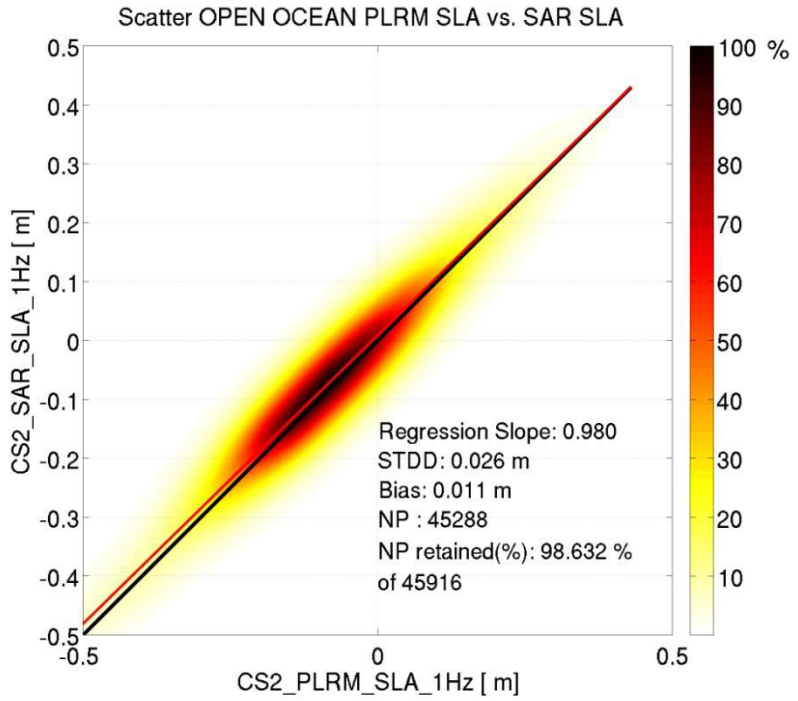

Figure 4.5: Scatter Plot in the open ocean between SAR SLA and PLRM SLA. Color scale gives data density. NP is the number of points.

Also, the DOTi scatterplots in Figure 4.6 versus a third party dataset as the BSH model show again that SAR DOTi and PLRM DOTi exhibit very similar statistics and performance with respect to the model. The SAR STDD (0.129 m) is very slightly better than the PLRM STDD (0.134 m).

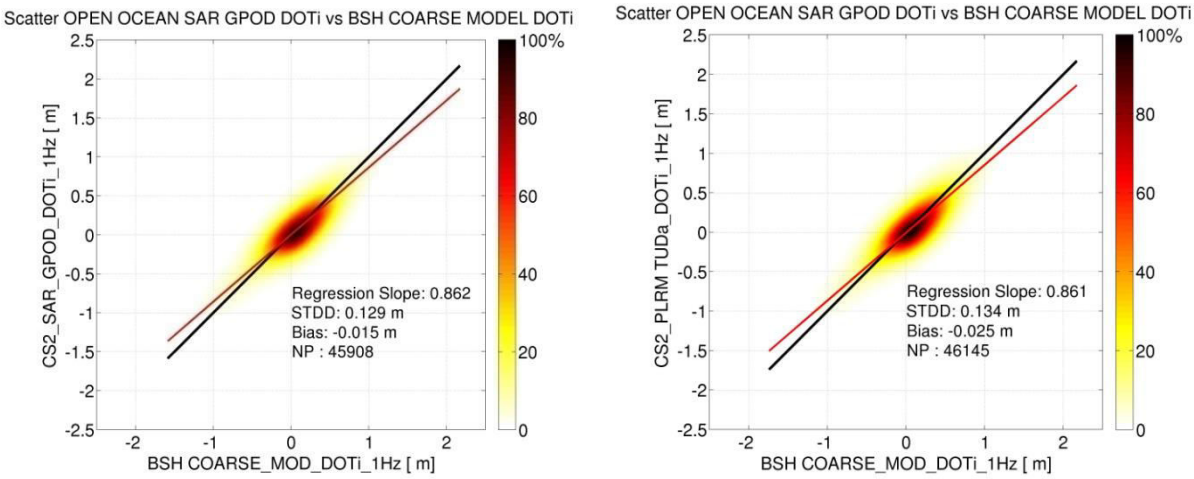

Figure 4.6: Scatter Plot in the open ocean between SAR SLA versus BSH SLA (left) and PLRM SLA versus SLA BSH . Color scale gives data density. NP is the number of points.

Also from the DOTi histogram for SAR, PLRM and BSH model depicted in Figure 4.7, the data distribution looks to be very well consistent between the three datasets.

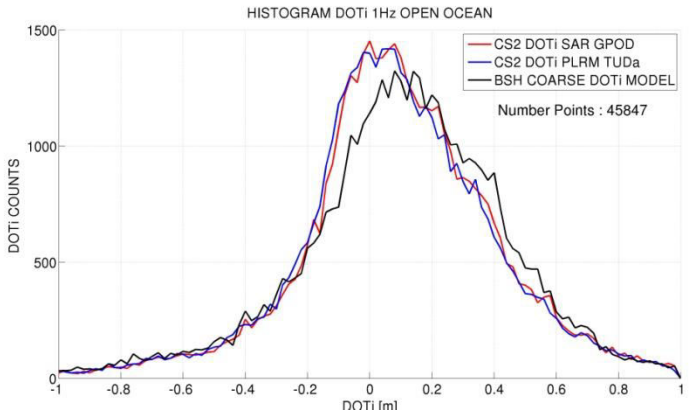

Figure 4.7 : Histogram of SAR DOTi, PLRM DOTi and BSH DOTi in the open ocean

Passing to the validation of SWH, the scatterplot between SAR SWH and PLRM SWH has been produced in Figure 4.8 to validate SAR SWH versus PLRM SWH. In this case, a bias of 6 cm is observed between SAR SWH and PLRM SWH. The source of this bias can be linked to the range walk effect, as reported by (Scagliola et al., 2018) which has reported an expected bias of 5 cm. The STTD between SAR and PLRM (17.5 cm) is also much better than the one found in Fenoglio-Marc et al., 2015 (24 cm). The regression slope is 4% higher than the unity which means SAR SWH tends to overestimate high wave heights with respect PLRM. The number of retained point after data screening is again very high (99.96 %)

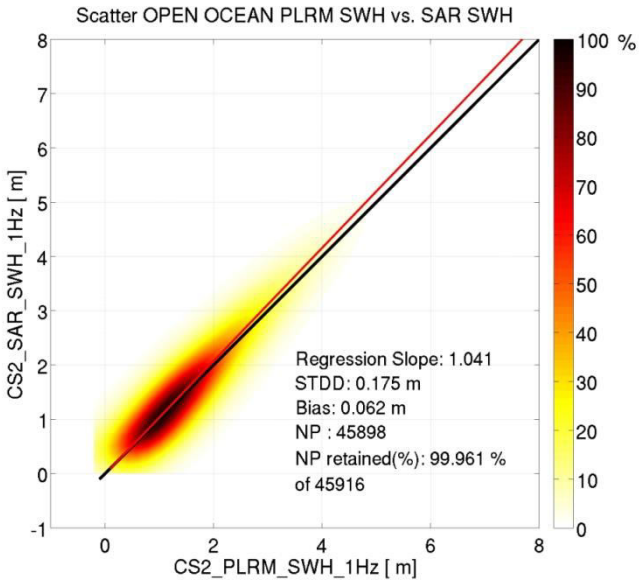

Figure 4.8: Scatter Plot in the open ocean between SAR SWH versus PLRM SWH. Color scale gives data density. NP is the number of points.

Again a useful exercise is the cross-comparison of the altimeter wave height versus a numerical wave model. In Figure 4.9, the scatterplots of SAR SWH and PLRM SWH versus ECMWF models are shown: the two datasets SAR and PLRM show very similar statistics with SAR having a slightly lower STDD but also a slightly higher bias. In Figure 4.10, I have remade the same scatterplot using now the DWD Wave Model.

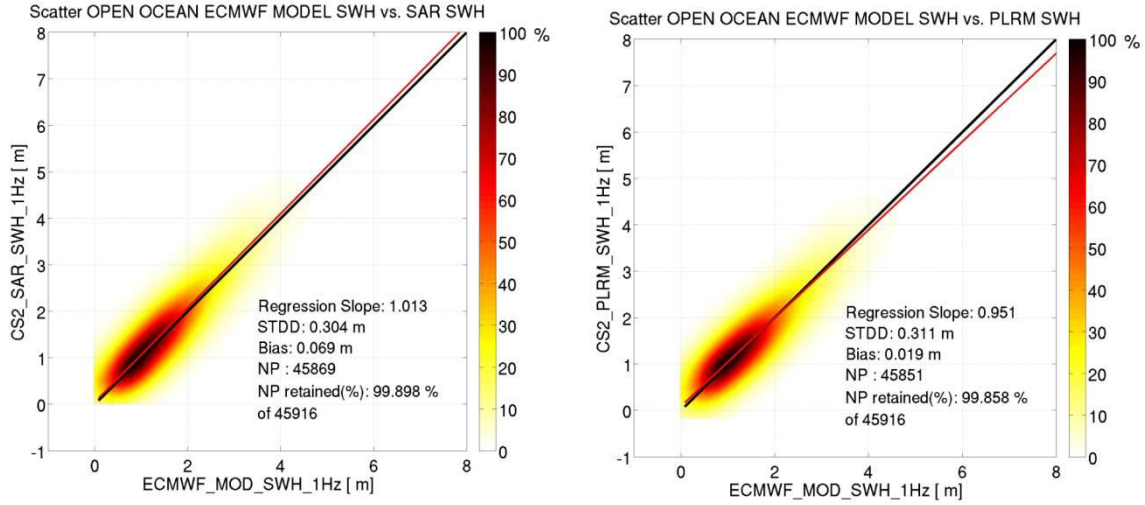

Figure 4.9: Scatter Plot in the open ocean between SAR SWH versus ECMWF SWH (left) and between PLRM SWH and ECMWF SWH (right). Color scale gives data density. NP is the number of points.

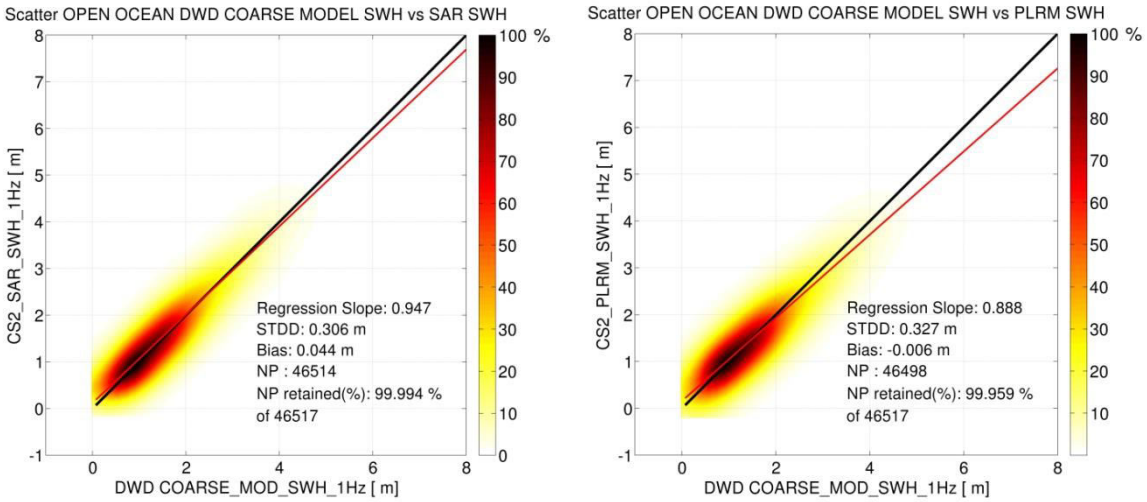

Figure 4.10: Scatter Plot in the open ocean between SAR SWH versus DWD SWH (left) and between PLRM SWH and DWD SWH (right). Color scale gives data density. NP is the number of points.

The statistics of the cross-comparison versus the DWD wave model does not change significantly but again SAR SWH behaves against model slightly better than PLRM. The histograms in Figure 4.11 also show that the cross-comparison between the two altimetry SWH datasets and models is excellent. I only report a slight discrepancy of SAR SWH from PLRM and wave models at very low part of SWH distribution.

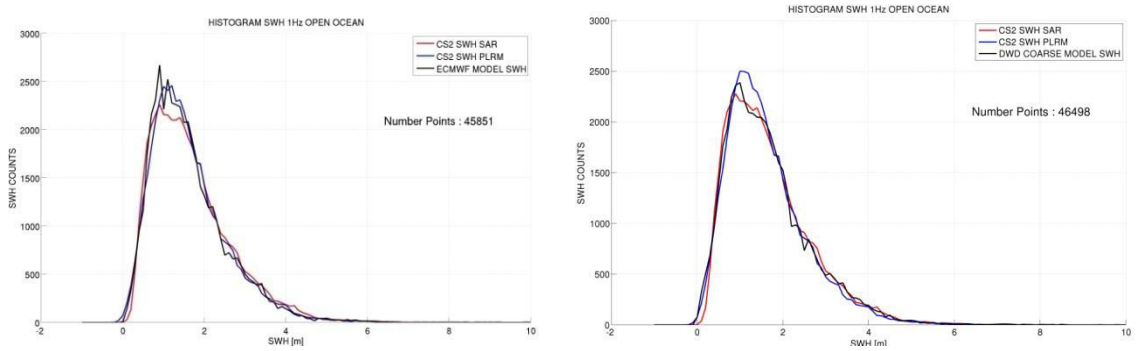

Figure 4.11: Histograms between SAR, PLRM and ECMWF Model (on left) and between SAR, PLRM and DWD Model (on right)

Finally, I validate the altimetry wind speed in the open ocean. Also for the wind speed, the consistency between SAR and PLRM, as shown by the scatterplot in Figure 4.12, is excellent: the STDD between SAR U10 and PLRM U10 is only 26 cm/sec (once again better than the one reported in Fenoglio-Marc et al., 2015) and there is no significant bias with the regression slope basically equal to unity.

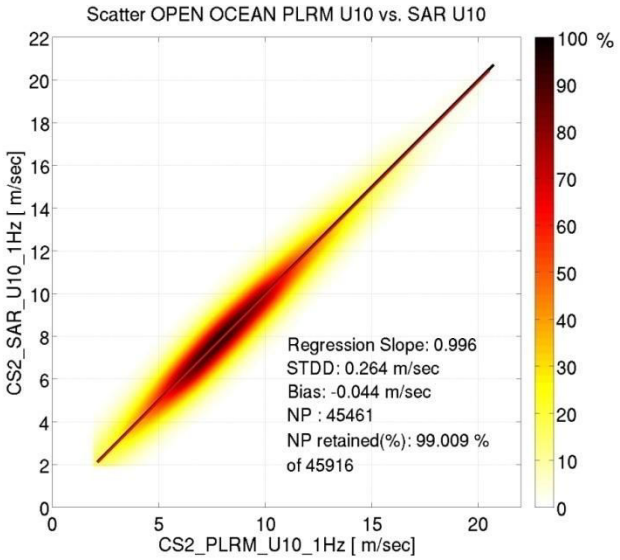

Figure 4.12: Scatterplot between SAR wind speed and PLRM wind speed in the open ocean

The behaviour of the altimetry wind speed with respect the ECMWF model is also very good as displayed in Figure 4.13.

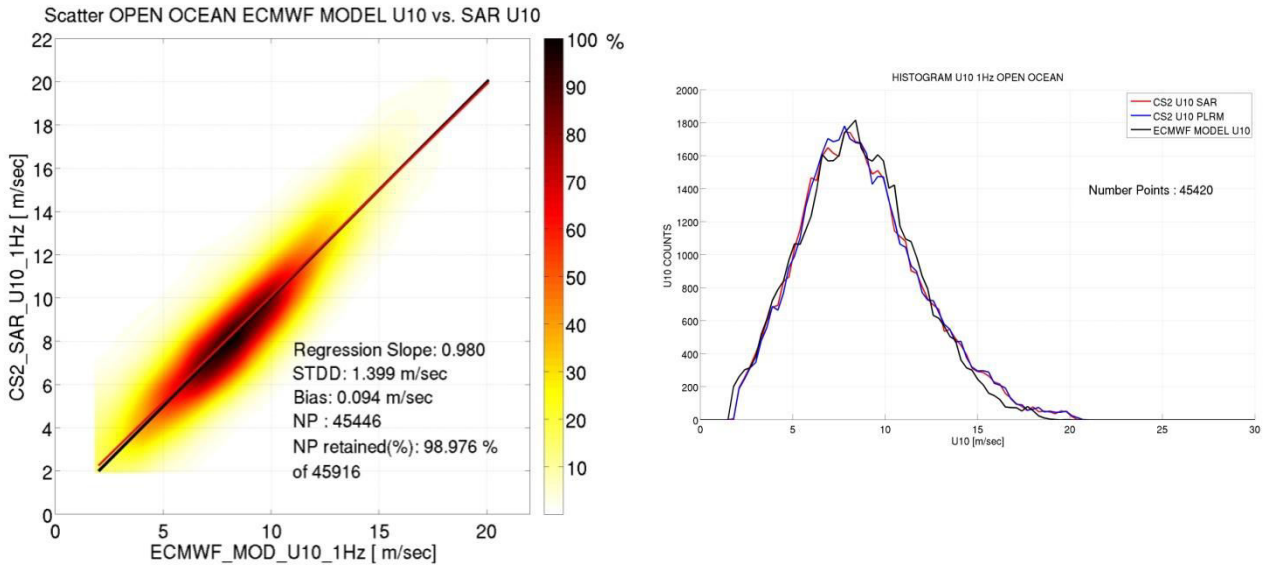

Figure 4.13: Scatterplot between SAR wind speed and ECMWF wind speed in the open ocean (left) and Histogram of the SAR, PLRM and ECMWF wind speed

All the statistics of the cross-comparison between the SAR marine geophysical quantities versus the ones from the reference datasets (PLRM, ocean circulation model and wave model) are reported in Table 4.1 and Table 4.2.

Measurement in open ocean	DOTi				SLA			
Index	median cm	std cm	Slope	N Points	median cm	std cm	Slope	N Points
PLRM	8.9	34.1	-	46145	0.1	15.0	-	46145
SAR	10.0	33.0	-	45908	1.1	15.0	-	45908
BSH Model	13.2	37.0	-	46516	3.9	17.4	-	45908
SAR-PLRM	1.1	2.6	0.99	45288	1.1	2.6	0.98	45288
SAR- BSH MODEL	-1.5	12.9	0.86	45908	-1.5	12.9	0.66	45908
PLRM-BSH MODEL	-2.5	13.4	0.86	46145	-2.1	13.3	0.55	46145

Table 4.1: Statistics for SAR, PLRM, BSH Model DOTi and SLA

Measurement in open ocean	SWH				U10			
Index	median cm	std cm	Slope	N Points	median cm/sec	std cm/sec	Slope	N Points
PLRM	148.0	92.2	-	46485	859.0	333.0	-	46485
SAR	152.0	97.0	-	46516	859.0	331.0	-	46516
ECMWF Model	147.0	92.0	-	46121	854.0	308.0	-	46121
SAR-PLRM	6.2	17.5	1.04	45916	-4.4	26.4	0.99	45916
SAR- ECMWF MODEL	6.9	30.4	1.01	45916	9.4	139.9	0.98	45916
PLRM-ECMWF MODEL	-4.0	32.0	0.88	45916	13.0	141.0	1.03	45916

Table 4.2: Statistics for SAR, PLRM, ECMWF Model SWH and U10

c) DEPENDENCY PLOTS

I refer to a dependency plot as a plot of the difference between a geophysical measurement and a reference versus a state variable. State variable can be SWH (i.e. sea state), mispointing (attitude state), and altitude rate (orbital state). Against all these state variables it is preferable the geophysical measurement to have a dependency as flat as possible. In this way, one can assume that the geophysical measurement and the reference have the same functional dependency from the state variables.

Assumed as reference the PLRM SLA, the dependency plots for the quantity SAR SLA versus the state variables SWH, mispointing and altitude rate are shown in Figure 4.14:

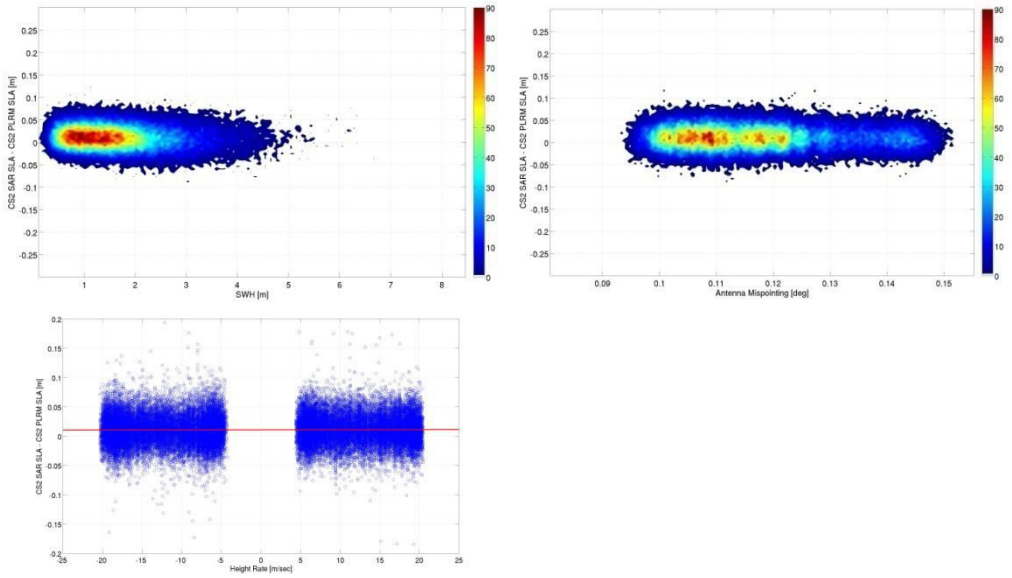

Figure 4.14: Dependency plot of SAR SLA versus SWH, mispointing and altitude rate with PLRM SLA as reference

Being all three dependency plots flat and well centred around zero, it can be concluded that there is no major dependency between SAR and PLRM SLA versus the three state variables.
Again, assumed as reference the PLRM SWH, the dependency plots for the quantity SAR SWH versus the state variables SWH, mispointing and altitude rate are depicted in Figure 4.15:

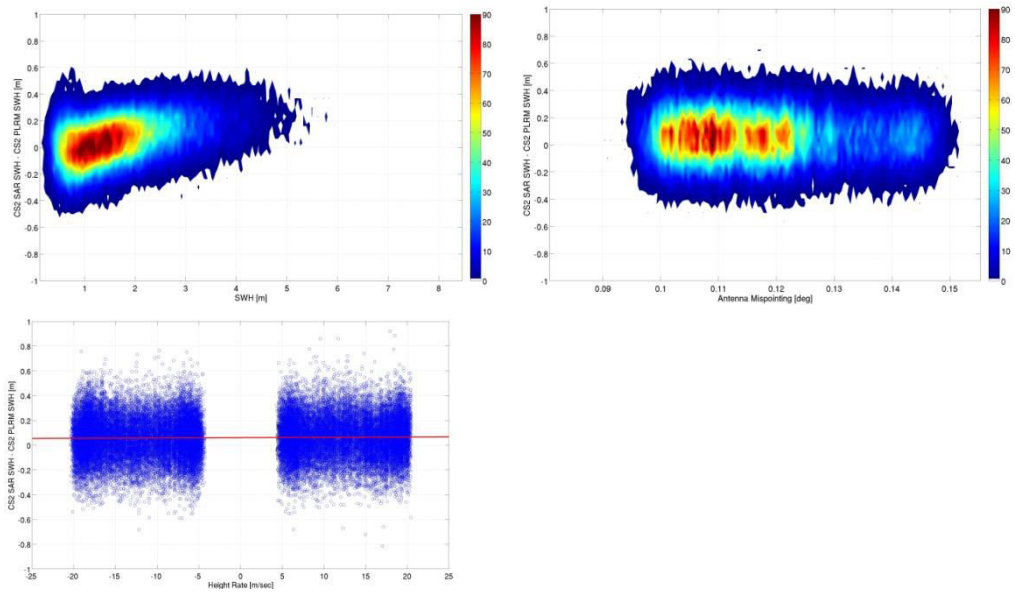

Figure 4.15: Dependency plot of SAR SWH versus SWH, mispointing and altitude rate with PLRM SWH as reference

In this case, whereas there is no dependency between mispointing and altitude rate, there is a clear linear dependency of SAR SWH versus the sea state (SWH) with respect PLRM SWH. This behaviour has been reported by other experts (Raynal et al., 2018) and it will require a further study to be understood.
Finally, assumed PLRM sigma nought as reference, the dependency plots for the quantity SAR Sigma0 versus the state variables sea state (SWH), mispointing and altitude rate are depicted in Figure 4.16:

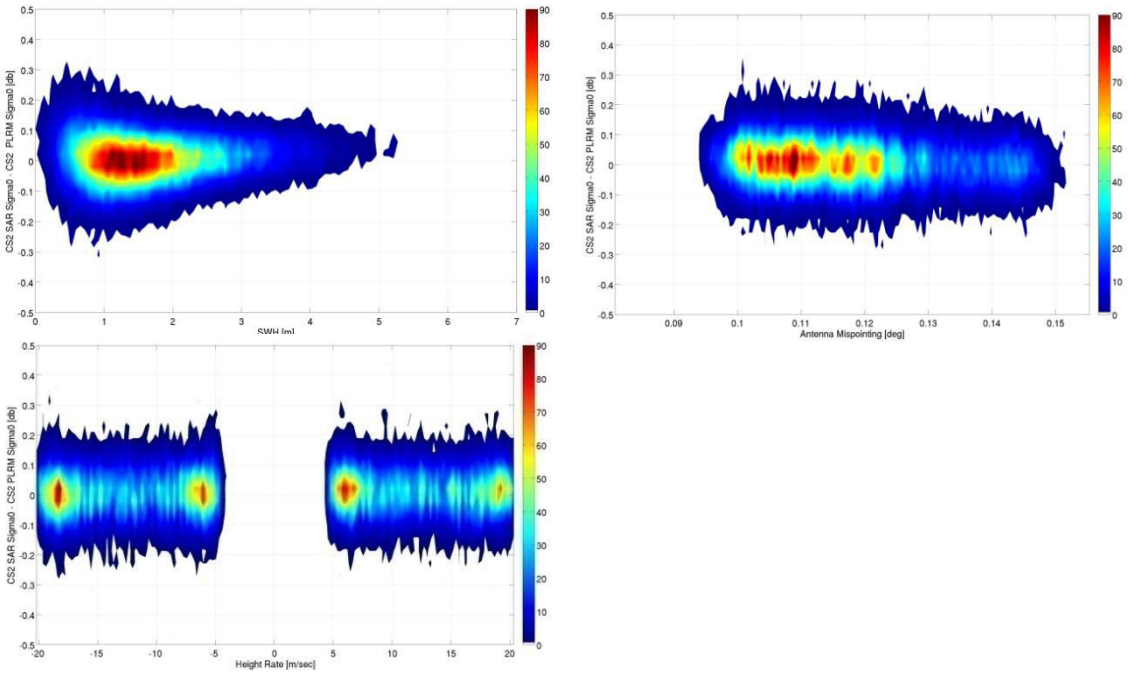

Figure 4.16: Dependency plot of SAR Sigma0 versus SWH, mispointing and, altitude rate with PLRM Sigma0 as reference

Also in this case as for the SLA case, being all three dependency plots flat and well centred around zero, it can be concluded that there is no major dependency between SAR and PLRM SLA versus the three state variables.

d) IN SITU VALIDATION

(Bonnefond et al., 2018) has reported a standard deviation of only 1.5 cm for the SSH retracked by the SAMOSA+ retracker, averaging together the results from Ajaccio and Senetosa in situ stations for the CryoSat-2 pass #4794. In case of SAMOSA2 retracker (i.e. the SAMOSA-based open ocean retracker) the standard deviation was slightly higher, though still excellent (1.7 cm).

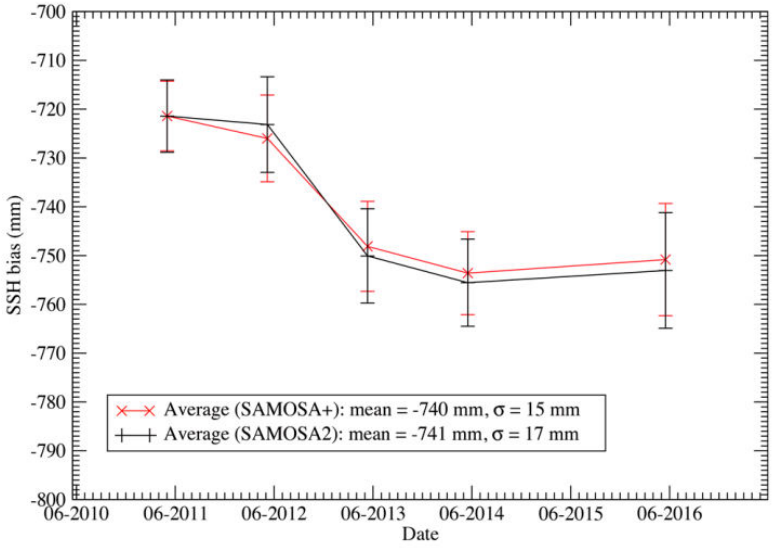

Figure 4.17: Standard deviation of SAMOSA+ and SAMOSA2 SSH, averaging together the results at Ajaccio and Senetosa for the CryoSat-2 Pass #4794, from (Bonnefond et al., 2018)

4.1.3 COASTAL ZONE RESULTS

In this section, I present the results that have been obtained by the SAMOSA+ retracker in the coastal zone versus the results produced by the TALES PLRM retracker (Buchhaupt et al., 2018) and the numerical ocean circulation/wave models. The validation against the tide gauges and buoys is carried out both in the coastal zone and in the open ocean in order to prove the seamless continuity between the open ocean and the coastal zone results.
The coastal zone is defined here as the band of 0-10 km from the coast.

4.1.3.1 IN SITU VALIDATION

a) VALIDATION OF SLAio

The validation metrics used in coastal zone for the cross-comparison of altimetric and in situ data includes the following three parameters: regression slope, correlation and standard deviation of the differences (stdd) between in situ and 1-Hz altimetric measurements. I perform also the comparison in open-ocean to analyse the data degradation when passing from open-ocean to coastal zone conditions. PLRM data have been retracked both with the SINC2 and TALES retrackers in order to analyse how the two retrackers behave.
For a given in situ station, the lag in time between in situ and altimeter data is selected to be less than 30 minutes. I further select, for each satellite track, the altimeter measurement nearest in space to that station which is, for the validation in the coastal zone:

- between 0 kilometres and 10 kilometres from the tide gauge
- below 10 kilometres from the coast

and for the validation in open ocean:

- between 10 kilometres and 20 kilometres from the tide gauge
- more 10 kilometres away from the coast.

The fiducial tide gauges locations are shown in Figure 4.1: they are Helgoland station (HELG), Koserow station (KOSE), Leuchtturm Alte Weser station (LHAW), Sassnitz station (SASS) and Warnemünde station (WARN). The first two are located in the German Bight; the latter three are in the Western Baltic Sea. Tide gauge sea level records are available between January 2010 and July 2015 with a temporal sampling of one minute.
In making the cross-validation of altimetry versus tide gauge, I have removed the mean sea surface along the CryoSat-2 passes using the DTU15 mean sea surface model. This is a necessary operation because CryoSat-2 is a satellite with a long repeat cycle (369 days) and hence different relative passes in the same repeat cycle sample differently the mean sea surface (see Fenoglio, 2015 and Cancet et al., 2013). I have also removed the tidal dynamics between the tide gauge and CryoSat-2 passes using the TPXO8-ATLAS tide model because it is expected the tide to vary between tide gauge position and CryoSat-2 pass, being the region of interest a high dynamic tidal area.
Hence, the altimetric quantity that I have used in the tide gauge cross-comparison is the SLAio (Eq. 4.7), i.e. SLAi corrected for the TPXO8-ATLAS ocean tide. Since the purpose of this study is not the estimation of the CryoSat-2 absolute range bias, I do not carry out an absolute validation between CryoSat-2 altimeter and tide gauges heights using GNSS data which the tide gauges are equipped with, but simply I have removed the mean of tide gauge elevation measurements from the in situ data.
Finally, few sparse PLRM outlier points whose SLAio was bigger than 2 m have been removed.

In Figure 4.18, I show respectively the scatter plots between the SAR, PLRM and Tide Gauge elevations in the coastal zone at the five selected stations while in Table 4.3 and Table 4.4 I summarize the corresponding statistics from the in situ cross-comparison in terms of stdd, correlation and slope respectively in the coastal zone and open ocean.

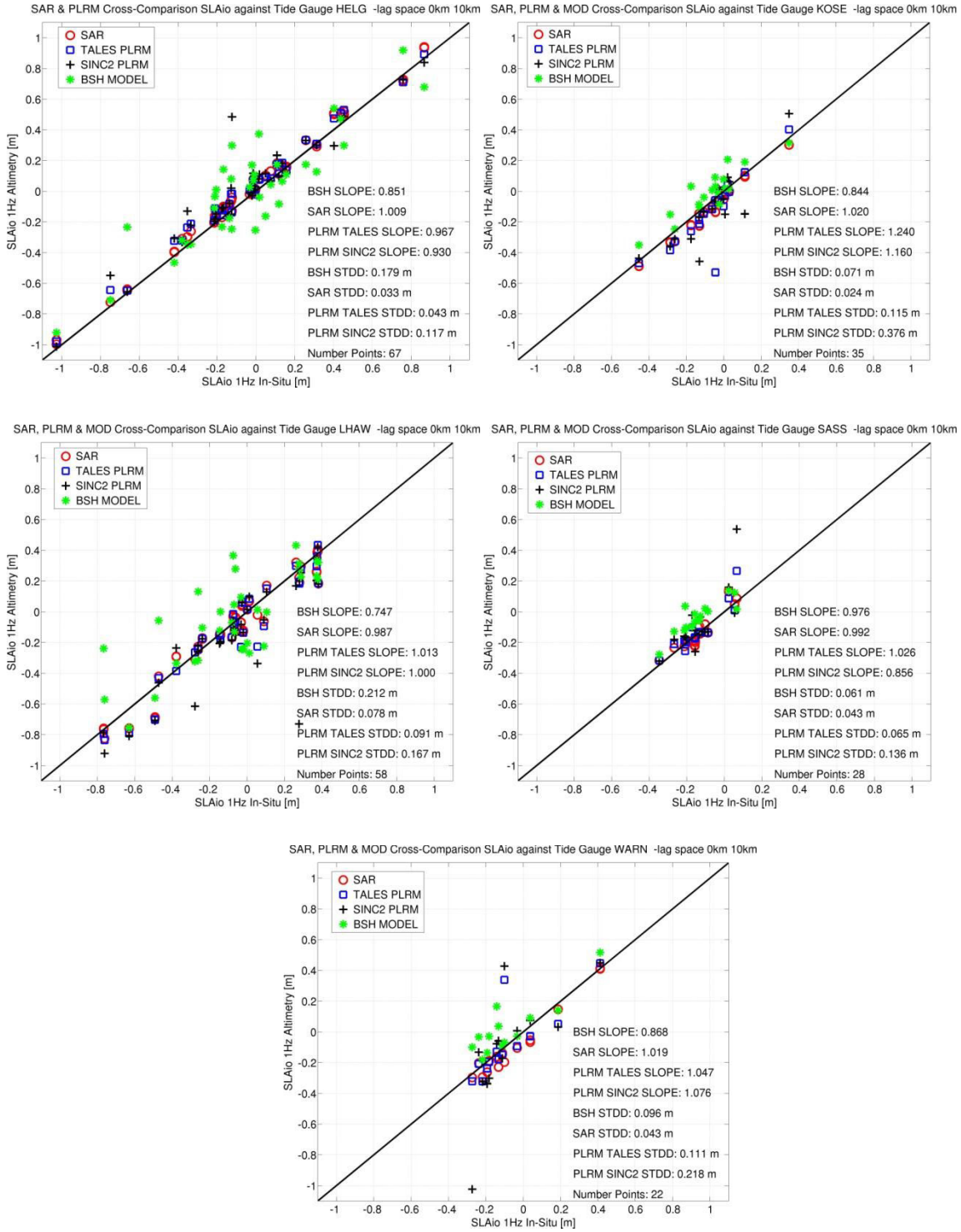

Figure 4.18: Scatter Plot between SAR (red circles), PLRM TALES (blue squares), PLRM SINC2 (black crosses), BSH Model (green diamonds) SLAio and Tide Gauge SLAio in the coastal zone (0-10 km from the coast) at Helgoland station (top left), Kose station (top right), Leuchtturm Alte Weser station (middle left), Sassnitz station (middle right) and Warnemünde station (bottom left). The distance between station and altimeter is smaller than 10 kilometres

COASTAL ZONE	PLRM TALES			PLRM SINC2			SAR			BSH			
Index	stdd cm	slope	Corr	stdd cm	slope	Corr	stdd cm	slope	Corr	stdd cm	slope	Corr	Number of Points
HELG	4.2	0.96	0.96	11.7	0.93	0.86	3.3	1.00	0.97	18.0	0.85	0.75	67
KOSE	11.5	1.24	0.96	37.6	1.16	0.86	2.4	1.02	0.97	7.1	0.84	0.75	35
LHAW	9.1	1.01	0.96	16.7	1.00	0.86	7.8	0.99	0.97	21.2	0.75	0.75	58
SASS	6.5	1.03	0.89	13.6	0.86	0.78	4.3	0.99	0.95	6.1	0.98	0.85	28
WARN	11.1	1.05	0.87	21.8	1.07	0.74	4.3	1.02	0.97	9.6	0.87	0.87	22

Table 4.3: Statistics of the SLAio in situ cross-comparison for SAR, PLRM TALES, PLRM SINC2 and BSH Model dataset in the coastal zone (0-10 km). The distance from the station is between 0 and 10 kilometres.

OPEN OCEAN	PLRM TALES			PLRM SINC2			SAR			BSH			
Index	stdd cm	slope	Corr	stdd cm	slope	Corr	stdd cm	slope	Corr	stdd cm	slope	Corr	Number of Points
HELG	5.3	1.00	0.98	6.9	1.01	0.98	4.7	1.00	0.99	17.2	0.87	0.85	91
KOSE	3.7	0.95	0.97	3.1	0.94	0.98	2.5	0.96	0.99	7.5	1.00	0.90	65
LHAW	7.4	0.94	0.98	10.9	0.94	0.96	6.7	0.94	0.98	19.7	0.81	0.86	83
SASS	4.5	0.97	0.97	5.0	0.94	0.97	3.6	0.91	0.98	8.3	0.83	0.90	43
WARN	3.6	0.91	0.98	4.5	0.92	0.97	3.4	0.92	0.98	7.4	0.78	0.94	46

Table 4.4 : Statistics of the SLAio in situ cross-comparison for SAR, PLRM TALES, PLRM SINC2 and BSH Model dataset in open ocean (10-20 km). The distance from the station is between 10 and 20 kilometres.

From Table 4.3 and Table 4.4, the average stdd in open ocean (distance to coast between 10 and 20 km) is 4.1 cm, 4.9 cm, 6.08 cm and 12.02 cm for SAR, PLRM TALES, PLRM SINC2 and BSH model respectively, while in the coastal zone (distance to coast between 0 and 10 km) the average stdd is 4.4 cm, 8.4 cm, 20.3 cm and 12.4 cm for SAR, PLRM TALES, PLRM SINC2 and BSH model respectively.

One can notice that the stdd in open ocean with respect to the Baltic stations (KOSE, SASS, WARN) are generally lower than the stdd of the German Bight stations (HELG and LHAW): this is attributable to higher

residual errors in tide modelling (TPXO8-ATLAS) at the German Bight stations whereas for the Baltic stations, the tidal amplitudes being smaller, these errors are less impacting.
One can also notice that the number of points decreases when passing from open ocean to coastal zone conditions. This is due to the fact that, in order to build a 1 Hz measurement, at least 6 water (i.e. distance to coast > 0 m) 20 Hz measurements are necessary and this can be not always the case because the 1 Hz segment (7 km) can be partially or almost totally over land in case the distance to coast is very close to zero.
As to the regression slope, in open ocean the average slope is 0.94, 0.95 and 0.95 for SAR, for PLRM TALES and for PLRM SINC2 respectively; while in the coastal zone, the average slope is 1.00, 1.05 and 1.00 for SAR, for PLRM TALES and for PLRM SINC2 respectively. The BSH average slope is lower than altimetry with value of 0.85 in open ocean and 0.8 in the coastal zone.
Hence, from this cross-comparison against tide gauges, I conclude that SAR gives the best performance in the coastal zone, having a smaller average stdd (4.4 cm) than PLRM TALES (8.4 cm) and PLRM SINC2 (20.3 cm). Moreover, PLRM TALES is superior to SINC2 in the coastal zone as it exhibits a significantly lower average stdd than SINC2 PLRM; this is confirmed also by the average correlation coefficient in the coastal zone (0.82 for SINC2 PLRM and 0.93 for TALES PLRM while for SAR it is 0.96). The regression slopes are very close to one for all the three altimetry datasets. Similar conclusion is valid for the cross-comparison in open ocean, the average stdd being 4.1 cm, 4.9 cm and 6.08 cm for SAR, TALES and SINC2 respectively, which indicates that TALES outperforms SINC2 also in open ocean.
The cross-comparison of the BSH model elevation with in situ data gives a mean stdd of 12 cm both in the coastal zone and in open ocean and a mean correlation of 0.8 in coastal zone and 0.9 in open ocean. The BSH model results presented in Table 4.3 and Table 4.4 are in line with Dick et al., (2001) who reported a stdd between 7 and 12 cm at the stations WARN, SASS and KOSE. Anyhow, against the fiducial tide gauges, the BSH circulation model behaves worse in the coastal zone than radar altimetry.
Finally, I observe that, in general, the results in open ocean are in agreement with Fenoglio-Marc et al., (2015) but I underline an improvement in the SAR statistics between 10 and 20 kilometres from the coast, with a reduction of the stdd from 7 cm to 4.1 cm at Helgoland, which could arise from the aforesaid removal of the tidal dynamics and the mean sea surface gradient between the CryoSat-2 passes and tide gauge location.

b) VALIDATION OF SWH

The BfG/WSV operates three coastal directional wave rider (DWR) buoys (at Helgoland South, Helgoland Nord and Westerland) and two offshore platforms (named FINO1 and FINO3) equipped with an Acoustic Wave Current Profiler (AWAC). The location of FINO1 and FINO3 is depicted in Figure 4.1. The AWAC time series is available between January 2010 and July 2015 with a temporal sampling of 60 minutes. The DWR time series is available between January 2010 and December 2016 with a temporal sampling of 60 minutes till March 2013 and 30 minutes since March 2013 onwards.
As before, for a given in situ station the time lag between in situ data and 1-Hz altimeter data is selected to be less than 30 minutes. I further select, for each satellite track, the altimeter measurement nearest in space to each in situ station and within a selected interval of distance from the station. For the validation in the coastal zone, this interval is between 0 and 10 kilometres whereas for the validation in open ocean, the interval is between 10 and 20 kilometres.
Due to their offshore location, data from the FINO1 and FINO2 stations are considered only for the open-ocean analysis.
The reason to carry out the in situ analysis also in open ocean is to prove that SAMOSA+ and TALES provide accurate SWH measurements in the coastal zone as well as in open ocean conditions.
Figure 4.19 shows in coastal zone the scatter plots between the SAR, PLRM TALES, DWD model and DWR SWH measurements at Helgoland South (HELG SUD), at Helgoland North (HELG NORD) and at

Westerland (WES), while Table 4.5 summarizes the corresponding statistical results (std, mean, correlation and regression slope) for the same stations.

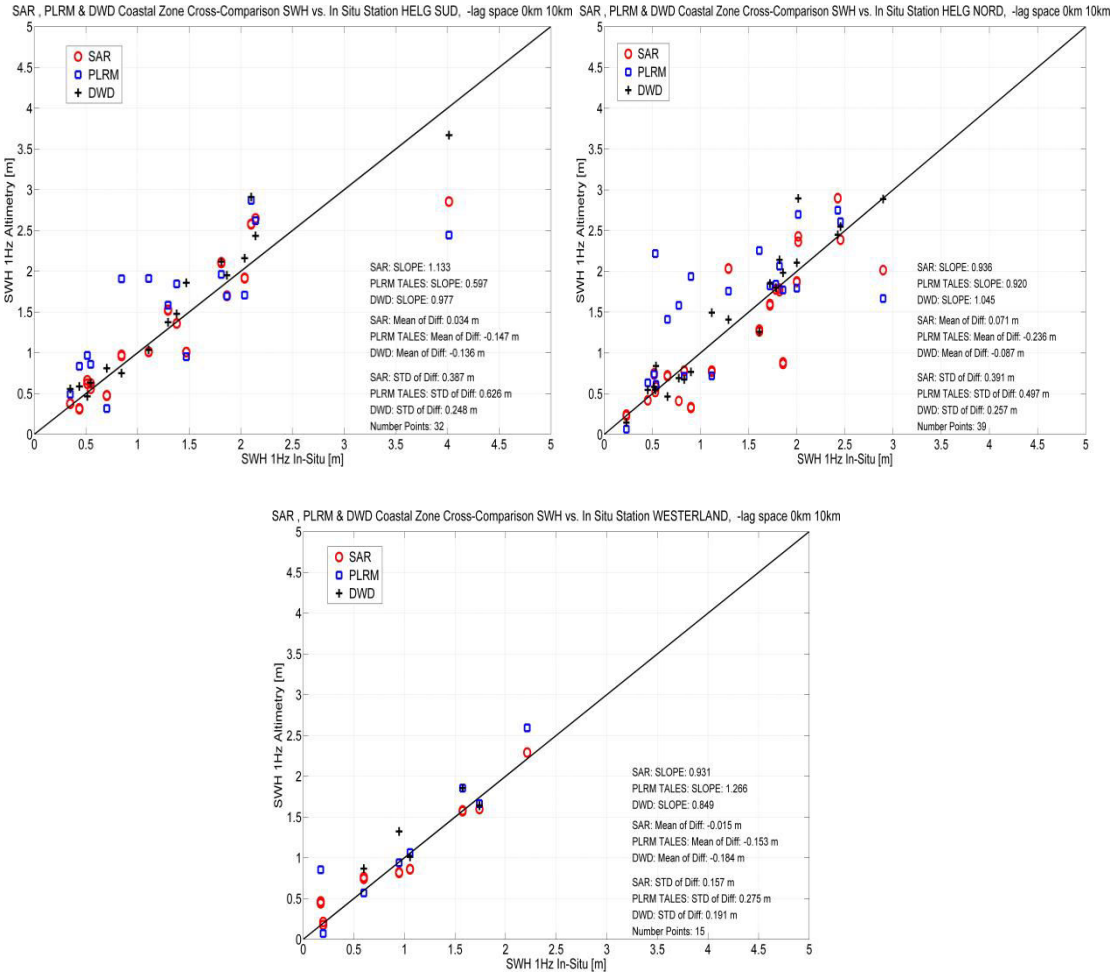

Figure 4.19: Scatter Plot between SAR (red circles), PLRM TALES (blue squares), DWD (black crosses) SWH and DWR SWH in coastal zone (0-10 km) at HELG SUD (top, left) , HELG NORD (top, right) and WES (bottom, left). The distance from the station is between 0 and 10 kilometres.

Measurement	DWD SWH				PLRM SWH				SAR SWH				
Index	**mean cm**	**stdd cm**	**Corr**	**slope**	**mean cm**	**stdd cm**	**Corr**	**slope**	**mean cm**	**stdd cm**	**Corr**	**slope**	**Number of Points**
HELG SUD DWR	-13.6	24.8	0.96	0.98	-14.7	62.6	0.73	0.60	3.4	38.7	0.91	1.13	32
HELG NORD DWR	-8.7	25.7	0.95	1.05	-23.6	49.7	0.78	0.92	7.1	39.1	0.87	0.94	39
WES DWR	18.4	19.1	0.89	0.85	-15.3	27.5	0.98	1.27	-1.5	15.7	0.95	0.93	15

Table 4.5: Statistics of the SWH in situ cross-comparison for SAR, PLRM TALES, DWD datasets in the coastal zone (0-10 km). The distance from the station is between 0 and 10 kilometres.

Figure 4.20 illustrates in open ocean the scatter plots between the SAR, PLRM TALES, DWD model and in situ SWH measurements (AWAC and DWR) at Helgoland South (HELG SUD), at Helgoland North (HELG NORD), at Westerland (WES), at FINO1 and FINO3. The corresponding statistical results (std, mean, correlation and regression slope) are reported in Table 4.6.

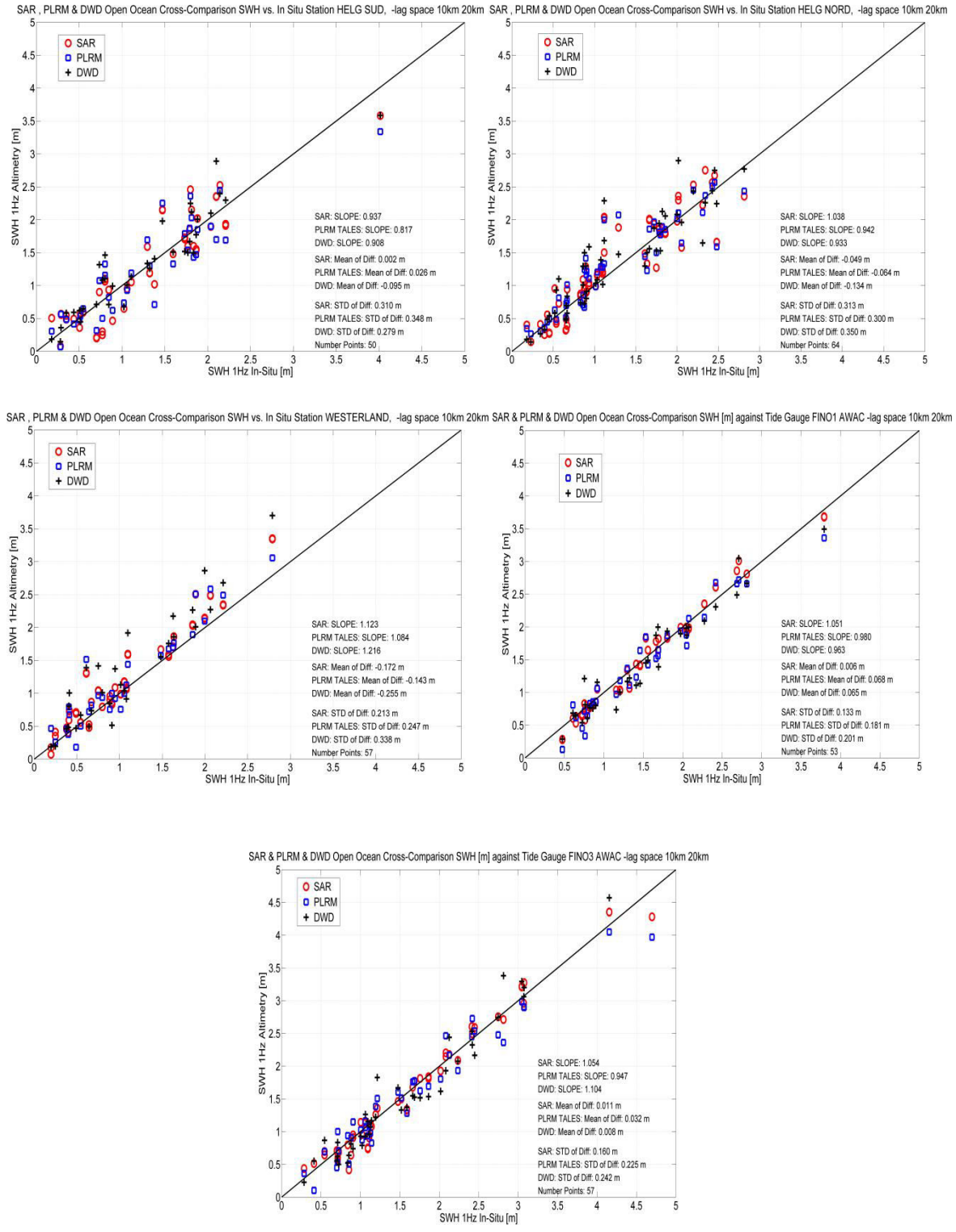

Figure 4.20: Scatter Plot between SAR (red circles), PLRM TALES (blue squares), DWD (black crosses) and in situ SWH in open ocean at HELG SUD (top-right) , HELG NORD (top-left), WES (middle-left), FINO1 (middle-right) and FINO3 (bottom-left). The distance from the station is between 10 and 20 kilometres.

Measurement	DWD SWH				PLRM SWH				SAR SWH				
Index	mean cm	stdd cm	Corr	slope	mean cm	stdd cm	Corr	slope	mean cm	stdd cm	Corr	slope	Number of Points
FINO1 AWAC	6.5	20.1	0.97	0.96	6.8	18.1	0.97	0.98	0.6	13.3	0.98	1.05	53
FINO3 AWAC	0.8	24.2	0.98	1.10	3.2	22.5	0.97	0.95	1.1	16.0	0.99	1.05	57
HELG SUD DWR	-9.5	27.9	0.93	0.91	2.6	34.8	0.88	0.81	0.2	31.0	0.91	0.94	50
HELG NORD DWR	-13.4	35.0	0.87	0.93	-6.4	30.0	0.89	0.94	-4.9	31.3	0.89	1.04	64
WES DWR	-25.5	33.8	0.93	1.21	-14.3	24.7	0.94	1.08	-17.2	21.3	0.96	1.12	57

Table 4.6 : Statistics of the SWH in situ cross-comparison for SAR, PLRM TALES, DWD datasets in open-ocean. The distance from the station is between 10 and 20 kilometres.

From Table 4.5, I compute an average stdd of 31.1 cm for SAR, 46.6 cm for PLRM and 23.2 cm for DWD. From these statistical results, I conclude that SAR outperforms TALES PLRM in the coastal zone, but still the DWD regional model exhibits the lowest stdd with respect to in situ data. Therefore, SWH in SAR mode, notwithstanding representing an advancement against a coastal PLRM SWH solution, still can be subject of further improvement.

Again from Table 4.5 the average regression slopes are 0.91 for SAR, 0.93 for PLRM and 0.96 for DWD: hence the regression slopes are very close to 1 for all the three datasets.

In open-ocean conditions, from Table 4.6, I compute an average stdd of 22.6 cm for SAR, 26.6 cm for PLRM and 28.2 cm for DWD. Hence, in open-ocean conditions, the dataset with the best consistency against in situ data is the SAR.

None of the three datasets exhibits a large bias (-1.3 cm for DWD, -17 cm for PLRM, +3 cm for SAR in the coastal zone and -8.2 cm for DWD, -1.6 cm for PLRM , -4 cm for SAR in open-ocean) with respect to the in situ stations measurements.

Finally, one can observe that the results for SAR SWH in open-ocean are in general agreement with Fenoglio-Marc et al., (2015) who reported values for the average stdd over the FINO1 and FINO3 in situ stations of 14.5 cm in SAR mode (now I obtain against FINO1 and FINO3 an average SAR stdd of 14.6 cm). However, the new results show a significant improvement in the PLRM SWH, being now the PLRM stdd 20.3 cm while in Fenoglio-Marc et al., (2015) it was 32.5 cm; this can be attributable to the new numerical fast convolution waveform model used in TALES. From Table 4.6, it is also evident that the stdd are generally lower for the AWAC stations than for DWR stations (this is an expected outcome since it is known that AWAC stations perform better than DWR buoys).

At FINO1 and FINO3 a drop of the number of points can also be noticed, when passing from open-ocean to coastal zone conditions, due to the averaging performed from 20 Hz to 1 Hz.

4.1.3.2 CROSS-VALIDATION BETWEEN SAR, TALES PLRM AND MODEL DATA

In order to assess quantitatively the benefit of the SAR mode in the coastal zone, the SAR and PLRM TALES datasets have been cross-compared, the results being presented in this section. In sections b), c), and d), the results from the ocean circulation model are used as reference, since these are deemed to be exempt from land contamination errors.

a) DOT GEOGRAPHICAL MAPS

In this subsection, the geographical maps of the DOT in SAR and PLRM modes are shown in order to illustrate how well the SAR altimetry can measure the sea level up to the coastline (see Figure 4.21 and Figure 4.22). I emphasize that the SAR DOT in the coastal zone along the Baltic Sea appears very precise (in the sense that I do not observe along the coast many red points indicating errors higher than 2 meter, notwithstanding the complex coastal morphology) while in the German Bight residual errors still appear in the Wadden Sea, mainly along the Frisian Islands and Danish Islands. That area is characterized by the presence of wetlands, mudflats and sand banks, and hence it is not surprising that altimetry still shows some limitations there. Errors can also arise from residual inaccuracies in ocean tidal modelling (and hence not only from the SAMOSA+ retracking). The progress with respect to conventional altimetry can be better appreciated when the same geographical map (DOT) is plotted for the PLRM case (Figure 4.22) in which larger errors (red points along the coast, indicating errors higher than 2 meters) occur, all located around the coastline.

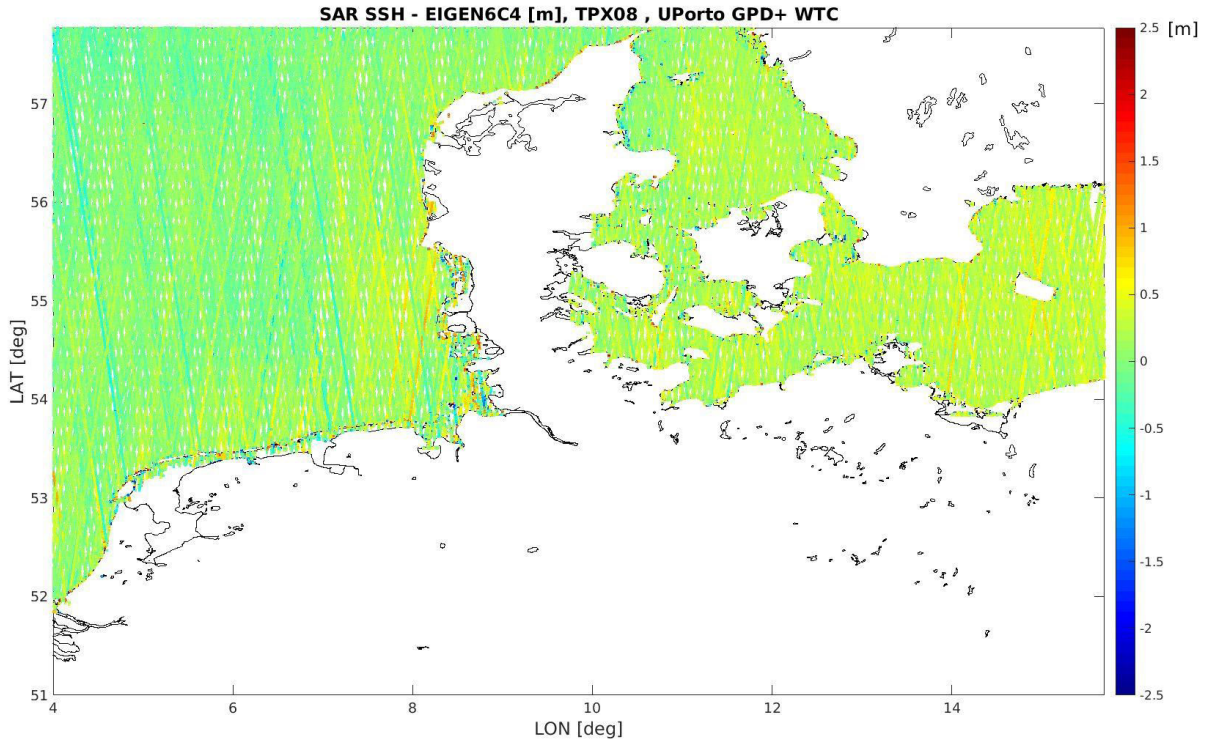

Figure 4.21: Zoom of SAR DOT (SSH minus Geoid) map in the area of interest

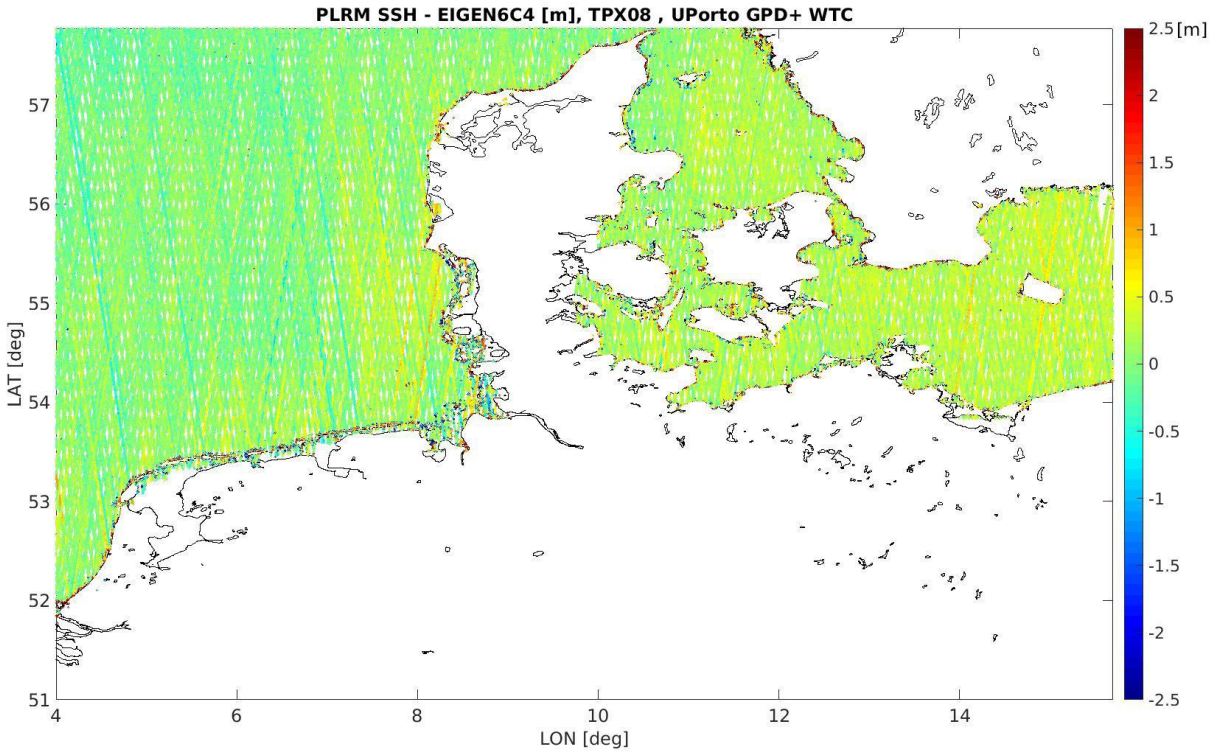

Figure 4.22: Zoom of PLRM DOT (SSH minus Geoid) map in the area of interest

From Figure 4.21 and Figure 4.22, it can be observed that both SAR and PLRM DOT generally increase as one go from the North Sea to the Baltic Sea. This is a known ocean dynamic feature of the area under study (see for instance Ekman and Mäkinen, 1996). The main reason for this is the large difference in salinity between the North Sea and the Baltic, related to river inflow in the Baltic (Schall et al., 2016).

b) RESULTS AS FUNCTION OF DISTANCE TO COAST

In this section, I analyse the three geophysical quantities SLA, SWH and U10 versus the distance to the coast. Figure 4.23 gives the SLA for SAR and PLRM as cloud of points and as median curve versus the distance to the coast. What can be observed is that the distribution of SLA is less spread in SAR than in PLRM, with 98.3% of the points within ± 1 m in SAR while the corresponding percentage for PLRM is 94.1%. One can also notice that, in SAR mode, the data spread from the mean sea surface (an indicator of land contamination) begins around 0-1 km from the coast in SAR and at around 3-4 km in PLRM. Also in the critical band 0-2 km from the coast, SAR is much less affected by land contamination compared to PLRM, as the median curve in SAR is closer to zero than the corresponding PLRM curve). From Figure 4.23, it is also evident that PLRM exhibits more negative outliers than positive outliers: this could be something related to the low-elevated geometrical morphology of the coastline under study. The reflections from land appear generally placed after the waveform's leading edge rather than before and consequently they will show up in PLRM data as negative outliers.

Figure 4.24 shows the percentage of 20 Hz SLA within ± 1 m versus the distance to coast. At 10 kilometres from coast, SAR and PLRM SLA have the same percentage while this parameter, going towards the coastline, is systematically higher in SAR mode than in PLRM mode. The value of 99% is reached in PLRM mode at five kilometres from the coast and in SAR mode at 3 kilometres. Similarly, the value of 98% is reached at 2 and 3.5 kilometres respectively in SAR and PLRM modes. I remark that in SAR mode, at distances less than 1 kilometre from the coast, 94% of the SLA are still in the range ±1 meter.

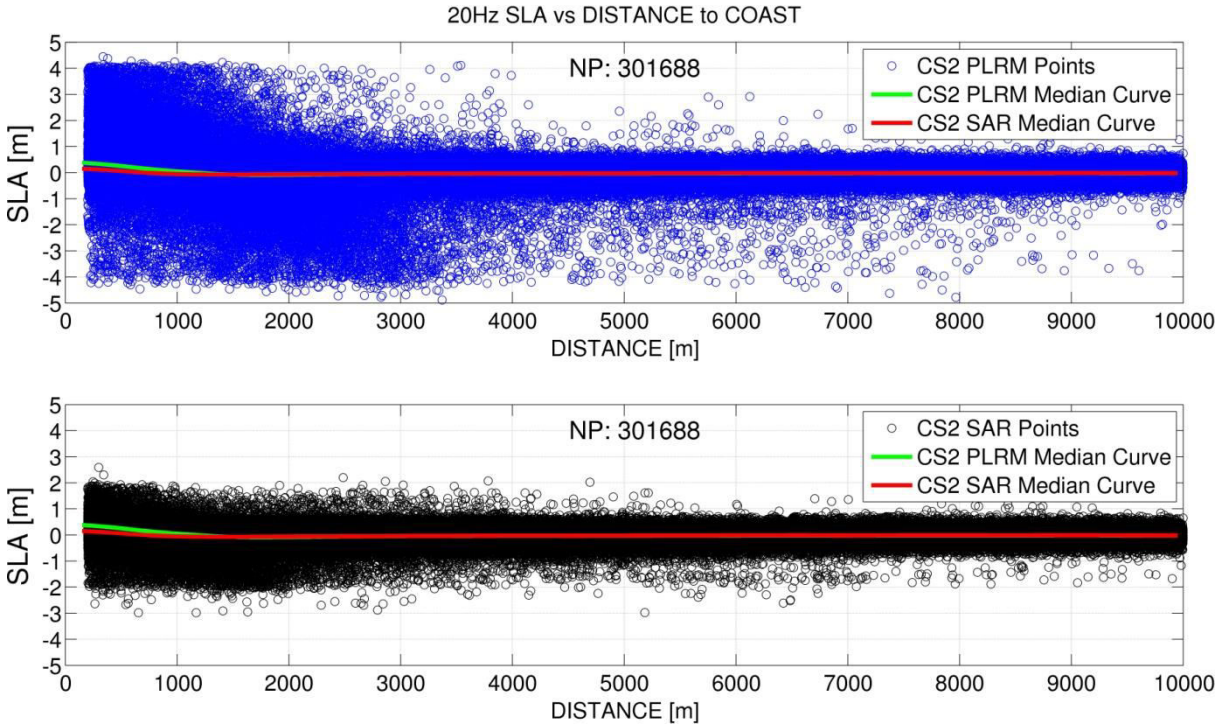

Figure 4.23: SLA cloud of points for SAR (bottom) and PLRM (top) versus distance to coast. NP is the number of points. Median Curves of both datasets are shown (red for SAR and green for PLRM)

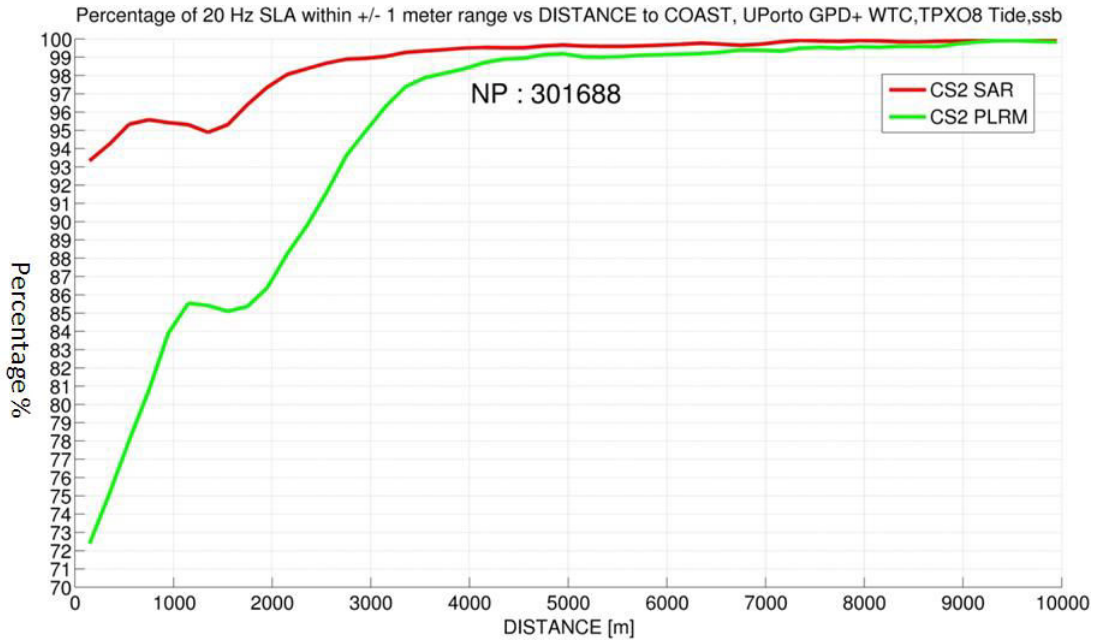

Figure 4.24: Percentage of 20 Hz SLA within ± 1 meter range versus the distance to the coast in SAR mode (red) and in PLRM mode (green). NP is the number of points.

Similarly, in Figure 4.25 and Figure 4.26, the same kind of plot for the SWH and U10 quantities respectively was computed.

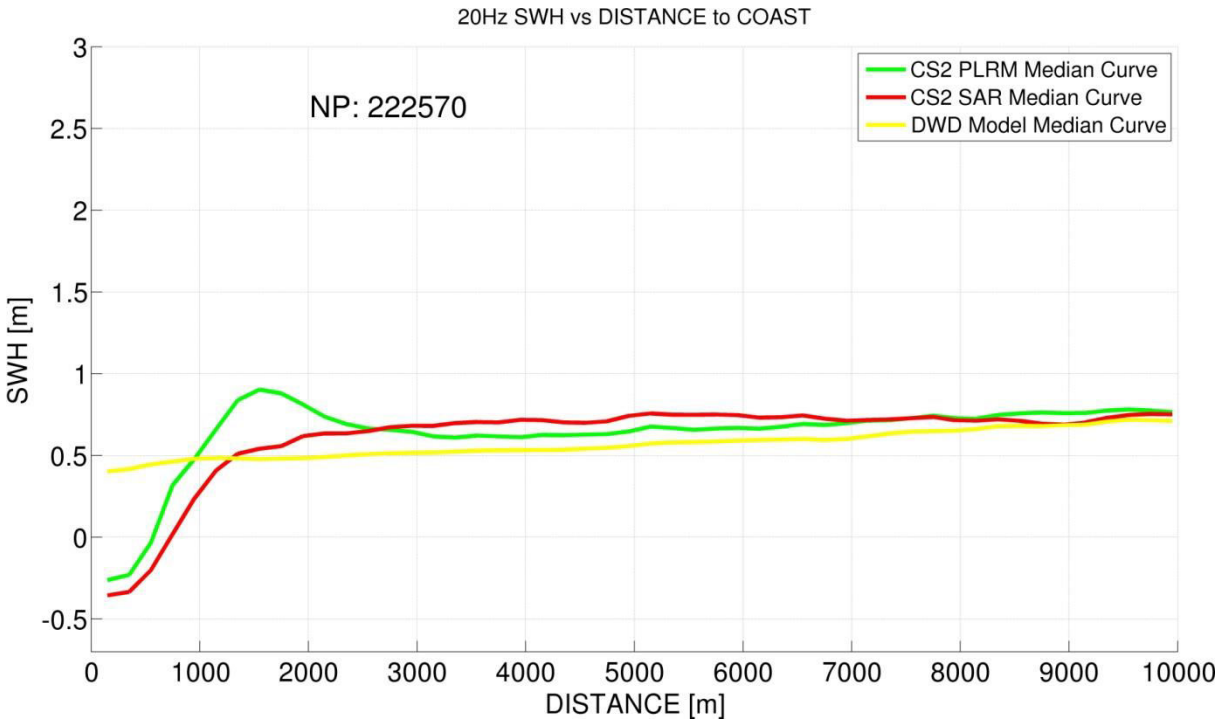

Figure 4.25: SWH median of points curve for SAR (red curve), PLRM (green curve) and DWD model (yellow line) versus distance to the coast. NP is the number of points.

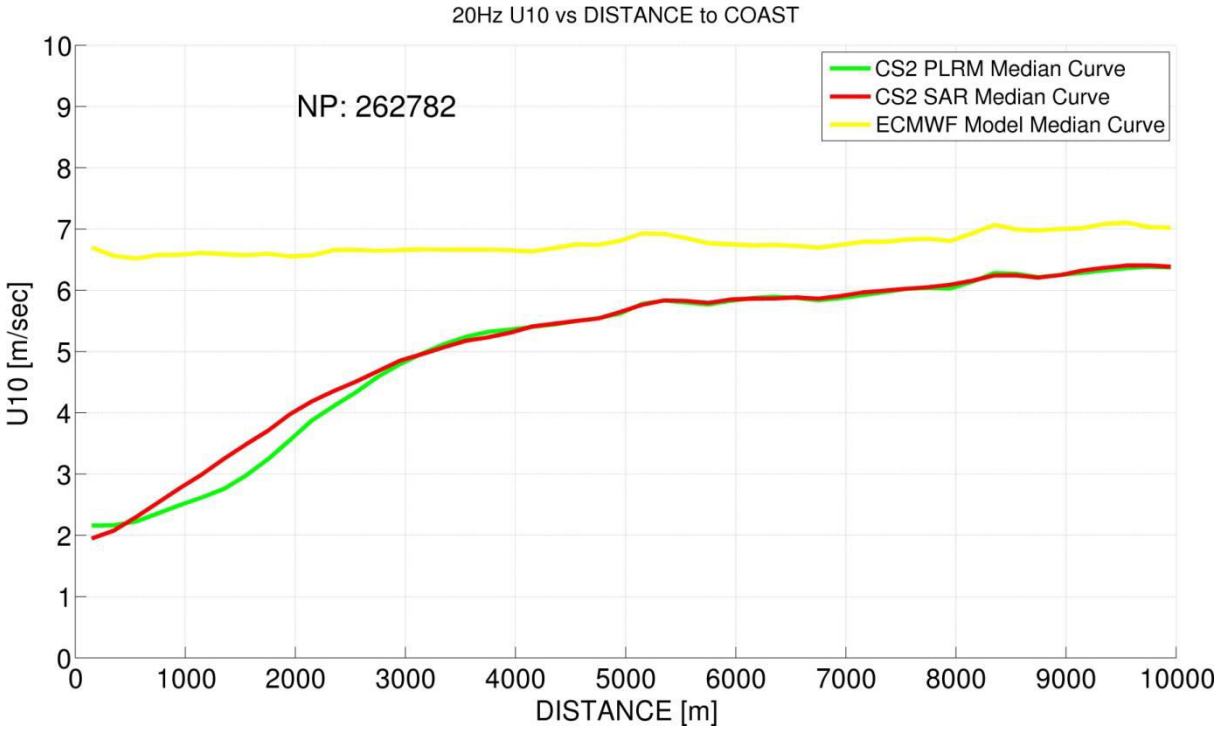

Figure 4.26: U10 median of points curve for SAR (red curve), PLRM (green curve) and ECMWF (yellow line) model versus distance to the coast. NP is the number of points.

Figure 4.25 illustrates that the DWD wave model exhibits a stable and slightly decreasing level of SWH up to the shoreline; the same decreasing trend is shown by SAR SWH up to 1.5 km from the coast where SAR mode data feature an abrupt drop in the SWH; the same drop is observed in PLRM mode just preceded by a rising phase which starts at around 3 km. Likely, when the SWH altimetry measurements are in the coastal band 0-3km, they get too contaminated and the measurements become invalid.

SAR, PLRM and DWD SWH do not exhibit large median differences (less than 20 cm) between each other till 2.5 km from the coast.
Similarly, Figure 4.26 shows that the ECMWF model's wind speed keeps a stable level of around 6.5 m/sec whereas the wind speeds from altimetry (SAR and PLRM) exhibit a common tendency to decrease when moving towards the shore. It is not clear which behaviour between the two is the correct one and whether this decreasing trend is a geophysical signal. Nevertheless, given the poor space gridding of the ECMWF global model (0.1 deg), the model may not hold a geophysical content in the coastal band 0-10 km and the signal shown could result from the extrapolation of open ocean values.
SAR and PLRM U10 do not show a significant bias, but one can observe a bias of +1.5 m/sec between the ECMWF model and altimetry in the coastal zone.

Figure 4.27 shows a bar plot of the SLA standard deviation in 200 meter bins of distance to coast for SAR, PLRM/TALES and BSH sea level model. This plot is meant to give an idea of the level of accuracy achieved by SAR and PLRM SLA in the coastal zone. When computing the SLA for SAR, PLRM and BSH, I remove the same TPXO8-ATLAS tide model for all three datasets. One can notice in Figure 4.27 that the BSH SLA std is basically constant up to the coast (with values around 25-30 cm) while the SAR SLA std has a value very close to the BSH model up to 3 km; closer to the coast, the SAR std starts to increase up to a value of 50 cm at the shoreline.
The SLA std in PLRM mode is much higher than the SAR std and the BSH std for all values of distance to coast (reaching a value of 1 meter at the shoreline).

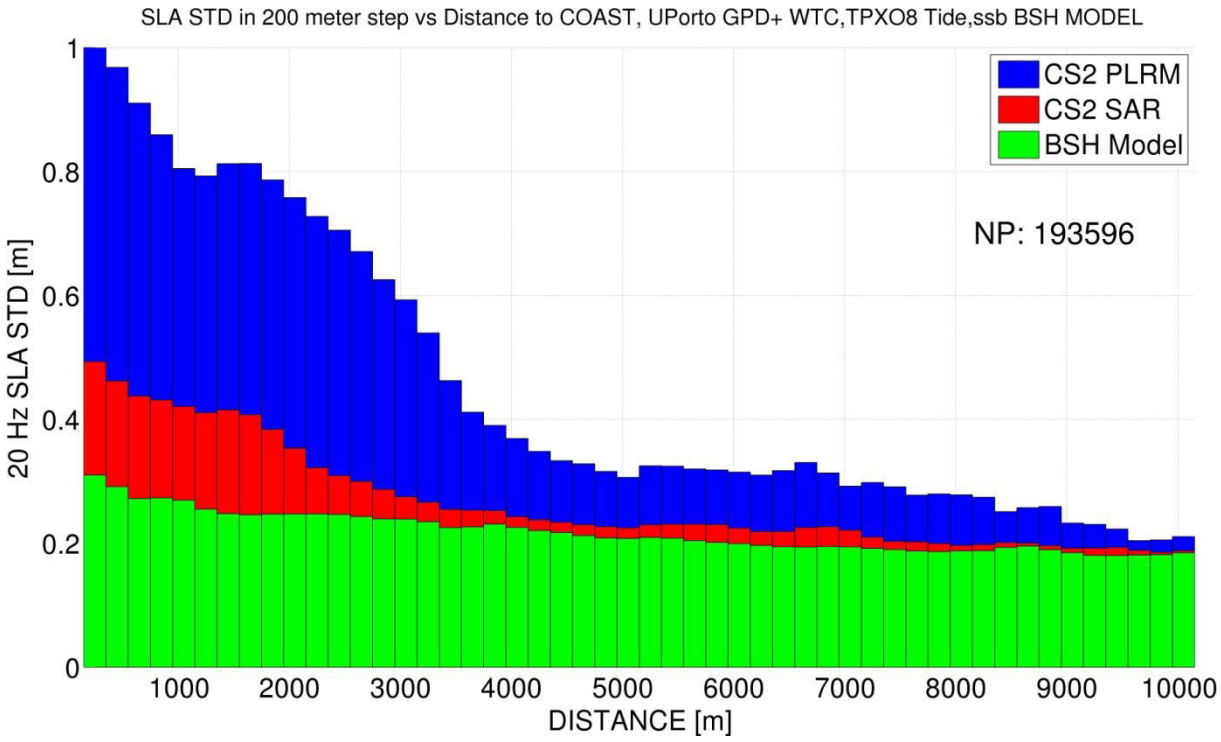

Figure 4.27: SLA std in 200 meter bins of distance to coast for SAR, PLRM-TALES and BSH Model. NP is the number of points.

Figure 4.28 and Figure 4.29 give a similar plot as in Figure 4.27 for respectively SWH and U10 parameters. From Figure 4.28, SAR SWH measurement outperforms PLRM SWH measurements but still the DWD wave model features a level of std lower than SAR.
This could indicate that SAR SWH is an advancement in term of performance with respect to PLRM in the coastal zone but also that further improvements in SAR are possible.
In this regard, I remind that here SAR SWH is still estimated as in Fenoglio-Marc et al., (2015), with no specific optimization. Future work in this direction is needed.

In Figure 4.29, the ECMWF wind speed model features a constant level of std versus distance to coast of around 3 m/sec whereas altimetry SAR and PLRM wind speeds exhibit only a slightly higher level of standard deviation.

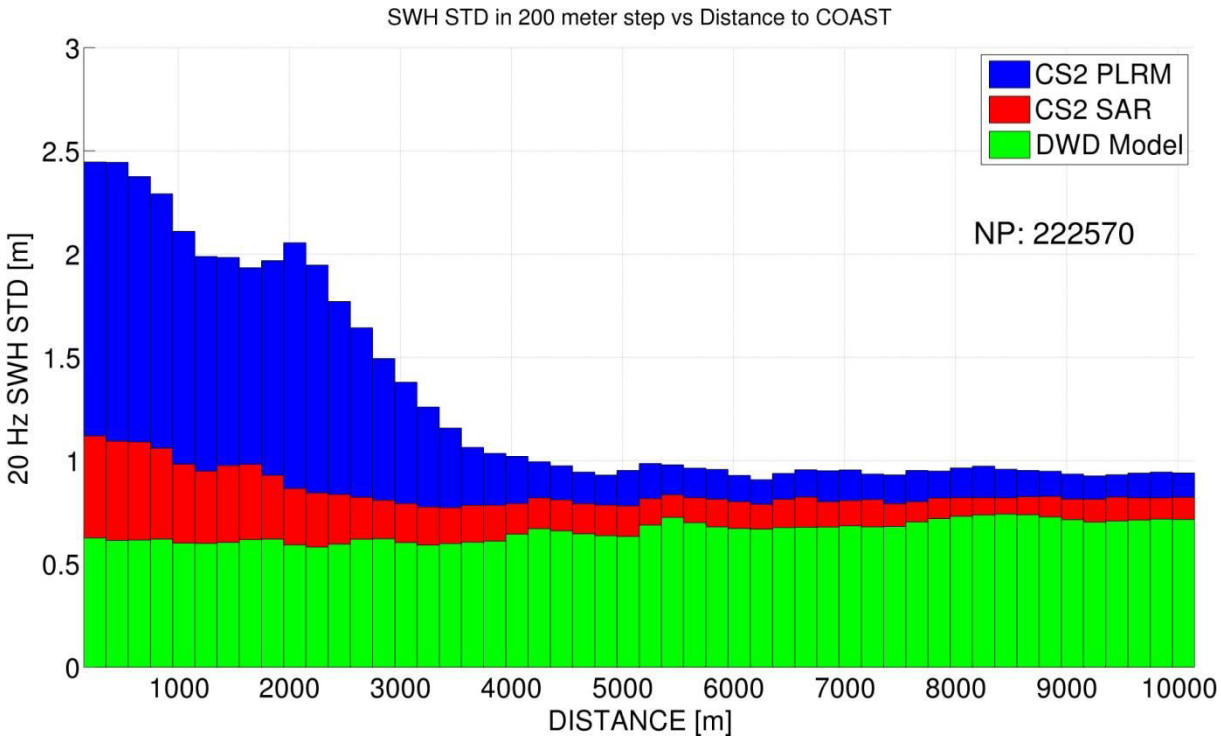

Figure 4.28: SWH std in 200 meter bins of distance to coast for SAR, PLRM and DWD Model. NP is the number of points.

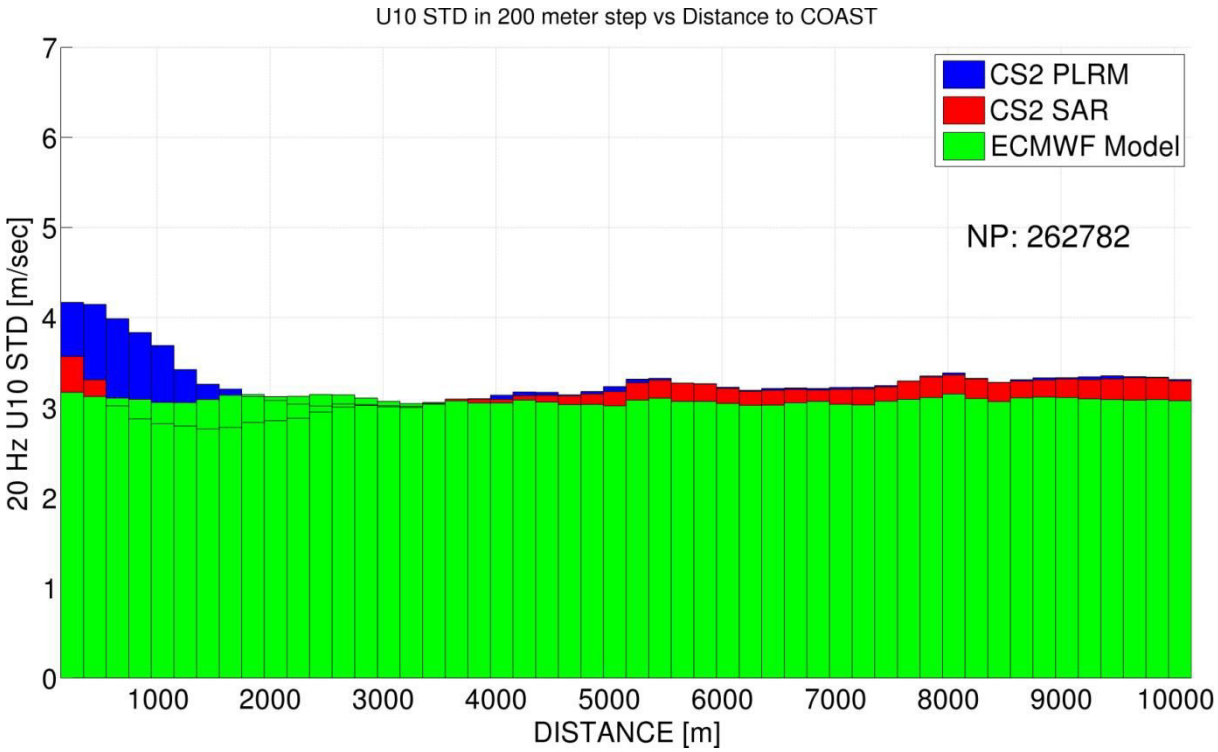

Figure 4.29: U10 std in 200 meter bins of distance to coast for SAR, PLRM and ECMWF Model. NP is the number of points.

Figure 4.30 illustrates the noise floor estimation in SAR and in PLRM. Whereas in open-ocean, the noise floor from PLRM (from the waveform's early samples) and from SAR mode data look consistent (Figure 4.30-left), in the coastal zone (Figure 4.30-right) the PLRM noise floor level increases with distance to coast while in SAR mode, the estimation is basically stable and independent from the distance to the coast. One can expect that the PLRM noise floor estimation increases with distance to coast because the waveform's early samples are contaminated by land reflections in proximity of the coast.

Being the noise floor in SAR mode estimated as described in section 2.1 (and hence not depending on waveform early samples), the SAR noise floor estimation is not affected by this issue and exhibits a stable value for all distances to coast.

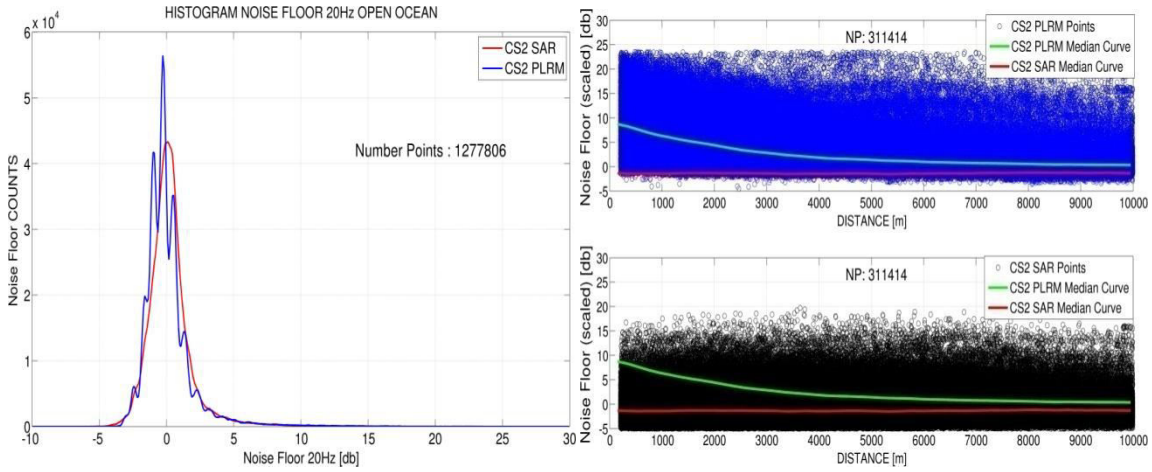

Figure 4.30: Histogram of the Noise Floor estimation in open-ocean (left) and noise floor estimation (point cloud and median) vs. distance to coast for PLRM (top-right) and SAR (bottom-right). NP is the number of points.

c) SLA AND DOTi SCATTER AND DISTRIBUTION

In this section, the consistency between SAR, PLRM and ocean model data in the coastal zone is analysed via scatter plots and histograms. The quantities considered are SLA and DOTi.

The scatter plot between PLRM and SAR SLA data (Figure 4.33-left, Table 4.7) shows the consistency between SAR and PLRM measurements. Median, standard deviation of the differences (stdd) and regression slope are 0.9 cm, 52 cm and 0.78 respectively. The scatter plot of SAR and PLRM DOTi (Figure 4.33-right, Table 4.7) presents similar bias and stdd but a larger slope (slope changes from 0.77 for SLA to 0.93 for DOTi). This statistical outcome is expected as the ocean tide is not removed in model DOTi and hence DOTi has higher ocean dynamics (std 0.42) compared to model SLA (std 0.22) (see Table 4.7).

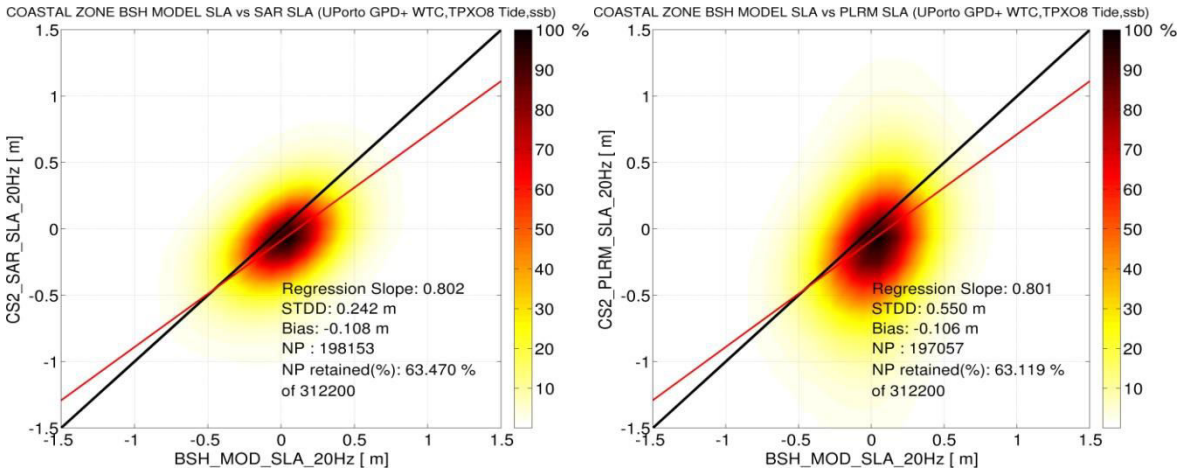

Figure 4.31: Scatter Plot in the coastal zone between SAR SLA and BSH Model SLA (left) and PLRM SLA and BSH Model SLA (right). Color scale gives data density. NP is the number of points.

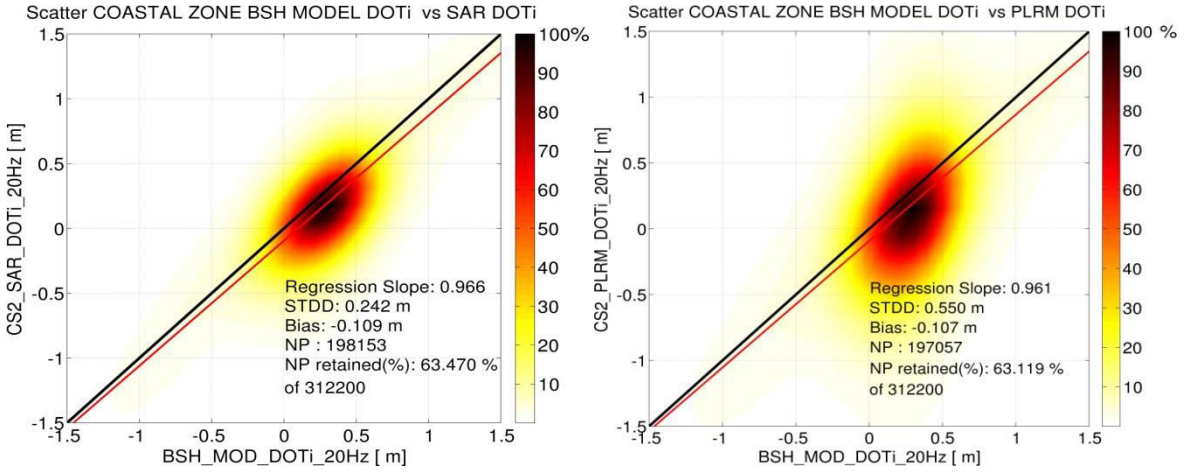

Figure 4.32: Scatter Plot in the coastal zone between SAR DOTi and BSH Model DOTi (left) and PLRM DOTi and BSH Model DOTi (right). Color scale gives data density. NP is the number of points.

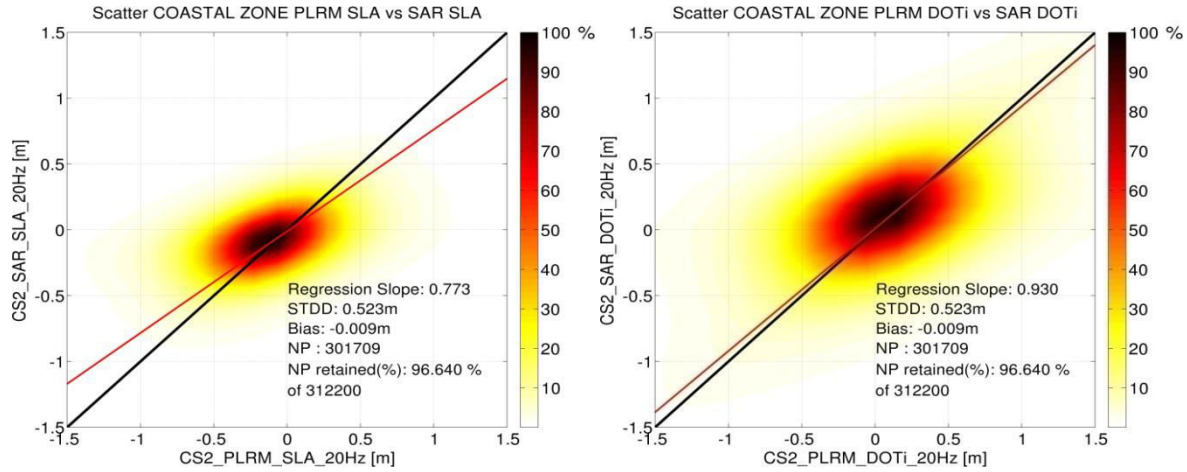

Figure 4.33: Scatter Plot in the coastal zone between SAR SLA and PLRM SLA (left) and SAR DOTi and PLRM DOTi (right). Color scale gives data density. NP is the number of points.

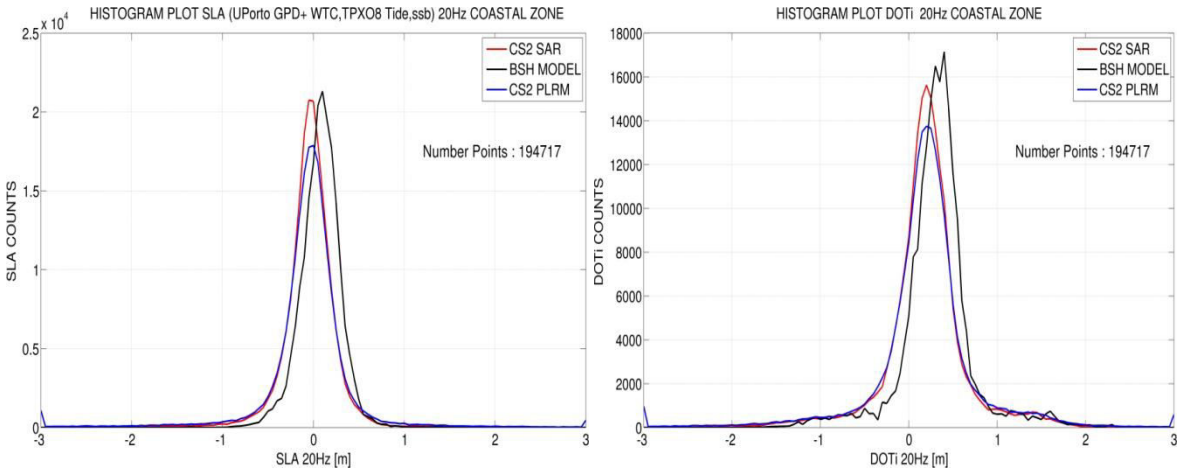

Figure 4.34: Histogram Plot in the coastal zone between SAR SLA PLRM SLA and BSH Model (left) and between SAR DOTi PLRM DOTi and BSH Model DOTi (right)

The scatter plot between altimetric and ocean model SLA data shows a good consistency between SAR and ocean model, with bias, stdd and slope of -10 cm, 24 cm and 0.8 respectively (Figure 4.31-left, Table 4.7). The consistency is lower for PLRM data, with stdd twice as large (55 cm) and similar slope (Figure 4.31-right, Table 4.7). The scatter plot between altimetric and ocean model DOTi (Figure 4.32, Table 4.7) has a higher slope than the corresponding plot for SLA (Figure 4.31, Table 4.7), due to the ocean tide in DOTi as discussed above.

From the histograms in Figure 4.34, I report a bias around 10 cm between SAR/PLRM DOTi and BSH Model DOTi (BSH DOTi higher than SAR/PLRM DOTi). The same bias is also observed between SAR/PLRM SLA and BSH Model SLA. This bias can arise from the BSH model being referred to a different reference level than satellite altimetry (Schall et al., 2016).

The statistics from the scatter plots are summarised in Table 4.7 where it can seen for instance that the correlation coefficient between the altimetric and BSH model DOTi is higher in SAR (0.85) than in PLRM (0.58).

Measurement in the coastal zone	**DOTi**					**SLA**				
Index	**median cm**	**std cm**	**Corr**	**Slope**	**N Points**	**median cm**	**std cm**	**Corr**	**Slope**	**N Points**
PLRM	19.2	69.7	-	-	305049	-2.2	60.3	-	-	305049
SAR	19.5	44.3	-	-	307979	-2.4	29.8	-	-	307979
BSH Model	32.3	42.6	-	-	200887	9.5	22.7	-	-	200887
SAR-PLRM	-1.0	52.2	0.61	0.93	301709	-1.1	52.3	0.45	0.78	301709
SAR- BSH MODEL	-10.7	24.4	0.85	0.97	198153	-10.8	24.2	0.46	0.80	198153
PLRM-BSH MODEL	-10.8	55.7	0.58	0.96	197057	-10.3	55.1	0.26	0.80	197057

Table 4.7: Statistics for SAR, PLRM, BSH Model DOTi and SLA

d) MONTHLY MEAN TIME SERIES

In this subsection, I compute the monthly mean and std time series of instantaneous DOT (DOTi), SWH and Wind Speed (U10) in the region under study in the time interval from July 2010 to March 2016 for SAR, PLRM and ocean model. Here, the monthly mean and std are the mean and standard deviation of the all measurements available in the month. When computing the time series, I restrict my analysis to the band of 0-10 km (coastal zone).

From Figure 4.35, one can observe that DOTi monthly mean time series from SAR, PLRM TALES and BSH model exhibit a very similar behaviour as the correlation coefficient is 0.93 between SAR and BSH and 0.90 between PLRM and BSH. The bias between BSH and altimetry is 12 cm for SAR and 13 cm for PLRM, which is due to a different reference surface as discussed above. However, BSH and SAR average monthly std are respectively 36 and 42 cm whereas PLRM std is around 62 cm (see Table 4.8). As a result of this, it can be concluded that the DOTi monthly mean time series is measured in SAR mode much more precisely than in PLRM mode. I emphasize how the SAR and BSH model std are very close to each other and this is a

significant result. In the time series July 2010-March 2016, there is a data gap around February 2012, as mentioned in section in the introduction.

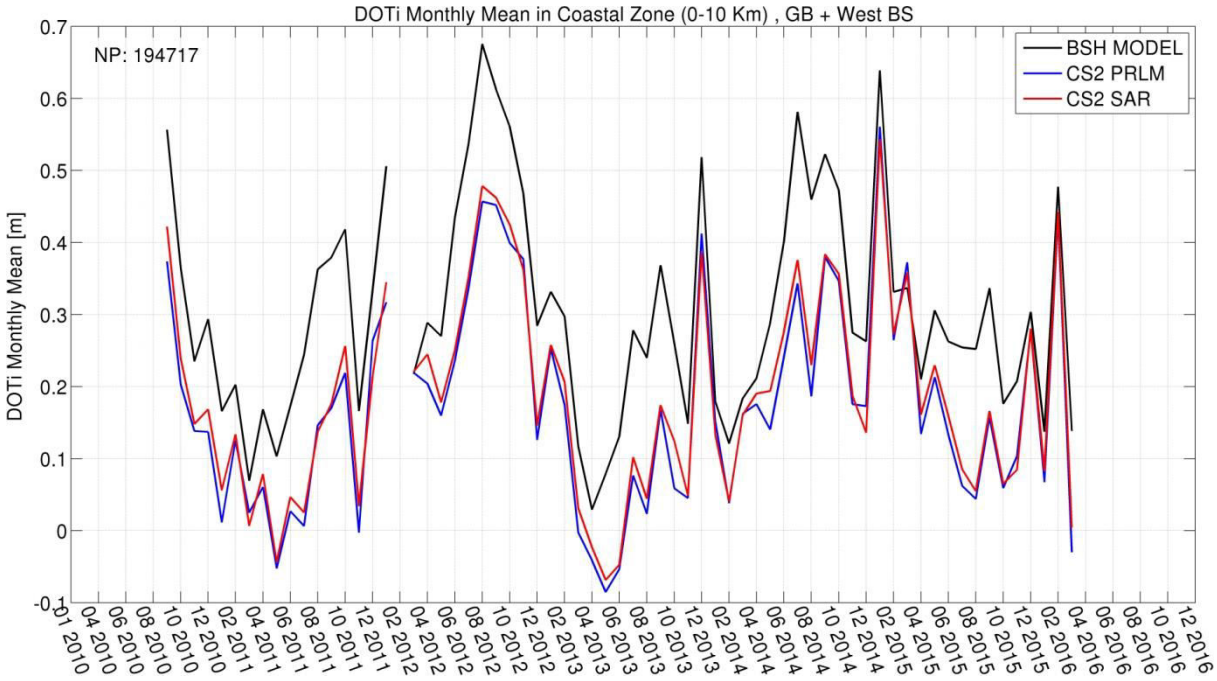

Figure 4.35: DOTi monthly mean time-series in the coastal zone (0-10 km) for SAR, PLRM and BSH Model. NP is the number of points.

Figure 4.36 represents the SWH monthly mean time series showing that all three datasets are consistent in recording the monthly mean variability (correlation coefficient is 0.86 between DWD and SAR and 0.87 between DWD and PLRM). Again, from Table 4.8, this monthly mean variability is returned much more precisely in SAR mode (SAR average std is 0.81 m whereas PLRM std is around 1.21 m). The std of the DWD wave model data is lower than the corresponding SAR (0.59 m) value and indicates that further improvement in SAR SWH estimates in coastal zone are possible. There is no significant bias between SAR SWH, PLRM SWH and DWD SWH in the coastal zone (Table 4.8).

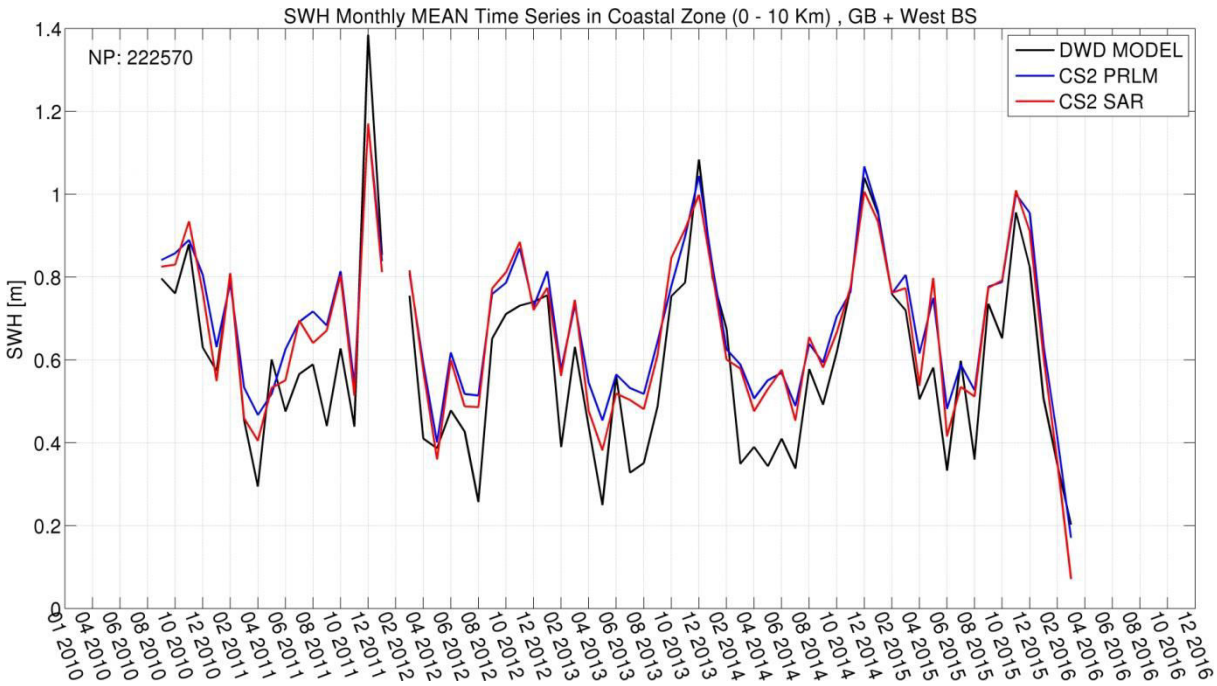

Figure 4.36: SWH monthly mean time-series in the coastal zone (0-10 km) for SAR, PLRM and DWD Model. NP is the number of points.

Finally, Figure 4.37 presents the monthly mean time series for U10, indicating that all three datasets again are quite consistent in recording the monthly mean variability (correlation coefficient of 0.94). but, from Table 4.8 (average std column), this monthly mean variability is returned slightly more precisely in SAR mode (SAR average std is 2.98 m/sec whereas PLRM std is around 3.16 m/sec). The std of the wind speed model data is only slightly lower than the corresponding SAR value (2.68 m/sec). I report a bias in coastal zone between altimetry (SAR and PLRM) U10 and ECMWF wind speed of about 1.5 m/sec. The reason for this bias is unexplained.

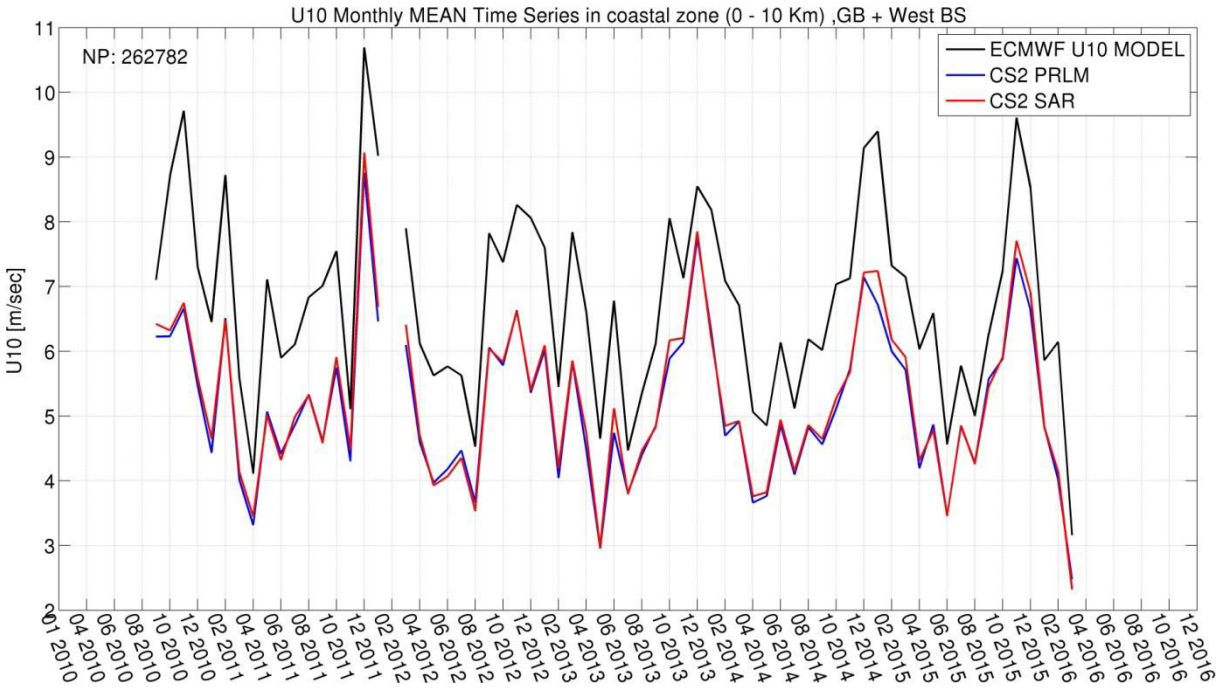

Figure 4.37: U10 monthly mean time-series in the coastal zone (0-10 km) for SAR, PLRM and ECMWF Model. NP is the number of points.

Measurement	DOTi			SWH			U10		
Index	mean cm	average std cm	Corr with model	mean cm	average std cm	Corr with model	mean cm/sec	average std cm/sec	Corr
PLRM	18.2	62.7	0.90	69.7	121.8	0.87	515.3	316.1	0.94
SAR	19.7	42.3	0.93	67.3	81.8	0.86	522.4	298.8	0.94
Ocean Model	31.3	36.1	-	59.2	59.2	-	673.5	268.4	-

Table 4.8: Statistics for SAR, PLRM, Ocean Model DOTi, SWH and U10

From all these results above, I conclude that the SAMOSA+ retracker improves significantly the results achievable in by PLRM mode without degrading the results in open ocean and ensuring the continuity between coastal zone and open ocean.

4.2 SENTINEL-3 MARINE RESULTS

Prior to present the marine results achieved with Sentinel-3 mission, I describe the region of interest, the geophysical and range corrections and the third party data which I have been using to derive my results. The formulation used to apply the range corrections and the terminology for the several geophysical topographic quantities (sea surface height, sea level anomaly, dynamic ocean topography, etc.) is the same as presented in section 4.1.1.3

4.2.1 REGION OF INTEREST AND DATA

4.2.1.1 REGION OF INTEREST

The region of interest, selected for this thesis work in validating the Sentinel-3 data in open ocean and coastal zone, is bound by the geographic coordinates (35° N to 60° N; 12° W to 16° E) . From this rectangle, all the points over the Mediterranean Sea have been eliminated. Hence my region of interest consists of the North Sea, German Bight, West Baltic Sea, Celtic Seas, Bay of Biscay and Iberian Coast. Sentinel-3 operates in SAR mode over this region. I will refer to this region as North East Atlantic. The study area is depicted in Figure 4.38 with the geoid as background overlay (in metres) and Sentinel-3A ground tracks. The fiducial tide gauges and buoys locations are shown as green triangles and purples squares respectively in Figure 4.39.

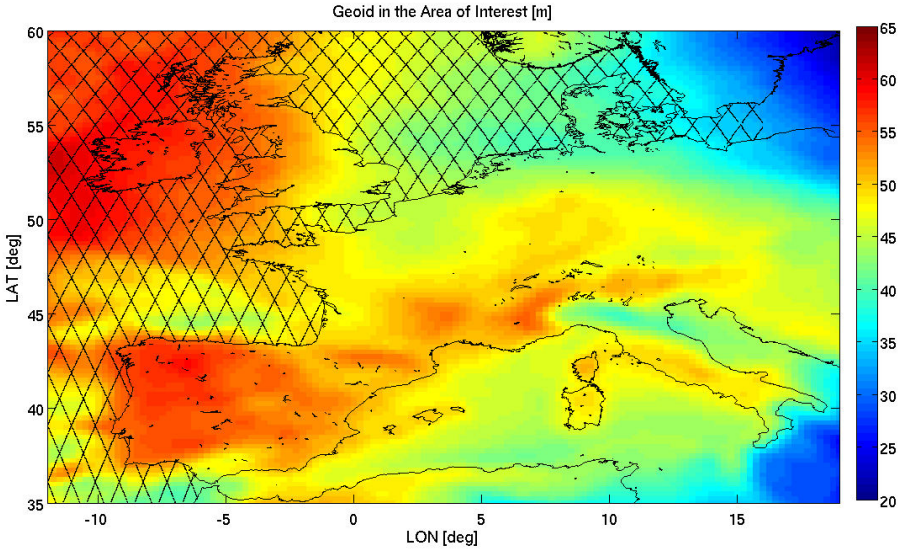

Figure 4.38: Region of interest for the validation of Sentinel-3A data with the geoid (EIGEN-6C4 model) as background overlay (metres) and the Sentinel-3A ground tracks over ocean (note that the data over the Mediterranean have been removed).

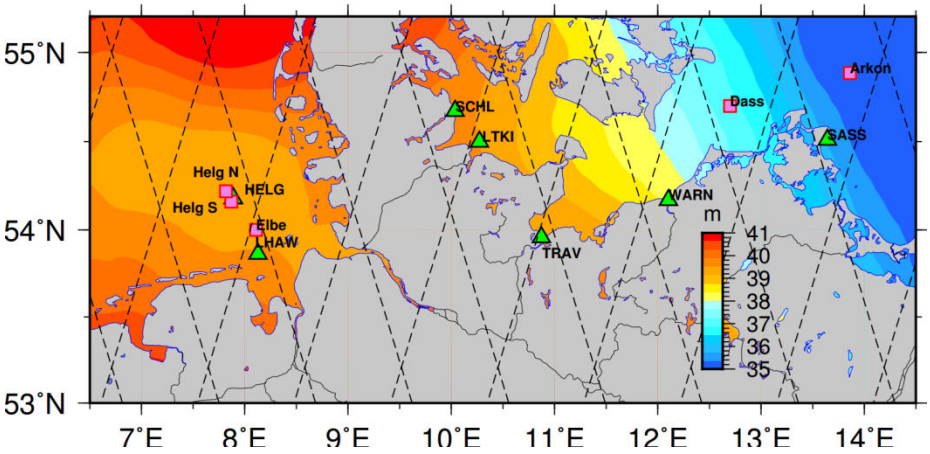

Figure 4.39: Zoom of the region under analysis in German Bight and West Baltic Sea showing the location of the tide gauge stations (triangle), GNSS stations (circle) and the sea-state stations (square) used in this study and the Sentinel-3A ground tracks. The overlay background is the German Combined quasiGeoid 2016 (GCG2016) in metres. Image courtesy of Luciana Fenoglio-Marc.

Sentinel-3A SAR data are processed from L1A up to geophysical level (L2) to provide Sea Surface Height, Significant Wave Height and Wind Speed at 10 meter over the sea surface, posted at a rate of 20 Hz, using the SAMOSA+ and SAMOSA++ retracker.

Furthermore, I have procured in the same area of interest the Sentinel-3A data from the Marine PDGS (Payload Ground Segment), see EUMETSAT Marine SRAL Product Handbook (2017). This dataset will be referred as "SAR Marine".

The selected time of interest is the whole mission time from 15 June 2016 to 31 December 2018.

A very first dataset screening is applied rejecting data over land, over inland water and over very shallow water (depth less than 2 m) and data with departure from the mean sea surface (MSS) larger than 15 meters.

4.2.1.2 AUXILIARY THIRD PARTY DATA

The auxiliary third party data which have been procured in my area of interest are the same as the ones used for Cryosat-2 and described in section 4.1.1.2 with two differences: I have updated the DTU15 mean sea surface model with DTU18 mean sea surface model (Andersen et al., 2018) and I have replaced the

BSH/DWD ocean circulation and wave model with GCOAST (Geesthacht Coupled cOAstal model SysTem) sea level circulation and wave model from Helmholtz-Zentrum Geesthacht (HZG) (Stanev et al., 2016).
This model is a coupled wave and ocean model system with a high resolution grid (3.6 km x 3.6 km) and a temporal sampling of one hour. Components of the coupled model system are the circulation ocean model NEMO (Nucleus for European Modeling of the Ocean), the ice model LIM3 (Louvain-la-Neuve sea Ice Model-3) and the wave model WAM (WAve Model). The atmospheric forcing is taken from the ECMWF ERA-5 (ECMWF Re-Analysis 5) dataset (Copernicus Climate Change Service, 2017).
The GCOAST/HZG ocean model used in this study covers the North East Atlantic region [40° N to 65° N; 20° W to 30° E].
The reason for the replacement of the BSH/DWD model with GOAST/HZG is that the GCOAST/HZG model covers better my region of interest in the North East Atlantic.

4.2.1.3 GEOPHYSICAL AND RANGE CORRECTIONS

The geophysical and range corrections which have been procured in my area of interest are the same as the ones used for Cryosat-2 and described in section 4.1.1.3.
Along with TPOXO8-ATLAS, the recent ocean equilibrium tide solution developed in 2018 by OSU (Oregon State University) TPXO9-ATLAS model (Egbert and Erofeeva, 2002) has been also used. This solution, available at http//:volkov.oce.orst.edu/tides/tpxo9_atlas.html, is a model that combines, in a data fusion approach, the global solution (TPXO9) and regional high resolution solutions (Egbert et al., 2010). The TPXO9-ATLAS model features a1/30 degree resolution, obtained by combining 1/6 degree base global solution TPXO9 and 1/30 resolution local solutions for all coastal areas, including the Arctic and Antarctic. The global solution TPXO9 is the most recent model of the TPXO series of fully-global models of ocean tides, which best-fits, in a least-squares sense, the Laplace Tidal Equations and altimetry data and is based on the updated bathymetry and on the assimilation of more data compared to previous versions. A high-resolution bathymetry model at 2 arcminutes (approx. 3 km) resolution was retrieved from the same source.
In addition, the recent tide model FES2014b (Carrere et al., 2015) has been procured and it will be used in order to assess whether it brings any improvement with respect to TPXO8-ATLAS and TPXO9-ATLAS model in the coastal zone. FES2014b (Finite Element Solution) is based on the resolution of the shallow water hydrodynamic equations in a spectral configuration and using a global finite elements mesh with increasing resolution in shallow water and polar regions. Furthermore, FES2014b also benefits from data assimilation, taking advantage of higher accuracy in the updated altimetric dataset, longer time series and better altimeter standards with respect the previous model versions.
Finally, the University of Porto (UPorto) has developed for the Sentinel-3 mission two versions of WTC from the GNSS-derived path Delay Plus algorithm, in short GPD+ (Fernandes and Lázaro, 2016).
GPD+ are continuous (valid over all surface types), consistent and calibrated WTC based on data combination from all available wet path delays in the vicinity of the estimation point. Estimations are obtained by space-time objective analysis (OA) taking into account the variability of the WTC field and the accuracy of the observations. Input data used are: valid measurements from the on-board MWR (when they exist, as per Sentinel-3), GNSS-derived WTC from coastal and island stations and WTC from scanning imaging MWR aboard various remote sensing satellites. First guess values in the OA procedure (which are the adopted WTC in the absence of observations) are derived from the best available atmospheric model, in the specific case the European Centre for Medium Range Weather Forecasts (ECMWF) operational model. More details about the method, applied for most of altimetry missions, can be found in (Fernandes et al., 2010, 2015, Fernandes and Lázaro, 2016).
The two types of GPD+ WTC developed by UPorto (Fernandes and Lázaro, 2018) for the Sentinel-3 mission are:

- GPD1 or “à la CryoSat”: WTC derived solely from third party data, i.e., not including Sentinel-3 on-board MWR observations
- GPD2: usual GPD WTC, i.e., using all available observations including valid Sentinel-3 MWR values

Whereas the solution GPD2 uses the state-of-the-art MWR correction from the Sentinel-3 on-board MWR, preserving their valid observations over the ocean, the solution GPD1, computed in the same way as for the CryoSat-2 mission (Fernandes and Lázaro, 2016), which does not carry any on-board radiometer, serves as an independent validation reference for the Sentinel-3 MWR-derived WTC (Fernandes and Lázaro, 2018).

4.2.2 OPEN OCEAN RESULTS

In this section, I present the results that have been obtained by the SAMOSA++ and SAMOSA+ retracker in open ocean and 1 Hz versus the analogous results produced by marine PDGS in SAR mode and the numerical ocean circulation/wave models. The validation against the tide gauges and buoys in the open ocean will be treated in section 4.3.2 along with the one in coastal zone since it will be used to prove the seamless continuity between the open ocean and the coastal zone results.
As preamble, I recall the result reported by (Dinardo et al., 2018b) who has shown how the two altimeters on board of Sentinel-3A and Cryosat-2 show very similar performance, though some difference exist in term of accumulated looks. The default tracking gate for CryoSat-2 mission is 34 whereas for Sentinel-3A is 44. Hence, for geometrical reasons, CryoSat-2 can receive and accumulate more looks (around 200 looks accumulated) than Sentinel-3 (around 180 looks accumulated). As result of this, the precision of CryoSat-2 is very slightly better than Sentinel-3’s one (see Figure 4.40 and Figure 4.41).

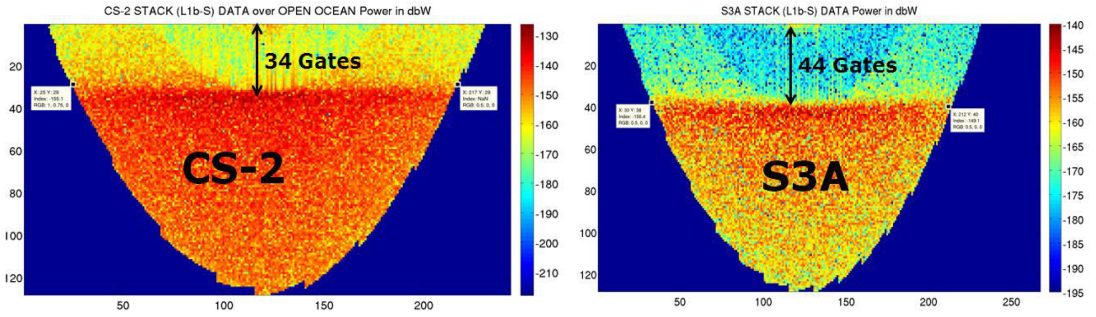

Figure 4.40: Stack data from CryoSat-2 (left) and Stack data from Sentinel-3 (right). The position of the stack is more advanced for Cryosat-2. This allows CryoSat-2 to receive and accumulate more looks

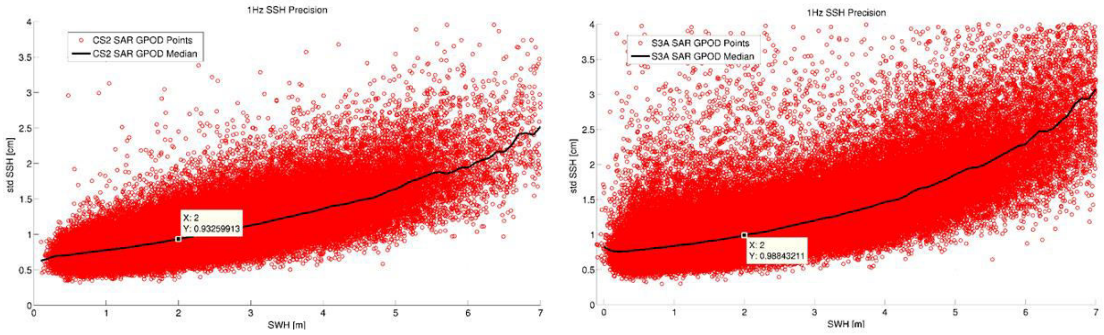

Figure 4.41: SSH Precision Plot for CryoSat-2 (left) and Sentinel-3 (right) for the same region, time period and with same geo-corrections. CryoSat-2 is more precise (1 Hz range noise 0.93 cm) than Sentinel-3 (range noise 0.98 cm)

4.2.2.1 CROSS-VALIDATION BETWEEN SAMOSA++, SAMOSA+, SAR MARINE AND MODEL DATA

a) SLA AND SWH PRECISION CURVE

In this sub-section, the precision plots for the SAMOSA++ and SAMOSA+ are shown in the Figure 4.42 and Figure 4.43. SAR Marine precision (in green for the median curve) is shown in the plots as reference.

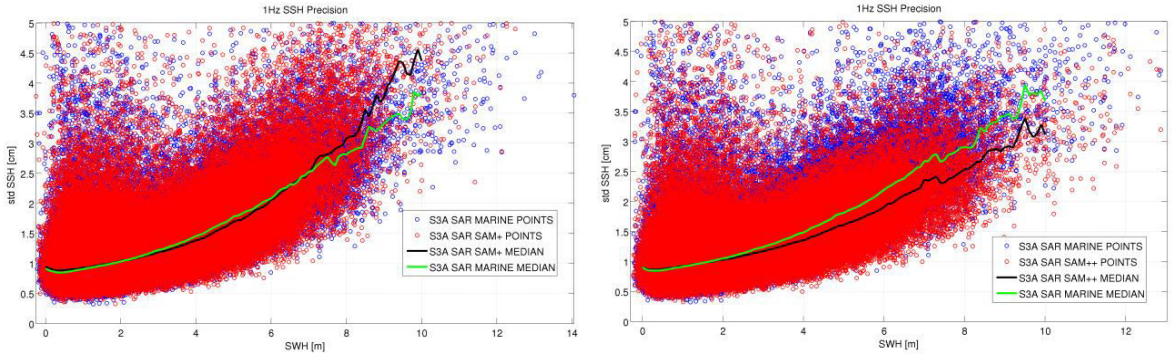

Figure 4.42: SSH Precision Plot for the SAMOSA+ (left) and for the SAMOSA++ dataset (right)

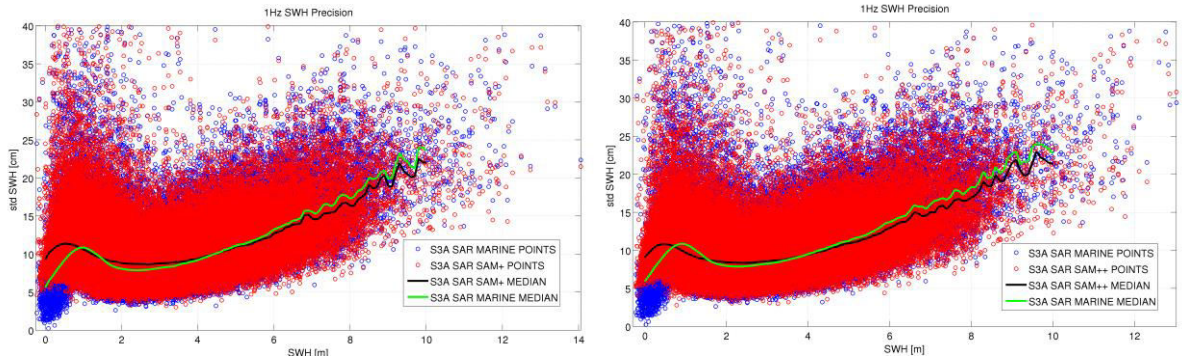

Figure 4.43: SWH Precision Plot for the SAMOSA+ (left) and for the SAMOSA++ dataset (right)

The precision reached by the three datasets SAMOSA++, SAMOSA+ and SAR Marine are very close to each other . What can be noticed for the case SAMOSA++ is that the range (SSH) noise for high sea state regimes is significantly reduced with respect to the case SAR Marine and SAMOSA+ (a percentage improvement of 20 %). This can be an indication that SAMOSA++ succeeds to fit better the waveform and retrieve the range in case of big waves. No significant difference is noticed as far as concerns the SWH noise.

b) SLA , SWH AND U10 SCATTERPLOTS

In this sub-section, I proceed to validate the accuracy of the results from SAMOSA++ and SAMOSA+ retrackers in open ocean by means of scatterplots with respect the SAR Marine dataset and ocean numerical model.

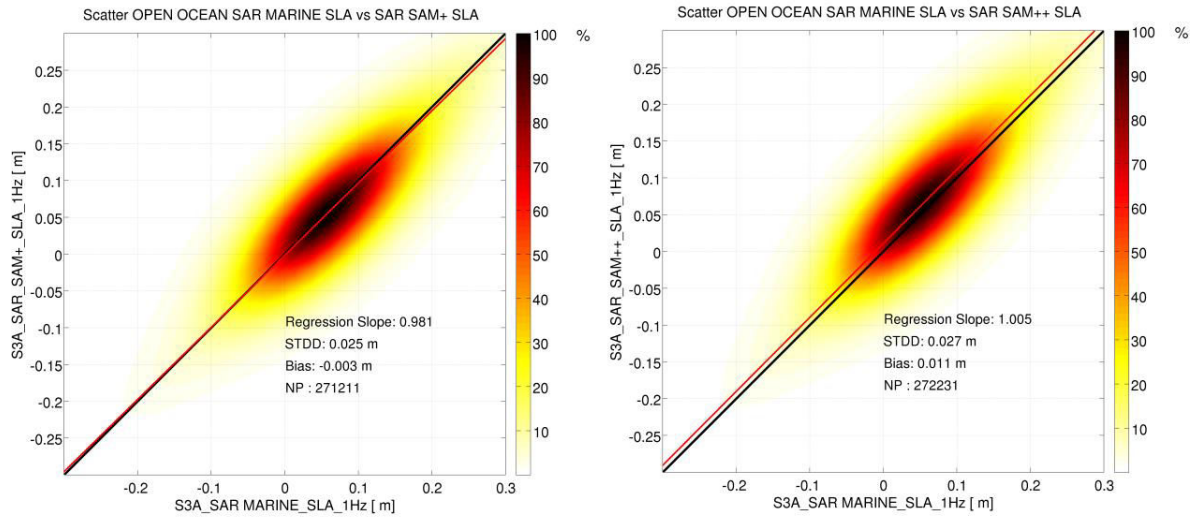

Figure 4.44: Scatterplot between SLA SAMOSA+ and SLA SAR Marine (left) and Scatterplot between SLA SAMOSA++ and SLA SAR Marine (right). Color code is data density in percentage

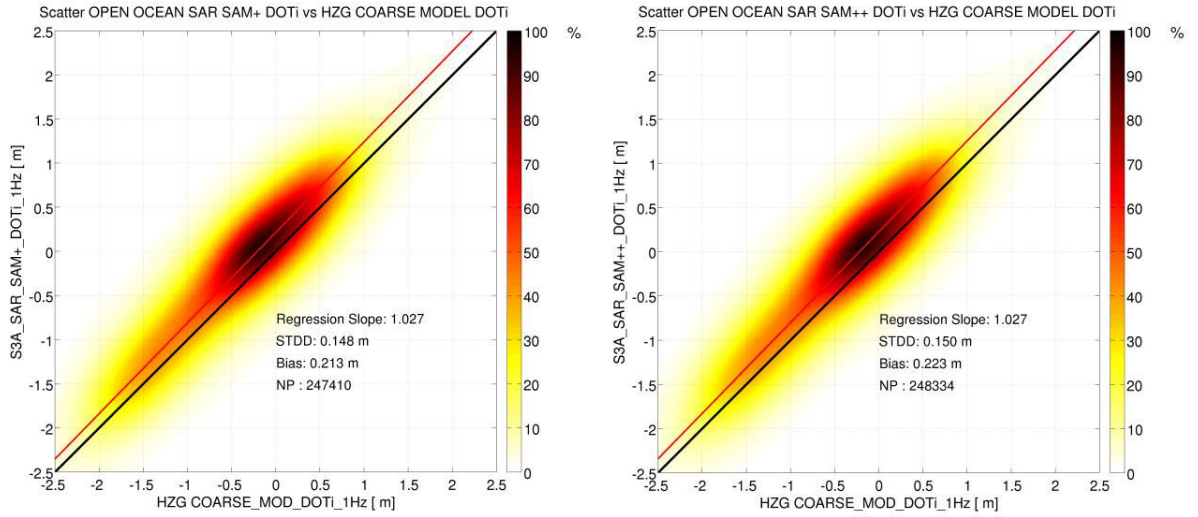

Figure 4.45: Scatterplot between DOTi SAMOSA+ and DOTi GCOAST/HZG Model (left) and Scatterplot between DOTi SAMOSA++ and DOTi GCOAST/HZG Model (right). Color code is data density in percentage

As far as concerns the quantity SLA, the consistency between SAMOSA++ and SAMOSA+ versus the SAR Marine is excellent, being the standard deviation of the difference (stdd) only 2.5 cm for the case SAMOSA+ and only 2.7 cm for the case SAMOSA++ (see Figure 4.44). Also the consistency of DOTi versus the GCOAST/HZG model is very similar between the two dataset (14.8 cm for SAMOSA+ and 15.0 cm for SAMOSA++) as as shown in Figure 4.45. But I have to point out that SAMOSA++ introduces a bias of +1cm with respect the SAMOSA+ case.

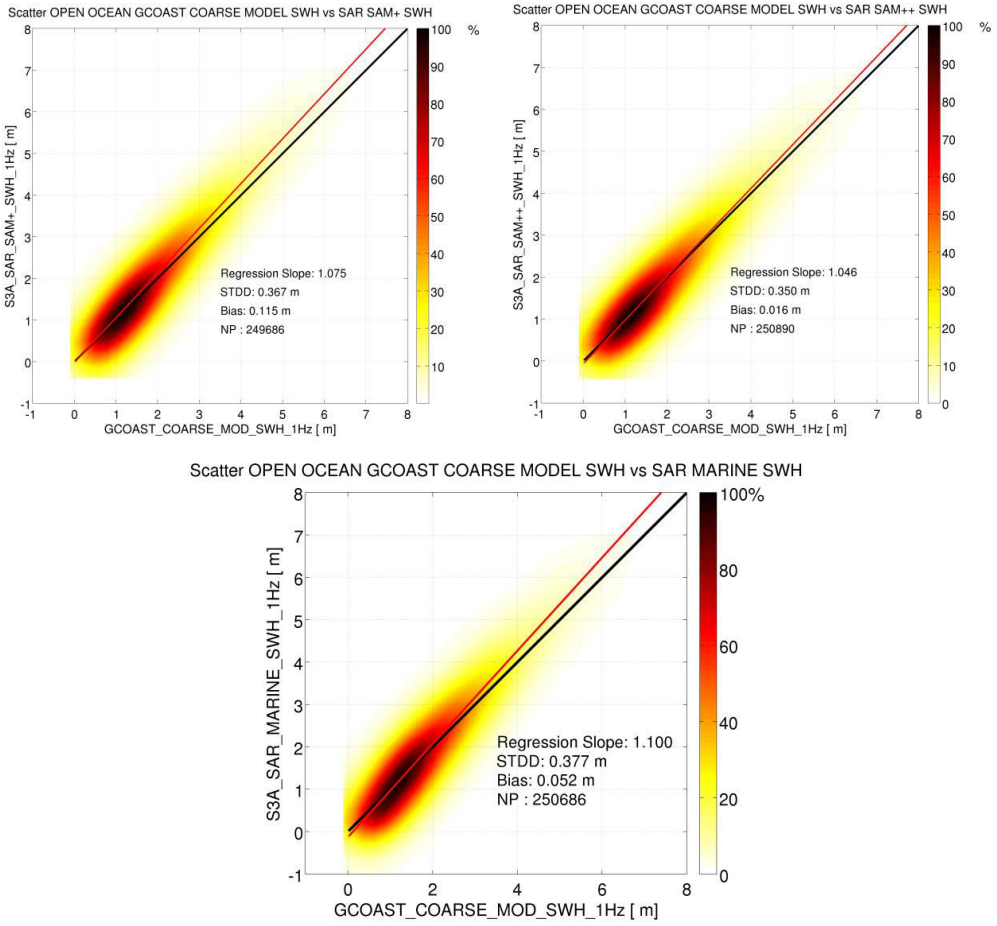

Figure 4.46: Scatterplot between SWH SAMOSA+ and SWH GCOAST/HZG Model (top-left), Scatterplot between SWH SAMOSA++ and SWH GCOAST/HGZ Model (top-right) and between SAR Marine and SWH GCOAST/HGZ Model (bottom). Color code is data density in percentage

Regarding the SWH, the scatterplots between SAMOSA++ SWH and SAMOSA+ SWH versus GCOAST/HZG model are displayed in Figure 4.46. Here, one can notice how for the case SAMOSA++ the SWH has no significant bias with respect the GCOAST/HZG model while the stdd gets slightly reduced with respect the case SAMOSA+ and also the regression slope is closer to one. Hence, it can be concluded that the SAMOSA++ SWH is slightly more consistent with the GCOAST/HZG model than the case SAMOSA+.

Finally, as far as it concerns U10, the consistency of SAMOSA++ and SAMOSA+ versus the SAR Marine is shown again by means of scatterplots in Figure 4.47. Once again, the three dataset are very consistent to each others, being the stdd only 0.255 m/sec for the case SAMOSA+ versus SAR Marine and 0.214 m/sec for the case SAMOSA++ versus SAR Marine and with no significant bias.

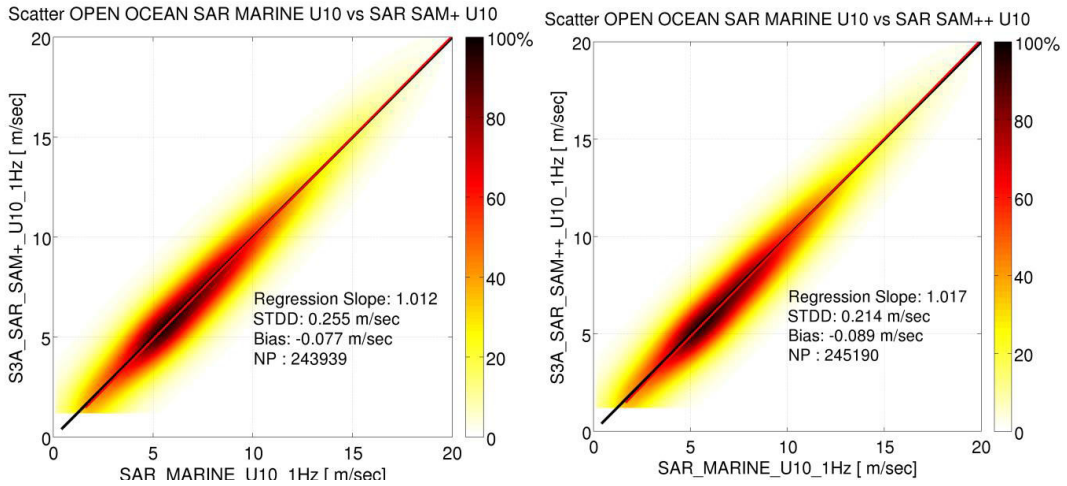

Figure 4.47: Scatterplot between U10 SAMOSA+ and U10 SAR Marine (left) and Scatterplot between U10 SAMOSA++ and SAR Marine (right)

c) DEPENDENCY PLOTS

The dependency plots are analyzed in this section. See section 4.1.2.1-c for the definition of dependency plot. About the dependency of SAMOSA+ and SAMOSA++ versus the sea state, using SAR marine as reference, one can notice immediately a slightly more pronounced dependency with the sea state for the case SAMOSA++. Indeed while the SAMOSA+ has flat cloud centred around zero with respect the SAR Marine dataset (see Figure 4.48 left), the same cloud has a tendency to diverge for high values of SWH (see Figure 4.48-right). Hence, in substance, the tracker bias (Fu and Cazenave, 2001) between SAMOSA+ and SAMOSA++ is not the same. This has been estimated for SAMOSA++ case as 0.7% of the SWH (hence for waves as high as 4 meter there is an average difference of 2.5 cm). It is not clear whether this is a small error to be fixed on the SAMOSA++ side or is a difference triggered by geophysical reasons. I remind that also for the range noise a difference was observed for big waves (noise reduction): it could be that, thanks to the RIP, the SAMOSA++ can fit better the waves or can take better in account the non linear sea level distributions.
About the SWH, the dependency plots of SAMOSA++ SWH and SAMOSA+ SWH versus the sea state (SWH) using SWH GCOAST/HZG as reference are depicted in Figure 4.49. From it, it can be concluded that the SAMOSA++ case has slightly less dependency versus GCOAST/HZG SWH than the case SAMOSA+. This dependency is present in both cases and is around 11% in case of SAMOSA+ and 9% in case of SAMOSA++.

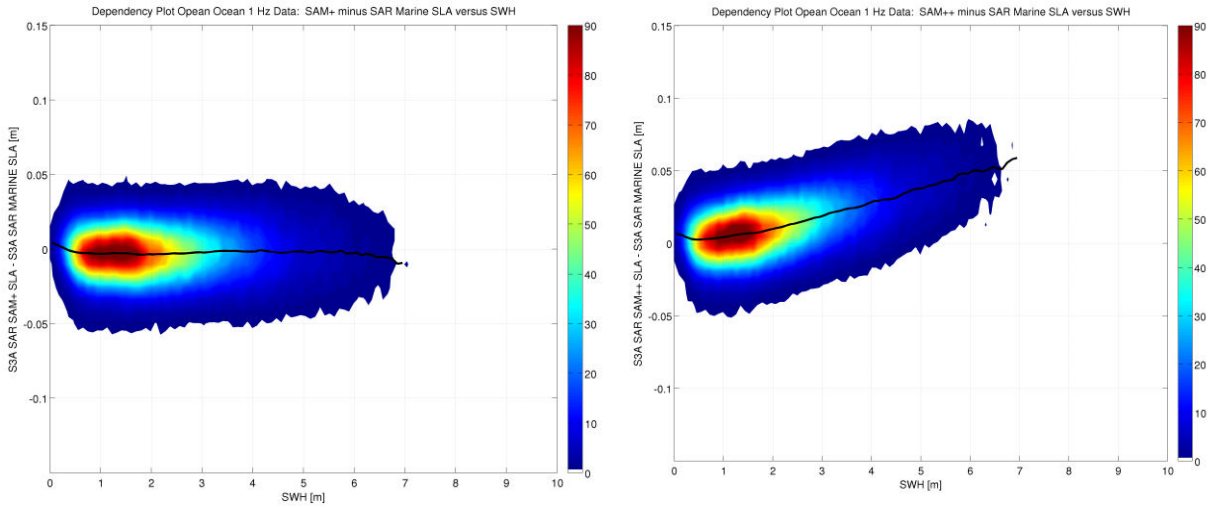

Figure 4.48: SLA Dependency plot versus sea state (SWH) with SAR marine SLA as reference for the case SAMOSA+ (left) and SAMOSA++ (right) in open ocean. Color code is data density in percentage

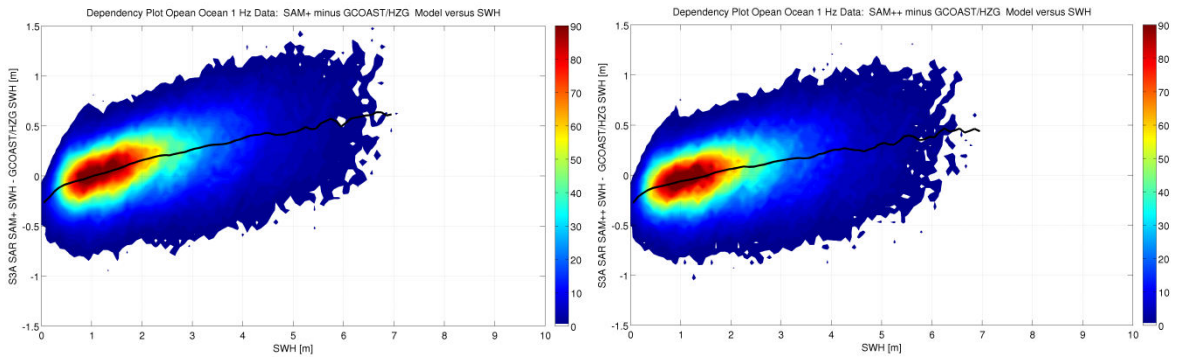

Figure 4.49: SWH Dependency plot versus sea state (SWH) with GCOAST/HZG SWH Model as reference for the case SAMOSA+ (left) and SAMOSA++ (right) in open ocean. Color code is data density in percentage

My conclusions are that the SAMOSA++ retracker, in this first realization, already performs decently well over open ocean as far as concern SLA, SWH and U10. For the SLA only a small tracker bias of 0.7% of the SWH was found while the SAMOSA++ SWH are clearly closer to GCOAST/HZG wave model than the case SAMOSA+. Furthermore, the SLA increases by +1 cm in case SAMOSA++ and the SAMOSA++ range noise is clearly lower for high sea state regimes. The wind speeds are in excellent agreement between the three cases (stdd around 20 cm/sec).

d) MEAN SQUARE SLOPE AND PITCH ESTIMATION FROM THE RIP

Using the SAMOSA++ retracker, the pitch and the mean square slope s^2 have been extracted from the RIP for the time period June 2016 to December 2018 in the region of interest. The corresponding time series of mean of one day is given in Figure 4.50. A clear annual cycle is visible for the mean square slope whereas the pitch features a slight drift in the first year of the mission and then it stabilizes around a value of 0.05 deg for the remaining part. A more extensive analysis on global scale would be needed to assess the significance of this parameter and to understand to what is correlated.

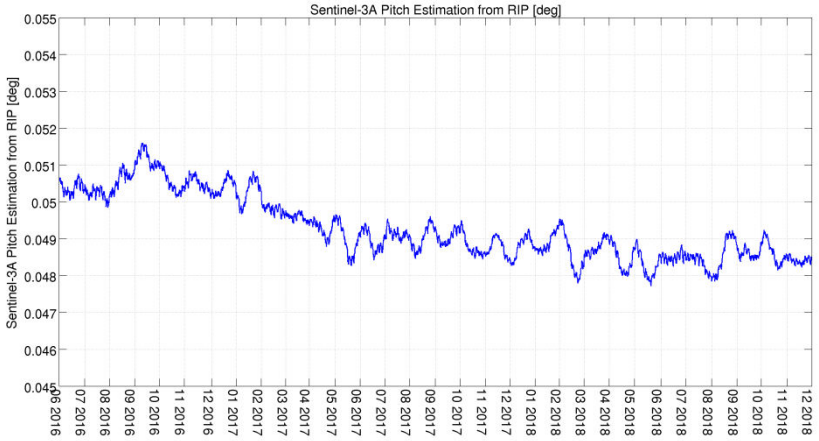

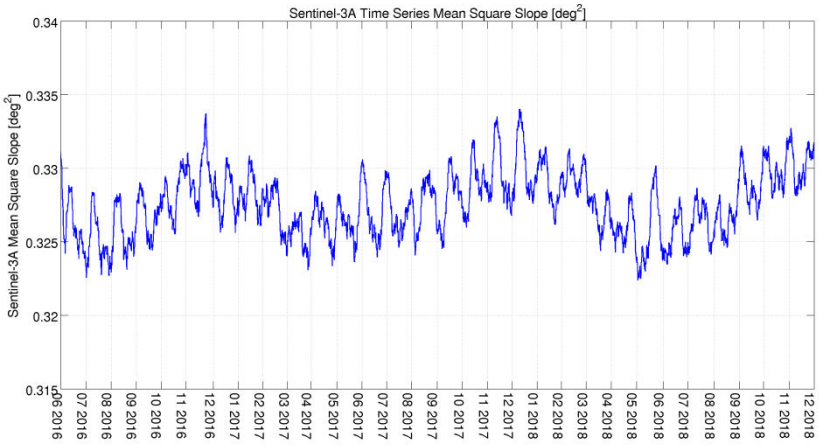

Figure 4.50: Time Series for Sentinel-3A Pitch (top) and Mean Square Slope (bottom) as estimated from the RIP (mean value for one day)

4.2.3 COASTAL ZONE RESULTS

After validating the three datasets against each other and the numerical model in open ocean, in this section, I present the results that have been obtained by the SAMOSA++ and SAMOSA+ retracker in the coastal zone and at 20 Hz versus the analogous results produced by SAR Marine, the numerical ocean circulation/wave models and tide gauges. The coastal zone is defined here as the strip between 0 and 10 km from the coast. The validation against the tide gauges and buoys will be treated in this chapter as well.

As preamble, I recall the result reported by (Dinardo et al., 2018b) who has shown how in the coastal zone the altimeters on board of Sentinel-3 and Cryosat-2 show very similar performance but Sentinel-3 has a slight better accuracy (see Figure 4.51). This slight superiority is attributed to the usage of the OLTC mode on board of Sentinel-3 (CryoSat-2 has not something similar on board).

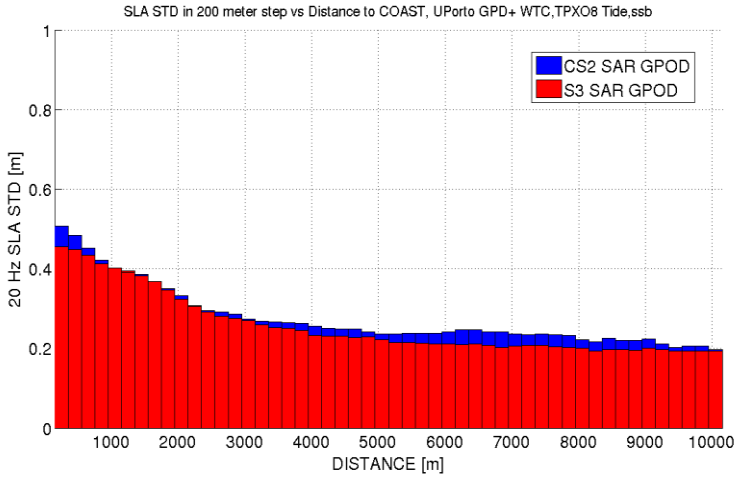

Figure 4.51: Standard deviation binned every 200 meter in the coastal zone: Sentinel-3A ha a slightly lower level of standard deviation than CryoSat-2

4.2.3.1 CROSS-VALIDATION BETWEEN SAMOSA++, SAMOSA+, SAR MARINE AND MODEL DATA

a) RESULTS AS FUNCTION OF DISTANCE TO COAST

In this section, the two geophysical quantities 20 Hz SLA and SWH versus the distance to the coast are analyzed. Figure 4.52 gives the SLA for SAMOSA++ and SAMOSA+ as cloud of points (red for

SAMOSA++ and blue for SAMOSA+) and as median curve versus the distance to the coast (green for SAMOSA+ and black for SAMOSA++). What can be observed is that the distribution of SLA is less spread in case of SAMOSA++ than in SAMOSA+, with 98.9% of the points within ± 1 m for SAMOSA++ while the corresponding percentage for SAMOSA+ is 97.2%. Particularly, in the critical band 0-2 km from the coast, SAMOSA++ is much less affected by land contamination compared to SAMOSA+, as the median curve in SAMOSA++ is slightly closer to zero than the corresponding SAMOSA+ curve. Also in the band between 2 and 10 km, the SAMOSA+ shows more sporadic outliers than the case SAMOSA++

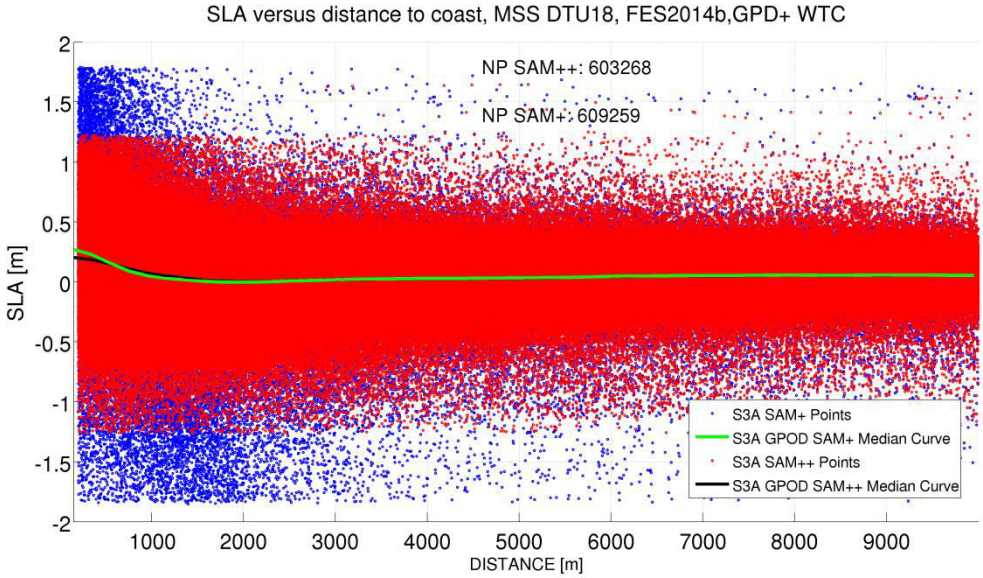

Figure 4.52: SLA cloud of points for SAMOSA++ (red points and black curve) and SAMOSA+ (blue points and green curve) versus distance to coast. NP is the number of points.

Figure 4.53 (left panel) shows the percentage of 20 Hz SLA measurements within ± 1 m versus the distance to coast. For distances larger than 2-3 kilometers from the coast, SAMOSA+ (red curve) and SAMOSA++ (black curve) SLA have similar percentages and for both this percentage is systematically higher than the corresponding for SAR Marine (blue curve). But at the shoreline, 98% of points are still within ± 1 m range for the SAMOSA++ case while for SAMOSA+ and SAR Marine this number drops to 92% and 83% respectively. Hence, the SAMOSA++ returns less outlier values than SAMOSA+ and SAR Marine for all the range of the distances to the coast. On the right side of Figure 4.53, the percentage of the un-defaulted points (i.e. measurements not set to a Fill Value as NaN by the retracker) is depicted for the three datasets versus distance to the coast: also from this plot, one can conclude that SAMOSA++ returns a larger percentage of available measurements than the other two datasets.

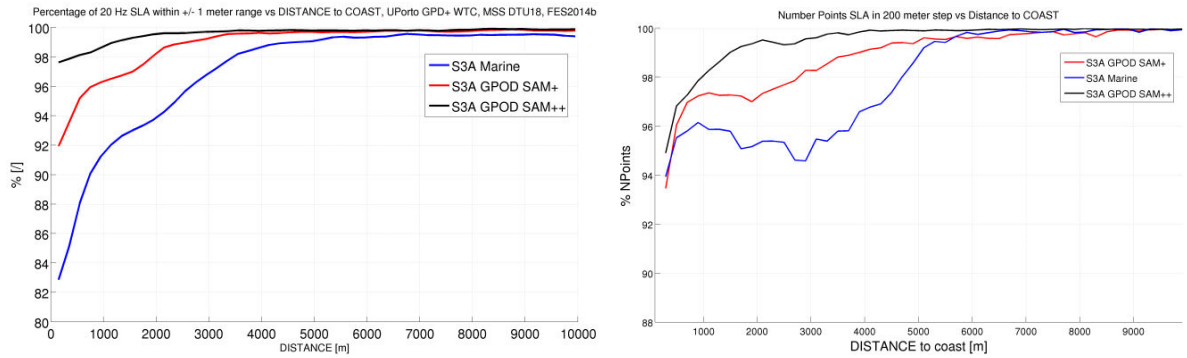

Figure 4.53: On the left, percentage of 20 Hz SLA within ± 1 meter range versus the distance to the coast for SAMOSA++ (black curve), for SAMOSA+ (red curve) and SAR Marine (blue curve). On the right, percentage of 20 Hz SLA un-defaulted measurements versus the distance to the coast for SAMOSA++ (black curve), for SAMOSA+ (red curve) and SAR Marine (blue curve)

Similarly, in Figure 4.54, the plot as in Figure 4.52 is presented for the SWH parameter.

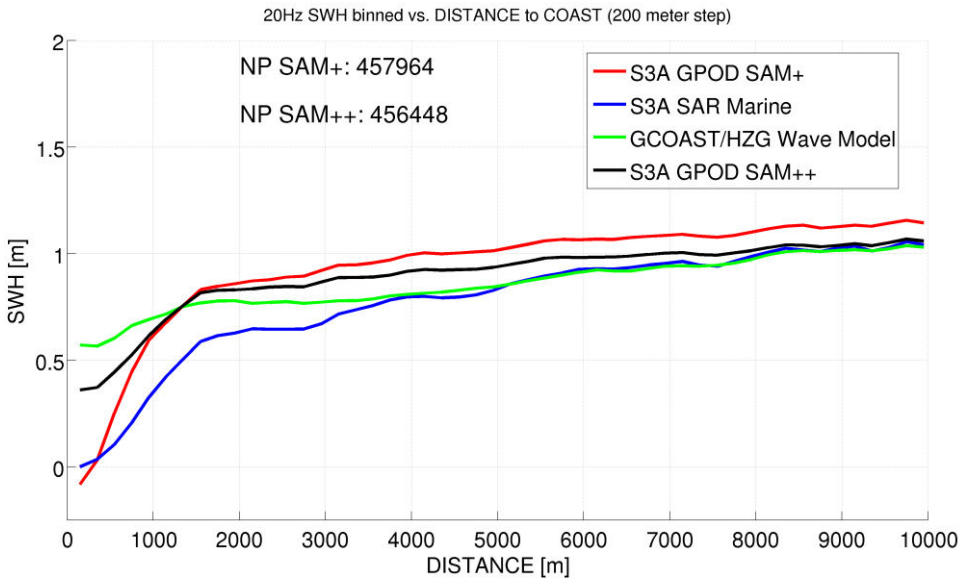

Figure 4.54: 20 Hz SWH median of points curve for SAMOSA++ (black curve), SAMOSA+ (red curve), SAR Marine (blue curve), GCOAST/HZG wave model (green curve) versus distance to the coast. NP is the number of points

Figure 4.54 illustrates that the GCOAST/HZG wave model shows a stable behaviour up to the shoreline; a similar trend is exhibited by all the three altimetric SWH datasets but at 1.5 km from the coast, the SAR Marine SWH level drops while SAMOSA+ and SAMOSA++ are more stable, SAMOSA++ being slightly closer to the wave model.

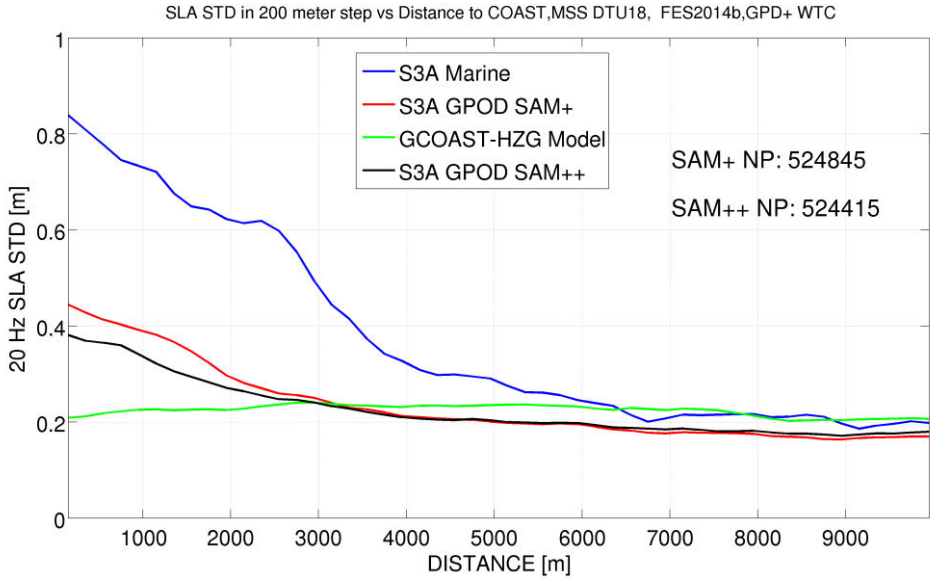

Figure 4.55: SLA std in 200 meter bins of distance to coast for GCOAST/HZG model (green curve), SAR Marine (blue curve), SAMOSA+ (red curve) and SAMOSA++ (black curve)

Figure 4.55 shows a plot of the SLA standard deviation in 200 meter bins of distance to coast for SAR Marine (blue curve), SAMOSA+ (red curve), SAMOSA++ (black curve) and GCOAST model (green curve). This plot is meant to give an idea of the level of errors in the three altimetry datasets in the coastal zone. From this plot, hence, it can be observed that the SLA std for the SAR Marine is much higher than the SAMOSA+ std and SAMOSA++ std for all values of distance to coast (SAR Marine reaching a value of almost 0.8 meter at the shoreline). Furthermore, SAMOSA++ systematically leads to smaller SLA std values than SAMOSA+ in the critical band between 0-3 km. The improvement is around 20% at shoreline.

Noticeably, SAMOSA++ and SAMOSA+ have basically the same level of std between 3 and 10 km. Hence, the improvement brought by SAMOSA++ is basically in the strip 0-3 km from the coast.
Figure 4.56 gives a similar plot as in Figure 4.55 for SWH. From it, the GCOAST/HZG wave model features the lowest level of std. SAMOSA++ is the second best with a lower level of std with respect to SAMOSA+ and SAR Marine for all the values of distance to coast except in the very proximity of the shorelines (less than 1 km). It is not clear whether this abrupt change of std represents a geophysical variability that the SAMOSA++ retracker is capable of capturing or whether it is a warning of residual errors in the SAMOSA++ estimates in the band 0-1 km. This will require a more in depth investigation.

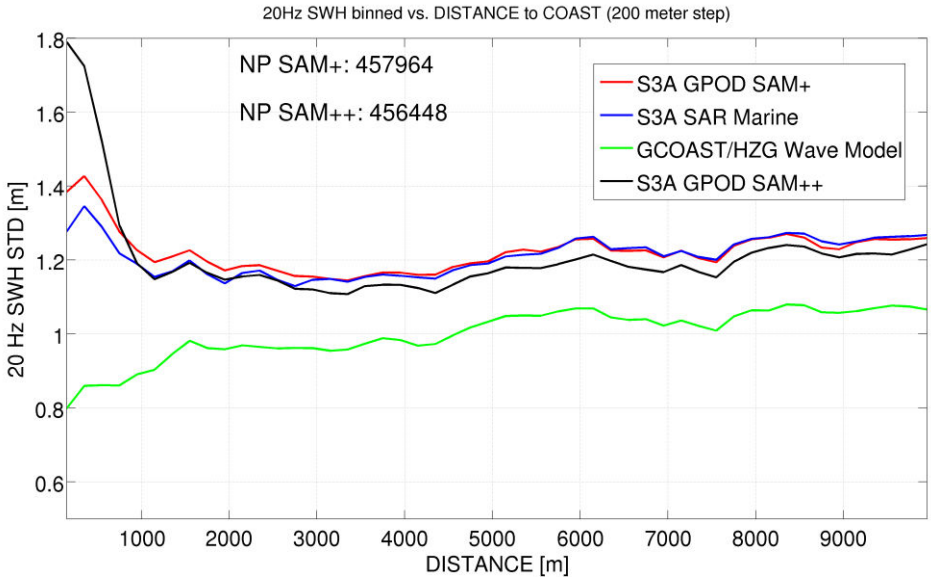

Figure 4.56: SWH std in 200 meter bins of distance to coast for HZG wave model (green curve), SAR Marine (blue curve), SAMOSA+ (red curve), SAMOSA++ (black curve)

Finally, Figure 4.57 depicts the SAMOSA++ SLA std versus the distance to the coast when the three tide models FES2014b, TPXO8-ATLAS and TPXO9-ATLAS are used in the SLA estimation. From this figure, it is clear that FES2014b prevails slightly over TPXO8-ATLAS and TPXO9-ATLAS tide model in my region of interest with TPXO9-ATLAS being slightly superior to TPXO8-ATLAS.
Given the better behavior in terms of std reduction provided by the FES2014b tide model in the region under analysis, this will be the tide model adopted for the in situ validation carried out in this chapter.
Finally, the reduction in the std brought by GPD+ wet tropospheric corrections (solutions 1 and solution 2) compared to the ECMWF model is depicted in right panel of Figure 4.57 versus distance to the coast, when using the SAMOSA++ SLA. From Figure 4.57-right, one can appreciate that both GPD1 and GPD2 solutions provide an improvement (i.e. reduction of std) with respect to the ECMWF WTC (in particular in the band 0-1 km from the shoreline) and that GPD2 is slightly superior to GPD1. This means that, as expected, the WTC that incorporates the measurements of the Sentinel-3 on-board MWR is slightly better than the corresponding solution that only uses third party data. For this reason, GPD2 will be the solution used for the in situ validation in this chapter.
It is worth noticing that, particularly in the critical band 0-1 km from the coast, the effect of the WTC is significantly larger than that of the tide model (reduction of std of 0.1 to 0.5 cm for the former versus less than 0.1 cm for the latter).

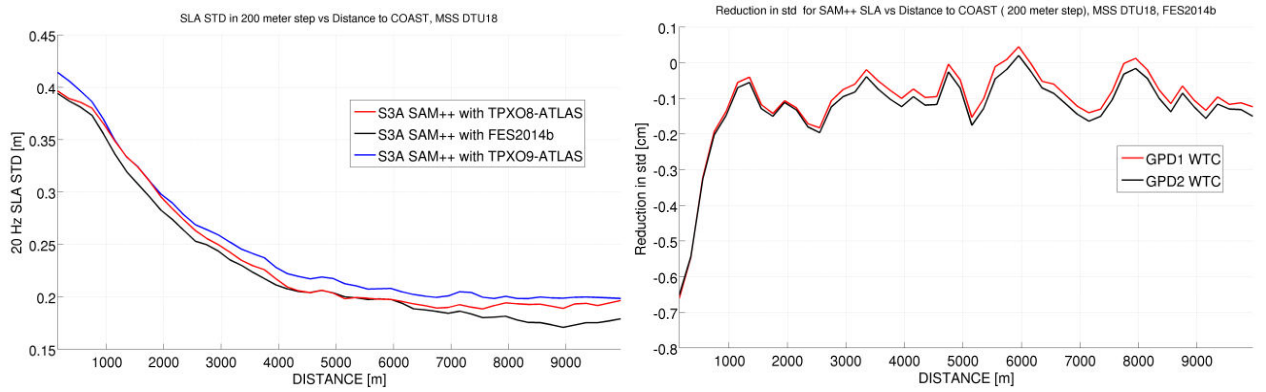

Figure 4.57: On the left, the SLA std in 200 meter bins of distance to the coast for SAMOSA++ with TPXO8-ATLAS tide model (blue curve), with TPXO9-ATLAS tide model (red curve), and with FES2014b (black curve). On the right, the reduction in std versus the distance to the coast for the case SAMOSA++ with GPD1 WTC (red curve) and with GPD2 WTC (black curve) when compared to ECMWF WTC

b) RESULTS VIA SCATTERPLOTS

In this section, the consistency between SAMOSA+, SAMOSA++, SAR Marine and ocean model data in the coastal zone is assessed by means of scatter plots. The quantities considered are DOTi and SWH at 20 Hz.
Figure 4.58 gives the scatterplot between SAMOSA+ DOTi and GCOAST/HZG DOTi (top-left), SAMOSA++ DOTi and GCOAST/HZG DOTi (top-right) and between SAR Marine and GCOAST/HZG DOTi (bottom) whereas Figure 4.59 gives the scatterplot between SAMOSA+ SWH and GCOAST/HZG SWH (top-left), between SAMOSA++ SWH and GCOAST/HZG SWH (top-right) and between the SAR Marine SWH and GCOAST/HZG SWH (bottom).
From both Figure 4.58 and Figure 4.59, SAMOSA++ dataset shows a slightly better consistency (in term of STDD) versus the GCOAST/HZG circulation and wave model in comparison with the SAMOSA+ and SAR Marine whereas both SAMOSA++ and SAMOSA+ dataset outperform SAR Marine. Indeed, the DOTi stdd between SAMOSA++ and model DOTi is 25.8 cm while it is 26.9 cm and 49.8 cm respectively for SAMOSA+ DOTi and SAR Marine DOTi. Analogously, the SWH stdd between SAMOSA++ and model SWH is 70.4 cm while it is 73.3 cm and 82.1 cm respectively for SAMOSA+ SWH and SAR Marine SWH. While the three altimetry SWH datasets have no significant bias with respect to the GCOAST/HZG model, the three altimetry DOTi datasets have a bias of around 10 cm with respect to the GCOAST/HZG DOTi.

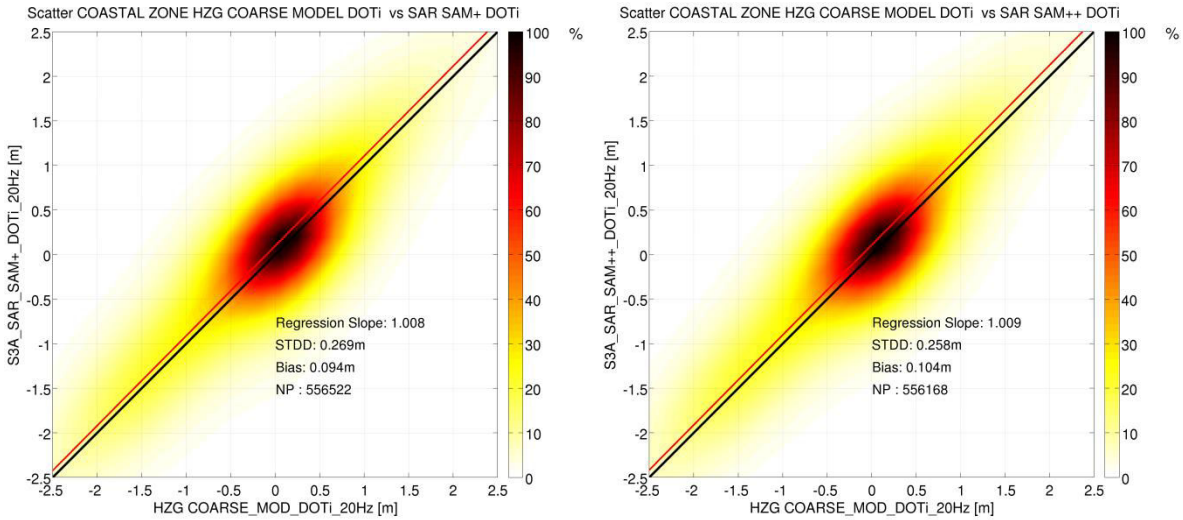

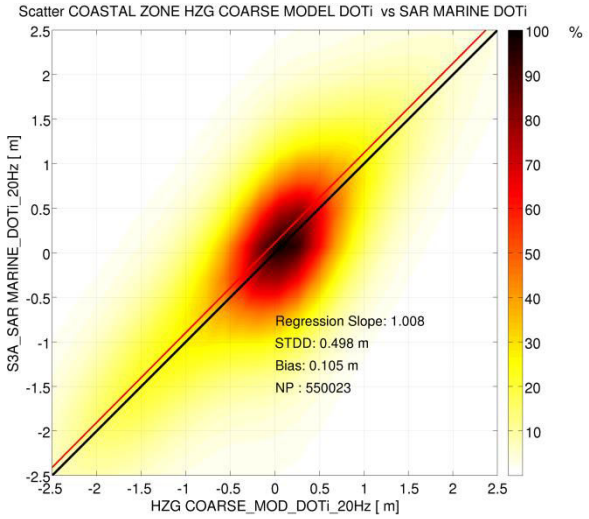

Figure 4.58: Scatter Plot in the coastal zone between SAMOSA+ DOTi and GCOAST/HZG Model DOTi (top-left), between SAMOSA++ DOTi and GCOAST/HZG Model DOTi (top-right) and between SAR Marine DOTi and GCOAST/HZG Model DOTi (bottom). Color scale gives data density. NP is the number of points

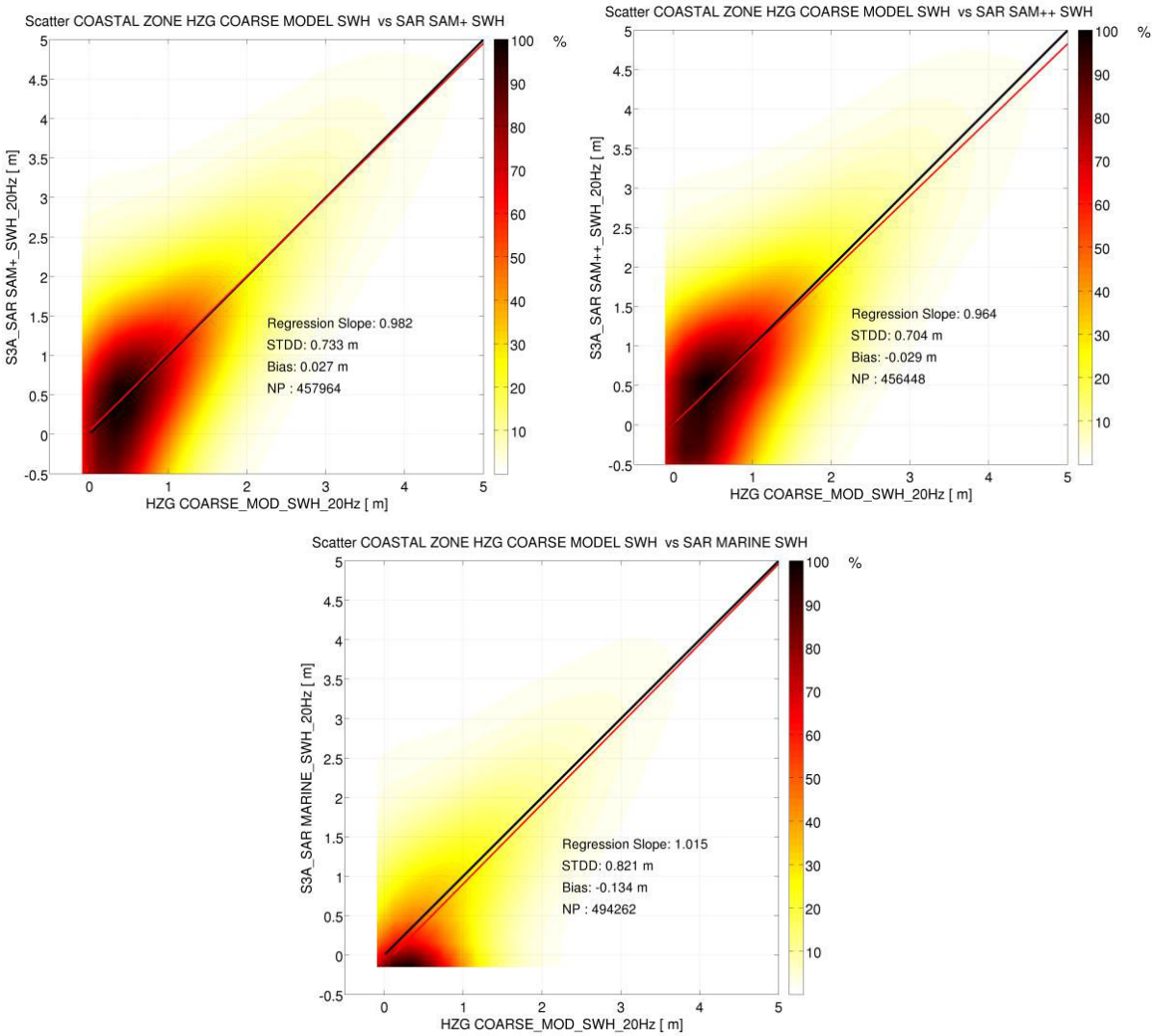

Figure 4.59: Scatter Plot in the coastal zone between SAMOSA+ SWH and GCOAST/HZG Model SWH (top-left), between SAMOSA++ SWH and GCOAST/HZG SWH (top-right) and between SAR Marine SWH and GCOAST/HZG Model SWH (bottom). Color scale gives data density. NP is the number of points

The statistics from the scatter plots are summarized in Table 4.9. The correlation coefficient between the altimetric DOTi and the GCOAST/HZG model DOTi is higher in SAMOSA++ (0.972) than in SAMOSA+ (0.969) and in SAR Marine (0.907). Hence, from this cross-comparison with the GCOAST/HZG model, the conclusion is reached that the SAMOSA++ is slightly superior to SAMOSA+ in the coastal zone as the estimated geophysical parameters are closer to the ocean circulation and wave models. SAR Marine is the dataset performing worst but this was expected as the SAR marine retracker is not a coastal zone dedicated solution.

Measurement in the coastal zone	**DOTi**					**SWH**				
Index	**median cm**	**std cm**	**Corr**	**Slope**	**N Points**	**median cm**	**std cm**	**Corr**	**Slope**	**N Points**
SAMOSA++	18.5	109.7	-	-	556168	94.0	118.9	-	-	456448
SAMOSA+	17.2	110.6	-	-	556552	101.1	122.1	-	-	457964
SAR Marine	18.6	118.4	-	-	550023	83.8	126.7	-	-	494262
GCOAST/HZG	13.0	106.8	-	-	-	87.6	102.0			-
SAMOSA++ minus GCOAST/HZG	10.4	25.8	0.97	1.01	556168	-2.9	70.4	0.81	0.96	456448
SAMOSA+ minus GCOAST/HZG	9.4	26.9	0.97	1.01	556522	2.7	73.3	0.80	0.98	457964
SAR Marine - GCOAST/HZG	10.5	49.8	0.90	1.01	550023	-13.4	82.1	0.76	1.01	494262

Table 4.9: Statistics for SAMOSA++, SAMOSA+, SAR Marine and GCOAST/HZG for DOTi and SWH in the coastal zone

c) MONTHLY TIME SERIES IN THE COASTAL ZONE

In this subsection, I compute the monthly mean and std time series of instantaneous DOT (DOTi) and SWH in the region under study in the time interval from June 2016 to December 2018 for SAMOSA++, SAMOSA+, SAR Marine and ocean model. Here, the monthly mean and std are the mean and standard deviation of all measurements available in each month. When computing the time series, I restrict my analysis to the band of 0-10 km from the coast (coastal zone).

The time series for DOTi are reported in Figure 4.60-left. The DOTi monthly mean time series from SAMOSA++, SAMOSA+, SAR marine and GCOAST/HZG model exhibit a very similar behavior as the correlation coefficient is 0.94 between SAMOSA++ and model, 0.93 between SAMOSA+ and model and 0.92 between SAR Marine and the model (see Table 4.10). The bias between GCOAST/HZG model and altimetry is around 10 cm for SAMOSA+ and SAR Marine and 12 cm for SAMOSA++ and this is due mainly to a different reference surface, as discussed before. However, SAR Marine average monthly std is around 1.164 m while the SAMOSA++ and SAMOSA+ average monthly std are respectively 1.094 m and 1.097 m and hence closer to the GCOAST/HZG std (1.065 m).From these results, it can be concluded that the DOTi monthly mean in the coastal zone is measured by SAMOSA++ and SAMOSA+ much more accurately than by the SAR Marine, with SAMOSA++ having a slight superiority.

Figure 4.60**:** On the left, DOTi monthly mean (top) and std (bottom) time-series in the coastal zone (0-10 km) for SAMOSA++ (black line), SAMOSA+ (red line) SAR Marine (blue line) and GCOAST/HZG Model (green line). On the right, SWH monthly mean (top) and std (bottom) time-series in the coastal zone (0-10 km) for SAMOSA++ (black line), SAMOSA+ (red line), SAR Marine (blue line) and GCOAST/HZG Model (green curve)

Figure 4.60-right represents the corresponding SWH monthly mean time series showing that all the four datasets (SAMOSA++, SAMOSA+, SAR marine and GCOAST model) are consistent in recording the monthly mean variability (correlation coefficient is 0.96 between GCOAST and SAR Marine and is 0.98 between GCOAST and SAMOSA++/SAMOSA+). From Table 4.10, this SWH monthly mean variability is returned slightly more precisely by SAMOSA++ (SAMOSA++ average std is 1.157 m whereas SAMOSA+ std and SAR marine are respectively 1.179 and 1.167 m) than by SAMOSA+ and SAR Marine. The std of the GCOAST/HZG wave model data is lower than the corresponding altimetry ones (0.947 m) value and indicates that a further improvement in SAR SWH estimates in coastal zone is possible. There is no significant bias between SAMOSA++ SWH, SAMOSA+ SWH, SAR Marine SWH and GCOAST SWH in the coastal zone (see Table 4.10).

Measurement	**DOTi**			**SWH**		
Index	**median cm**	**average std cm**	**corr**	**median cm**	**average std cm**	**corr**
SAMOSA++	12.2	109.4	0.94	93.7	115.7	0.98
SAMOSA+	10.0	109.7	0.93	99.9	117.9	0.98
SAR Marine	9.2	116.4	0.92	84.5	116.7	0.96
GCOAST/HZG	0.8	106.5	/	91.7	94.7	/

Table 4.10: Statistics for SAMOSA++, SAMOSA+, SAR Marine and Ocean Model for DOTi and SWH

Hence, from all the results in this section the conclusion is reached that the SAMOSA++ overcomes SAMOSA+ in the coastal zone showing less std versus the distance to the coast and being closer to the ocean circulation and wave models.

4.2.3.2 IN SITU VALIDATION

a) VALIDATION OF SLAio

As done for CryoSat-2, also for Sentinel-3 I select, for each satellite track, the altimeter measurement nearest in space to that station which is, for the validation in the coastal zone:

- between 0 kilometres and 10 kilometres from the tide gauge
- below 10 kilometres from the coast

and for the validation in open ocean:

- between 10 kilometres and 20 kilometres from the tide gauge
- more 10 kilometres away from the coast

The fiducial tide gauges locations are shown in Figure 4.39 as green triangles: they are Helgoland (HELG), Sassnitz (SASS), Schleimünde (SCHL),Warnemünde (WARN) and LichtTurm Kiel (LTKI) for the validation in open ocean and LichtTurm Alte Weser (LTAW), LichtTurm Kiel (LTKI) and Travemünde (TRAV) for the validation in the coastal zone.. In making the cross-validation of altimetry versus tide gauge, I have removed the mean sea surface along the Sentinel-3 passes using the DTU18 mean sea surface model. Hence, the altimetric quantity that I have used in the tide gauge cross-comparison is the SLAio i.e. SLAi corrected for the FES2014b ocean tide in this case. Since the purpose of this study is not the estimation of the Sentinel-3 absolute range bias, I do not carry out an absolute validation between Sentinel-3 altimeter and tide gauges heights using GNSS data which the tide gauges are equipped with. Because the distance to the coast parameter available from the SAR Marine products is given at coarse resolution (EUMETSAT 2019), it has been recomputed at high resolution for this dataset exploiting the MOD44W water/land mask (Carroll et al., 2009).
In Figure 4.61 and Figure 4.62, the time series for the SAMOSA++, SAMOSA+, SAR Marine and Tide Gauge elevations in open ocean and the coastal zone are shown, while in Table 4.11 and Table 4.12 the corresponding statistics from the in situ cross-comparison are summarized in terms of stdd, correlation and slope respectively in the coastal zone and open ocean. Unfortunately, the Sentinel-3 track does not overpass Helgoland station in the coastal zone.

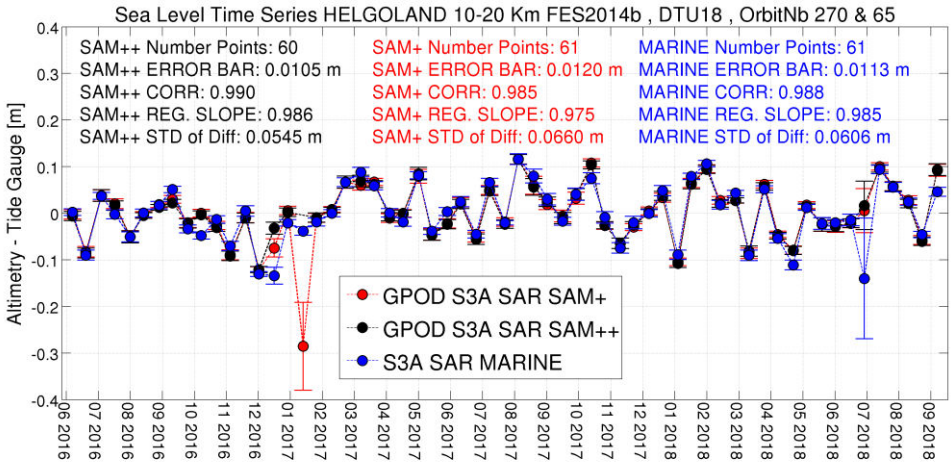

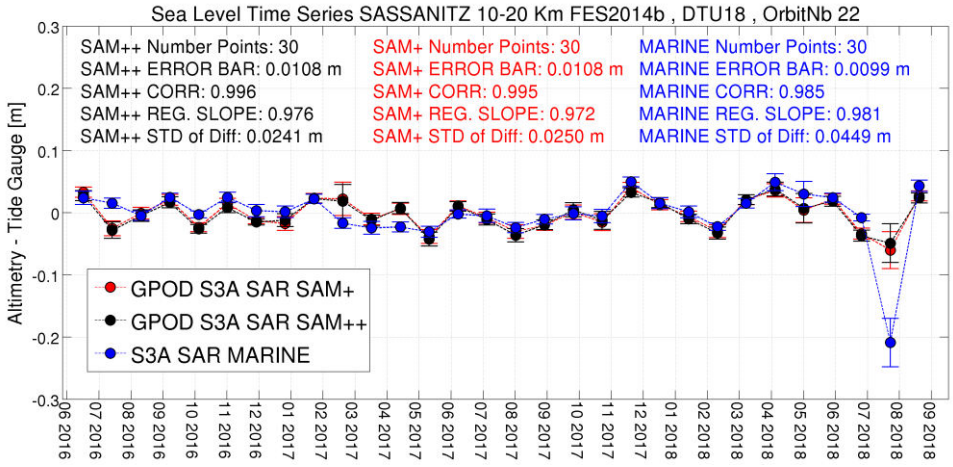
Sea Level Time Series SASSANITZ 10-20 Km FES2014b , DTU18 , OrbitNb 22
SAM++ Number Points: 30
SAM++ ERROR BAR: 0.0108 m
SAM++ CORR: 0.996
SAM++ REG. SLOPE: 0.976
SAM++ STD of Diff: 0.0241 m
SAM+ Number Points: 30
SAM+ ERROR BAR: 0.0108 m
SAM+ CORR: 0.995
SAM+ REG. SLOPE: 0.972
SAM+ STD of Diff: 0.0250 m
MARINE Number Points: 30
MARINE ERROR BAR: 0.0099 m
MARINE CORR: 0.985
MARINE REG. SLOPE: 0.981
MARINE STD of Diff: 0.0449 m
GPOD S3A SAR SAM+
GPOD S3A SAR SAM++
S3A SAR MARINE
Altimetry - Tide Gauge [m]

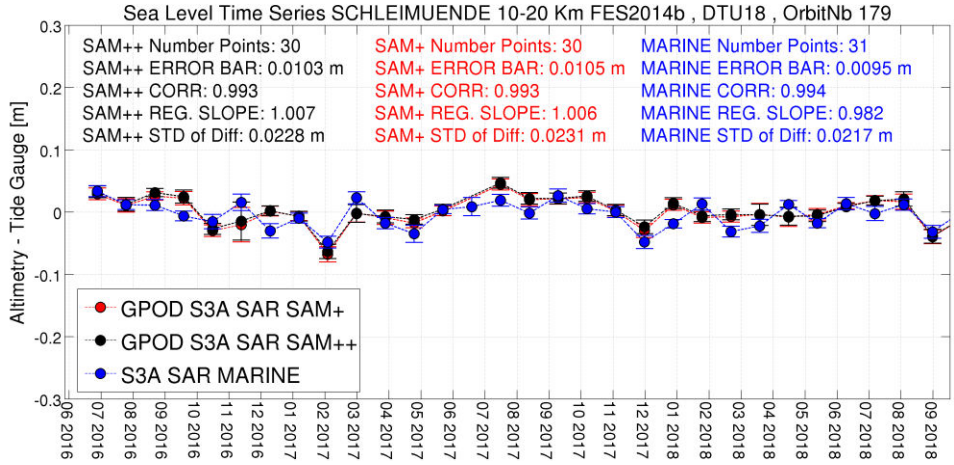
Sea Level Time Series SCHLEIMUENDE 10-20 Km FES2014b , DTU18 , OrbitNb 179
SAM++ Number Points: 30
SAM++ ERROR BAR: 0.0103 m
SAM++ CORR: 0.993
SAM++ REG. SLOPE: 1.007
SAM++ STD of Diff: 0.0228 m
SAM+ Number Points: 30
SAM+ ERROR BAR: 0.0105 m
SAM+ CORR: 0.993
SAM+ REG. SLOPE: 1.006
SAM+ STD of Diff: 0.0231 m
MARINE Number Points: 31
MARINE ERROR BAR: 0.0095 m
MARINE CORR: 0.994
MARINE REG. SLOPE: 0.982
MARINE STD of Diff: 0.0217 m
GPOD S3A SAR SAM+
GPOD S3A SAR SAM++
S3A SAR MARINE
Altimetry - Tide Gauge [m]

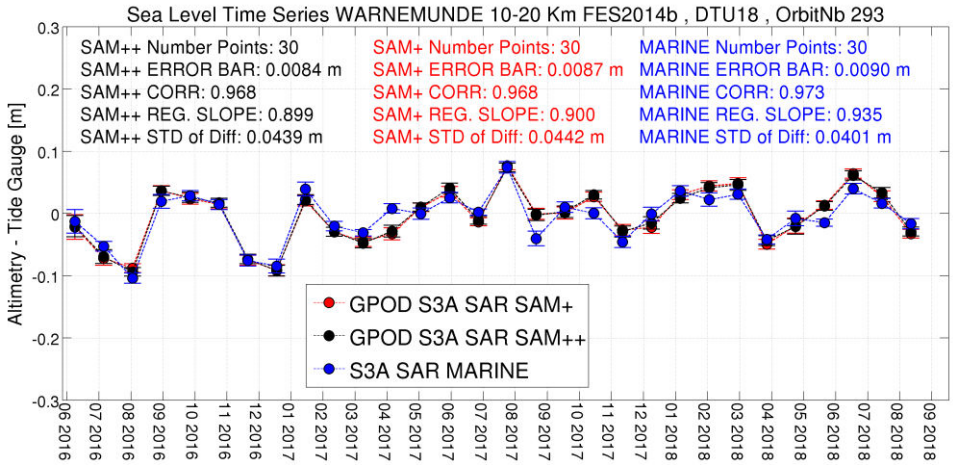
Sea Level Time Series WARNEMUNDE 10-20 Km FES2014b , DTU18 , OrbitNb 293
SAM++ Number Points: 30
SAM++ ERROR BAR: 0.0084 m
SAM++ CORR: 0.968
SAM++ REG. SLOPE: 0.899
SAM++ STD of Diff: 0.0439 m
SAM+ Number Points: 30
SAM+ ERROR BAR: 0.0087 m
SAM+ CORR: 0.968
SAM+ REG. SLOPE: 0.900
SAM+ STD of Diff: 0.0442 m
MARINE Number Points: 30
MARINE ERROR BAR: 0.0090 m
MARINE CORR: 0.973
MARINE REG. SLOPE: 0.935
MARINE STD of Diff: 0.0401 m
GPOD S3A SAR SAM+
GPOD S3A SAR SAM++
S3A SAR MARINE
Altimetry - Tide Gauge [m]

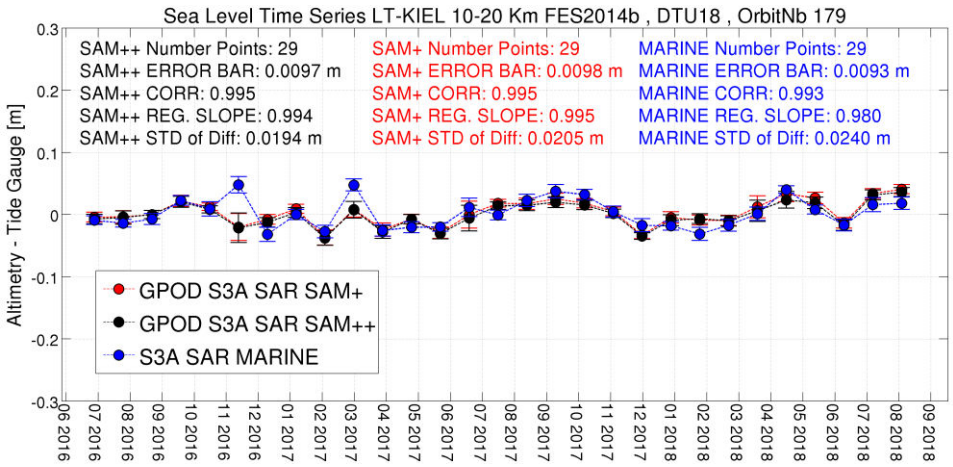

Figure 4.61: Time Series of the SLAio difference between SAMOSA+ (red circles), SAMOSA++ (black circles), SAR Marine (blue circles) in open ocean conditions (10-20 km from the coast) at Helgoland (first row), Sassanitz (second row), Schleimuende (third row), Warnemunde (fourth row) and LT-Kiel (fifth row). The distance from the station is between 10 and 20 km.

Data	SAMOSA++ SLAio				SAMOSA+ SLAio				SAR Marine SLAio			
Index	stdd cm	corr	slope	N Points	stdd cm	corr	slope	N Points	stdd cm	corr	slope	N Points
HELG	5.4	0.99	0.98	60	6.6	0.98	0.97	61	6.0	0.98	0.98	61
SASS	2.4	0.99	0.97	30	2.5	0.99	0.97	30	4.4	0.98	0.98	30
SCHL	2.2	0.99	1.00	30	2.3	0.99	1.00	30	2.1	0.99	0.98	30
WARN	4.3	0.96	0.89	30	4.4	0.96	0.90	30	4.0	0.97	0.93	30
LT-KIEL	1.9	0.99	0.99	29	2.0	0.99	0.99	29	2.4	0.99	0.98	29

Table 4.11: Statistics of the SLAio in situ cross-comparison for SAMOSA++, SAMOSA+ and SAR Marine dataset in open ocean (10-20 km from the coast). The distance from the station is between 10 and 20 km.

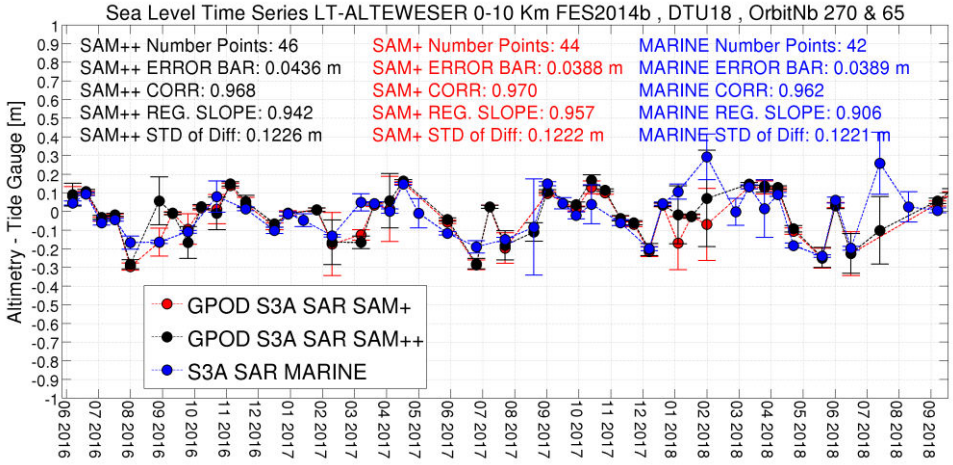

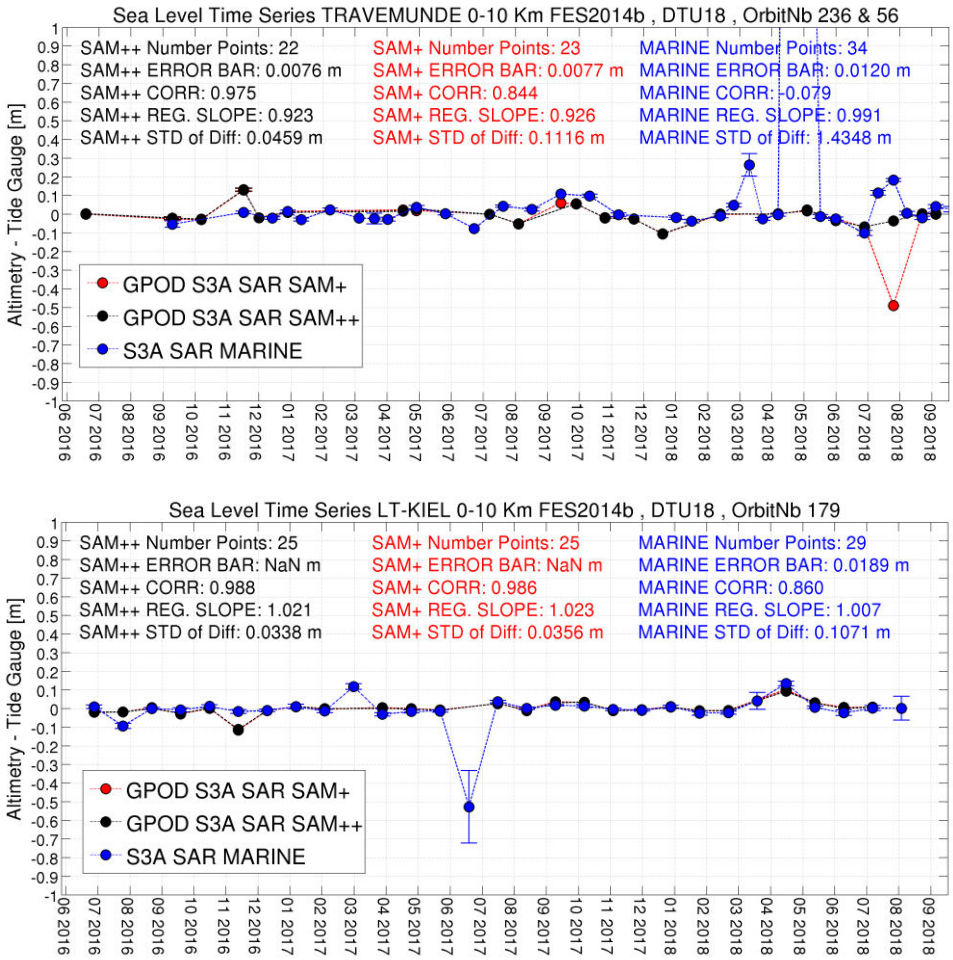

Figure 4.62: Time Series of the SLAio difference between SAMOSA+ (red circles), SAMOSA++ (black circles), SAR Marine (blue circles) in the coastal zones conditions (0-10 km from the coast) at Light House Alte-Wasser (top), Travemunde (middle) and Light House Kiel (bottom). The distance between station and altimeter is smaller than 10 km.

Data	SAMOSA++ SLAio				SAMOSA+ SLAio				SAR Marine SLAio			
Index	stdd cm	corr	slope	N Points	stdd cm	corr	slope	N Points	stdd cm	corr	slope	N Points
LTAW	12	0.96	0.94	46	12	0.97	0.95	44	12	0.96	0.90	42
TRAV	4.5	0.97	0.92	22	11	0.84	0.92	23	143	0.97	0.99	34

Table 4.12: Statistics of the SLAio in situ cross-comparison for SAMOSA++, SAMOSA+ and SAR Marine dataset in the coastal zone (0-10 km). The distance from the station is between 0 and 10 km

In open ocean, for distance to coast between 10 and 20 km, the average SLAio standard deviation of the difference is 3.2 cm, 3.5 cm and 3.8 cm for SAMOSA++, SAMOSA+ and SAR Marine respectively (Table 4.11). In coastal zone, for distance to coast between 0 and 10 km, the average stdd is 6.6 cm, 8.8 cm and 55 cm for SAMOSA++, SAMOSA+ and SAR Marine respectively (Table 4.12). In open ocean, the average correlation is 0.99, 0.98 and 0.98 for SAMOSA++, SAMOSA+ and SAR Marine respectively; while in the coastal zone, the corresponding average correlations are 0.97, 0.93 and 0.93 respectively.

The regression slopes are very close to one for all three altimetry datasets. One could notice a slight superiority of SAMOSA++ results with respect to the SAMOSA+ and SAR Marine in the open ocean case but in general the three solutions are very close to each other in the open ocean conditions.

In the coastal zone, at LTAW, the three altimetric dataset behave very closely to each other (stdd 12 cm), the Sentinel-3 track being on average at 9 km from the shoreline, hence almost in open sea, whereas at LT-KIEL and TRAV, the SAMOSA++ prevails significantly over the other two datasets as for these two stations the Sentinel-3 tracks are in the very proximity of the coast (2 km and 1 km respectively).In general, the stdd with respect to the Baltic stations (SASS, WARN, TRAV, LT-KIEL, SCHL) are generally lower than the stdd of the German Bight stations (HELG and LHAW): this is attributable to higher residual errors in the tide modeling (FES2014b) at the German Bight stations whereas for the Baltic stations, the tidal amplitudes being smaller, these errors are less impacting.

b) VALIDATION OF SWH

The BfG/WSV institution operates five directional wave rider (DWR) buoys at Helgoland South, Helgoland Nord, Darsser, Elbe and Arkona. The locations of these five buoys are shown in Figure 4.39 as purple squares. The DWR time series are available between January 2016 and December 2018 with a temporal sampling of 30 minutes. As before, for a given in situ station, the time lag between in situ data and 1-Hz altimeter data is selected to be less than 30 minutes. For each satellite track, I select the altimeter measurement nearest in space to each in situ station and within a selected interval of distance from the station. The validation of the altimetry SWH versus in situ data will be only in open ocean (interval of distance between 10-20 km) since there is no occurrence of a Sentinel-3A track in the coastal zone (i.e. 0-10 km from the coast) in the proximity of the above-mentioned 5 buoys.
Figure 4.63 depicts the time series of the SWH difference between the buoys data and SAMOSA+, SAMOSA++, SAR Marine and GCOAST/HZG wave model data at Helgoland South (HELG-SUD), Helgoland North (HELG-NORD), Arkona (ARK), Darsser (DAR), and Elbe (ELB), while the corresponding statistical results (std, mean, correlation and regression slope) are summarized in Table 4.13 for the same stations.

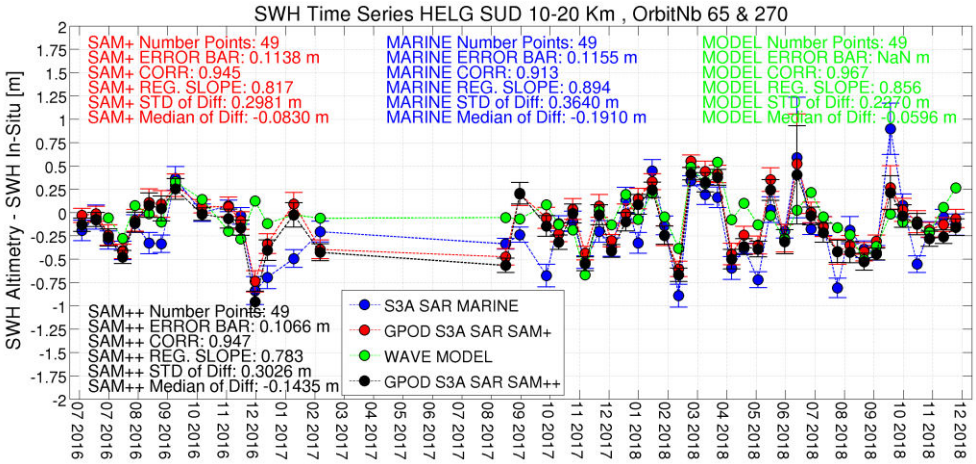

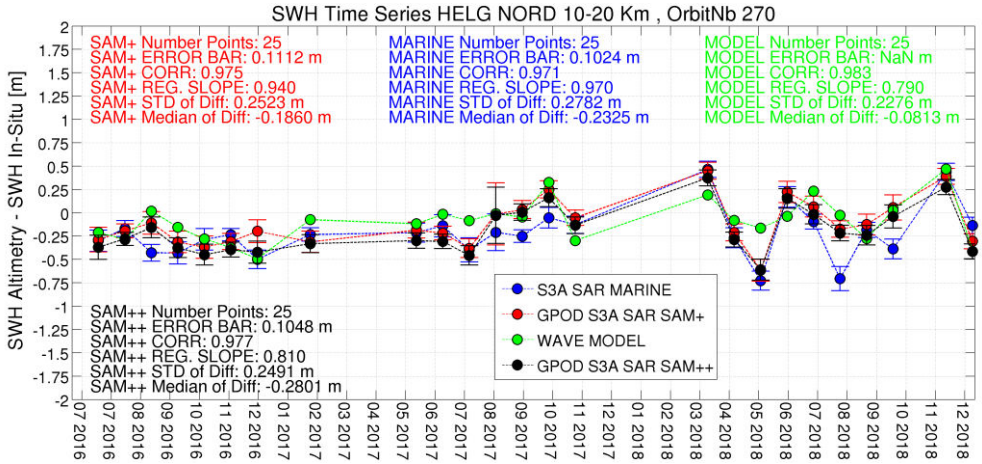
SWH Time Series HELG NORD 10-20 Km , OrbitNb 270
SAM+ Number Points: 25
SAM+ ERROR BAR: 0.1112 m
SAM+ CORR: 0.975
SAM+ REG. SLOPE: 0.940
SAM+ STD of Diff: 0.2523 m
SAM+ Median of Diff: -0.1860 m
MARINE Number Points: 25
MARINE ERROR BAR: 0.1024 m
MARINE CORR: 0.971
MARINE REG. SLOPE: 0.970
MARINE STD of Diff: 0.2782 m
MARINE Median of Diff: -0.2325 m
MODEL Number Points: 25
MODEL ERROR BAR: NaN m
MODEL CORR: 0.983
MODEL REG. SLOPE: 0.790
MODEL STD of Diff: 0.2276 m
MODEL Median of Diff: -0.0813 m
SAM++ Number Points: 25
SAM++ ERROR BAR: 0.1048 m
SAM++ CORR: 0.977
SAM++ REG. SLOPE: 0.810
SAM++ STD of Diff: 0.2491 m
SAM++ Median of Diff: -0.2801 m
S3A SAR MARINE
GPOD S3A SAR SAM+
WAVE MODEL
GPOD S3A SAR SAM++
SWH Altimetry - SWH In-Situ [m]

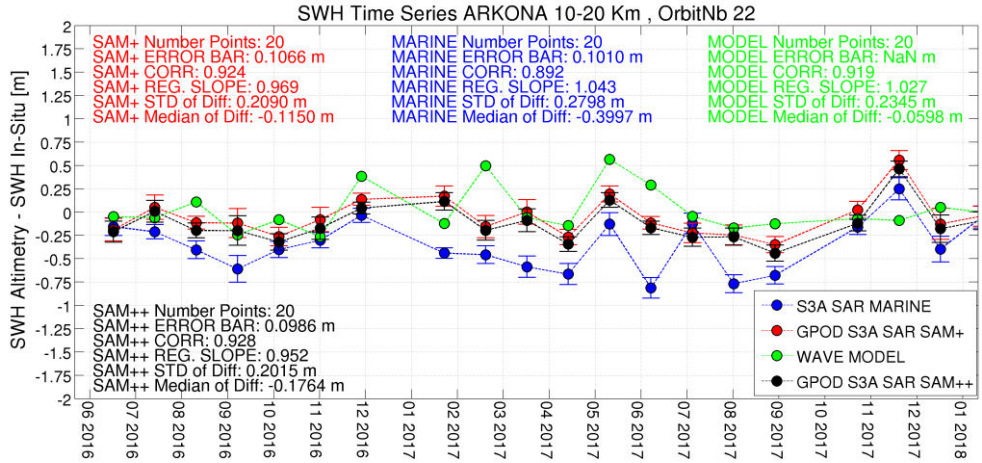
SWH Time Series ARKONA 10-20 Km , OrbitNb 22
SAM+ Number Points: 20
SAM+ ERROR BAR: 0.1066 m
SAM+ CORR: 0.924
SAM+ REG. SLOPE: 0.969
SAM+ STD of Diff: 0.2090 m
SAM+ Median of Diff: -0.1150 m
MARINE Number Points: 20
MARINE ERROR BAR: 0.1010 m
MARINE CORR: 0.892
MARINE REG. SLOPE: 1.043
MARINE STD of Diff: 0.2798 m
MARINE Median of Diff: -0.3997 m
MODEL Number Points: 20
MODEL ERROR BAR: NaN m
MODEL CORR: 0.919
MODEL REG. SLOPE: 1.027
MODEL STD of Diff: 0.2345 m
MODEL Median of Diff: -0.0598 m
SAM++ Number Points: 20
SAM++ ERROR BAR: 0.0986 m
SAM++ CORR: 0.928
SAM++ REG. SLOPE: 0.952
SAM++ STD of Diff: 0.2015 m
SAM++ Median of Diff: -0.1764 m
S3A SAR MARINE
GPOD S3A SAR SAM+
WAVE MODEL
GPOD S3A SAR SAM++
SWH Altimetry - SWH In-Situ [m]

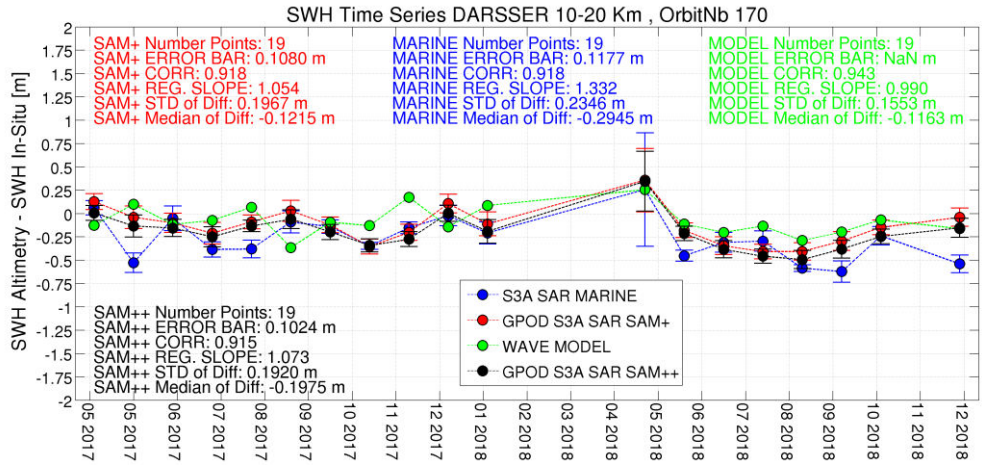
SWH Time Series DARSSER 10-20 Km , OrbitNb 170
SAM+ Number Points: 19
SAM+ ERROR BAR: 0.1080 m
SAM+ CORR: 0.918
SAM+ REG. SLOPE: 1.054
SAM+ STD of Diff: 0.1967 m
SAM+ Median of Diff: -0.1215 m
MARINE Number Points: 19
MARINE ERROR BAR: 0.1177 m
MARINE CORR: 0.918
MARINE REG. SLOPE: 1.332
MARINE STD of Diff: 0.2346 m
MARINE Median of Diff: -0.2945 m
MODEL Number Points: 19
MODEL ERROR BAR: NaN m
MODEL CORR: 0.943
MODEL REG. SLOPE: 0.990
MODEL STD of Diff: 0.1553 m
MODEL Median of Diff: -0.1163 m
SAM++ Number Points: 19
SAM++ ERROR BAR: 0.1024 m
SAM++ CORR: 0.915
SAM++ REG. SLOPE: 1.073
SAM++ STD of Diff: 0.1920 m
SAM++ Median of Diff: -0.1975 m
S3A SAR MARINE
GPOD S3A SAR SAM+
WAVE MODEL
GPOD S3A SAR SAM++
SWH Altimetry - SWH In-Situ [m]

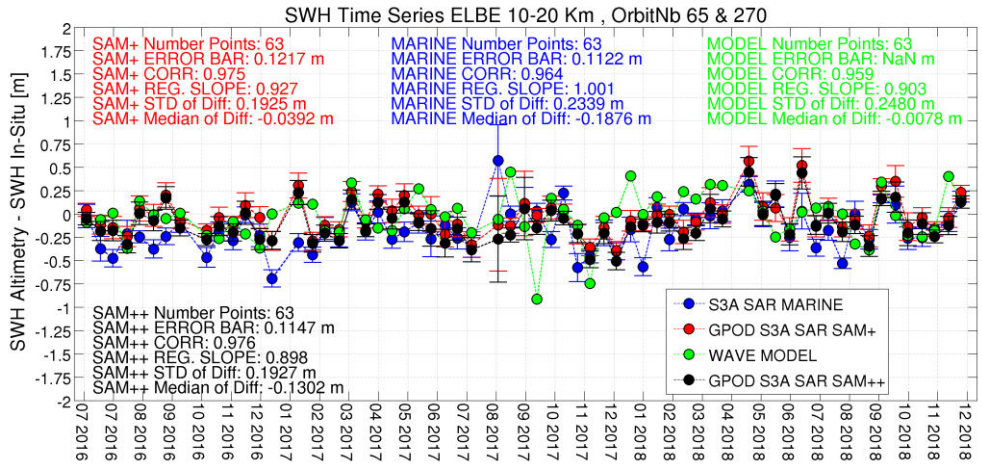

Figure 4.63: Time Series of the SWH difference between SAMOSA+ (red circles), SAMOSA++ (black circles), SAR Marine (blue circles) and GCOAST/HZG wave model (green circles) SWH in open ocean at HELG SUD (first row), HELG NORD (second row), ARK (third row), DAR (fourth row) and ELB (fifth row). The distance from the station is between 10 and 20 km.

Data	GCOAST/HZG SWH				SAMOSA++ SWH				SAMOSA+ SWH				SAR Marine SWH				
Index	med cm	stdd cm	corr	slope	med cm	stdd cm	corr	slope	med cm	stdd cm	corr	slope	med cm	stdd cm	corr	slope	N Points
HELG SUD DWR	-5.9	22.7	0.96	0.85	-14.3	30.2	0.94	0.78	-8.3	29.8	0.94	0.81	-19.1	36.4	0.91	0.89	49
HELG NORD DWR	-8.1	22.7	0.98	0.79	-28.1	24.9	0.97	0.81	-18.6	25.2	0.97	0.94	-23.2	27.8	0.97	0.97	25
ARK DWR	-5.9	23.4	0.91	1.02	-17.6	20.1	0.93	0.95	-11.5	20.9	0.92	0.96	-39.9	27.9	0.89	1.04	20
DAR DWR	-11.6	15.5	0.94	0.99	-19.7	19.2	0.91	1.07	-12.1	19.6	0.91	1.05	-29.4	23.4	0.91	1.33	19
ELB DWR	-0.0	24.8	0.95	0.90	-13.0	19.2	0.97	0.89	-3.9	19.2	0.97	0.92	-18.7	23.3	0.96	1.00	63

Table 4.13: Statistics of the SWH in situ cross-comparison for SAMOSA++,SAMOSA+, SAR Marine and GCOAST/HZG model in open ocean. The distance from the station is between 10 and 20 km.

From Table 4.13, I compute an average stdd of 22.7 cm for SAMOSA++, 22.9 cm for SAMOSA+, 27.7 cm for SAR Marine. The average correlation is 0.94, 0.94 and 0.93 for SAMOSA++, SAMOSA+ and SAR Marine respectively. From these statistical results, the conclusion is reached that SAMOSA++ slightly outperforms SAMOSA+ whereas both SAMOSA+ and SAMOSA++ behave better than the SAR Marine. The GCOAST/HZG regional model exhibits the lowest stdd (21.8 cm) and higher correlation (0.96) with respect to in situ data. Again from Table 4.13 the average regression slopes are 0.90 for SAMOSA++, 0.93 for SAMOSA+, 1.04 for SAR Marine and 0.91 for GCOAST/HZG: hence the regression slopes are very close to 1 for all datasets. All four datasets exhibit a slight negative bias (-18 cm for SAMOSA++, -11 cm for SAMOSA+, -26 cm for SAR Marine and -6 cm for GCOAST/HZG) with respect to the in situ station measurements.

In conclusion, the validation against in situ data has been carried out. From this analysis, it came out that the three solutions Sentinel-3A SAMOSA++, SAMOSA+ and SAR Marine for the sea level behave very closely to each other in open ocean conditions with an stdd of around 3.5 cm (with only a slight superiority of SAMOSA++). However, in the coastal zone, the SAMOSA++ retracker clearly outperforms the other two solutions with an average stdd of 6.6 cm, 8.8 cm and 55 cm for SAMOSA++, SAMOSA+ and SAR Marine respectively. The validation of altimetry SWH against in situ data has confirmed that the SAMOSA++ has slightly improved the SWH measurement in the open ocean with an average stdd of 22.7 cm, 22.9 cm 27.7 cm for SAMOSA++, SAMOSA+ and SAR Marine respectively.

4.3 SENTINEL-3 INLAND WATER RESULTS

In this section, I show the results obtained processing Sentinel-3 data over inland water targets.
Sentinel-3 mission has as secondary mission objective to provide a monitoring of inland water (river & lake) level (Drinkwater M. and Rebhan H., 2007). This monitoring goal is of fundamental importance to understanding of the role freshwater cycle in climate. In order to comply with this difficult objective, Sentinel-3 radar altimeter operates in SAR mode worldwide and hence over all inland water targets. Furthermore, the Sentinel-3 altimeter is complemented with the OLTC (Open Loop Tracking Command) tracking mode. In this specific tracking mode, the tracking range commanded by the sensor is based on the height extracted from a DEM uploaded on board. The heights of more than 32'000 inland water targets have been stored inside this DEM. Therefore, OLTC will enable Sentinel-3 to keep all these inland water targets whose height has been stored in the DEM well within the tracking window. This is fundamentally different from what was done by the previous altimeters (as CryoSat-2) whose tracking range was decided autonomously by the sensor on the base of the analysis of the previous returns.
Furthermore, Sentinel-3, in difference to CryoSat-2, has a short revisit time (27 days) which permits to build easily time series over inland water virtual stations.
Having also on board a collocated optical sensor (as OLCI), it makes possible to image the inland water target at the same time of the altimetric acquisition and hence to know the extension of the lake or the width of the river which brings, using the Manning's equation (Manning R., 1889), to infer the water discharge.
Finally, the worldwide coverage of inland water targets by Sentinel-3 mission has been doubled with the launch of Sentinel-3B on 25 April 2018.
Hence, for the joint combination of OLTC, revisit time, SAR coverage and collocated optical imagery, Sentinel-3 seems to represent the best platform ever to monitor hydrological targets from the space.
In this thesis work, I have proceeded to process from L1A data all the Sentinel-3A acquisitions over the Bracciano Lake from April 2016 to October 2010 and the Sentinel-3A acquisitions over the River Po from April 2016 to November 2011.

a) BRACCIANO LAKE RESULTS

Lake Bracciano is a lake of volcanic origin with a very circular shape located 32 km northwest of Rome. It is one of the major lakes of Italy and has a circular perimeter of approximately 32 km and a diameter of 7 km. Its inflow is from precipitations only as there are no inflowing rivers. Since the lake serves as a drinking water reservoir for the city of Rome, it has been under control since 1986 to avoid the pollution of its waters and to monitor the water level.
The Sentinel-3A ascending pass with orbit relative number #213 overflies every 27 days the Bracciano Lake almost in the middle, as shown in Figure 4.64:

Figure 4.64: Sentinel-3A Ascending Pass with orbit number #213

For the Bracciano's Lake acquisitions, I have processed the L1A products selecting at L1b the application of the Hamming window, zero-padding and the extended window whereas the data have been processed at L2 both with SAMOSA+ and SAMOSA++ retracker in order to appreciate the improvement brought by SAMOSA++ with respect the SAMOSA+.
The geo-corrections are applied as described in equation (2.11) using a model wet tropospheric correction derived from ECMWF and the GIM iono correction **(**Iijima et al., 1999**)**.
While processing data, the first operation to undertake is to ascertain whether the tracking window is properly locked on the Bracciano's Lake by the OLTC commanding.
In Figure 4.65, the radar signature of the Bracciano's Lake (radar echogram) is shown:

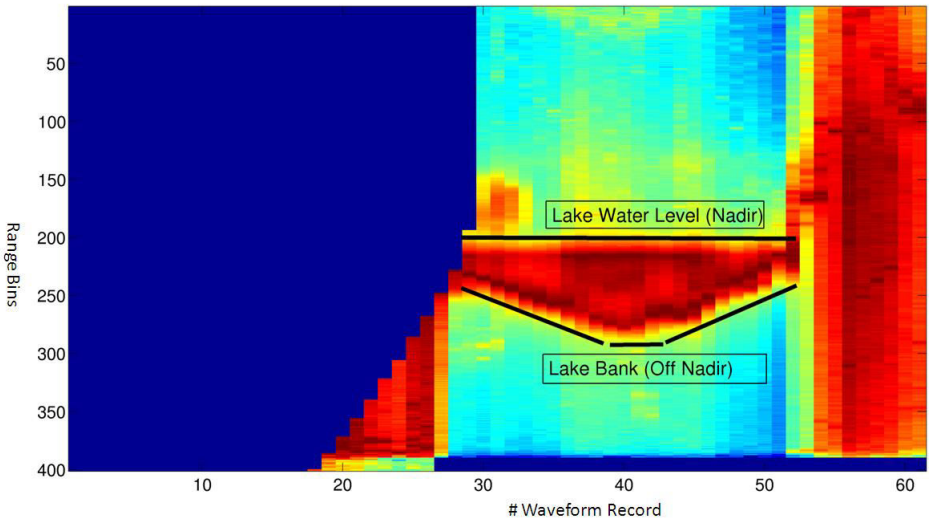

Figure 4.65: Sentinel-3A Radar Echogram from Bracciano Lake

From it, it can be concluded that the altimeter locks well the lake in the tracking window except for its very early part on the south bank which is cut-off. Furthermore, the nadir radar signal from Bracciano water is heavily contaminated by the off nadir returns from side banks of the Lake. From it, it can be easily recognized the circular shape of the Lake border. Instead, in Figure 4.66, the stack data from the Lake center is depicted: from it, one can see the off-nadir reflection to be stronger than the one from nadir.

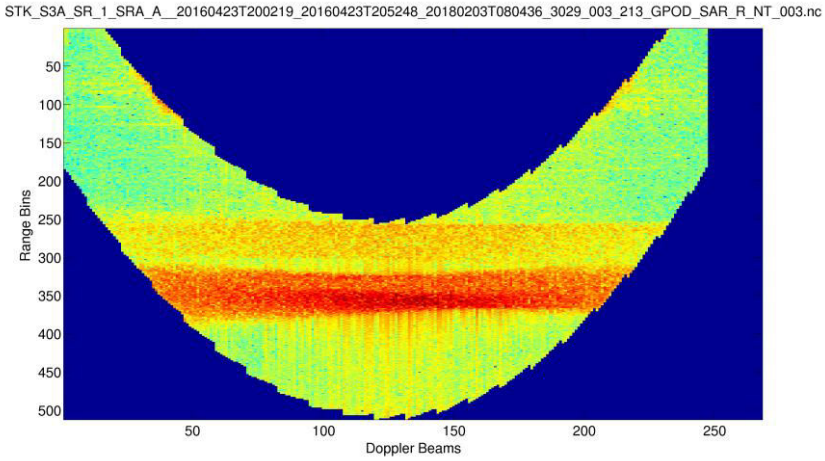

Figure 4.66: Sentinel-3A Stack Data from Bracciano Lake (the strong red stripe of energy is the off-nadir reflection)

As reference in situ dataset, I use the data collected by the Bracciano Smartlake group (www.braccianosmartlake.com) which post a daily measurement of the lake water elevation "*sul livello del mare (slm)"* (above sea level) and read the measurement from a gauging bar at lake's south bank. In case a measurement is missing, the gap has been recovered by cubic interpolation. Finally, the University of Maryland MODIS water/land mask (Carroll et al., 2009) has been used to identify the measurements collocated over the lake.

Because of a drought which has hit Italy in 2017 and for the consequent intensive water drainage by the Regional Water Supply Agency (ACEA), the Lake Bracciano has suffered a significant drop of the water level between March and December 2017, as registered as well by Bracciano Smartlake in situ data.

In Figure 4.67, the time series of the water level measured by the SRAL altimeter (red points) is compared to Smartlake in situ measurements time series (blue points) for the case retracker SAMOSA+. The Elevation is with respect to datum WGS84.

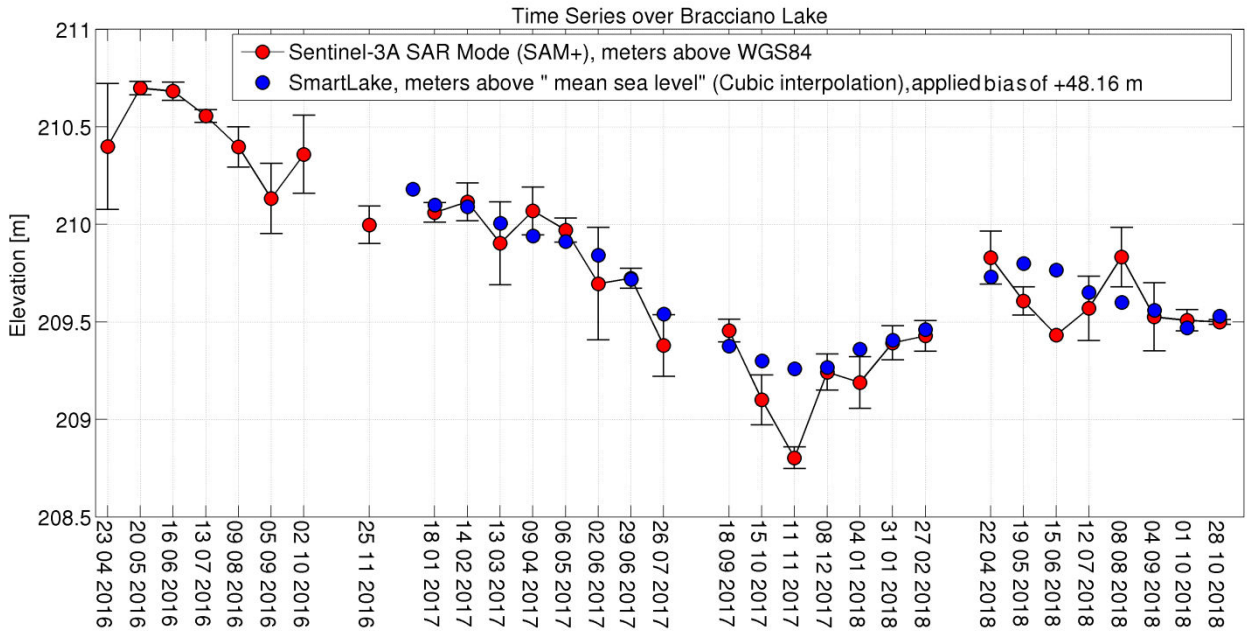

Figure 4.67 : Sentinel-3A SAMOSA+ Time Series Over Bracciano Lake (red points) and in situ data from Smartlake group (blue points)

The altimetric data have been screened in post-processing in case the moving standard deviation between 5 consecutive measurements is higher than 20 cm. The error bar on top of the altimetric measurement is simply the standard deviation of all the retained measurements. The STDD between SAMOSA+ altimetric

elevations and in situ data is 15 cm while the average error bar size is 11 cm. Some measurements are missing because they are rejected by the screening criteria, for instance on 11 Nov 2017, 22 08 201, and 26 03 2018.

Therefore, using the SAMOSA+ retracker results, one can still monitor the drop occurred in the Bracciano Lake during summer 2017 and the subsequent slow recovery of the lake but with data gaps time to time and fairly poor accuracy.

In Figure 4.68, the same time series as retracked by SAMOSA++ is shown (red points). A clear improvement is observed because the STDD between altimetric elevations and in situ data drops to 6 cm and the average error bar size is now set to 4 cm and there is no more any major outlier, though some altimetric measurements are still slightly out of the error bar. I believe that sporadic precipitation events may be the main responsible for this.

Anyhow, using the retracker SAMOSA++, Sentinel-3A can monitor very well the drop of the lake level and the subsequent recovery.

Furthermore, I have placed on top of the Sentinel-3A time series also two Sentinel-3B measurements (green points) when Sentinel-3B was operated in tandem configuration with Sentinel-3A. Only two measurements from Sentinel-3B were available from that time because these are the measurements acquired in open loop (OLTC). When the Sentinel-3B is in closed loop (autonomous tracking) over the lake, the altimeter fails completely to track the lake.

Finally, the same time series from the OCOG retracker is shown in Figure 4.69. The STDD between OCOG altimetric elevations and in situ data is 7.5 cm and the average error bar size is now set to 10 cm and there are two edited measurements on 05 09 2016 and 26 03 2018. A clear bias is visible between the OCOG retracker and SAMOSA++ retracker: this was expected as OCOG is an empirical retracker

Therefore, the accuracy of the OCOG retracker is better than the one from SAMOSA+ but lower than the one from SAMOSA++.

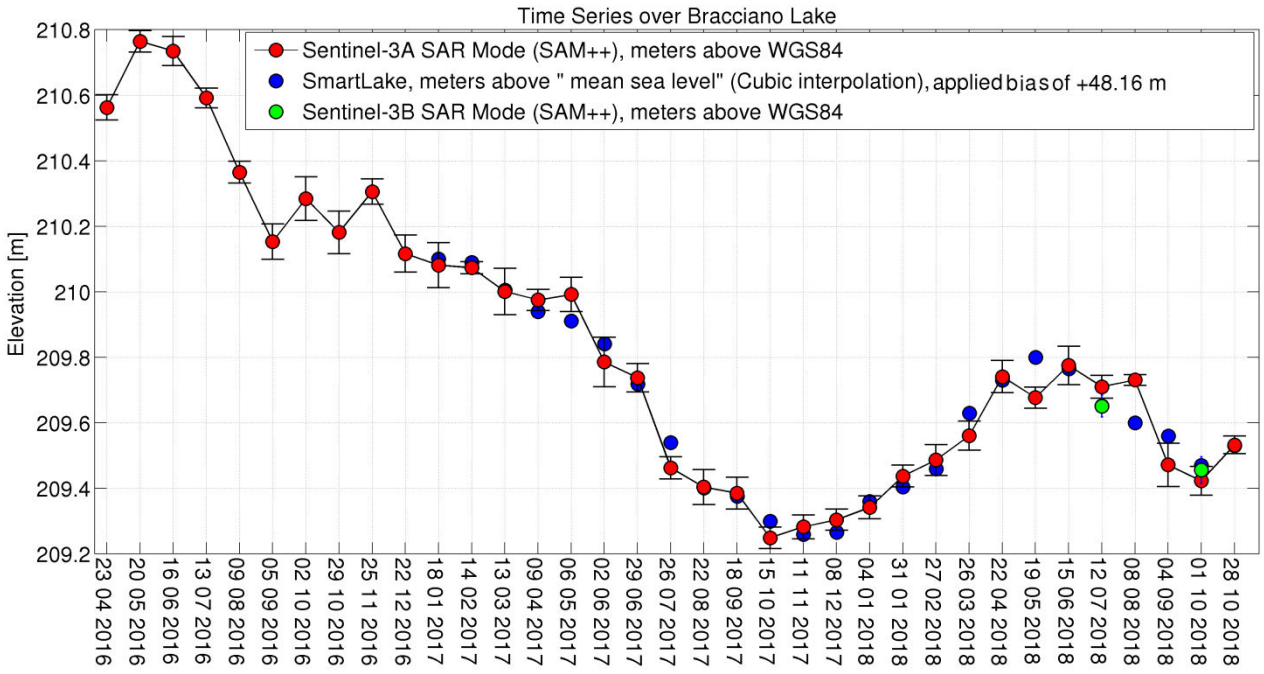

Figure 4.68: SAMOSA++ Time Series Over Bracciano Lake from Sentinel-3A (red points) from Sentinel-3B (green points), and in situ data from Smartlake group (blue points)

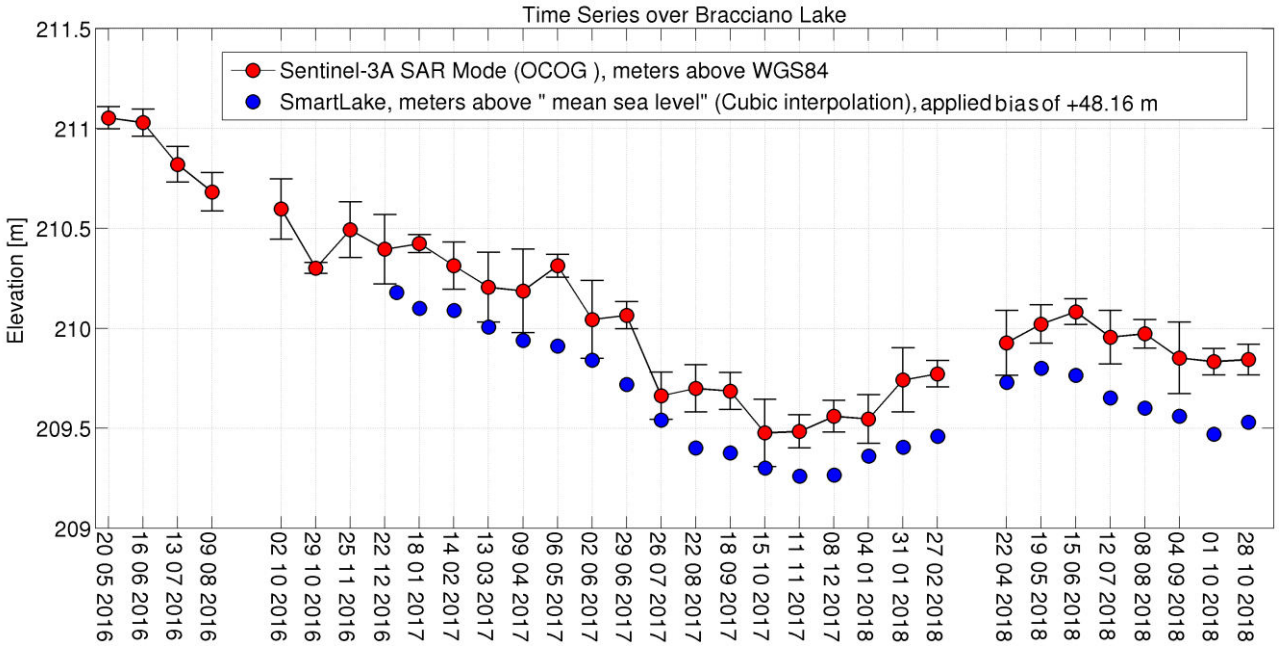

Figure 4.69: Sentinel-3A OCOG Time Series Over Bracciano Lake (red points) and in situ data from Smartlake group (blue points)

b) RIVER PO RESULTS

The Po river is the longest italian river (650 km) flowing eastward across the Pianura Padana and ending in Adriatic Sea near Venice with a delta characterized by wetlands and ponds. It can be subject to sporadic flooding during autumn or spring time and is constantly monitored by Italian civil protection service and AIPO (Agenzia Interregionale per il fiume Po) for flooding alert. Its section width can range from few hundred meters up to 4 km during a flooding event.
It has been already subject of several studies in order to evaluate the possibility to monitor efficiently from space exploiting satellite altimetry data either in conventional altimetry (Tarpanelli et al., 2013) or with SAR altimetry (Schneider et al., 2018).
Sentinel-3A samples around 10 times the river during its repeat cycle but in this thesis work I have selected the following 5 virtual stations:

- Borgoforte (Sentinel-3A pass with relative orbit number #79)
- Cremona (Sentinel-3A pass with relative orbit number #156)
- Piacenza (Sentinel-3A pass with relative orbit number #22)
- Pontelagoscuro (Sentinel-3A pass with relative orbit number #136)
- Sermide (Sentinel-3A pass with relative orbit number #38)

Since the width of the river can be very narrow (specially in summer time), in order to be sure to have at least three or four measurements from the watercourse, the L1A Sentinel-3 data have been processed at a posting rate of 80 Hz. Hamming window, zero-padding and window extension were applied as well.
At L2, the waveforms have been retracked using the SAMOSA++ retracker.

Figure 4.70: Sentinel-3A pass with relative orbit number #22 crossing the Po over Piacenza: the Po width is only 450 meter at transect but thanks to 80 Hz gridding, one can have 6 80 Hz measurements to use

The in situ data at the virtual stations location have been collected from the AIPO website (https://www.agenziapo.it/) with a temporal sampling of 10 minutes. They provide the "hydrometric level" of the river.

The geo-corrections are applied as defined in equation 2.11 using a model wet tropospheric correction derived from ECMWF and the GIM ionospheric correction (Iijima et al., 1999).

Furthermore, the average of the time series has been removed both from the altimetric dataset and from the in situ dataset. Finally, the University of Maryland MODIS water/land mask (Carroll et al., 2009) has been used to identify the measurements collocated over the Po River.

The time series of the Sentinel-3A altimetric elevation from SAMOSA++ and the time series of the AIPO in situ data at the 5 virtual stations are shown in Figure 4.71, Figure 4.72, Figure 4.73, Figure 4.74 and Figure 4.75:

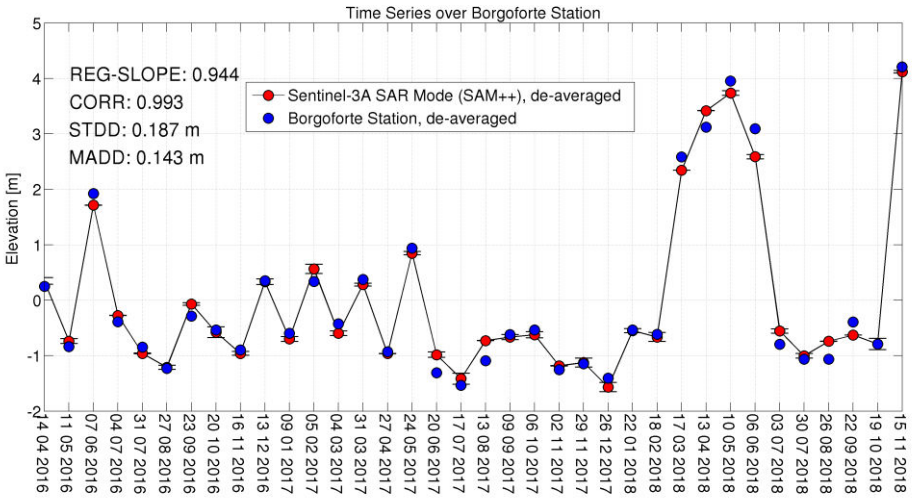

Figure 4.71: Sentinel-3A SAMOSA++ Time Series over Borgoforte Station (red points) and AIPO Time Series (blue-points). Altimetry data are produced at a posting rate of 80 Hz.

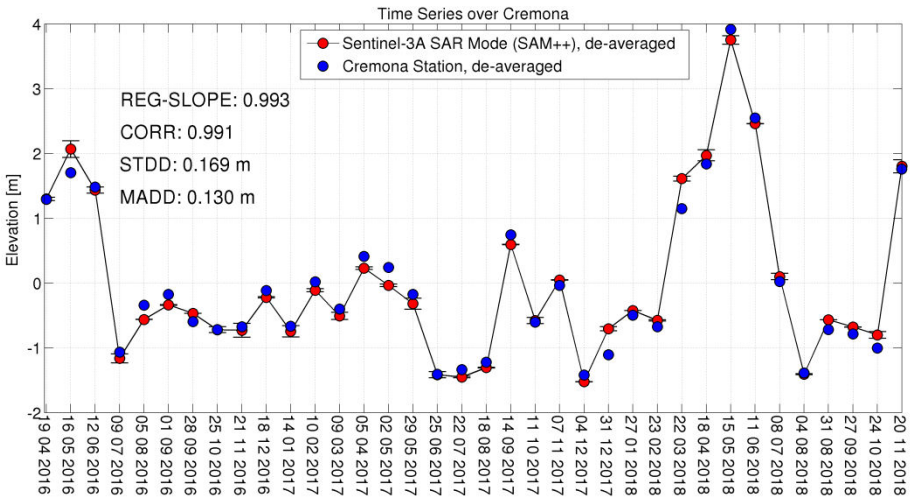

Figure 4.72: Sentinel-3A SAMOSA++ Time Series over Cremona Station (red points) and AIPO Time Series (blue-points). Altimetry data are produced at a posting rate of 80 Hz.

The error bar on top of the altimetric measurement is simply the standard deviation of all the retained measurements. The altimetric data have been screened out in post-processing in case the moving standard deviation between 3 consecutive measurements is higher than 20 cm.

Over all the 5 virtual stations, the SAMOSA++ retracker has worked well with high correlation and regression slope values (around 0.99). The worst case is Pontelagoscuro with a STDD of 23 cm and one big outlier whereas the best case is Piacenza with a STDD of 9 cm. Piacenza is also the case where the in situ station is closer to the satellite pass (2.5 km). In average, the STDD with respect to in situ data was 16 cm.

All the altimetric time series were able to monitor accurately the flooding phase occurred during the spring 2017 (an increase of water level up to 4 meter) and also the recent abrupt flooding occurred in mid-November 2018 (again a water rise of 4 meter). The results at the 5 virtual stations have been summarized in Table 4.14.

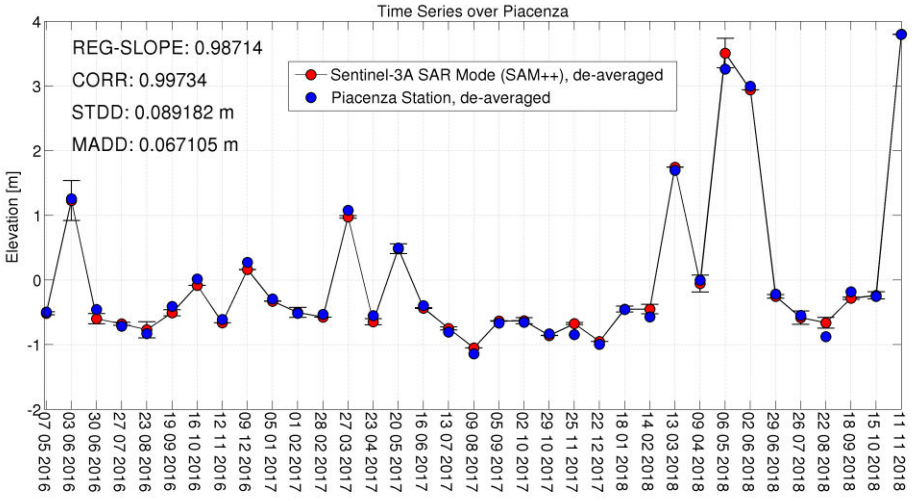

Figure 4.73: Sentinel-3A SAMOSA++ Time Series over Piacenza Station (red points) and AIPO Time Series (blue-points). Altimetry data are produced at a posting rate of 80 Hz.

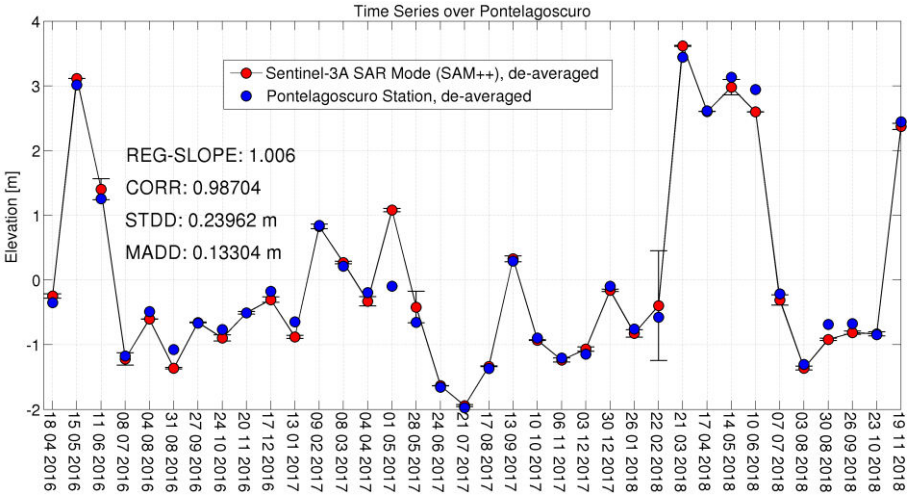

Figure 4.74: Sentinel-3A SAMOSA++ Time Series over Pontelagoscuro Station (red points) and AIPO Time Series (blue-points). Altimetry data are produced at a posting rate of 80 Hz.

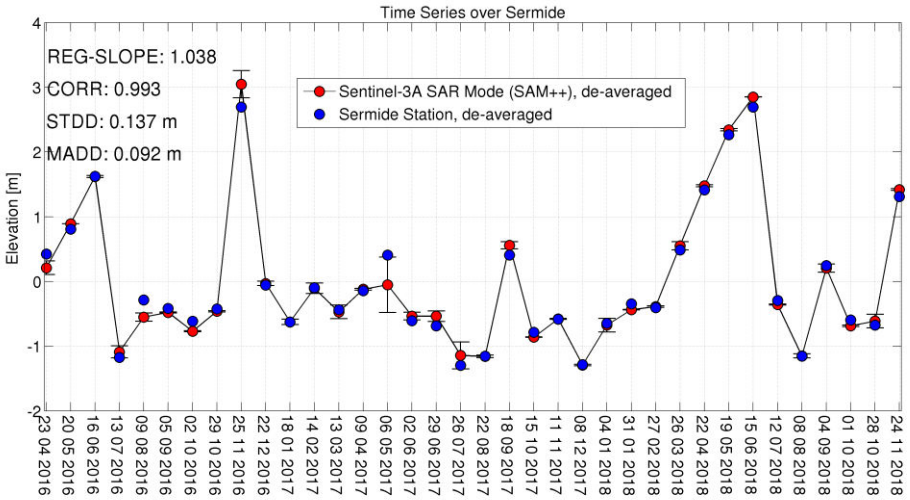

Figure 4.75: Sentinel-3A SAMOSA++ Time Series over Sermide Station (red points) and AIPO Time Series (blue-points). Altimetry data are produced at a posting rate of 80 Hz.

SAMOSA++ 80 Hz	STDD (cm)	CORR	MADD (cm)	REG-SLOPE
Borgoforte	18.7	0.99	14.3	0.94
Cremona	16.9	0.99	13.0	1.00
Piacenza	9.0	1.00	6.7	0.99
Pontelagoscuro	23.9	0.99	13.3	1.01
Sermide	13.7	1.00	9.2	1.04

Table 4.14: Statistics at the 5 Po virtual stations with SAMOSA++

On the other side, the time series of the Sentinel-3A altimetric elevation from SAMOSA+ and the time series of the AIPO in situ data at the 5 virtual stations are shown in Figure 4.76, Figure 4.77, Figure 4.78, Figure 4.79, and Figure 4.80.

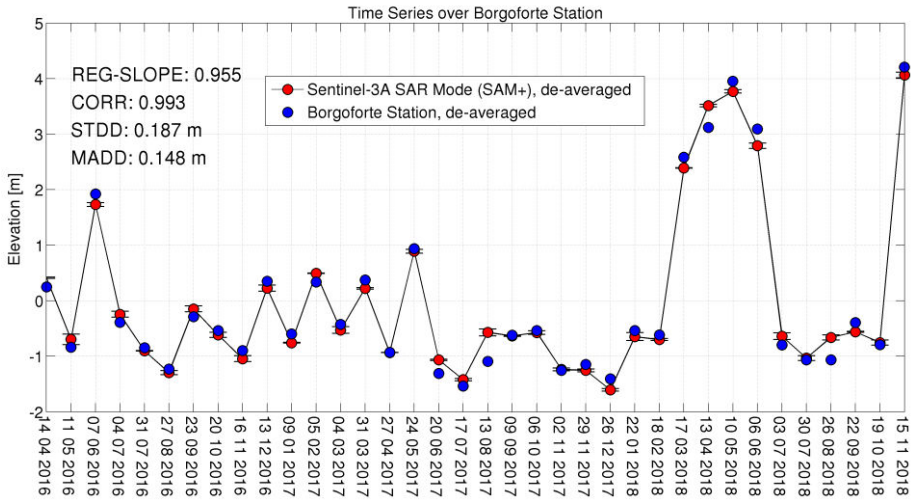

Figure 4.76: Sentinel-3A SAMOSA+ Time Series over Borgoforte Station (red points) and AIPO Time Series (blue-points). Altimetry data are produced at a posting rate of 80 Hz.

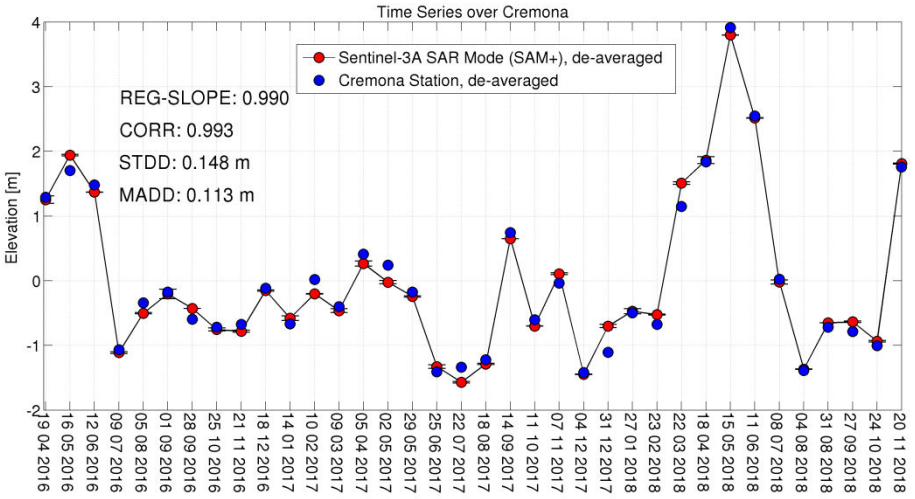

Figure 4.77: Sentinel-3A SAMOSA+ Time Series over Cremona Station (red points) and AIPO Time Series (blue-points). Altimetry data are produced at a posting rate of 80 Hz.

While over Borgoforte, Cremona and Piacenza the SAMOSA+ STDD take very similar values to the case SAMOSA++, SAMOSA++ clearly over-performs SAMOSA+ over the stations of Pontelagoscuro and Sermide.

In average, the SAMOSA + STDD with respect to in situ data was 25 cm.The results at the 5 virtual stations have been summarized in Table 4.15.

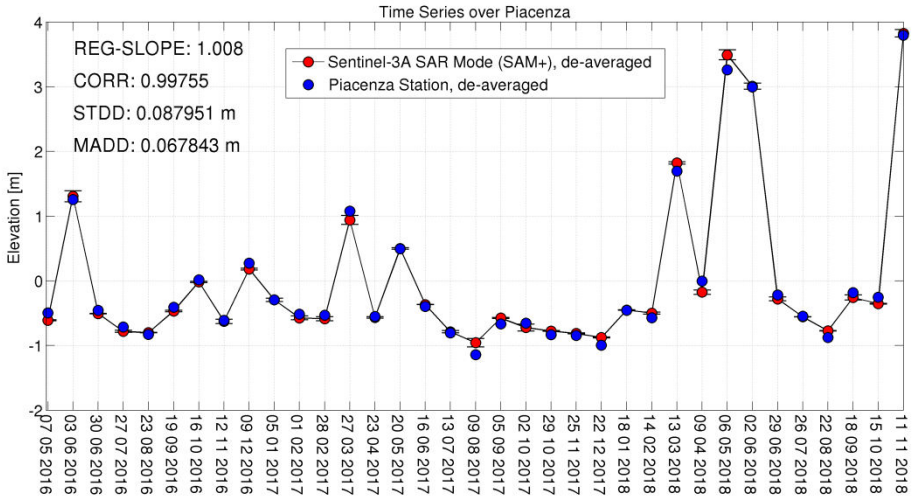

Figure 4.78: Sentinel-3A SAMOSA+ Time Series over Piacenza Station (red points) and AIPO Time Series (blue-points). Altimetry data are produced at a posting rate of 80 Hz.

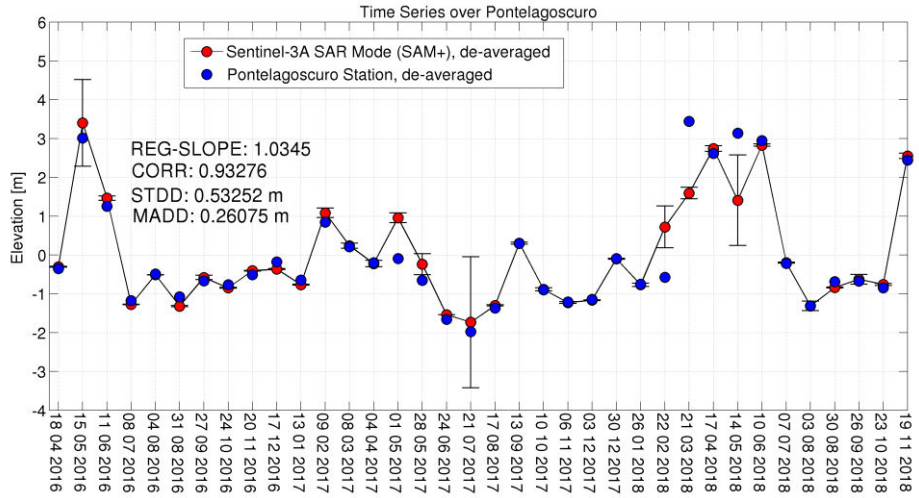

Figure 4.79: Sentinel-3A SAMOSA+ Time Series over Pontelagoscuro Station (red points) and AIPO Time Series (blue-points). Altimetry data are produced at a posting rate of 80 Hz.

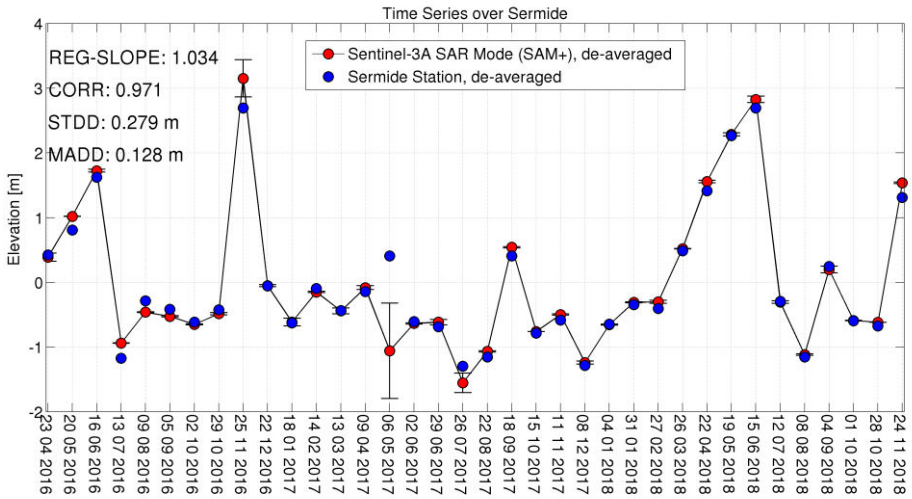

Figure 4.80: Sentinel-3A SAMOSA+ Time Series over Sermide Station (red points) and AIPO Time Series (blue-points). Altimetry data are produced at a posting rate of 80 Hz.

SAMOSA+ 80 Hz	STDD (cm)	CORR	MADD (cm)	REG-SLOPE
Borgoforte	18.7	0.99	14.8	0.95
Cremona	14.8	0.99	11.3	1.00
Piacenza	8.8	1.00	6.7	1.01
Pontelagoscuro	53.2	0.93	26.0	1.03
Sermide	27.9	0.97	12.8	1.03

Table 4.15: Statistics at the 5 Po virtual stations with SAMOSA+

As far as concerns the results from the OCOG retracker in the ESA land products, the time series are reported in Figure 4.81, Figure 4.82, Figure 4.83, Figure 4.84, and Figure 4.85.

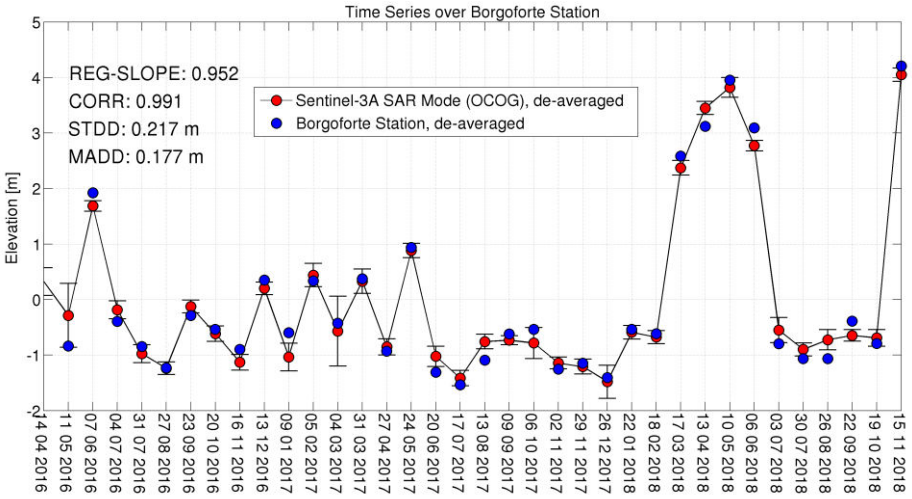

Figure 4.81: Sentinel-3A OCOG Time Series over Borgoforte Station (red points) and AIPO Time Series (blue-points). Altimetry data are produced at a posting rate of 80 Hz.

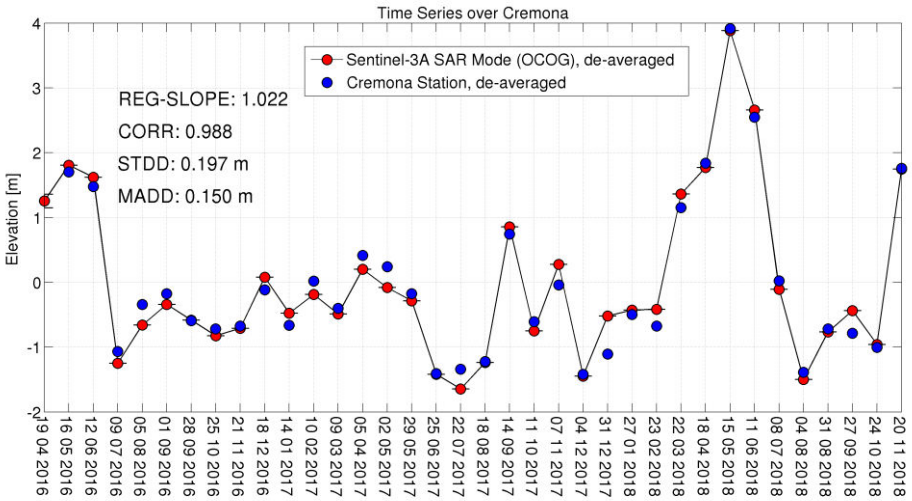

Figure 4.82: Sentinel-3A OCOG Time Series over Cremona Station (red points) and AIPO Time Series (blue-points). Altimetry data are produced at a posting rate of 80 Hz.

OCOG clearly under-performs with respect SAMOSA++. It is considered that the most of the improvement of SAMOSA++ dataset with respect the OCOG dataset comes from the 80 Hz data gridding frequency used on SAMOSA++ side. In average, the OCOG STDD with respect to in situ data was 30 cm. The results at the 5 virtual stations have been summarized in Table 4.16.

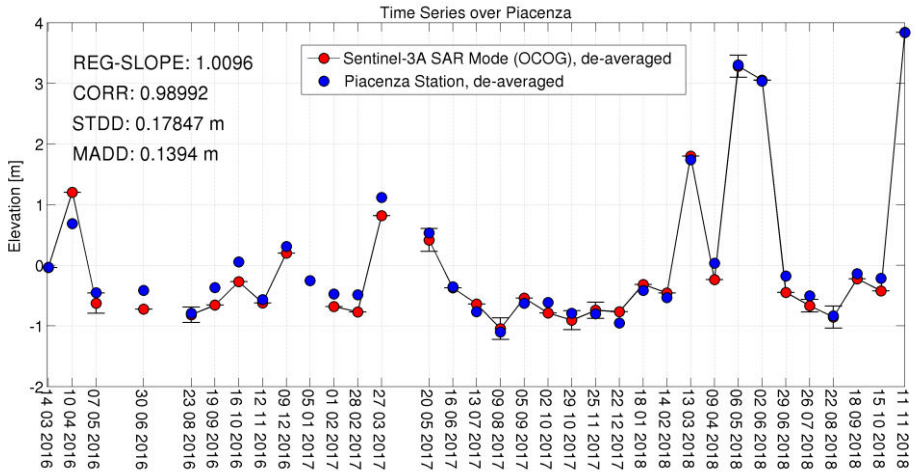

Figure 4.83: Sentinel-3A OCOG Time Series over Piacenza Station (red points) and AIPO Time Series (blue-points). Altimetry data are produced at a posting rate of 80 Hz.

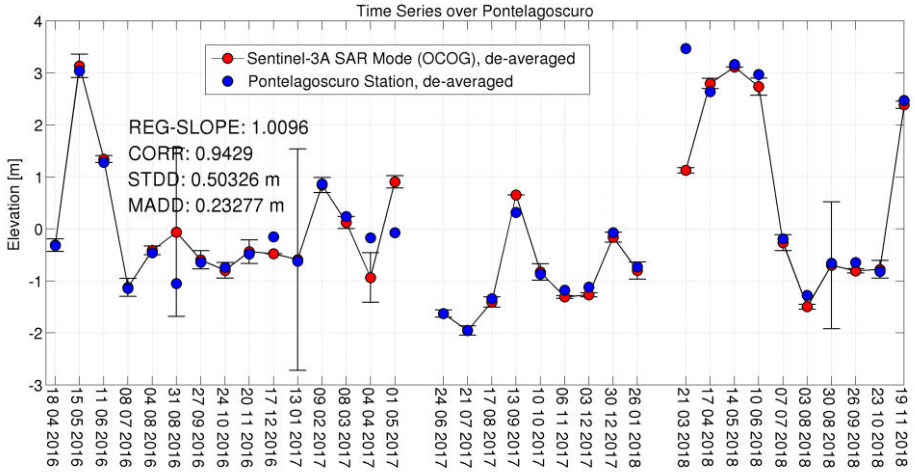

Figure 4.84: Sentinel-3A OCOG Time Series over Pontelagoscuro Station (red points) and AIPO Time Series (blue-points). Altimetry data are produced at a posting rate of 80 Hz.

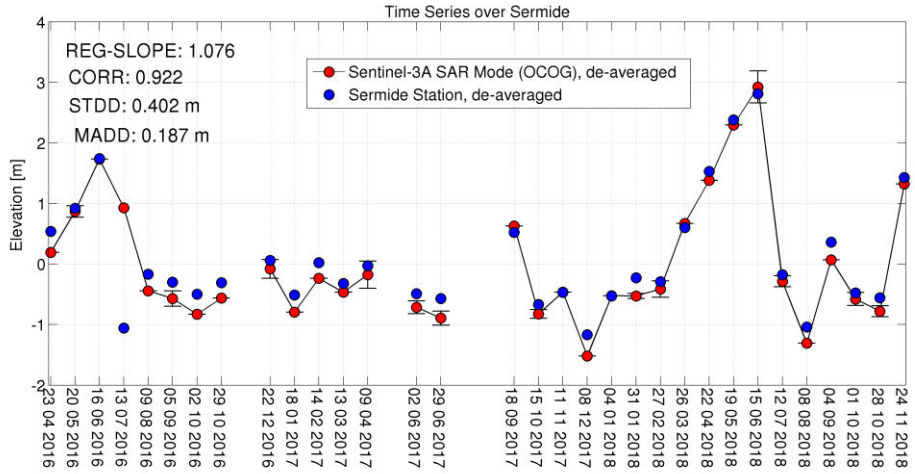

Figure 4.85: Sentinel-3A OCOG Time Series over Sermide Station (red points) and AIPO Time Series (blue-points). Altimetry data are produced at a posting rate of 80 Hz.

OCOG 20 Hz	STDD (cm)	CORR	MADD (cm)	REG-SLOPE
Borgoforte	21.7	0.99	17.7	0.95
Cremona	19.7	0.99	15.0	1.02
Piacenza	17.8	0.99	14.0	1.01
Pontelagoscuro	50.3	0.94	23.2	1.01
Sermide	40.2	0.92	18.7	1.08

Table 4.16: Statistics at the 5 Po virtual stations with OCOG

4.4 SENTINEL-3 AND CRYOSAT-2 SEA ICE RESULTS

In this section, I show the results obtained by (Laforge et al., 2019) for CryoSat-2 and Sentinel-3 missions over sea ice when the SAMOSA+ retracker is used to compute the sea-ice freeboard.
The sea ice freeboard is the height of the ice floes over the free water surface. It can be measured making the difference between the height of the ice floes and the height of the water at a crack between two floes (lead).

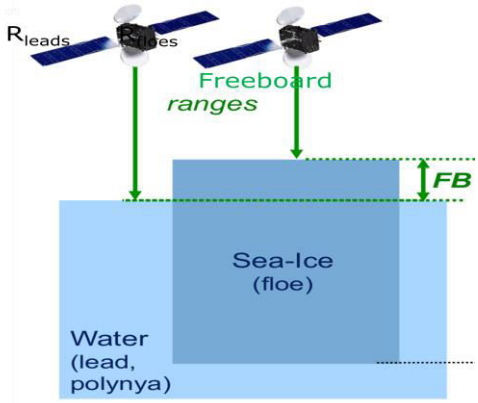

Figure 4.86: Sea Ice Freeboard from space. Picture from (Laforge et al., 2019)

One of the biggest "plus" of SAMOSA+ retracker over sea ice is expected to be that same retracking model (SAMOSA) is used both on ice floes and water leads since this will imply to a seamless topographic continuity when switching between the two surface state conditions: diffusive and specular.
Furthermore, it is worth to point out that, when retracking the SAR data over sea-ice, different L1b processing baselines can be implemented in order to identify the one which is more appropriate for the process to retrieve sea ice freeboard. Among the different possible processing options, the processing options picked up over sea ice have been: the application of the zero-padding in range dimension and the extension of the radar window by a factor of two. Furthermore, in order to test the impact of the Hamming window two runs were made: one with Hamming window and one without. When the weighting window has been not applied, a RIP detection method (Laforge et al., 2019) was instead used in order to screen out off-ranging errors from the azimuth ambiguities.
In Figure 4.87, I report the time series of the measured freeboard for the time frame (2013-2017) from the SAMOSA+ retracker as derived in (Laforge et al., 2019):

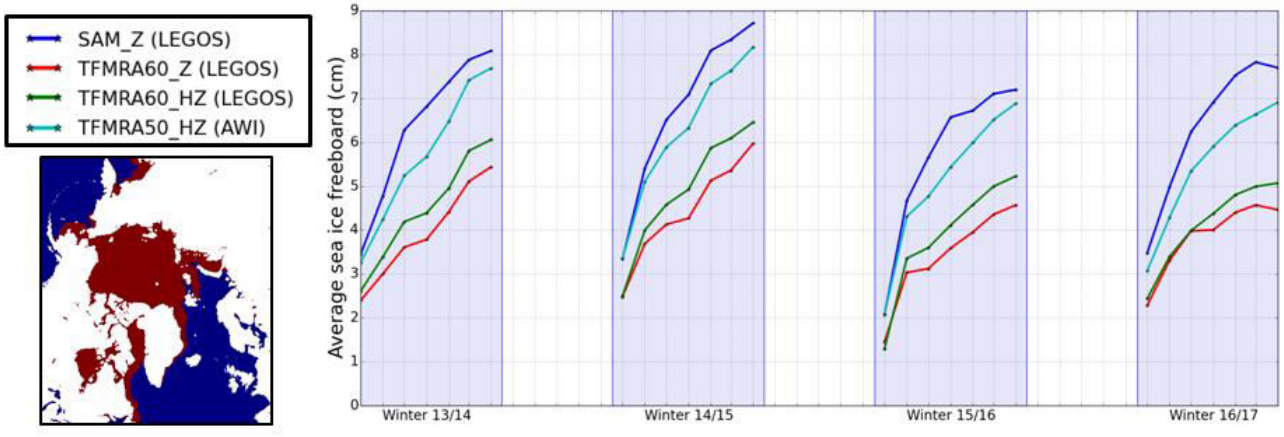

Figure 4.87: Sea Ice Freeboard from Cryosat-2 in the time frame [2013-2017] from SAMOSA+ (blue curve), from TFMRA retracker-threshold 60% LEGOS implementation (red curve), from TFMRA retracker-threshold 50% AWI implementation (cyan curve) and from TFMRA threshold 60% with Hamming Weighting LEGOS implementation (green curve). Picture from (Laforge et al., 2019)

The freeboard time series from the SAMOSA+ retracker (blue curve) is the closest one to the results from AWI in house implementation of the TFMRA (cyan curve). Furthermore, (Laforge et al., 2019) has cross-compared the freeboard solution from the several sources versus the in situ freeboard measurements from NASA's Operation IceBridge campaign (2014, 2105, 2017) computing the root mean square difference (RMSD) and bias for the different solutions described in Figure 4.88.

As shown in Figure 4.88, the solution providing the best consistency in term of RMSD and bias is the one computed from the SAMOSA+ retracker with a RMSD of 5.9 cm (very close to the expected IceBridge freeboard error).

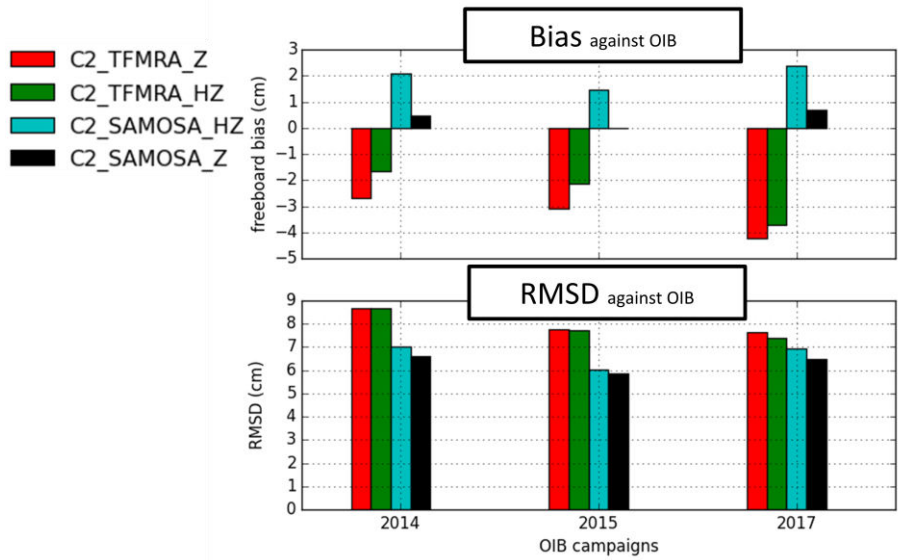

Figure 4.88: RMSD and bias for the freeboard solution from SAMOSA+ (black curve), from TFMRA retracker-threshold 60% LEGOS implementation (red curve) and from TFMRA threshold 60% with Hamming Weighting LEGOS implementation (green curve). Picture from (Laforge et al., 2019)

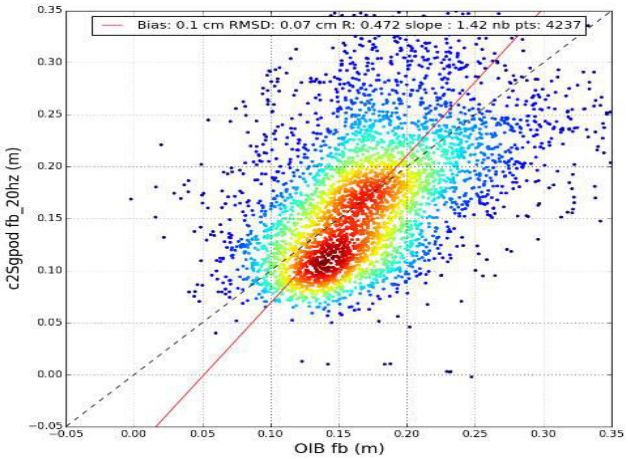

Figure 4.89: Scatterplot between SAMOSA+ (with Zero-Padding) freeboard and Operational IceBridge freeboard for 2014 campaign. RMSD is 7 cm and bias 0.1 cm. Picture from (Laforge et al., 2019)

Finally, (Laforge et al., 2019) has computed the freeboard also from the Sentinel-3 data processed in the same processing baseline as CryoSat-2 and again retracked by SAMOSA+, retrieving a excellent continuity between the two missions, as shown in Figure 4.90 and also shown from the sea ice freeboard maps in December 2016 from CryoSat-2 and Sentinel-3 missions in Figure 4.91.

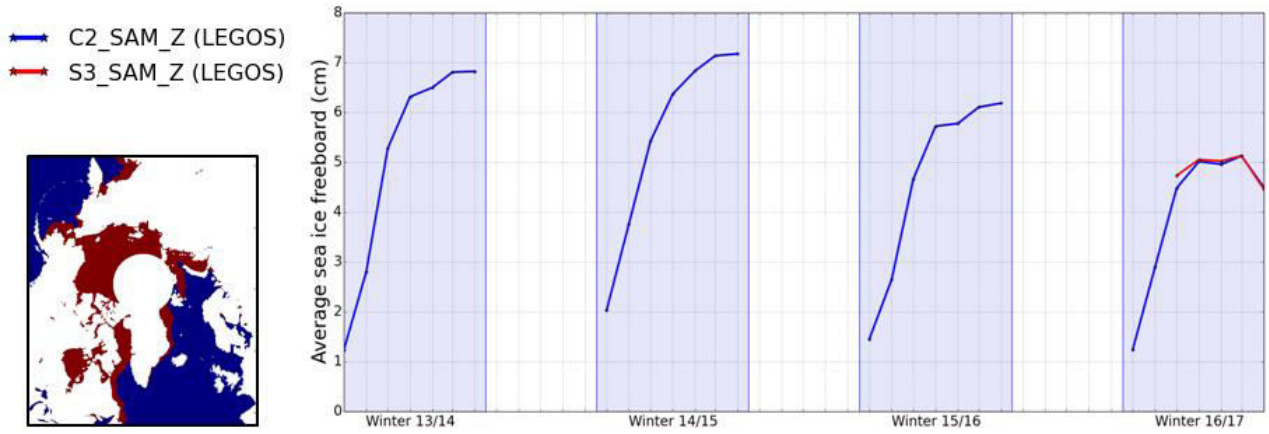

Figure 4.90: Sea Ice Freeboard from Cryosat-2 in the time frame [2013-2017] (blue curve) and from Sentinel-3 in the time frame [2016-2017] (red curve). Picture from (Laforge et al., 2019)

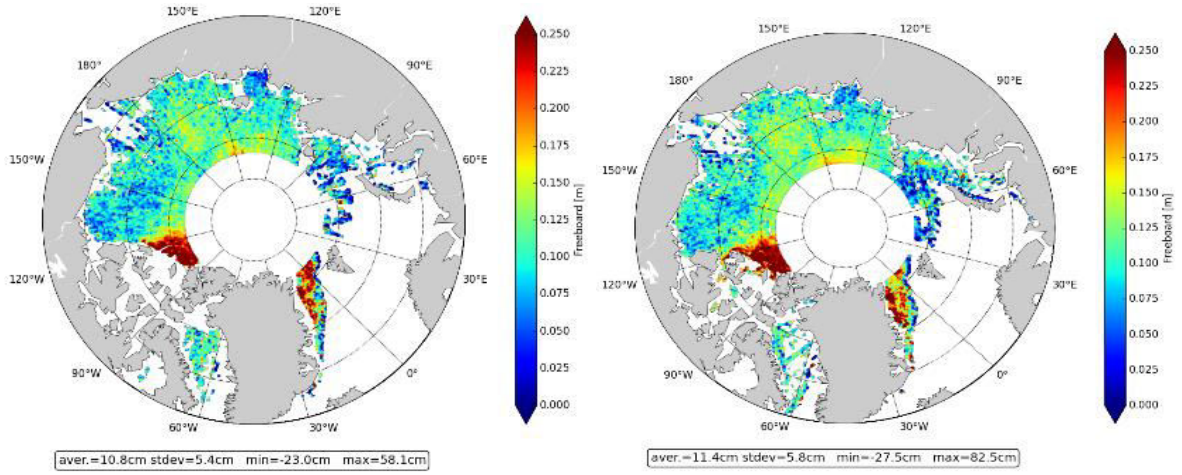

Figure 4.91: SAMOSA+ Sea Ice Freeboard from Cryosat-2 mission (left) and Sentinel-3 mission (right) during December 2016. Picture from (Laforge et al., 2019)

Hence, based on these results, I conclude that it is possible to measure the sea ice freeboard with a physical-based retracker (once you have designed to adapt to peaky echoes) as good as done usually by empirical retrackers as TFMRA (or even better) and that the Sentinel-3 and Cryosat-2 show very similar performances in sea ice freeboard's retrieval, provided that the processing start from L1A and is identical on both sides.

4.5 DISCUSSION

In this chapter, I have investigated, reported and discussed the improvements brought by the methodologies described in chapter 3 in terms of accuracy and precision for the three marine geophysical measurements (sea surface height, wave height and wind speed), for the inland water elevation and for the sea ice freeboard. In the marine context, the improvement has been validated versus PLRM altimetry data, against regional high-resolution ocean models, in situ data and PDGS data products for both CryoSat-2 and Sentinel-3. Instead, for the inland water applications, two test cases have been selected: one over a small lake and one over a narrow river. The improvements have been validated versus in situ data and PDGS data products. Finally, as far as sea ice is concerned, the results by (Laforge et al., 2019) based on the SAMOSA+ retracker have been presented along with their validation against in situ data.
I divide the discussion of the results in three sections: one for each thematic application.

a) MARINE RESULTS

As far as the CryoSat-2 mission is concerned, the results produced by the SAMOSA-based open ocean retracker (SAMOSA2) have been not presented here because already validated in (Fenoglio-Marc et al., 2015). I have focused my attention in validating the new SAMOSA+ retracker using the CryoSat-2 data in the North Sea and West Baltic Sea. Firstly, I have described the specific geophysical corrections (such as the TPXO8-ATLAS tidal model and the GPD+ wet tropospheric corrections) and third part data (such as the DTU15 MSS and the EIGEN-6C4 geoid) that have been used for this work and that are supposed to have a better performance in the coastal zone with respect to the default CryoSat-2 corrections. After this, I have shown the results by SAMOSA+ retracker in open ocean versus TALES PLRM retracker: the two retrackers are very consistent to each other with a standard deviation of the difference (stdd) of only 2.6 cm for SSH and a stdd of only 17 cm for SWH and a stdd of only 26 cm/sec for U10. Furthermore, the two retrackers show no cross-dependencies with respect to mispointing, sea state and height rate as far as regards SSH and U10. Only a cross-dependency for SWH with respect to the sea state was reported but this is a result already well-known in SAR altimetry and reported by several experts (Raynal et al., 2018). Afterwards, I have

validated the SAMOSA+ data versus ocean circulation and wave model: in both cases the consistency was very good (stdd of around 13 cm for DOTi against the BSH model, stdd of around 30 cm for SWH against ECMWF and DWD model, and stdd around 1.3 m/sec for U10 against ECMWF model. At the end, I have presented a remarkable result obtained by (Bonnefond at al., 2018) which has reported a std of only 1.5 cm with respect to the in situ stations at Ajaccio and Senetosa. Based on all these findings and results, I conclude that the SAMOSA+ retracker works fine over open ocean.

This is not a surprising result because over open ocean generally SAMOSA+ fallbacks to the SAMOSA2 which has been already validated in (Fenoglio-Marc, 2015).

After having validated SAMOSA+ over open ocean, I have proceeded to validated it in the coastal zone and to assess in particular the improvement brought by SAR altimetry in the coastal zone. I conclude that the analysis brings strong evidence that, in the region of interest, SAR altimetry outperforms state of art PLRM pulse-limited altimetry in the coastal zone and brings satellite altimetry coastal elevations much closer to ocean model simulations and in situ data. Indeed, thanks to this aforesaid dedicated processing tailoring, the land contamination begins to affect the altimetric elevation measurements only at 2-3 km from the coast. Moreover, the statistical results of SLAio cross-comparison with respect to tide gauges in open ocean and coastal zone are very close to each other, with average stdd and correlation of 4.1 cm and 0.98 in open ocean and of 4.4 cm and 0.96 in coastal zone. This is indeed an indicator that only marginal accuracy degradation occurs in the transition between open-ocean to coastal zone conditions.

The in situ cross-comparison shows that in my region of interest the PLRM TALES retracker performs better than the SINC2 retracker in the coastal zone. However, the coastal performance of the TALES PLRM retracker is pretty satisfactory for sea level retrieval, with stdd 8.4 cm and correlation 0.93.

Furthermore, the SAR altimetry measures in the coastal zone the sea level monthly mean time series with nearly the same level of variability than the ocean model, being the DOTi standard deviation 36 cm for model, 42 cm for SAR while the std is 62 cm for PLRM. There is no significant bias in DOTi/SLA between SAR and PLRM datasets in the coastal zone (bias is around 1 cm) whereas I report a bias of 10 cm with respect to the BSH model DOTi/SLA, which is due to a different reference used in altimetry and in the model.

From the scatter plots analysis, I report that the stdd between SAR and BSH model in the coastal zone (24 cm) is less than half of the stdd between PLRM and BSH model in the coastal zone (55 cm). Also DOTi correlation coefficient behaves similarly (0.85 for DOTi SAR and 0.58 for DOTi PLRM).

It is also remarkable that more than 98.3% of the 20 Hz SAR SLA measurements in the coastal zone are within the range ± 1 meter, considering that a simple 3 sigma outlier criterion was applied and that at just one kilometre from the coast 94% of the 20 Hz SAR SLA are within the ± 1 meter range.

Hence, in the area under study SAR altimetry delivers a measurement of the DOTi much closer to the coast and confirms its future importance in improving ocean numerical models in coastal zone.

With respect to the validation against off-shore AWAC platforms in open ocean, I do not observe any specific bias between the three SWH datasets (TALES PLRM, SAR and DWD model) but I underline that I found a smaller SWH stdd in SAR (14.5 cm) than in TALES PLRM (stdd 20.3 cm), the latter one being also significantly smaller than the PLRM results in (Fenoglio-Marc et al., 2015).

Hence, given the results of the cross-comparison between in situ-station and altimetry, I conclude that in the area under study the two coastal retrackers SAMOSA+ and TALES are well suited both for the coastal zone and in open ocean conditions. Regarding the wind speed, I was able to measure its coastal monthly mean time series with a level of variability (std 2.98 m/sec) only slightly higher than the one exhibited by the ECMWF wind speed model (2.68 m/sec). I remark the necessity to use a dedicated high-resolution tidal model (such as TPXO8-ATLAS) when working with CryoSat-2 data in the coastal zone. The new wet tropospheric correction from the University of Porto (GPD+) exhibits only minor differences with respect to the ECMWF wet solution in this study region and it needs to be assessed in a region with higher tropospheric variability where improvements have been demonstrated (Fernandes et al., 2016).

As far as the Sentinel-3 mission is concerned, I have focused my attention in validating the novel SAMOSA++ retracker. Firstly, I have presented my area of interest which has been chosen as the North East Atlantic. Afterwards, the new third party data as mean sea surface DTU18 and the GCOAST/HZG ocean circulation and wave model have been introduced. I have also added a new tide model in the analysis: FES2014b whereas the GPD+ correction (Fernandes et al., 2016) was computed for the Sentinel-3 mission. The first objective was to assess the performance of the SAMOSA++ retracker in open ocean. Hence, the precisions plots for SSH and SWH have been shown: it was reported that the SAMOSA++ range noise for high sea state regimes is lower by about 20% than the one from SAMOSA+. Then, the scatter plots of SAMOSA+ and SAMOSA++ against the SAR Marine (Sentinel-3 PDGS data products) and against GCOAST/HZG model have been produced from which it came out an excellent agreement between the three datasets. Anyhow, it was reported a bias of +1cm for the SAMOSA++ retracker whereas the SAMOSA++ SWH are more in agreement with GCOAST/HZG model than SAMOSA+. The wind speeds from the three datasets: SAMOSA+, SAMOSA++, SAR Marine are as well in excellent agreement. Finally, the dependency plots for SAMOSA+ and SAMOSA++ have been presented. From their analysis, it was identified a minor dependency of the SAMOSA++ with the sea state of around 0.7% of the SWH. It is not clear the source of this tracker bias and it requires further investigation. Hence, my conclusion was that SAMOSA++ shows no major drawbacks over open ocean and is in good agreement with the SAMOSA+ and SAR Marine over open ocean.

After having demonstrated that the SAMOSA++ retracker does not degrade the results over open ocean, finally I have challenged the SAMOSA++ retracker in the coastal zone. At first, it was reported that the measurements from the SAMOSA++ retracker are less spread than for the SAMOSA+ retracker case and with less outliers. Then the SAMOSA++ retracker has more points within ±1 m range in the very proximity of the coast and also the SAMOSA++ SWH median in coastal zone behaves closely to the model. Finally the standard deviation of SAMOSA+, SAMOSA++ and SAR Marine versus the distance to coast has been shown from which it follows that SAMOSA++ retracker is the one which behaves better in measuring the SLA. Also the plot of the SWH std versus the distance to the coast has been produced from which also it follows that SAMOSA++ SWH behaves better than SAMOSA+ in the coastal zone. As last result, it was reported that in my region of interest FES2014b is superior to TPX08-ATLAS.

Then, I followed to cross-compare via scatterplot SAMOSA+ and SAMOSA++ against ocean numerical circulation and wave model. From this analysis, the SAMOSA++ DOTi and SWH data are the ones more consistent with the models in coastal zone. From the cross-comparison versus the in situ data, the difference between SAMOSA+ and SAMOSA++ are very negligible in open ocean while SLA and SWH results from SAMOSA+ overcomes the ones from SAMOSA+ in the coastal zone (an average stdd of 6.6 cm, 8.8 cm and 55 cm for SAMOSA++, SAMOSA+ and SAR Marine respectively as to SLAio and an average stdd of 22.7 cm, 22.9 cm, 27.7 cm for SAMOSA++, SAMOSA+ and SAR Marine respectively as to SWH). Anyhow, the conclusion was reached that the SAMOSA++ retracker is superior to SAMOSA+ in the coastal zone in measuring sea level and SWH. SAR Marine is by far the worst but this is not surprising because it is based on an open ocean solution.

b) INLAND WATER RESULTS

As far as the hydrological thematic applications are concerned, two test cases have been worked out: one over the Bracciano Lake and one over the Po River. Over the Bracciano Lake, at first the time series from the SAMOSA+ has been shown. It behaved poorly with respect the in situ data with a stdd of 15 cm and an error bar size of 11 cm. Then, the SAMOSA++ results have been presented with much better agreement with in situ data (stdd of 6 cm and error bar size of 4). Finally in order to demonstrate the improvement brought by SAMOSA++, the same time series was computed using the data from the OCOG retracker in the ESA Land product. The OCOG data behaved very well but they were not superior to SAMOSA++, having a stdd of 7 cm and an error bar size of 10 cm. After the Bracciano Lake, the SAMOSA++ retracker has been challenged

over the Po River for five virtual stations. At first, the data have been processed at L1b with a gridding of 80 Hz in order to have as many measurements from the water course as possible. The SAMOSA++ retracker worked well over these five stations with an average stdd of 16 cm and being able to monitor the flooding occurred recently in November 2018. The SAMOSA+ retracker scored with respect the same stations an average stdd of 25 cm whereas the OCOG retracker scored an average stdd of 30 cm. Hence, I have concluded that the SAMOSA++ retracker is capable to monitor fairly well the water level of the two analyzed test cases and with higher performance than SAMOSA+ and OCOG retracker.

c) SEA ICE RESULTS

As far as the sea ice thematic applications are concerned, the results by (Laforge at al., 2019) have been discussed and reported. (Laforge at al., 2019) has found out that the SAMOSA+ retracker is capable to measure sea ice freeboard, reconstructing time series which are very close to the ones from AWI built by TFMRA empirical retracker (Helm, 2014). It has also cross-compared the SAMOSA+ freeboard against NASA Operational Ice Bridge in situ data, finding out that the SAMOSA+ retracker is one of solutions having the best accuracy versus these in situ dataset. Furthermore, (Laforge at al., 2019) reports that the SAMOSA+ freeboard from Sentinel-3 is in very good agreement with the one from CryoSat-2.

5 Conclusions and Outlook

5.1 Conclusions

In this chapter, I reach the conclusions of the thesis. The conclusions will be presented addressing the questions which have been raised in the introduction.

— *Can we say that SAR Altimetry over open ocean is a consolidated and well-established technology which has now reached a state of full maturity?*

When I started to work with radar altimetry, SAR altimetry over ocean was still far to come: there was no flying SAR altimeter mission (CryoSat-2 was not yet launched), no one could know with absolute certainty how it would behave, experts could rely only on simulations, there was not a standard and consolidated way to process the data at L1b and mostly there was no validated physically-based model for the SAR return waveform (and of course no retracker). Since then, space agencies have invested considerable resources in making SAR Altimetry a reality, believing strongly in the concept and supporting the growth of the know-how. Now one can say that the result of this dedication and commitment both from space agencies and from experts paid off: users from all around the world benefit from more precise measurements with a better spectral characterization in open ocean and surely no one may argue that is necessary to go back. This does not mean that the all the work is concluded. SAR altimetry is still a relatively young discipline as Sentinel-3, the first mission with global SAR coverage, will finish soon only the third year in orbit. And, as for the pulse-limited altimetry experts took almost 20 years to consolidate the algorithms (more or less), also for SAR altimetry will be very likely the same.
Hence, research needs to be continued; today in the current state one can say that SAR altimetry is an operational technology to observe the ocean topography superseding the pulse-limited altimetry which is fated to be retired. In my thesis, I have outlined the possible lines of research, for instance, the dependency plot of SAR SWH with respect PLRM SWH shows still a linear trend versus the sea state: it is not clear whether this is linked to errors in the processing on SAR side, which one between the two datasets returns the truthful representation of the ocean waves, whether this has something to do with the swell effect or sea states and so on. Only recently, (Scagliola et al., 2018) has pointed out the reason for the small bias around +5 cm observed in SAR SWH linking to an approximation made during the L1b processing: very likely more findings like this will come. So the response to the raised question is yes: one can say that the SAR altimetry over open ocean is a consolidated and well-established technology which has reached a state of maturity but not the conclusion of its path.

— *Has SAR Altimetry delivered on the promise to allow a more accurate retrieval of the sea level in the coastal zone?*

The response to this question is a sound yes. The improvement is undisputable and this is even more clear when dedicated coastal SAR retracking is used as shown in (Dinardo et al., 2018).
I have proposed a suite of coastal retrackers (SAMOSA+ and SAMOSA++) with the objective in mind to ensure a full and seamless continuity between open ocean and coastal zone. These retrackers have shown to work properly returning measurements which are closer to numerical circulation models and tide gauges and furthermore they reduce the standard deviation of the marine measurements binned versus the distance to coast. On top of this, the new Sentinel-3 tracking mode

(OLTC) has shown to work properly as well making possible to track all the coastal zones worldwide. Hence now, with Sentinel-3, experts have at their disposal a sensor capable to bring a significant contribution to monitoring of the coastal processes. Now, the next step is to have independent assessment of these novel SAR coastal retrackers by expert groups, implement these SAR coastal retracking in an operational context, run them globally, introduce the coastal sea level data in the sea level rise budget and assess the contribution from the coastal data to global sea level rise.

— *Has SAR Altimetry delivered on the promise to allowing the monitoring of small rivers and lakes which were not possible to monitor with pulse limited altimetry?*

The response to this question is also a yes but without the contribution of the OLTC tracking mode this would not be fully achievable. I have stated that, in case of Sentinel-3B, when this was flying in tandem with Sentinel-3A and operated in SAR mode, Sentinel-3B was not capable to keep the tracking of the Bracciano Lake in closed loop (i.e. autonomous tracking mode). Hence, SAR altimetry helps but the first step is to guarantee that the signal from the small river and lake is in the receiving window. Then I have underlined that the SAMOSA+ retracker, which works fine on the marine surfaces, exhibits limitations over inland water. At this point, the newly designed retracker SAMOSA++ takes over pushing the performance at limit.
Plus, I have recalled the necessity to grid the measurements at higher possible grid step (as at 80 Hz) when trying to observe small targets such as river's transects. When this is done, the joint combination of SAR altimetry, OLTC, 80 Hz allows to monitor small river's transects as for Po River with an accuracy that can be as low as 9 cm in some specific cases. Once again the analysis needs to be repeated, if possible, at global scale and also for river and lakes in rough and rugged areas to reach a full confidence in these numbers. And, furthermore, the OLTC needs to be continuously updated with always new targets in order to better assist the altimeter to track those small targets.
What can be said for the time being is that Sentinel-3 is the best platform ever to make hydrology from space an operational technology.

— *Beyond pursuing it with the conventional empirical methods, will it be possible now with SAR Altimetry to have a physically-based solution to the sea ice freeboard retrieval problem?*

Recent findings based on SAMOSA+ (Laforge et al., 2019) has shown that this is possible: a physically-based solution to the sea ice freeboard retrieval problem is possible with an accuracy at least as good as the one achieved with empirical retrackers (or maybe even better). I believe that when empirical and physical solutions to this problem have comparable accuracy, the physical one should be preferred because it is based on a physical representation of the problem and not on arbitrary thresholds and hence it may offer continuity in the transition between ice-covered ocean and ice-free ocean. Furthermore, an empirical solution, in case of new mission, requires updating and tweaking the values of its thresholds and parameters based on the features of the new mission. On the other side, a physical formulation, being based on the physics of the problem, does not require to update the algorithm but it can be ready to be used from the very beginning of any new mission.

— *Is possible to design and build a retracker capable to work efficiently and reliably over any kind of surface and topography granting seamless transition from one surface to the other one?*

I have tried to do that with the SAMOSA++ retracker: it introduces the RIP echo as part of the physical model itself. This gives to the physical model the capacity to know at run time what kind of backscattering surface it is going to be applied on. This concept applies to all the surfaces: marine, inland water, sea ice and land. I have shown that this retracker works already with satisfactory performance over open ocean, coastal zone and inland waters (over some selected test cases) and soon will be tested over sea ice as well. Hence, it can be considered already a sort of "pan-thematic" retracker. Furthermore, it is "single step" solution and hence it should always ensure continuity between the different surfaces.

— *Can we measure with SAR Altimetry new marine geophysical quantities?*

A first test case of the mean square slope extraction from the RIP has been conducted. More analyses are necessary to understand and correlate this parameter with physical effects.

— *With the modern progress in media and computer science technologies such as grid computing and cloud storage, can be given to the scientists finally the possibility to focus essentially on the scientific aspects of the data exploitation delegating all the cumbersome processes of data processing, data storage and data interface to external and "ad hoc" pools or platforms?*

The time of an expert is a very limited resource and it should be used with attention and parsimony and not be spent in clerical operations. Very often, in the modern data analysis and data exploitation, a big share of time is not spent to analyze or exploit the data but to collect, order, clean them, interface to them and process them. The experts should be relieved from this burden in order to dedicate themselves more to science. Furthermore, the size of the Earth observation data is growing up exponentially as well as the computational load of the algorithms; hence this problem is getting bigger and bigger.
Having well in mind this set of problems, in the frame of this PhD, I have proceeded to link all the developed toolkits in an organic prototype which has been then deployed on the ESA G-POD grid environment. This saved me from the necessity to store Terabytes of input data and saved thousands of hours in processing them. All of this saved time has been then dedicated to the research and hence it was a well-paid effort. But my case was an exception.
Indeed, the response to the question is that nowadays I have the technological capacity to address this problem but for the time being this possibility is not yet given to scientists, at least for many of them.

— *Can we create on line and on demand altimetry services where users can easily process and personalize own processing and share all the results within the whole altimetry community?*

More users use a certain dataset, more the data can be improved receiving the feedbacks from these users. This is a kind of "golden rule" which has proved to be very valuable also in my case. Several bugs in my code have been identified thanks to the data sharing concept and, on the other side, several users have benefit from the on line services I have created making publications, accessing to new types of products not yet available in the official channels, and undertaking R&D activities. One can say that all of this was a virtuous example based on the concept "do ut des". Now this little personal example should be followed up and escalated as new paradigma in the Earth Observation science.

— *Can we push the limits of SAR Altimetry even further?*

The response to the question is also a yes and some personal hints will be given in the next section.

5.2 Outlook

When starting this thesis work, I knew that the time would not be sufficient to realize all what I had in mind. Indeed, I can say that I have kept some left-overs for future research:

- how does SAMOSA++ work over sea-ice ?
- what about SAR processing and SAMOSA++/SAMOSA+ retracking over ice sheets ?
- can we further improve SAMOSA++ with different processing options at L1b?
- what about SAMOSA++ implemented for CryoSat-2 mission ?
- what about 80 Hz gridding in SAR mode over open ocean ?

Whereas I do not have the response yet for the first two questions, regarding the third one I can say that I expect that, by applying zero-padding factors higher than two, one may find out how to best improve the data accuracy, particularly over sea ice. Indeed, the measurement of the freeboard relies strongly on the accuracy of the measurements at the lead between ice floes which is known to return a very peaky waveform (and RIP). Oversampling more this peaky signal with higher zero-padding factors could return a more numerically robust (and better) fit of the model to the echo.
This will be something very intriguing to be tested with CryoSat-2 mission, once that SAMOSA++ retracker will be implemented for CryoSat-2 mission, given the better coverage of the sea ice by CryoSat-2.
Furthermore, another L1b option to assess is the application of the stack's trimming in order to de-contaminate the waveform from off-nadir returns, which might be very beneficial over the inland water bodies and over sea ice.
As far as the last question is concerned, the 80 Hz gridding has been experimented for the moment only with inland water in this thesis work. It deserves also more insights over open ocean as it could improve the precision of the marine geophysical quantities and sample finer the sea surface.
Another intriguing research line is the compensation of the Hamming window in the SAMOSA model by LUT instead of a constant value (as so far done) for the α_p parameter.
I also plan to continue to investigate on the exploitation of the new geophysical measurements available from SAR altimetry as the mean square slope and of course I plan to continue to augment the G-POD Altimetry services with new features.
Finally, the Sentinel-6/Jason-CS mission will raise completely new perspectives and horizons (and of course problems to be solved), particularly related to the Doppler ambiguities and how to compensate them and related to the new opportunities offered by the SAR interleaved mode. Indeed, interleaved SAR represents the technology capable to push the limits of nowadays SAR altimetry even further.

APPENDIX A: Introduction to ESA G-POD SARvatore/SARINvatore Services

The scope of this section is to introduce the ESA G-POD (Grid Processing On Demand) SARvatore & SARINvatore services for the exploitation of the CryoSat-2 SAR/SARin data and Sentinel-3 A/B data (Dinardo, 2014). Indeed all the algorithms presented in this thesis have been collected and linked in prototypes (L1B and L2 processors) and then deployed on the ESA G-POD grid environments, creating hence processing services open to everyone.

The ESA Grid Processing on Demand (G-POD) system is a generic GRID-based operational computing environment providing users with a fast computational facility where EO application can be seamlessly plugged in.

Being now integrated in the G-POD platform, the processors can take hence advantage of the G-POD distributed computing platform (600 CPUs in ~90 Working Nodes) to timely deliver output data products and can interface directly with ESA-ESRIN L1A data catalogue (439'184SAR passes and 367'592 SARin passes for Cryosat-2 and 39'000 SAR passes for Sentinel-3A). Hence, accessing to the services, users and scientists can focus essentially on the scientific exploitation of the data, leaving the burden of the data processing, data collection and data storage to the G-POD system. This is particular relevant for SAR altimetry as a single L1A data product can size several gigabyte and not all the users have in house the technological means to handle and process these bulky data.

Also the data selection process is simplified via a handy graphic interface embedded in the service wherein users can pick-up with only few mouse clicks the satellite passes in their region and time of interest which are available in the service catalogue. Furthermore, it needs to highlight the extreme versatility of the tool since users can customize the processing chain with flags and parameters, according their specific requirements, acting upon a list of configurable options.

The service works over any kind of surfaces and has been recently enhanced for inland water, land, sea-ice and ice sheets, implementing the SAMOSA+ model and integrating ad-hoc models and auxiliary data.

Hence, in definitive, the G-POD service coined SARvatore (SAR Versatile Altimetric Toolkit for Ocean Research & Exploitation) is a web portal that allows any scientist to process on-line, on-demand and on-fly CryoSat-2 SAR/SARIN data and Sentinel-3 A/B data with user-selectable configuration from Level 1A up to Level-2.

After the task submission, users can follow in real time the status of the processing and, at the end of it, the output data products are generated in standard NetCDF format (using CF Convention), therefore being compatible with the Multi-Mission Radar Altimetry Toolbox and other NetCDF tools.

The processing services, initially developed to support in-house R&D studies and PhD research activities, has been extensively used by the worldwide Altimetry Community for research & development experiments, for on-site demonstrations in training courses and workshops, for cross-comparison to third party products, for producing data for publications and conferences, etc. etc. Following up this intense exploitation of the services, the service data products can be considered consolidated and fully validated.

All the data shown in this thesis work have been processed and extracted from the G-POD portal.

The service is open, free of charge and accessible online from everywhere.

- The SARvatore/SARinvatore services are available at the URLs:

https://gpod.eo.esa.int/services/CRYOSAT_SAR/
https://gpod.eo.esa.int/services/CRYOSAT_SARIN/
https://gpod.eo.esa.int/services/SENTINEL3_SAR/

- Join & Share forum available at:

https://wiki.services.eoportal.org/tiki-view_forum.php?forumId=105

- On Line Data Repository available at:

https://wiki.services.eoportal.org/tiki-index.php?page=SARvatore+Data+Repository&highlight=repository

- Services Wiki Pages are:

http://wiki.services.eoportal.org/tiki-index.php?page=GPOD+CryoSat-2+SARvatore+Software+Prototype+User+Manual
http://wiki.services.eoportal.org/tiki-index.php?page=GPOD+SENTINEL-3+SARvatore+Software+Prototype+User+Manual

In order to be granted the access to the service, you need an EO-SSO (Earth Observation Single Sign-On) credentials (for EO-SSO registration, go to https://earth.esa.int/web/guest/general-registration) and afterwards, you need to submit an e-mail to G-POD team (write to eo-gpod@esa.int), requesting the activation of the service for your EO-SSO user account.

APPENDIX B: Delay-Doppler Lexicon

Antenna 3dB (or Half-Power) Beamwidth	It is the angle between the half-power (-3 dB) points of the main lobe, when referenced to the peak effective radiated power of the main lobe. Beamwidth is usually expressed in degrees
Beam Forming	Process to form the Doppler Beam Fan from one burst
Beam Stacking	Process to gather in one data matrix all the Doppler Beams staring at the same surface location from all the bursts
Beam Steering	Process to steer all the 64 Doppler Beams formed from one burst in order to make the 64 Doppler Cells perfectly co-located with 64 surface locations
Burst	A series of 64 transmitted pulses
Burst Data	Received pulses from a burst
Doppler Angle	The angle between surface sample direction vectors and satellite velocity vector evaluated in the burst center
Doppler Beam	Each of the 64 synthetic beams in which the antenna 3dB along track beamwidth can be split by exploiting the Doppler effect due to the satellite motion with respect the ground
Doppler Beam Fan	Set of 64 contiguous Doppler Beams formed from one burst
Doppler Cell	Footprint on ground of each Doppler Beam
Doppler Centroid	Center of Doppler Beam Fan
Doppler Centroid Compensation	Process to steer the Doppler Beam Fan to Nadir
Gridding	Process to place the surface locations on ground
Ground Cell	Same as surface location
Look	A Doppler Beam represents a look. They need to be incoherently summed to build the SAR waveform
Look Angle	The angle between surface location direction vectors and satellite nadir vector evaluated in the burst center
Number of Look	Number of looks used to build the SAR waveform
Range Alignment	Process to align all the Doppler Beams of the stack data in range
RIP Waveform	Incoherent summation of the stack data in range direction
SAR Waveform	Incoherent summation of the stack data in azimuth direction
Stack Data	A collection of the all the Doppler Beams staring at the same surface location
Surface Location	Point on ground where we want to build the SAR waveform
Surface Sample	Same as surface location

List of Acronyms

ACEA	Azienda Comunale Elettricitá e Acque
ADCP	Acoustic Doppler Current Profiler
AGC	Automatic Gain Correction
AIPO	Azienda Interregionale per il fiume PO
ALES	Adaptive Leading Edge Sub-waveform retracker
ARK	ARKona
ASCAT	Advanced Scatterometer
AutoCAL	Automatic CALibration
AWAC	Acoustic Wave And Current profiler
BfG	Bundesanstalt für Gewässerkunde
BRI	Burst Repetition Interval
BSH	Bundesamt für Seeschifffahrt und Hydrographie
CCI	Climate Change Initiative
CF	Climate&Forecast
CoM	Center of Mass
CORR	CORRelation
CryoSat-2	Cryosphere Satellite 2
DAC	Dynamic Atmospheric Correction
DAR	DARsser
DEM	Digital Elevation Model
DDM	Delay-Doppler Map
DORIS	Doppler Orbit and Radio Positioning Integration by Satellite
DOT	Dynamic Ocean Topography
DOTi	Dynamic Ocean Topography instantaneous
DTU	Danmarks Tekniske Universitet
DWD	Deutscher WetterDienst
DWR	coastal Directional Wave Rider
ECMWF	European Centre for Medium-Range Weather Forecasts
ELB	Elbe
ENVISAT	ENVIronmental SATellite
EO-SSO	Earth Observation Single Sign-On
ERA-5	Re-Analysis 5
ERS	European Remote Sensing Satellite
ESA	European Space Agency
ESRIN	European Space Research INstitute
EUMETSAT	EUropean organization for the exploitation of METeorological SATellites
EWAM	European Wave model
FEM	Finite Elements Model
FES	Finite Element Solution
FFT	Fast Fourier Transform

FBR	Full Bit Rate
GCOAST	Geesthacht Coupled cOAstal model SysTem
GEC	GErman Coasts
GIM	Global Ionosphere Map
GME	Global-Model and Europe
GNSS	Global Navigation Satellite System
GPD	GNSS-derived Path Delay
GSL	GNU Scientific Library
GSM	Global Sea state Model
GWAM	Global WAM
HELG	HELGoland station
HELG-SUD	HELGoland SUD station
HELG-NORD	HELGoland NORD station
HZG	Helmholtz Zentrum Geesthacht
Jason-CS/Sentinel6	Jason Continuity of Service/Sentinel-6 altimetry mission
JPL	Jet Propulsion Lab
KOSE	KOSErow station
L1A	Data Level 1A
L1b	Data Level 1b
L2	Data Level 2
LIM3	Louvain-la-Neuve sea Ice Model-3
LHAW	LeucHtturm Alte Weser station
LM	Local-Model
LPF	Low Pass Filter
LRM	Low Resolution Mode
LRR	Laser Retro-Reflectoarray
LSE	Least Square Estimator
LSE-GN	Least Squares Estimator Gauss-Newton
LSE-LM	Levenberg-Marquard
LSM	Local Sea State Model
LST	Local Solar Time
LTAW	LichtTurm Alte Weser
LTKI	LichtTurm KIel
LUT	Look-Up Table
MADD	Median Absolute Deviation Difference
METOP	METeorological OPerational satellite
MLE	Maximum Likelihood Estimator
MODIS	Moderate Resolution Imaging Spectroradiometer
MSS	Mean Sea Surface
MWR	MicroWave Radiometer
NaN	Not a Number

NASA	National Aeronautics and Space Administration
NEMO	Nucleus for European Modeling of the Ocean
OCOG	Offset Center Of Gravity
OLCI	Ocean and Land Colour Imager
OLTC	Open-Loop Tracking Command
OSU	Oregon State University
PDE	Partial Differential Equations
PDGS	Payload Data Ground Segment
PhD	Philosophiae Doctor
PLRM	Pseudo Low Resolution Mode
PP	Pulse Peakiness
PRF	Pulse Repetition Frequency
PTR	Point Target Response
R&D	Research & Development
RDSAR	ReduceD-SAR
REG	REGression
RF	Radio Frequency
RIP	stack Range Integrated Power
RIR	Range Impulse Response
RMSD	Root Mean Square Difference
SAMOSA	SAR Altimetry MOde Studies and Applications
SAR	Synthetic Aperture Radar
SARvatore	SAR Versatile Altimetric Toolkit for Ocean Research & Exploitation
SARin	SAR interferometry (Altimetry)
SARINvatore	SARin Versatile Altimetric Toolkit for Ocean Research & Exploitation
SASS	SASSnitz station
SCHL	SCHLeimünde
SI-MWR	Scanning Imaging MicroWave Radiometers
SINC	Signal Model Involving Numerical Convolution
SIRAL	Synthetic Interferometric Radar ALtimeter
SLA	Sea Level Anomaly
SLAi	Sea Level Anomaly instantaneous
slm	*sul livello del mare* (above sea level)
SNR	Signal to Noise Ratio
SRAL	Synthetic Radar ALtimeter
SRTM	Shuttle Radar Topography Mission
SSB	Sea State Bias
SSH	Sea Surface Height
SSHi	SSH instantaneous
STD	STandard Deviation
STDD	STandard Deviation of Difference

STM	Surface Topography Mission
SWBD	SRTM Water Body Data
SWH	Significant Wave Height
TALES	Tu-Darmstadt Adaptive Leading Edge Sub-waveform retracker
TB	Terabyte
TFMRA	Threshold First Maximum Retracker Algorithm
TRAV	Travemünde
UFSAR	UnFocused Synthetic Aperture Radar
FFSAR	Fully Focused Synthetic Aperture Radar
UNESCO	United Nations Educational Scientific and Cultural Organization
URL	Universal Resource Locator
WAM	WAve Model
WARN	WARNemünde station
WES	WESterland station
WSV	Wasserstrassen und SchifffahrtsVerwaltung des Bundes
WTC	Wet Tropospheric Correction
ZP	Zero-Padding

List of Mathematical Symbols in the Equations

Greek Symbols

$\boldsymbol{\alpha}$	Earth roundness coefficient
$\boldsymbol{\alpha_p}$	3 dB PTR dimensionless width
$\boldsymbol{\Gamma}$	Bernoulli Gamma function
$\boldsymbol{\Gamma_{k,\ell}(0)}$	Gamma function of the SAMOSA waveform model for k range bin and ℓ Doppler beam index
$\boldsymbol{\Delta R_\ell}$	ℓ-th stack beam slant range shift
$\boldsymbol{\Delta\theta_{Look}}$	look angle angular separation
$\boldsymbol{\Delta f_{dop}}$	Doppler frequency angular separation
$\boldsymbol{\Delta R}$	range bin width
$\boldsymbol{\theta_{Look}}$	Doppler Beam look angle
$\boldsymbol{\theta_{Pitch}}$	Antenna Pitch mispointing
$\boldsymbol{\theta_{Roll}}$	Antenna Roll mispointing
$\boldsymbol{\theta_x}$	3dB antenna pattern beamwidth in along track direction
$\boldsymbol{\theta_y}$	3dB antenna pattern beamwidth in across track direction
λ_0	RF carrier wavelength
$\boldsymbol{\lambda_s}$	sea surface skewness
$\boldsymbol{\nu}$	inverse of the mean square slope
$\boldsymbol{\xi}$	generic independent variable
$\boldsymbol{\sigma_{RIP}}$	standard deviation of the RIP
$\boldsymbol{\sigma_z}$	surface elevation standard deviation
$\boldsymbol{\sigma_c}$	sigma composite
$\boldsymbol{\sigma_0}$	backscattering coefficient
$\boldsymbol{\sigma_p}$	3dB Range PTR time width
$\boldsymbol{\tau}$	waveform time-delay
$\boldsymbol{\tau_B}$	Burst length

Latin Symbols

$\boldsymbol{A_{RIP}}$	Amplitude of the RIP
ASAR	resolution ground-cell area in SAR-mode
$\mathbf{B_r}$	received radar bandwidth
BRI	Burst Repetition Interval
c	light speed in the vacuum
dac	dynamic atmospheric correction
DOTi	Instantaneous Dynamic Ocean Topography
DOT	Dynamic Ocean Topography
dry_tropo	dry tropospheric path correction
E	Entropy of the waveform
equi_tide ocean	equilibrium tide

$\mathbf{f_0}$	zero order term of the SAMOSA SAR return waveform model
$\mathbf{f_1}$	first order term of the SAMOSA SAR return waveform model
$\mathbf{G_0}$	antenna pattern gain at boresight
h	altitude of the satellite center of mass above the reference ellipsoid
$\mathbf{I_{nu}^{sc}}$	Scaled Modified Bessel function of first kind and order nu
$\mathbf{I_{nu}}$	Modified Bessel function of first kind and order nu
$\mathbf{I_p}$	in-phase component of the pulse p
iono_delay	ionospheric path delay
IWH	inland water height
k	k-th range bin
$\boldsymbol{\ell}$	ℓ-th Doppler Beam index
L	total number of Doppler beams to be accumulated
$\mathbf{L_{atm}}$	two ways atmosphere losses
$\mathbf{L_y}$	pulse-limited radius
$\mathbf{L_x}$	along-track resolution size
$\mathbf{L_z}$	vertical resolution
load_tide	ocean loading tide
longperiod_tide	ocean long period equilibrium tide
LP	leading Edge Position range bin
MSS	Mean Sea Surface Height
N	number of the waveform range bin
$\mathbf{N_L}$	number of Doppler Beams staring the same surface location (looks)
$\boldsymbol{N_{pulses}}$	Number of pulses in a burst
$\boldsymbol{P_{ML}}$	multi-looked SAR (Delay-Doppler) waveform model
$\boldsymbol{P_{SL}}$	single-look SAR (Delay-Doppler) waveform model
$\mathbf{PDF_{\sigma z}}$	sea surface elevation probability density function
$\mathbf{P_{FS}}$	Flat Surface Impulse Response
$\mathbf{P_{PTR}}$	system point target response
Pr	Return Power Model
pole_tide	geocentric polar tide
PP	waveform Pulse Peakiness
$\mathbf{PP_{RIP}}$	RIP Pulse Peakiness
PRF	Pulse Repetition Frequency
Pu	waveform amplitude
$\boldsymbol{Q_p}$	quadrature component of the pulse p
R	radar altimeter retracker range
$\mathbf{R_{Earth}}$	mean Earth radius
$\mathbf{R_f(0)}$	Fresnel coefficient at normal incidence angle
RIP	Stack Range Integrated Power
$\boldsymbol{RIP_{az}}$	Stack Range Intergrated Power in azimuth direction
$\boldsymbol{RIP_{act}}$	Stack Range Intergrated Power in across track direction

RW	size of the radar receiving window
R_cor_land	range and geophysical correction over land
R_cor_sea	range and geophysical correction over sea
$\mathbf{s^2}$	mean square slope of the sea surface
SLA	Sea Level Anomaly
SLAi	Instantaneous Sea Level Anomaly
SLAio	Instantaneous Sea Level Anomaly without tide
solidearth_tide	solid earth tide
ssb	sea state bias
SSHi	Instantaneous Sea Surface Height
SSH	Sea Surface Height
SWH	Significant Wave Height
t	waveform time
$\mathbf{t_0}$	waveform two way epoch
Tracker_Delay	on board tracker time delay
Tx_Pwr	Transmitted Peak Power
U10	Marine Wind Speed at 10 meter
$\mathbf{V_s}$	satellite velocity magnitude
$\mathbf{W_k}$	waveform power sample at range bin k
wet_tropo	wet tropospheric path correction
x_l	along track coordinate
y_k	across track coordinate
$\langle \mathbf{z} \rangle$	sea height mean
$\mathbf{z_{EM}}$	Electro-Magnetic bias

BIBLIOGRAPHY

Abdalla, S. (2012). Ku-Band Radar Altimeter Surface Wind Speed Algorithm. Marine Geodesy, 35 (sup1), pp. 276-298. 2012. http://doi.org/10.1080/01490419.2012.718676

Abdalla S., Dinardo S., Benveniste J., Janssen P., (2018). Assessment of CryoSat-2 SAR mode wind and wave data. Advances in Space Research. http://doi.org/10.1016/j.asr.2018.01.044

Ablain, M., Cazenave, A., Larnicol, G., Balmaseda, M., Cipollini, P., Faugère, Y., Fernandes, M. J., Henry, O., Johannessen, J. A., Knudsen, P., Andersen, O., Legeais, J., Meyssignac, B., Picot, N., Roca, M., Rudenko, S., Scharffenberg, M. G., Stammer, D., Timms, G., and Benveniste J. (2015). Improved sea level record over the satellite altimetry era (1993–2010) from the Climate Change Initiative project, Ocean Sci., 11, 67-82, 2015. http://doi.org/10.5194/os-11-67-2015.

Abileah, Ron. (2017). Envisat RA-2 Individual Echoes: A Unique Dataset for a Better Understanding of Inland Water Altimetry Potentialities. Journal of Remote Sensing. http://doi.org/10.3390/rs9060605

Abramowitz, M., Stegun, I. (1964). Handbook of Mathematical Functions. Dover Publications, New York, 1964.

Andersen O.B., Stenseng L., Piccioni. G, Knudsen P.: The DTU15 MSS (Mean Sea Surface) and DTU15LAT (Lowest Astronomical Tide) (2016). Reference Surface, Paper 1579, ESA Living Planet Symposium 2016, Prague, Czech Republic.

Andersen, O., Knudsen, P., & Stenseng, L. (2018). A New DTU18 MSS Mean Sea Surface – Improvement from SAR Altimetry. 172. 25 years of progress in radar altimetry symposium, Portugal.

Balanis, C.A. (2016). Antenna Theory: Analysis and Design, ISBN 1118642066, 9781118642061, John Wiley & Sons, 4th Edition, 2016

Bamber J. L. (1994) Ice sheet altimeter processing scheme. International J. of Remote Sensing 15 (4) pp 925-938. https://doi.org/10.1080/01431169408954125

Barjenbruch, U., Mai, S., Ohle, N., Mertinatis U. (2002). Monitoring Water Level, Waves and Ice With Radar Gauges. Proc. of the Hydro 2002 Conf., pp 328 - 337, Kiel, Germany.

Bercher, N.; Dinardo, S.; Lucas, B.M.; Fleury, S.; Calmant, S.; Crétaux, J.-F.; Femenias, P.; Boy, F.; Picot, N.; Benveniste, J. (2013): Applications of CryoSat-2 SAR & SARIn modes for the monitoring of river water levels. In Proceedings of the CryoSat Third User Workshop, Dresden, Germany, 12–14 March 2013; pp. 1–7.

Berry, P.A.M., Freeman, J.A., Rogers, C., Benveniste, J., 2007; "Global analysis of EnviSat RA-2 burst mode echo sequences". IEEE Geoscience and Remote Sensing, Volume 45, Issue 9, Pages 2869-2874. https://doi.org/10.1109/TGRS.2007.902280

Berry, P.A.M., Smith, R.G. and Benveniste, J. (2012) EnviSat altimetry for river and lakes monitoring. International Geoscience and Remote Sensing Symposium (IGARSS), pp. 1844-1847, http://dx.doi.org/10.1109/IGARSS.2012.6351150

Birkett, C.M.; Beckley, B.D (2010): Investigating the Performance of the Jason-2/OSTM Radar Altimeter over Lakes and Reservoirs. Mar. Geod. 2010, 33, 204–238. https://doi.org/10.1080/01490419.2010.488983

Björck, Å. (1996). Numerical Methods for Least Squares Problems. SIAM. ISBN 0-89871-360-9.

Boergens, E.; Nielsen, K.; Andersen, O.B.; Dettmering, D. (2017); Seitz, F. River Levels Derived with CryoSat-2 SAR Data Classification—A Case Study in the Mekong River Basin. Remote Sens. 2017, 9, 1238. https://doi.org/10.3390/rs9121238

Bonnefond, P.; Laurain, O.; Exertier, P.; Boy, F.; Guinle, T.; Picot, N.; Labroue, S.; Raynal, M.; Donlon, C.; Féménias, P.; Parrinello, T.; Dinardo, S. (2018) Calibrating the SAR SSH of Sentinel-3A and CryoSat-2 over the Corsica Facilities. *Remote Sens.* 2018, *10*, 92. https://doi.org/10.3390/rs10010092

Boy F., Desjonqueres J.D., Picot N., Moreau T., Raynal M (2017a). CryoSat-2 SAR-mode over oceans: processing methods, global assessment, and benefits IEEE Trans. Geosci. Remote Sens., 55 (1), 2017, pp. 148-158, https://doi.org/10.1109/TGRS.2016.2601958

Boy F. , Moreau T., Thibaut P., Rieu P.,Aublanc J., Picot N., Femenias P., Mavrocordatos C. (2017b): New stacking method for removing the SAR sensitivity to swell, Oral presentation, Ocean Surface Topography Science Team, 2017, Miami. URL (last accessed 02 January 2020): https://meetings.aviso.altimetry.fr/fileadmin/user_upload/IPM_04__New_Stacking_Process_Boy_OSTST2017.pdf

Brown, G. S. (1977). The Average Impulse Response of a Rough Surface and Its Applications. IEEE Transactions on Antennas and Propagation, Vol. AP-25, No. 1, January, pp. 67-74. http://doi.org/10.1109/TAP.1977.1141536

Buchhaupt, C., Fenoglio L., Dinardo, S., Scharroo R., Becker M. (2018). A Fast Convolution Based Waveform Model for Conventional and Unfocused SAR Altimetry. Advances in Space Research. https://doi.org/10.1016/j.asr.2017.11.039

Cancet, M., Bijac S., Chimot J., Bonnefond P., Jeansou E., Laurain O., Lyard F., Bronner E., Femenias P. (2013). Regional in situ validation of satellite altimeters: Calibration and cross-calibration results at the Corsican sites, Advances in Space Research, Volume 51, Issue 8, p. 1400-1417. http://dx.doi.org/10.1016/j.asr.2012.06.017

Carrere, L; Lyard, F.; Cancet, M.; Guillot, A.(2015): FES 2014, a new tidal model on the global ocean with enhanced accuracy in shallow seas and in the Arctic region, EGU General Assembly 2015, held 12-17 April, 2015 in Vienna, Austria. id.5481

Carrère, L., Lyard F. (2003). Modelling the barotropic response of the global ocean to atmospheric wind and pressure forcing - comparisons with observations, Geophys. Res. Let., 30(6), pp 1275. http://doi.org/10.1029/2002GL016473

Carroll, M., Townshend, J., DiMiceli, C., Noojipady, P., Sohlberg, R. (2009): A New Global Raster Water Mask at 250 Meter Resolution. International Journal of Digital Earth, volume 2 number 4, 2009. http://doi.org/10.1080/17538940902951401

Cipollini P., Gommenginger C., Coelho H., Fernandes J., Gómez-Enri J., Martin-Puig C., Snaith H., Vignudelli S., Woodworth P., Dinardo S., J. Benveniste J. (2009). Experimental coastal altimetry data from the COASTALT project, Additional Contribution to the OceanObs'09 Conference, Venice. URL (last accessed 22 January 2019): http://www.oceanobs09.net/proceedings/ac/FCXNL-09A02-1710143-1-COASTALT_shortpaper_OceanObs.pdf

Cipollini, P., Benveniste J., Bouffard J., Emery W., Fenoglio-Marc F., Gommenginger C. et al. (2010). The Role of Altimetry in Coastal Observing Systems, Proceedings of OceanObs'09: Sustained Ocean Observations and Information for Society (Vol. 2), Hall, J., Harrison, D.E. & Stammer, D., Eds., ESA Publication WPP-306. http://doi.org/10.5270/OceanObs09.cwp.16

Cipollini P., Benveniste J., Donlon C.: Coastal Altimetry (2012). Recent progress and application to storm surge research, IEEE IGARSS 2012, Munich, Germany.

Cipollini P., Calafat F.M. (2016). Extended evaluation of CryoSat-2 SAR data in the Coastal Zone, CryoSat Plus 4 Oceans—CCN1 Technical Note, vol. 1.2, pp 30. http://www.satoc.eu/projects/CP4O/docs/CP4O_CCN_Coastal_NOC_v1.2.pdf

CLS Report (2015). Coastal and Hydrology Altimetry product (PISTACH) handbook. CLS-DOS-NT-10-246. SALP-MU-P-OP-16031-CN 01/00. (URL: https://www.aviso.altimetry.fr/fileadmin/documents/data/tools/hdbk_Pistach.pdf)

Copernicus Climate Change Service (C3S) (2017): ERA-5: Fifth generation of ECMWF atmospheric reanalyses of the global climate. Copernicus Climate Change Service Climate Data Store (CDS), dataset available at https://cds.climate.copernicus.eu/cdsapp#!/home

Collins M., Knutti R., Arblaster J. , Dufresne J.-L., Fichefet T., Friedlingstein P., Gao X., Gutowski W., Johns T., Krinner G., Shongwe M., Tebaldi C., Weaver A., Wehner M., Long-term Climate Change: Projections, Commitments and Irreversibility. Cambridge, United Kingdom and New York, NY, USA: Cambridge University Press, 2013, book section 12, pp. 1029–1136. [Online]. Available: www.climatechange2013.org

Cotton D. (2015). CP40 Final Report, Executive Summary and Abstract, CP4O-FR-01. (URL: http://www.satoc.eu/projects/CP4O/docs/CP4O_FinalReport.pdf)

CP40 Project Report (2014a). Algorithm Theoretical and Validation Document, CP40 Project WP4000. (URL: http://www.satoc.eu/projects/CP4O/docs/CP4O_WP4000_Starlab_ATBD_v1.0.pdf)

CP40 Project Report (2014b). Cryosat-2 Data Processing for CP40, CP40 Project WP4000, 2014. (URL: http://www.satoc.eu/projects/CP4O/docs/ESRIN%20EOP-SER%20for%20CP40.pdf)

Crétaux J-F. , Jelinski W. , Calmant S., Kouraev A., Vuglinski V. , Bergé Nguyen M. , Gennero M-C., Nino F., Abarca Del Rio R. , Cazenave A. , Maisongrande P., SOLS: A Lake database to monitor in Near Real Time water level and storage variations from remote sensing data, J. Adv. Space Res. (2011), http://doi.org/10.1016/j.asr.2011.01.004

CRUCIAL (2016): Cryosat-2 Success over Inland Water and Land, Final Report (ESA)

Cullen R.A., Wingham D.J. (2002). CryoSat level 1b processing algorithms and simulation results, Geoscience and Remote Sensing Symposium IGARSS 2002 IEEE International. http://dx.doi.org/10.1109/IGARSS.2002.1026246

Curlander J. C., McDonough R. N. Synthetic Aperture Radar: Systems and Signal Processing, ISBN: 978-0-471-85770-9 November 1991

Dick S., Kleine E., Müller-Navarra S.H., Klein H., Komo H. (2001). The operational circulation model of BSH (BSH cmod). Model description and validation, Berichte des Bundesamtes für

Seeschifffahrt und Hydrographie 29/2001, Hamburg, Germany, Bundesamtes für Seeschifffahrt und Hydrographie.

Dinardo S., Lucas B., Benveniste J. (2011). SAR Altimetry in Coastal Zone: Performances, Limits, Perspectives, Fifth Coastal Altimetry Workshop, Presentation, San Diego. URL: http://www.coastalt.eu/sandiegoworkshop11

Dinardo S., Lucas B., Benveniste J. (2013). SAR Altimetry at 80 Hz, OSTST 2013, Boulder. URL: https://www.aviso.altimetry.fr/fileadmin/documents/OSTST/2013/posters/Dinardo_coastal.pdf

Dinardo S., Lucas B., Benveniste J. (2014). SAR Altimetry Processing on Demand Service for Cryosat-2 at ESA G-POD, p. 386, Proc. of 2014 Conference on Big Data from Space (BiDS'14), 2014. http://ieeexplore.ieee.org/document/6928554/

Dinardo S., Lucas B., Benveniste J. (2015). Sentinel-3 STM SAR ocean retracking algorithm and SAMOSA model, Geoscience and Remote Sensing Symposium (IGARSS), IEEE International, 2015. http://dx.doi.org/10.1109/IGARSS.2015.7327036

Dinardo S., Fenoglio, L., Buchhaupt C., Becker M., Scharroo R., Fernandes M. J, Benveniste, J. (2018a). Coastal SAR and PLRM altimetry in German Bight and West Baltic Sea. Advances in Space Research. 62. http://doi.org/10.1016/j.asr.2017.12.018

Dinardo S., Fenoglio, L., Buchhaupt C., Becker M., Scharroo R., Fernandes M. J, Benveniste, J. (2018b). Two Years of Coastal SAR and PLRM Altimetry in the North East Atlantic with Sentinel-3A and CryoSat-2, 11th Coastal Altimetry Workshop, Oral Presentation. Abstract Book URL (last access 02 January 2020): https://www.dropbox.com/s/yvih426ccx7b33x/Abstract%20Book%20CAW-11.pdf

Drinkwater, M and H Rebhan, 2007, Sentinel-3 Mission Requirements Document (MRD) Issue 2 revision 0, EOP-SMO/1151/MD-md, https://earth.esa.int/c/document_library/get_file?folderId=13019&name=DLFE-799.pdf

Egbert G., Erofeeva S. (2002). Efficient Inverse Modeling of Barotropic Ocean Tides. J. Atmos. Oceanic Technol., 19, 183204, TPXO8-ATLAS Tide Model data, http:volkov.oce.orst.edu/tides/tpxo8_atlas.html, http://dx.doi.org/10.1175/1520-0426(2002)019%3C0183:EIMOBO%3E2.0.CO;2

Egbert G. D., Erofeeva S. Y., Ray R. D. (2010). Assimilation of altimetry data for nonlinear shallow-water tides: Quarter-diurnal tides of the Northwest European Shelf, Cont. Shelf Res., 30, 668–679, 2010.

Egido, A., Smith, W. (2017). Fully Focused SAR Altimetry: Theory and Applications. IEEE Transactions on Geoscience and Remote Sensing. PP. 1-15. http://doi.org/10.1109/TGRS.2016.2607122

Ekman M., Mäkinen J. (1996). Mean sea surface topography in the Baltic Sea and its transition area to the North Sea: A geodetic solution and comparisons with oceanographic models, J. Geophys. Res., 101(C5), 11993–11999, 1996. http://dx.doi.org/10.1029/96JC00318

ESA Report (2007). CryoSat Mission and Data Description, ESA/ESTEC. (URL: http://esamultimedia.esa.int/docs/Cryosat/Mission_and_Data_Descrip.pdf)

ESA Report (2012). CryoSat-2 Product Handbook, MSSL/UCL. (URL: http://emits.sso.esa.int/emits-doc/ESRIN/7158/CryoSat-PHB-17apr2012.pdf)

ESA Report (2013). Guidelines for the SAR (Delay-Doppler) L1b Processing; European Space Agency/ESRIN (URL: https://wiki.services.eoportal.org/tiki-download_wiki_attachment.php?attId=2540)

ESA Report (2016). Guidelines for sigma nought extraction from CryoSat-2 SAR data; European Space Agency/ESRIN, 2016. URL (last accessed 22 January 2019): https://wiki.services.eoportal.org/tiki-download_wiki_attachment.php?attId=4237

EUMETSAT (2017) Sentinel-3 SRAL Marine User Handbook , EUM/OPS-SEN3/MAN/17/920901, December 2017, available at (last accessed 22 January 2019): https://www.eumetsat.int/website/wcm/idc/idcplg?IdcService=GET_FILE&dDocName=PDF_S3_SRAL_HANDBOOK&RevisionSelectionMethod=LatestReleased&Rendition=Web

EUMETSAT (2019) Sentinel-3 STM L2 Marine Product Notice, EUM/OPS-SEN3/DOC/16/893228, February 2019, available at https://www.eumetsat.int/website/home/News/DAT_4256227.html

Fenoglio-Marc L., Dinardo S., Scharroo R., Roland A., Dutour Sikiric M., Lucas B., Becker M., Benveniste J., Weiss R. (2015). The German Bight: A validation of CryoSat-2 altimeter data in SAR mode, Advances in Space Research, 55, 11, 2641-2656. http://dx.doi.org/10.1016/j.asr.2015.02.014

Fenoglio-Marc L., Scharroo R., Annunziato A., Mendoza L., Becker M., Lillibridge J. (2015). Cyclone Xaver seen by geodetic observations, Geophys. Res. Lett., 42, 9925–9932, 2015. http://dx.doi.org/10.1002/2015GL065989.

Fenoglio-Marc L., Buchhaupt C. (2017a). TB-RDSAR for GPOD, Altimetry Coastal and Open Ocean Performance, Algorithm Theoretical Basis Document, ESA, EOEP-SEOM-EOPS-TN-17-046

Fenoglio-Marc L., Dinardo S., Buchhaupt C., Uebbing B., Scharroo R., Kusche J., Becker M., Benveniste J. (2017b) Coastal altimetry from CryoSat-2, poster at North-American CryoSat Science Meeting and Geodetic Mission Workshop, March 2017.

Fernandes M. J., Lázaro C., Nunes A. L., Pires N., Bastos L., and Mendes, V. B. (2010). GNSS-derived Path Delay: an approach to compute the wet tropospheric correction for coastal altimetry, IEEE Geosci. Remote Sens Lett., 7, 596–600. http://dx.doi.org/10.1109/LGRS.2010.2042425

Fernandes M. J., Lázaro C., Ablain M., Pires N. (2015). Improved wet path delays for all ESA and reference altimetric missions, Remote Sensing of Environment, 169, 50-74, ISSN 0034-4257, http://dx.doi.org/10.1016/j.rse.2015.07.023

Fernandes M. J., Lázaro C. (2016). GPD+ Wet Tropospheric Corrections for CryoSat-2 and GFO Altimetry Missions, Remote Sensing 2016, 8(10), 851. http://dx.doi.org/10.3390/rs8100851, http://www.mdpi.com/2072-4292/8/10/851

Fernandes, M.J.; Lázaro, C. (2018) Independent Assessment of Sentinel-3A Wet Tropospheric Correction over the Open and Coastal Ocean. Remote Sens. 2018, 10, 484. https://doi.org/10.3390/rs10030484

Förste, C., Bruinsma S..L., Abrikosov O., Lemoine J, Marty J. C., Flechtner F., Balmino G., Barthelmes, F., Biancale, R (2014). EIGEN-6C4 The latest combined global gravity field model

including GOCE data up to degree and order 2190 of GFZ Potsdam and GRGS Toulouse, http://doi.org/10.5880/icgem.2015.1

Fu, L., Cazenave A. (2001). Satellite altimetry and earth sciences: a handbook of techniques and applications, Academic Press.

Gill P. E., Murray W., (1978). "Algorithms for the solution of the nonlinear least-squares problem". SIAM Journal on Numerical Analysis. 15 (5): 977–992. http://doi.org/10.1137/0715063

Gommenginger C., Martin-Puig C., Amarouche L., Raney K. R. (2014). Review of State of Knowledge for SAR Altimetry Over Ocean, Eumetsat Report, EUM/RSP/REP/14/749304.

Guccione, P.; Scagliola, M.; Giudici, D. (2018): 2D Frequency Domain Fully Focused SAR Processing for High PRF Radar Altimeters. Remote Sens. 2018, 10, 1943. https://doi.org/10.3390/rs10121943

Guo J.Y., Gao Y.G., Hwang C.W., Sun J.L. (2010). A multi-subwaveform parametric retracker of the radar satellite altimetric waveform and recovery of gravity anomalies over coastal oceans. Sci. China Earth Sci. 53 (4), 610–616. https://doi.org/10.1007/s11430-009-0171-3

Hayne G.S. (1980). Radar altimeter mean return waveforms from near-normal-incidence ocean surface scattering: IEEE Transactions on Antennas and Propagation, 28, 5, 687-692, http://dx.doi.org/10.1109/TAP.1980.1142398

Helm, V., Humbert, A., and Miller, H. (2014): Elevation and elevation change of Greenland and Antarctica derived from CryoSat- 2, The Cryosphere, 8, 1539–1559, https://doi.org/10.5194/tc-8-1539-2014

Horn R. A., Johnson C.R. (2012). Matrix analysis. Cambridge University.

Idris N. H., Deng X. (2012). The Retracking Technique on Multi-Peak and QuasiSpecular Waveforms for Jason-1 and Jason-2 Missions near the Coast, Marine Geodesy, 35:sup1, 217-237. https://doi.org/10.1080/01490419.2012.718679

Iijima B. A., Harris I. L., Ho C. M., Lindqwister U.J., Mannucci A.J., Pi X., Reyes M.J., Sparks L.C., Wilson B.D. (1999): Automated daily process for global ionospheric total electron content maps and satellite ocean altimeter ionospheric calibration based on Global Positioning System data. Journal of Atmospheric and Solar-Terrestrial Physics; 61(16):1205–1218. http://dx.doi.org/10.1016/S1364-6826(99)00067-X

IPCC, Climate Change 2013: The Physical Science Basis. Contribution of Working Group I to the Fifth Assessment Report of the Intergovernmental Panel on Climate Change. Cambridge, United Kingdom and New York, NY, USA: Cambridge University Press, 2013. [Online]. Available: www.climatechange2013.org

Kay, S. M. (1993). Fundamentals of Statistical Signal Processing: Estimation Theory. Prentice Hall. p. 47. ISBN 0-13-042268-1.

Kurtz N. T., Galin N., Studinger, M. (2014). An improved CryoSat-2 sea ice freeboard retrieval algorithm through the use of waveform fitting, Cryosphere, 8, 1217-1237. https://doi.org/10.5194/tc-8-1217-2014

Kwok R. and Rothrock D. (2009), Decline in arctic sea ice thickness from sub-marine and icesat records: 1958–2008, Geophysical Research Letters, vol. 36, no. 15, 2009. https://doi.org/10.1029/2009GL039035

Laforge A., Fleury S., Dinardo S., Remy R., Garnier F. , Verley J. Benveniste J. (2019): Inter-comparison of SAR processing and retracker for an improved altimetric freeboard estimation (in prep.)

Lebedev S., Vignudelli S., Cipollini P., Lyard F., Roblou L., Kostianoy A., Mamedov R. et al. (2008). Exploiting satellite altimetry in coastal ocean through the ALTICORE project, Russian Journal of Earth Sciences Vol. 10, Es1002. http://dx.doi.org/10.2205/2007es000262

Lyard F., Lefèvre F., Letellier T., Francis O. (2006). Modelling the global ocean tides: a modern insight from FES2004, Ocean Dynamics, 56, 394-415. http://doi.org/10.1007/s10236-006-0086-x

Madsen, K., Nielsen, H.B. and Tingleff, O. (2004) Methods for Non-Linear Least Squares Problems. 2nd Edition, Informatics and Mathematical Modelling (IMM), Technical University of Denmark (DTU), http://www2.imm.dtu.dk/pubdb/views/edoc_download.php/3215/pdf/imm3215.pdf

Manning, R. (1889). On the flow of water in open channels and pipes. Transactions of the Institution of Civil Engineers of Ireland, 20, 161–207.

Martin-Puig C., Marquez J., Ruffini G., Raney K.R., Benveniste, J. (2008). SAR Altimetry Applications over Water, ESA SeaSAR Workshop, 21-25 January, SP-656.

Moore P., Birkinshaw S.J., Americo A., Restano M., Benveniste J. (2018): CryoSat-2 Full Bit Rate Level 1A processing and validation for inland water applications, Advances in Space Research, 2018,ISSN 0273-1177, https://doi.org/10.1016/j.asr.2017.12.015

Moreau T. et al. (2016), "Effect of swell and wind-waves on the altimeter-derived estimates: Analyzing real and simulated data", Oral presentation, Ocean Surface Topography Science Team 2016, La Rochelle, November 1-4. URL (last accessed 02 January 2020): https://meetings.aviso.altimetry.fr/fileadmin/user_upload/tx_ausyclsseminar/files/ERR_05_OSTST_2016_SAR_Errors_SeaStates_TMoreau_10h00.pdf

Müller, F. L., Dettmering, D., Bosch, W., and Seitz, F. (2017): Monitoring the Arctic seas: How satellite altimetry can be used to detect open water in sea-ice regions, Remote Sensing, 9, 551, https://doi.org/10.3390/rs9060551, http://www.mdpi.com/2072-4292/9/6/551,

Neumann B., Vafeidis A.T., Zimmermann J., Nicholls R.J. (2015). Future Coastal Population Growth and Exposure to Sea-Level Rise and Coastal Flooding - A Global Assessment. PLoS ONE 10(3): e0118571. http://dx.doi.org/10.1371/journal.pone.0118571

Nielsen, K., Stenseng, L., Andersen, O.B., Knudsen, P., (2017). The Performance and Potentials of the CryoSat-2 SAR and SARIn Modes for Lake Level Estimation. Water 9, 374. https://doi.org/10.3390/w9060374

Passaro M., Cipollini P., Vignudelli S., Quartly G., Snaith H. M. (2014). ALES: A multi-mission adaptive subwaveform retracker for coastal and Remote Sensing of Environment, 173-189. https://doi.org/10.1016/j.rse.2014.02.008

Passaro M., Dinardo S., Quartly G.D., Snaith H., Benveniste J., Cipollini P., Lucas B. (2016). Cross-calibrating ALES Envisat and CryoSat-2 Delay-Doppler: A coastal altimetry study in the Indonesian Seas. Adv. Space Res. 58, 289-303. http://dx.doi.org/10.1016/j.asr.2016.04.011

Passaro, M., Müller, F. L., and Dettmering, D. (2017): Lead detection using Cryosat-2 delay-doppler processing and Sentinel-1 SAR images, 30 Advances in Space Research, 62, 1610–1625, https://doi.org/10.1016/j.asr.2017.07.011, http://www.sciencedirect.com/science/article/pii/S0273117717305057, 2017

Pukelsheim F. (1994). The Three Sigma Rule. American Statistician 48: 88–91.

Raney K.R. (1998). The Delay Doppler radar altimeter, IEEE Transactions on Geoscience 542 and Remote Sensing, 36, 1578-1588. https://doi.org/10.1109/36.718861

Raney, K. R. (2012). CryoSat SAR-mode looks revisited. IEEE Geoscience and Remote Sensing Letters - IEEE GEOSCI REMOTE SENS LETT. 9. 393-397. https://doi.org/10.1109/LGRS.2011.2170052

Ray C., Martin-Puig C., Clarizia M.P., Ruffini G., Dinardo S., Gommenginger C., Benveniste J. (2015). SAR Altimeter Backscattered Waveform Model, IEEE Trans. GeoSci. and Rem. Sens., 53, 2, 911 – 919. http://dx.doi.org/10.1109/TGRS.2014.2330423

Raynal, M.; Labroue, S.; Moreau, T.; Boy, F.; Picot, N. (2018) From conventional to Delay Doppler altimetry: A demonstration of continuity and improvements with the Cryosat-2 mission Advances in Space Research, Volume 62, Issue 6, p. 1564-1575. www.doi.org/10.1016/j.asr.2018.01.006

Rinke, A., Maslowski, W., Dethloff, K., and Clement, J. (2006): Influence of sea ice on the atmosphere: A study with an Arctic atmospheric regional climate model, Journal of Geophysical Research: Atmospheres, 111, https://doi.org/10.1029/2005JD006957 , https://agupubs.onlinelibrary.wiley.com/doi/abs/10.1029/2005JD006957, 2006

Roblou L., Lyard F., Henaff M. L., Maraldi C. (2007). X-track: a new processing tool for altimetry in coastal oceans, 2007 IEEE International Geoscience and Remote Sensing Symposium, Barcelona,5129-5133.
http://dx.doi.org/10.1109/IGARSS.2007.4424016

Roscher, Ribana & Uebbing, Bernd & Kusche, Jürgen. (2017). STAR: Spatio-Temporal Altimeter Waveform Retracking using Sparse Representation and Conditional Random Fields. Remote Sensing of Environment. Vol. 201. https://doi.org/10.1016/j.rse.2017.07.024

Rosmorduc V., Benveniste J., Bronner E., Dinardo S., Lauret O., Maheu C., Milagro-Pérez M., Picot N., (2011). Radar Altimetry Tutorial, http://www.altimetry.info/radar-altimetry-tutorial/

Rothrock D. A., Yu Y., Maykut G. A. (1999), Thinning of the arctic sea-ice cover, Geophysical Research Letters, vol. 26, no. 23, pp. 3469–3472, 1999. https://doi.org/10.1029/1999GL010863

Scagliola M., Fornari M.., Bouffard J., Femenias P., Parrinello T. (2015). Main evolutions and expected quality improvements in Baseline C Level1b products, ESA Technical Note, C2-TN-ARS-GS-5154.

Scagliola M., Fornari M., Tagliani N. (2015), Pitch Estimation for CryoSat by Analysis of Stacks of Single-Look Echoes, in IEEE Geoscience and Remote Sensing Letters, vol. 12, no. 7, pp. 1561-1565, July 2015. https://doi.org/10.1109/LGRS.2015.2413135

Scagliola S., Fornari M., Recchia L.(2018): Fast and accurate Delay/Doppler processing: applying range walk compensation while preserving the computational complexity, Ocean Surface Topography Science Team Conference, Oral Presentation, Azores , 2018. URL (last accessed 02 January 2020): https://meetings.aviso.altimetry.fr/fileadmin/user_upload/IPC_02_Scagliola.pdf

Schall J., Löcher A., Kusche J., Rietbroek R., Sudau A. (2016): Consistency of geoid models, radar altimetry, and hydrodynamic modelling in the North Sea, Marine Geodesy, http://dx.doi.org/10.1080/01490419.2016.1152334

Scharroo R. (2002). A Decade of ERS Satellite Orbits and Altimetry, Delft Univ. Press, Delft, Netherlands.

Scharroo R. (2016). RADS RDSAR Algorithm Theoretical Basis Document, Version0.3, CP4O Project Report, 2014 - updated May 2016. (URL: http://www.satoc.eu/projects/CP4O/docs/tud_rdsar_atbd.pdf)

Smith W. H. F., Scharroo R. (2014). Waveform aliasing in satellite radar altimetry. IEEE Transactions on GEOSCIENCE and REMOTE SENSING, 53,1671–1682. http://doi.org/10.1109/TGRS.2014.2331193

Smith, Walter. (2018). Spectral Windows for Satellite Radar Altimeters. Advances in Space Research. 62. http://doi.org/10.1016/j.asr.2018.01.012

Schneider, R, Tarpanelli, A, Nielsen, K, Madsen, H & Bauer-Gottwein, P. (2018), Evaluation of multi-mode CryoSat-2 altimetry data over the Po River against in situ data and a hydrodynamic model Advances in Water Resources, vol. 112, pp. 17-26. http://doi.org/10.1016/j.advwatres.2017.11.027

Stanev E., Schulz-Stellenfleth J., Staneva J., Grayek S., Grashorn S., Behrens A., Koch W., Pein J., (2016). Ocean Forecasting: From Regional to Coastal Scales. Ocean Science Discussions. 1-50. http://doi.org/10.5194/os-2016-25

Stroeve J. C., Kattsov V., Barrett A., Serreze M., Pavlova T., Holland M., Meier W. N. (2012): Trends in arctic sea ice extent from cmip5, cmip3 and observations, Geophysical Research Letters, vol. 39, no. 16, 2012. https://doi.org/10.1029/2012GL052676

Tarpanelli, A., Brocca L., Melone, F., Moramarco T. Lacava T., Faruolo, M & Pergola N., Tramutoli V. (2013). Toward the estimation of river discharge variations using MODIS data in ungauged basins. Remote Sensing of Environment. 136. 47-55. https://doi.org/10.1016/j.rse.2013.04.010

Tayfun A. (1980). Narrow-band nonlinear sea waves. Journal of Geophysical Research. 85 (C3), 1543–1552. http://dx.doi.org/10.1029/jc085ic03p01548

Tilling, Rachel & Ridout, A & Shepherd, Andrew. (2016). Near-real-time Arctic sea ice thickness and volume from CryoSat-2. Cryosphere. 10. 2003-2012. https://doi.org/10.5194/tc-10-2003-2016

Tseng K.H., Shum C.K., Yi Y., Fok H.S., Kuo C.Y., Lee H., Cheng X., Wang X. (2013). Envisat altimetry radar waveform retracking of quasi-specular echoes over the ice-covered Qinghai lake. Terr. Atmos. Ocean. Sci. ,24, 615–627. http://dx.doi.org/10.3319/TAO.2012.12.03.01

Vignudelli S., Kostianoy A. G., Cipollini P., Benveniste J. (2011). Coastal Altimetry. Berlin Heidelberg. Springer-Verlag. http://dx.doi.org/10.1007/978-3-642-12796-0.

Villadsen, H.; Andersen, O.B.; Stenseng, L.; Nielsen, K.; Knudsen, P. (2015): CryoSat-2 altimetry for river level monitoring—Evaluation in the Ganges–Brahmaputra River basin. Remote Sens. Environ. 2015, 168, 80–89. https://doi.org/10.1016/j.rse.2015.05.025

Walsh E.J., Vandemark D. C., Friehe C.A, Burns S.P., Khelif D., Swift R.N., Scott J.F. (1998): Measuring Sea Surface Mean Square Slope With A 36-Ghz Scanning Radar Altimeter Journal Of Geophysical Research, Vol. 103, No. C6, Pages 12,587-12,601, June 15, 1998 https://doi.org/10.1029/97JC02443

Wingham D. J., Rapley C. G., Griffiths H. (1986): New technique in satellite altimeter tracking systems IGARSS'86 Symposium Digest 1 (ESA Publications Division, Noordwijk) pp. 185-190

Wingham, D. J., Phalippou, L., Mavrocordatos, C., Wallis D. (2004): The Mean Echo and Echo Cross Product From a Beamforming Interferometric Altimeter and Their Application to Elevation Measurement. IEEE Transactions on Geoscience and Remote Sensing, 42, 2305-2323. http://dx.doi.org/10.1109/TGRS.2004.834352